

Electronic Structure Of Ni-Mn Based Heusler Alloys

Thesis submitted for the degree of
Doctor of Philosophy (Science)

in

Physics (Theoretical)

by

SOUMYA DIPTA PAL

Department of Physics
University of Calcutta
2018

*Dedicated to my parents, my wife and my most
beloved son*

Acknowledgements

Though only my name appears on the front page of this thesis, this could not be successful without continuous guidance, inspiration, support, help and mentorship of some individuals in my both professional and personal life. On the occasion of the submission of my long-waited thesis I would like to express my heartfelt gratitude to all of them.

First and foremost, I would like to express my special appreciation and thanks to my supervisors Dr. Chhayabrita Biswas and Prof. Priya Mahadevan, who have supported me throughout my research work. Without their proper guidance I could not even think about this thesis. I have also learned from them how to write a scientific article. Moreover, I have been acquainted with scientific ethics by them. I am very grateful for their continuous assistance, friendly attitude in any discussion. I am really fortunate enough to have them as my supervisors.

I would also like to thank every person of S. N. Bose Centre, for providing me excellent research facilities and a comfortable environment all along. It seems my second home. I wish to acknowledge funding from DST Nanomission under the umbrella of the Thematic Unit of Computational Material Science and DAE-BRNS.

I would also like to thank DST-KEK for financial assistance to do XRD experiment in Photon factory, Japan. We also wish to thank Dr. M. K. Mukhopadhyay and Mr. Satish Poddar for their help during experiment.

I would like to convey special thanks to my juniors Sagar, Shishir, Poonam. Whenever, I need any help I approached them. In my research work Sagar has helped me a lot. Expressing thanks is not sufficient for him.

I am thankful to my seniors Abhinav da, Prashant da, Debraj da, Rajiv da, Saikat Da, Soumyajit da, Hirak da, Kapil da, Ashis da, Bipul da, Tanumoy da, Biswaiit da, Dibakar da, A P Jena da. They helped me in many circumstances whenever I face any problem. Whenever I have problems related to computer or any software, two names always came to mind are A P Jena da and Rajiv da. I shared a lot of things with my cubical mate Biswaiit da and Dibakar da. I would also like to thank Sandeep Da for his help and useful scientific discussions. I would like to thank Aslam, Chandan, Avisek and all my juniors of S N Bose Centre for providing cheerful environment in different interactions.

Finally, it would be never possible to complete my thesis without the continuous support from my family. I am really fortunate to have my mother and father throughout my career as well as my life. They have unconditional love, affection and most importantly believe on me. My father is my role model. With me, my mother also eagerly waited for the completion of the thesis. I am grateful to my late father in law, mother in law, sister-in-laws, co-brothers Sudipta Da, Surojit

da, my nephew Swapnil, niece Tinni, uncles, aunties for their constant love. I also want to thank my elder brothers Tanumoy and Abhirup for their useful discussions and suggestions. Lastly, the person without whose support it never be possible to fulfill my dream is my wife Subarna. She is always with me as a best friend, as a real life partner. I shared each and every problem with her and every time her suggestions helped me. She motivated me a lot when I became depressed. She is invaluable to me.

Soumyadipta Pal
Kolkata, July, 2018

List of Publications

Thesis work:

1. **Soumyadipta Pal**, Chhayabrita Maji, and Priya Mahadevan, “*The band Jahn-Teller effect in Ni₂MnGa: What drives it?*”, **Phys. Rev. B** submitted (2018).
2. **Soumyadipta Pal**, Sagar Sarkar, S. K. Pandey, Chhayabrita Maji, and Priya Mahadevan, “*Driving force for martensitic transformation in Ni₂Mn_{1+x}Sn_{1-x}*”, **Phys. Rev. B** 94, 115143 (2016).
3. **Soumyadipta Pal**, Priya Mahadevan, and C. Biswas “*Site occupancy trend of Co in Ni₂MnIn: Ab initio Approach*”, **AIP Conf. Proc.** 1665, 090020 (2015).
4. **Soumyadipta Pal**, Priya Mahadevan, and C. Biswas “*Role of Excess Mn for Martensitic Transformation in Ni₂Mn_{1+x}Sn_{1-x}: Ab initio Approach*”, **AIP Conf. Proc.** 1591, 58 (2014).
5. **Soumyadipta Pal**, Sandeep Singh, and C. Biswas, “*Effect of co-existing crystal structures on magnetic behavior of Ni₂Mn_{1+x}Sn_{1-x} magnetic shape memory alloy*”, **Manuscript in preparation**.
6. **Soumyadipta Pal**, Chhayabrita Maji, and Priya Mahadevan, “*Origin of martensitic transformation in Ni₂Mn_{1+x}In_{1-x}: Ab initio Approach*”, **Manuscript in preparation**.

Conference presentations:

1. **Soumyadipta Pal**, Priya Mahadevan, and C. Biswas, “*Driving force of Martensitic Transformation in Ni-Mn based alloys*”, **National Conference on Electronic Structure, 2017** - Poster Presentation at IISER Bhopal.
2. **Soumyadipta Pal**, Priya Mahadevan, and C. Biswas, “*Site occupancy trend of Co in Ni₂MnIn: Ab initio approach*”, **DAE-Solid State Physics Symposium 2014** - Poster Presentation at VIT University, Vellore, Tamilnadu.
3. **Soumyadipta Pal**, Priya Mahadevan, and C. Biswas, “*Role of excess Mn for martensitic transformation in Ni₂Mn_{1+x}Sn_{1-x}: Ab initio approach*”, **DAE-Solid State Physics Symposium 2013** - Poster Presentation at Thapar University, Patiala, Punjab.
4. **Soumyadipta Pal**, Sandeep Singh and C. Biswas, “*Magneto-structural coupling due to martensitic crystal structure evolution in Ni₂Mn_{1+x}Sn_{1-x}*”, **First users' meeting of the Indian Beamline at Photon Factory, KEK, Japan 2013** - Poster Presentation, organized by Saha Institute of Nuclear Physics, Kolkata.

5. **Soumyadipta Pal**, Priya Mahadevan and C. Biswas, “*Effect of Mn doping in $Ni_2Mn_{1+x}Sn_{1-x}$ alloys: Ab initio approach*”, **National Symposium on “Advances in Materials Science and Technology” (AMST - 2012)** - Poster Presentation, organized by Department of Physics, School of Sciences, Gujarat University.

Contributory work:

1. Sandeep Singh, **Soumyadipta Pal**, and C. Biswas, “*Disorder induced resistivity anomaly in $Ni_2Mn_{1+x}Sn_{1-x}$* ”, **J. Alloys Compd.** 616, 110 (2014).

Contents

Table of Contents	ix
1 Introduction	1
1.1 Heusler alloy	2
1.2 Martensitic transformation in Heusler alloy	4
1.3 Structural properties of Ni-Mn based Heusler alloy	5
1.3.1 Austenitic Phase	5
1.3.2 Martensitic Phase	6
1.4 Magnetic properties of Ni-Mn based Heusler alloy	10
1.4.1 Magnetic moment and thermomagnetization	10
1.4.2 Magnetic field induced phase transition and inverse magnetocaloric effect .	12
1.4.3 Negative magnetoresistance	15
1.4.4 Zero-field-cooled exchange bias effect	16
1.5 Motivation to investigate Heusler alloy	18
1.6 Outline of thesis	23
2 Theoretical and Experimental methods	37
2.1 Theoretical methods	38
2.1.1 Introduction	38
2.1.2 Born-Oppenheimer Approximation	38
2.1.3 Thomas-Fermi model	39
2.1.4 Hohenberg-Kohn theorems	40
2.1.5 Kohn-Sham equations	40
2.1.6 Electron exchange and correlation interactions	42
2.1.7 Plane-waves as basis functions	45
2.1.8 DFT implementation by Vienna <i>ab-initio</i> simulation package (VASP) .	45
2.1.9 Wannier functions	46
2.2 Experimental methods	47
2.2.1 Sample preparation: Arc melting	47
2.2.2 Differential Scanning Calorimetry (DSC)	48
2.2.3 X-ray diffraction	49
2.2.4 Magnetic susceptibility	52

2.2.5 Ultra-violet photo-electron spectroscopy (UPS)	53
3 The band Jahn-Teller effect in Ni₂MnGa: What drives it?	57
3.1 Introduction	58
3.2 Methodology	60
3.3 Results and Discussions	61
3.4 Conclusion	72
4 Origin of martensitic transformation of Ni₂Mn_{1+x}Sn_{1-x}	77
4.1 Introduction	78
4.2 Theoretical Method	79
4.3 Site Occupancy and Magnetic Ground State	80
4.4 Driving force for martensitic transformation	84
4.5 Theoretical realization of Orthorhombic structure	94
4.6 Conclusions	97
5 Crystal structure effect on properties of Ni-Mn-Sn	103
5.1 Introduction	104
5.2 Experimental and Theoretical Method	107
5.3 Results and Discussion	109
5.3.1 Temperature variations of crystal structure	109
5.3.2 Change in phase fraction of 4L and 14L with temperature	119
5.3.3 Thermo-susceptibility behavior	122
5.3.4 Magnetic ground state of Mn1-Mn2	123
5.3.5 Crystal structure effect on electronic structure	126
5.4 Conclusion	132
6 Electronic structure of Ni₂Mn_{1+x}In_{1-x} and Co doped Ni₂Mn_{1+x}In_{1-x}	139
6.1 Introduction	140
6.2 Computational Details	141
6.3 Results and Discussions	142
6.3.1 Electronic structure of Ni ₂ Mn _{1+x} In _{1-x}	142
6.3.2 Electronic structure of Co doped Ni-Mn-In	154
6.4 Conclusions	161
7 Conclusions	167
A Role of Coulomb correlations in the properties of Heusler alloys	173
A.1 Introduction	174
A.2 Theoretical and Experimental Methods	174
A.3 Results and Discussions	175
A.4 Conclusions	181

Chapter 1

Introduction

1.1 Heusler alloy

Heusler alloys have been extensively investigated for last hundred years since its discovery in 1903. It is named after German mining engineer and chemist F. Heusler who discovered that ferromagnetic alloys form with non-magnetic elements [1]. Heusler alloys are ternary intermetallic compounds with stoichiometric formula X_2YZ known as “full-Heusler alloy”. The X and Y are transition elements and Z is *p* block element. The Cu_2MnSn was the first full-Heusler alloy discovered by Heusler, which is ferromagnetic, even though its constituent elements are nonmagnetic.

The full-Heusler structure with chemical formula X_2YZ consists of interpenetrating face centered cubic (FCC) sublattices with atoms X, Y and Z having Wyckoff positions 8c ($1/4, 1/4, 1/4$ and $1/4, 1/4, 3/4$), 4a ($0, 0, 0$) and 4b ($1/2, 1/2, 1/2$), respectively which results in cubic $L2_1$ crystal structure with crystal symmetry $Fm\bar{3}m$ as shown in fig. 1.1 [1–6].

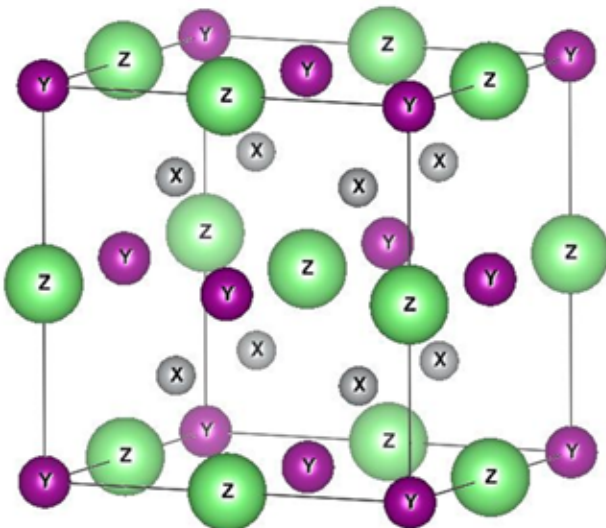


Figure 1.1 Cubic $L2_1$ crystal structure of Heusler alloys.

The physical properties of full-Heusler alloys are strongly dependent on the arrangement of the atoms. The disorder in the position modifies the properties. In the stoichiometric alloy from fully ordered perfect cubic $L2_1$ structure, one can achieve 9 different disordered structures by exchanging the atoms [7]. This type of disorder is referred to as “structural disorder”. Moreover, when doped atoms substitute the other parent atoms, one has off-stoichiometric alloys, which is

referred to as “chemical disorder”. Both types of disorder are required to explain the magnetic properties of Heusler alloys [8].

Heusler alloys have various magnetic properties like antiferromagnetism, helimagnetism, Pauli paramagnetism etc [9–12]. Mainly, they are considered to be ideal local moment systems [13–15] and magnetic ground state is described by Heisenberg type hamiltonian $H = -\sum_{i,j}^{i \neq j} J_{ij} S_i S_j$ [16]. In Mn based Heusler alloys (X_2MnZ), the magnetic moment is mainly localized on Mn. The localized character of the magnetization results from the exclusion of minority-spin electrons from the Mn $3d$ states. Since, the Mn - Mn distance is ≥ 4 Å, there is no significant direct interaction between the Mn atoms [14]. The Ruderman-Kittel-Kasuya-Yosida (RKKY) type indirect exchange interaction gives rise to magnetism in these materials. When the interaction is mediated by the X conduction electrons the alloy is ferromagnetic and if it is mediated by the Z conduction electrons, it can have either sign depending on the position of the Fermi level in the Mn-Z p - d hybrid states [13].

Heusler alloys are promising materials for contemporary research. The new class of off-stoichiometric magnetic shape memory alloys, Ni-Mn-Z (Z = Ga, Sn, In, Sb) Heusler alloys exhibit diverse physical properties such as magnetic shape memory effect, magnetocaloric effect, magnetic superelasticity effect, magnetoresistance, and exchange bias effect [17–23]. These fascinating properties make the alloys a potential candidate for applications in solid-state magnetic refrigeration [19], magnetic actuators [24, 25] and magnetic sensors [25] etc. This class of material is very important for replacing present way of cooling with hazardous gases. These magnetic shape memory alloys exhibit giant magnetocaloric effect, also, with applied pressure that are comparable to present materials used for solid-state refrigeration [26]. Moreover, these alloys offer cost effective technology. Furthermore, the interest in shape memory alloys has been driven by the enormous potential these materials represent in various fields ranging from medicine [27] to robotics [28] to aeronautics [29]. Most of these novel properties are related to martensitic transformation. In addition to their technological relevance, magnetic Heusler alloys are particularly interesting for fundamental investigations to understand the interplay between their complex crystal structure and magnetism.

1.2 Martensitic transformation in Heusler alloy

The martensitic transformation is mainly first order magneto-structural phase transformation which is shear-like displacive and diffusionless phase transformation. Both atomic shuffle and lattice distortive strain can be involved in displacive transitions. If the lattice-distortive displacement is large, high elastic strain energies are involved to control the transition. The martensitic phase transforms from an ordered phase, called “austenite”. The austenitic structure has higher symmetry than the martensitic structure. This transformation occurs by nucleation and growth of martensitic phase in the parent austenitic matrix (shown in fig. 1.2 (a)) accompanied by lattice distortion (for example cubic to tetragonal distortion shown in fig. 1.2 (b)). This induces a large strain around the martensitic phase boundary. Further progress of nucleation and growth requires reduction of this strain energy. This can be achieved via “slip” and “twinning” (shown in fig. 1.2 (c) and (d)) which are called “lattice invariant strain” [30]. The process of minimization of the strain is called strain accommodation. The differently oriented twinned structures are called twin variants. The interface between twins is called twin boundary. Generally, the transformation requires that these twin variants are accommodated to a habit plane as a lattice invariant interface maintaining the geometrical relationship between the two crystal structures. The lattice mismatch is compensated by twinning. A characteristic feature of martensitic transformations in Heusler alloys is the reversibility of various physical properties such as strain, magnetization, electrical conductivity etc. under thermal cycling. Although, due to its first order nature of phase transformation it does not trace the same path. So, hysteresis occurs during cooling and heating. The characteristic transformation temperatures are called martensitic start (M_s), martensitic finish (M_f) (during cooling) and austenitic start (A_s), austenitic finish (A_f) (during heating) temperatures. When the alloy is cooled below M_f , entire phase is composed of martensite variants and upon heating above A_f , the austenite phase is reconstructed completely. This phenomena of recovery of structure is also driven by stress, magnetic fields, electric fields etc.

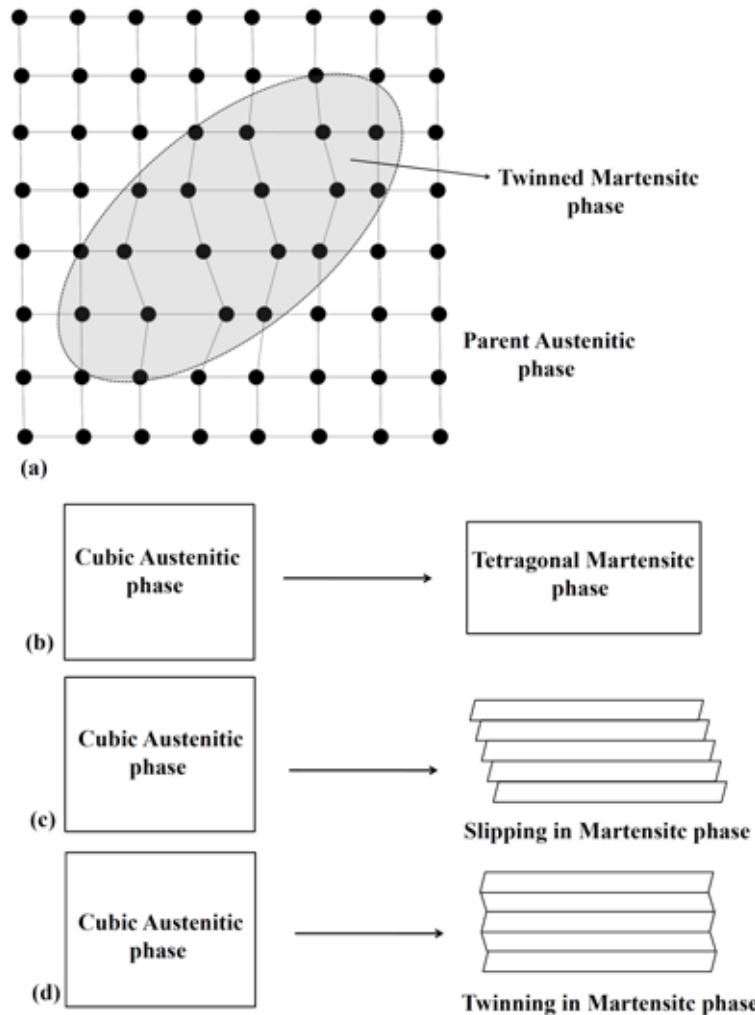


Figure 1.2 Schematic representation of (a) growth of martensitic phase in austenitic phase, (b) change of structure, strain accommodation by (c) slip and (d) twinning.

1.3 Structural properties of Ni-Mn based Heusler alloy

1.3.1 Austenitic Phase

The high-temperature phase of Ni-Mn based Heusler alloys is austenitic phase. This phase has the cubic L₂₁ structure ($Fm\bar{3}m$ space group). The typical L₂₁ structure is shown in fig. 1.1. This is the most ordered structure. The structure is formed by melting the individual constituent elements and rapid quenching of the melt. The L₂₁ structure might be transformed via the fully disordered

A2 phase having random occupation of every lattice site, or through the intermediate partially ordered B2' phase [31], in which only the Mn and Z atoms occupy arbitrary positions, or directly to the completely ordered body-centered cubic L2₁ phase [32, 33]. For example, in stoichiometric Ni₂MnGa, the B2' to L2₁ transition occurs at 1071 K. Above martensitic transition temperature the alloy remains in the L2₁ phase. The typical X-ray diffraction pattern of Ni-Mn-Sn alloy in austenitic phase is shown in fig. 1.3.

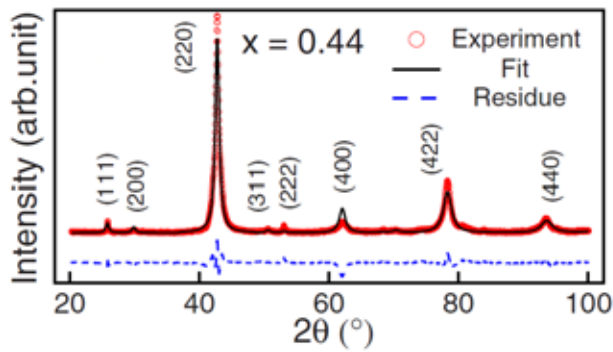


Figure 1.3 Room temperature X-ray diffraction pattern of Ni₂Mn_{1.44}Sn_{0.56} is fitted by Rietveld refinement. The residue is difference between experiment and fit and taken from Ref. [34].

1.3.2 Martensitic Phase

Martensitic transition in Ni-Mn based Heusler alloys have attracted a lot of attention due to their possible applications. Among these series of alloys, Ni₂MnGa is a ferromagnetic Heusler alloy, which is of recent interest because both the stoichiometric as well as off-stoichiometric Ni_{2+x}Mn_{1-x}Ga and Ni₂Mn_{1+y}Ga_{1-y} exhibit martensitic transformation under cooling or applied stress or external magnetic field. These alloys have a cubic L2₁ structure in the austenitic phase and exhibit a sequence of intermediate 6M (3-layered), 10M (5-layered), 14M (7-layered) modulated orthorhomhic or monoclinic martensite structures upon cooling below M_s with $c/a < 1$ and non-modulated (NM) tetragonal structures (L1₀) with $c/a > 1$ [35–37]. The structure depends on the composition variation as well as valence electron to atom ratio (e/a) of the alloy. The L2₁ structure generally transforms to the L1₀ tetragonally distorted structure which can be realized through a Bain lattice

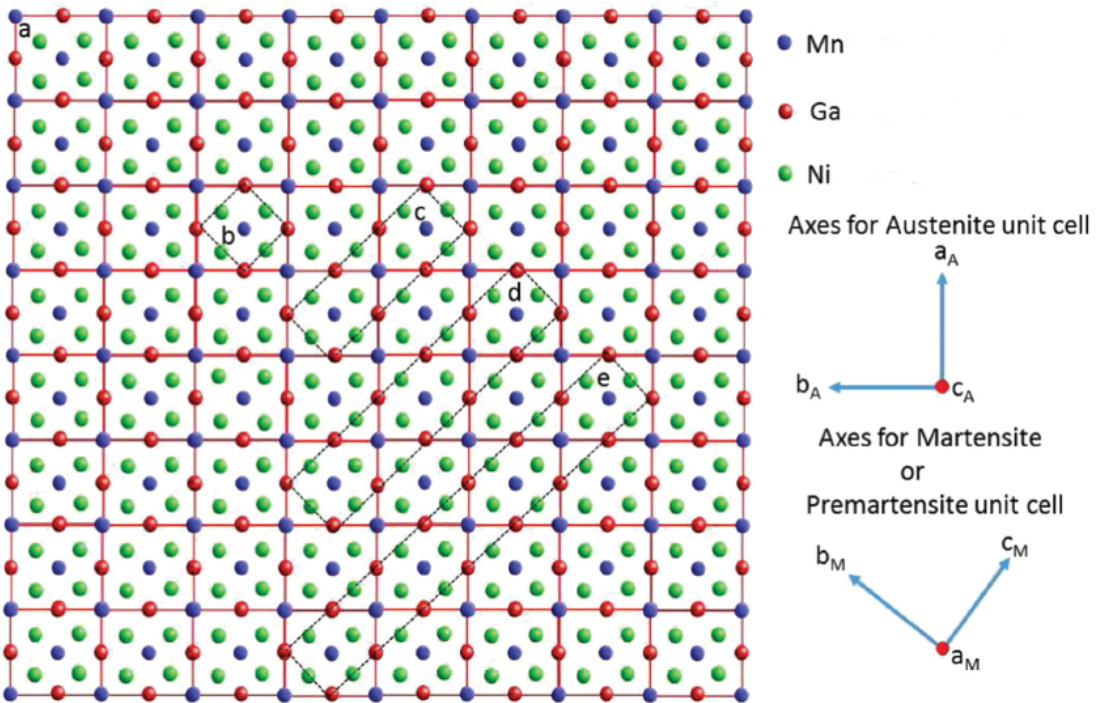


Figure 1.4 Schematic representation of unit cell orientation in (a) austenite and (b) NM (L_{10}) structure and (c) 6M premartensite, (d) 10M martensite and (e) 14M martensite superstructures. M and A correspond to the modulated martensite (or premartensite) and austenite, respectively. The orientation of crystallographic axes has been chosen in such a way that c_M , a_M and b_M are parallel to $[1\bar{1}0]$, $[110]$, and $[001]$ directions, respectively of the cubic austenite unit cell and taken from Ref. [45].

distortion [38] via different modulated structural phase sequences. The different phase sequences have been reported in Ref [39–44]. In fig. 1.4 schematic representation of unit cell orientation in austenite and NM (L_{10}) structure and 6M premartensite, 10M martensite and 14M martensite superstructures has been given [45]. However, in some cases austenite transforms to a mixture of layered structures [46]. The experimental phase diagram of $Ni_2Mn_{1+y}Ga_{1-y}$ is shown in fig. 1.5 which clarifies the phase sequence and dependence of e/a ratio on martensitic structure. These modulated structures can be described either as stacking of close-packed (110) planes in a long period or as the periodic shuffling of (110) planes along $[1\bar{1}0]$ direction. Depending upon this stacking, the modulated structure can be commensurate or incommensurate [47–49]. An incommensurate modulated structure is formed when the modulation vector (\mathbf{q}) is an irrational number.

The incommensurate phase transitions have been investigated both theoretically and experimentally by Bak *et al.* [50]. It was proposed that an incommensurate phase might undergo transformation to several intermediate commensurate structures (the “lock-in” phases) as there are always rational numbers close to an irrational number. However, the temperature variation of the modulation vector reveals no evidence of such “lock-in” phases [51]. Till now two type of models have been adopted to describe the twinned martensitic structures. The first model is based on the idea of Martynov [52]. The cell is considered to be modulated by periodical shuffling of basal plane (110) along [1 $\bar{1}$ 0] direction. The displacement of each plane from its ideal position is given by

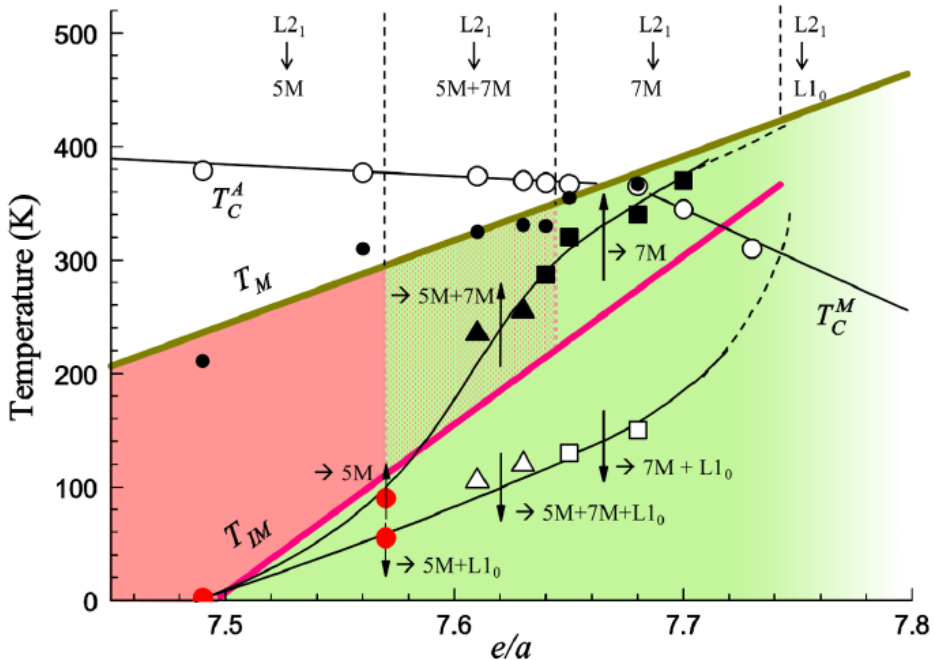


Figure 1.5 Experimental phase diagram for $\text{Ni}_2\text{Mn}_{1+y}\text{Ga}_{1-y}$. Open circles represent Curie temperatures in austenite (T_C^A) and martensite (T_C^M). Filled circles indicate the martensitic transition T_M (fitted by the green line). Intermartensitic transition temperatures are shown with open (forward) and filled (reverse transformation) squares (for $7\text{M} \leftrightarrow 7\text{M} + \text{L}1_0$) and triangles (for $5\text{M} + 7\text{M} \leftrightarrow 5\text{M} + 7\text{M} + \text{L}1_0$), respectively. New data points are plotted as red circles. The red line estimates the equilibrium intermartensitic transition boundary T_{IM} : Below the line, phase fractions of $\text{L}1_0$ are observed (green-colored area); above the line only 5M (red colored), a mixture of 5M and 7M (red textured), or only 7M (green colored) is observed. It is taken from Ref. [41]. It is important to mention that in literature sometimes 5M has been used instead of 10M and 7M has been used instead of 14M.

a function Δ_i containing three harmonic terms, $\Delta_i = A \sin(2\pi i/L) + B \sin(4\pi i/L) + C \sin(6\pi i/L)$, where L is the modulation period [36, 52, 53]. The values of the constants A , B and C are adjusted to fit the experimental relative diffraction intensities. In the second approach, the “nM” martensite determines the displacement of (110) planes of the martensitic lattice with a zigzag-like stacking fault, nomenclatured as $(a\bar{b})_x$, indicating “ a ” consecutive layers shifted towards a specific direction, with the “ b ” remaining layers shifting in the opposite direction; the subscript “ x ” refers to the number of blocks contained in the unit cell. The 14M structure is composed of five lattice planes stacked in one orientation and two planes in the other orientation. This stacking sequence is repeated twice to fulfill the atomic ordering. This is denoted as $(\bar{5}2)_2$ [36, 54–56]. Similarly, the 10M structure can be considered as $(3\bar{2})_2$ [57]. These nanotwin descriptions are based on the theory of adaptive martensite [58], where modulated structures are constructed by the accommodation of the geometrical mismatch at the interface between austenite and martensite.

The modulated martensitic structures have also been observed in off-stoichiometric Ni-Mn-Sn and Ni-Mn-In systems [59–63]. Sutou *et al.* [64] observed 4O martensite in melt-spun $\text{Ni}_{50}\text{Mn}_{37.5}\text{Sn}_{12.5}$. Moreover, Brown *et al.* [65] indicated 4-fold modulated orthorhombic (4O) martensitic structure for $\text{Ni}_{50}\text{Mn}_{36}\text{Sn}_{14}$. Krenke *et al.* [59] reported that the martensitic structure in bulk $\text{Ni}_{0.50}\text{Mn}_{0.50-x}\text{Sn}_x$ can be 10M (orthorhombic), 14M (monoclinic) and L1₀ (unmodulated double tetragonal), depending on the Sn content. Sometimes, 10M (orthorhombic) can also be referred as 10O [66], ‘O’ corresponds to orthorhombic structure. The structure of the martensite also depends on manufacturing conditions. Santos *et al.* [67, 68] observed a seven-layered orthorhombic martensite in $\text{Ni}_{50}\text{Mn}_{37}\text{Sn}_{13}$ produced by the melt-spinning rapid solidification technique, whereas Muthu *et al.* [69, 70] observed a four-layered orthorhombic (4O) martensite in the conventional arc-melted bulk $\text{Ni}_{50}\text{Mn}_{37}\text{Sn}_{13}$.

1.4 Magnetic properties of Ni-Mn based Heusler alloy

1.4.1 Magnetic moment and thermomagnetization

The structural transition in martensitic transformation of Heusler alloys are accompanied by magnetic transitions also. Most of the Ni-Mn-Ga alloys have ferromagnetic ground state in the martensitic phase, while Ni-Mn-Z ($Z = \text{Sn, In, Sb}$) systems have mixed (ferro/anti-ferro) magnetic state in both the austenite and martensite phase [24, 71–73]. The large decrease in the magnetization upon the martensitic transition confirms the enhancement of anti-ferromagnetic coupling between the Mn atoms at Mn site (Mn1) and Mn atom at Z site (Mn2) in off-stoichiometric alloys. The occurrence of exchange bias [73–75] and reentrant spin glass [76] like behaviour are reported in the martensitic phase, which also supports the presence of anti-ferromagnetic coupling.

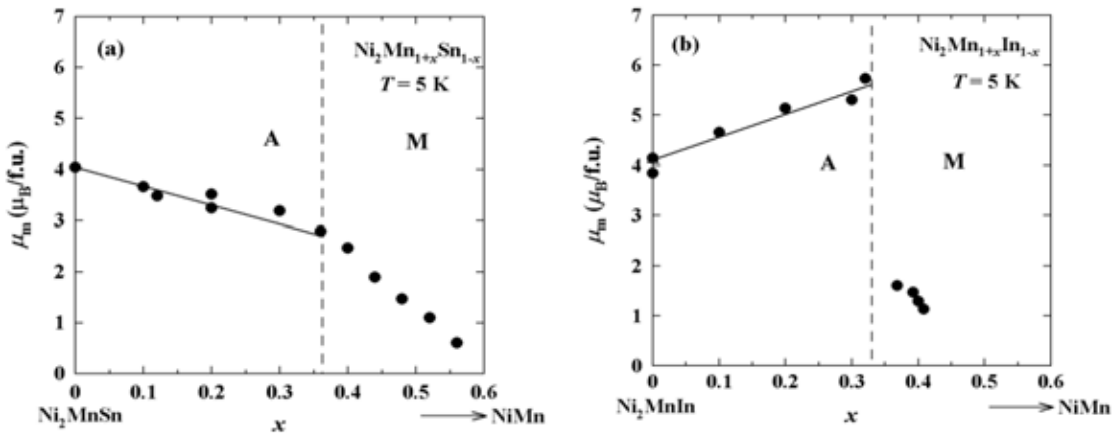


Figure 1.6 Concentration dependence of the total magnetic moment per formula unit (f.u.), μ_m , at 5 K for the $\text{Ni}_2\text{Mn}_{1+x}\text{Sn}_{1-x}$ [77] and the $\text{Ni}_2\text{Mn}_{1+x}\text{In}_{1-x}$ [78]. The solid line in the figure is the curve calculated using the simple model indicated in the Ref. [77]. A and M represent the austenitic phase and martensitic phase, respectively.

Kanomata *et al.* [77, 78] found that the magnetic moments per formula unit (μ_m) at 5 K for $\text{Ni}_2\text{Mn}_{1+x}\text{Sn}_{1-x}$ and $\text{Ni}_2\text{Mn}_{1+x}\text{In}_{1-x}$ estimated from the spontaneous magnetization can be plotted as a function of doping concentration (x) as shown in figs. 1.6(a) and (b), respectively. In both the cases, it is seen that the values of the magnetic moment of the samples in the martensitic phase region are relatively smaller than those in the austenitic phase region. It is very interesting to note

that the magnetic moment in the austenitic phase region linearly decreases with increasing x in the Ni-Mn-Sn system, while that increasing in the Ni-Mn-In system. The magnetic moment in the martensitic phase region decreases with x in both systems.

It should also be noted that the magnetic moments of the stoichiometric Ni_2MnSn and Ni_2MnIn ($x = 0$) alloys are almost $4 \mu_B/\text{formula-unit}$. Kanomata *et al.* have suggested that while the neighboring Mn atoms at the Mn sites are ferromagnetically coupled in the both cases, the magnetic coupling between the neighboring Mn atoms at the different sites, namely, the Mn at the Z sites, of the Ni-Mn-Sn alloys is certainly different from that of the Ni-Mn-In alloys. The Mn atoms substituted at the In sites in $\text{Ni}_2\text{Mn}_{1+x}\text{In}_{1-x}$ alloys are ferromagnetically coupled to the Mn atoms at the Mn sites [61], whereas the magnetic moment of the Mn atoms on the Sn sites in $\text{Ni}_2\text{Mn}_{1+x}\text{Sn}_{1-x}$ alloys are antiferromagnetically coupled to the Mn atoms on the Mn sites [59]. From the drastic change in the magnetic moment induced by the martensitic transformation, it is clear that the magnetic properties of these alloys are strongly affected by the lattice distortion and the atomic distances between the neighboring atoms.

The Ni-Mn-Z alloys exhibit a number of features in thermomagnetization (M(T)) behaviour during lowering of temperature under zero-field-cooled-heating (ZFC), field-cooled (FC) and field-heating (FH) process. The fig. 1.7 shows that in FC sequence magnetic moment of Ni-Mn-Z increases at austenitic Curie temperature (T_C^A) with decreasing temperature from high-temperature paramagnetic austenitic phase. Due to further lowering of the temperature, the drop in M(T) below M_s is a feature that is found in all Ni-Mn-Z alloys when measured in low external fields. This feature arises due to loss of ferromagnetic ordering between Mn atoms at M_s for martensitic transformation and the transformation finishes at M_f . At a lower temperature, magnetic moment again increases with decreasing temperature at martensitic Curie temperature (T_C^M) due to ferromagnetic ordering in martensitic phase. Similar to the martensite transformation, the reverse transformation occurs on heating at A_s and finishes at A_f in ZFC and FH sequence. The splitting between the ZFC and the FC or the FH magnetization curve is due to the presence of inhomogeneous phase below T_C^M , which arises from antiferromagnetic components that pin the ferromagnetic matrix [76].

However, at low temperatures Ni-Mn-Ga shows some differences. Here thermomagnetization

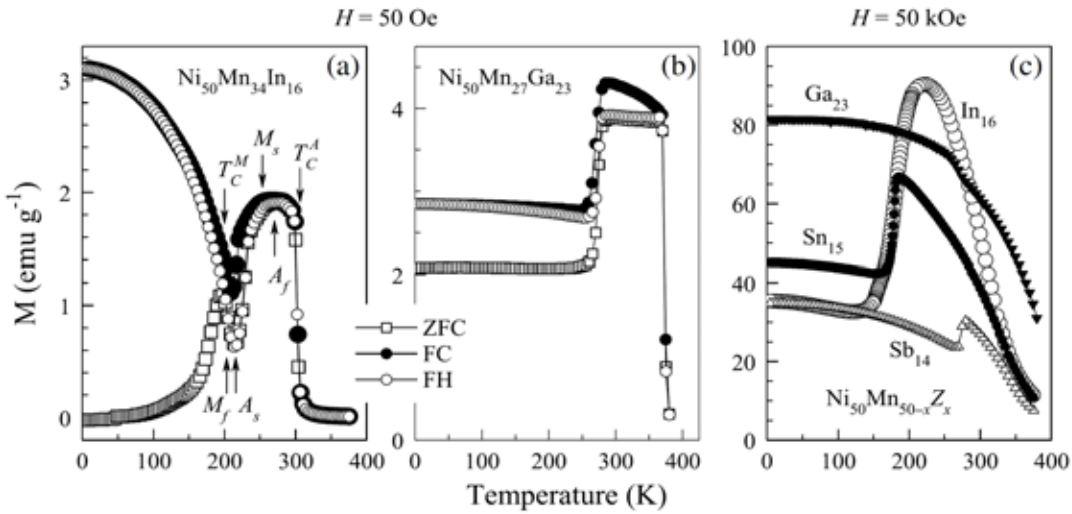


Figure 1.7 Thermo-magnetization behaviour of (a) Ni-Mn-In and (b) Ni-Mn-Ga at low magnetic field $H = 50$ Oe, (c) Ni-Mn-Z ($Z : \text{Ga}, \text{In}, \text{Sn}, \text{Sb}$) at high magnetic field $H = 50$ kOe. It is taken from Ref. [79]. M_s = martensitic start temperature, M_f = martensitic finish temperature, A_s = austenitic start temperature, A_f = austenitic finish temperature, T_C^A = austenitic Curie temperature, T_C^M = martensitic Curie temperature.

curve is flat contrast to Ni-Mn-In. This is because both the twin boundary mobility and the magnetocrystalline anisotropy are higher in the martensitic phase of Ni-Mn-Ga. Consequently, even in such small applied magnetic field, the variants are easily aligned along their easy axis giving rise to finite magnetic moment at low temperatures.

Moreover, when $M(T)$ is measured in high magnetic field, as shown in fig. 1.7(c), the drop in magnetization around martensitic transition temperature remains pronounced for Ni-Mn-Z ($Z : \text{Sn}, \text{In}, \text{Sb}$) except in the case of Ni-Mn-Ga, where a small increase in magnetic moment is found on decreasing temperature [79].

1.4.2 Magnetic field induced phase transition and inverse magnetocaloric effect

Most of the novel properties of Heusler alloys are caused by this magneto-structural martensitic transformation. One of the interesting properties exhibited by the Heusler alloys is shape memory

effect due to temperature variation. Furthermore, this can also be tuned by external magnetic field giving rise to magnetic shape memory effect. This is faster and more efficient than that driven by temperature or stress. Due to large entropy change around this martensitic transition, Ni-Mn-Ga gives rise to giant magnetocaloric effect [80, 81], which has significant technological application in magnetic refrigeration [82].

There is a significant difference between Ni-Mn-Ga and Ni-Mn-Z ($Z = \text{Sn}, \text{In}$) alloys in the magneto-structural transformation process under applied magnetic field. As opposed to the case in Ni-Mn-Ga, where the saturation magnetization in the martensite phase is higher than that in L₂₁ austenite phase, in Ni-Mn-Sn and Ni-Mn-In, the saturation magnetization in the martensite phase is lower than in the L₂₁ austenite phase [23, 59, 61, 79, 83, 84]. In Ni-Mn-Ga alloys the twinning stress associated with the martensitic phase is low, allowing easy displacement of the twin (variant) boundaries. For this alloy, the magnetocrystalline anisotropy energy (MAE) of magnetic field-favored martensite variant is larger than the energy required for twin boundary motion, then that variant will grow at the expense of others, resulting in a field-induced macroscopic shape change [83, 85, 86]. In addition to the MAE, the Zeeman energy (ZE) plays an important role in magnetic field-induced phase transformation. For Ni-Mn-Sn alloys, ZE is the magnetic energy responsible for field induced phase transition as it is higher than the MAE [24, 87].

To understand how Zeeman energy plays important role in magnetic field-induced phase transformation we have to consider the Gibbs free energy difference between the parent (austenite) and product (martensite) phases during martensitic transformation under applied magnetic field and can be expressed as:

$$\Delta G_{\text{total}}^{A \rightarrow M} = \Delta G_{\text{ch}}^{A \rightarrow M} - \Delta G_{\text{el}}^{A \rightarrow M} + \Delta E_{\text{irr}} + \Delta G_{\text{mag}}^{A \rightarrow M} - \Delta G_{\text{MAE}}^{A \rightarrow M} \quad (1.1)$$

where A and M represent the austenitic and martensitic phase. $\Delta G_{\text{total}}^{A \rightarrow M}$ is the total Gibbs free energy difference that needs to be less than zero to trigger the transformation. The $\Delta G_{\text{ch}}^{A \rightarrow M}$ is the chemical free energy difference between martensitic phase and austenitic phase. The $\Delta G_{\text{el}}^{A \rightarrow M}$ is the stored elastic energy due to transformation which leads to a broadening of the transition and ΔE_{irr} is the dissipation energy due to defect and dislocation and frictional energy spent due to the

movement of variants, which corresponds to energy dissipation and hysteresis. The $\Delta G_{\text{mag}}^{\text{A} \rightarrow \text{M}}$ is the ZE difference which can be expressed as

$$\Delta G_{\text{mag}}^{\text{A} \rightarrow \text{M}} = H \cdot M_{\text{austenite}}^S - H \cdot M_{\text{martensite}}^S \quad (1.2)$$

where H is the externally applied magnetic field and M^S is the saturation magnetization. The $\Delta G_{\text{MAE}}^{\text{A} \rightarrow \text{M}}$ is the difference between the magnetocrystalline anisotropy energies of austenite and martensite phases and can be expressed as

$$\Delta G_{\text{MAE}}^{\text{A} \rightarrow \text{M}} = (K_u \sin \theta)_{\text{austenite}} - (K_u \sin \theta)_{\text{martensite}} \quad (1.3)$$

where K_u represents the MAE and θ is the angle between the applied field direction and the easy axis of magnetization of phase domain. The magnetoelastic effects ($\Delta G_{\text{el}}^{\text{A} \rightarrow \text{M}}$) can be taken into account, however, they are usually negligible as compared to $\Delta G_{\text{mag}}^{\text{A} \rightarrow \text{M}}$ and $\Delta G_{\text{MAE}}^{\text{A} \rightarrow \text{M}}$. The $\Delta G_{\text{el}}^{\text{A} \rightarrow \text{M}}$ and ΔE_{irr} are related to mechanical energy [24]. Moreover, austenitic to martensitic transformation happens under conditions of local equilibrium. This equilibrium is defined by the balance of chemical, elastic and irreversible (dissipative) energy terms at the interface between martensitic phase and austenitic phase [88].

$$\Delta G_{\text{ch}}^{\text{A} \rightarrow \text{M}} - \Delta G_{\text{el}}^{\text{A} \rightarrow \text{M}} + \Delta E_{\text{irr}} = 0 \quad (1.4)$$

The net effect of the magnetic field depends on whether $\Delta G_{\text{mag}}^{\text{A} \rightarrow \text{M}} - \Delta G_{\text{MAE}}^{\text{A} \rightarrow \text{M}}$ term is positive or negative. If it is positive then the parent phase is more stable under a magnetic field, in other words, a magnetic field can be used to trigger the martensite to austenitic phase transformation [24].

For Ni-Mn-Ga alloys the magnetic entropy change ΔS associated with the structural transformation can be very large but usually occurs in a very narrow temperature range. This is clear from the following expression: the transformation temperature change (ΔT) induced by magnetic field change (ΔB) is approximately given by the Clausius-Clapeyron relation [89]:

$$\frac{\Delta B}{\Delta T} = \frac{\Delta S}{\Delta M} \Rightarrow \Delta T \approx \left(\frac{\Delta M}{\Delta S} \right) \Delta B \quad (1.5)$$

where T is the absolute temperature, B is the applied magnetic field, and ΔM and ΔS are the differences in magnetization and entropy between austenitic phase and martensitic phase, respectively. In most cases both phases show ferromagnetic nature across the structural transformation. The change of the saturated magnetization upon phase transition is small and thus the resultant Zeeman energy $\Delta M \cdot B$ is not large enough to drive the structural transformation. In Ni-Mn-Sn alloys a strong change of magnetization in martensitic phase due to excess Mn results in a large Zeeman energy $\Delta M \cdot B$. The enhanced Zeeman energy drives the structural transformation and causes a field induced metamagnetic behavior from the martensitic phase to the parent phase [87].

Moreover, for samples with compositions close to Ni_2MnZ ($Z = \text{Ga}, \text{Sn}$) stoichiometry an inverse MCE has been reported. This is found in $\text{Ni}_2\text{Mn}_{1+x}\text{Sn}_{1-x}$ alloys with compositions lying in the narrow range $0.40 \leq x \leq 0.48$, for which an inverse MCE is observed that is at least three times larger than Ni_2MnGa [19]. This is an extrinsic effect arising from the coupling at the mesoscale between the martensitic and magnetic domains. Applying a magnetic field adiabatically, rather than removing it as in ordinary MCE, causes the sample to cool. This is very important for room temperature refrigeration as an environment-friendly alternative to conventional vapor-cycle refrigeration. This has prompted intensive research in this field.

1.4.3 Negative magnetoresistance

Ni_2MnGa also exhibits negative magnetoresistance (MR) [90, 91]. Biswas *et al.* [90] studied the MR of the bulk Ni_2MnGa for austenitic, premartensitic and martensitic phases. The 5% negative MR was reported at 300 K and 8 Tesla for $\text{Ni}_{2.1}\text{Mn}_{0.9}\text{Ga}$. Banik *et al.* [92] showed that MR exhibits a monotonic increase in magnitude from 0.2% to 7.3% at 8 Tesla, as doping concentration (x) increases from 0.0 (Ni_2MnGa) to 0.35 ($\text{Ni}_{2.35}\text{Mn}_{0.66}\text{Ga}_{0.98}$). Negative MR for magnetic metals has been explained on the basis of *s-d* scattering model where *s* conduction electrons are scattered by localized *d* spins on the magnetic ions [93, 94].

Interestingly, off-stoichiometric $\text{Ni}_2\text{Mn}_{1+x}\text{Sn}_{1-x}$ alloys have also attracted recent research interest due to large negative MR during martensitic transformation. Koyama *et al.* [95] obtained

large MR about 50 % for $\text{Ni}_2\text{Mn}_{1+x}\text{Sn}_{1-x}$ ($x = 0.44$) with extremely high magnetic field (~ 17 Tesla) at 150 K. Recently Singh *et al.* [34] studied the MR properties of Ni-Mn-Sn ($0.40 \leq x \leq 0.52$) both below and above martensitic transition region and described the origin. Maximum -36 % MR at 170 K (vicinity of martensitic transition) has been achieved for $x = 0.40$ with 7 Tesla magnetic field. The origin has been discussed as a combined effect of mainly magnetic field induced reverse phase transition and disorder related residual resistivity. In austenitic phase the negative MR is due to *s-d* scattering. Below martensitic transition temperature at 150 K the MR arises due to opposition of rotation of magnetic spin within inhomogeneous ferromagnetic-antiferromagnetic mixed magnetic phase. At low temperature at 5 K, scattering of conduction electrons from localized Mn2 *d*-states gives rise to negative MR.

Moreover, Yu *et al.* [96] has reported that MR varies with In concentration in Ni-Mn-In and reaches a peak value of about -80% for the sample with $x = 0.36$ at ≈ 100 K with 6 Tesla magnetic field. The kinetic arrest of austenitic phase causes large MR [97]. Recently, Singh *et al.* [98] obtained large MR ($\sim -81\%$) for $x = 0.36$ in field-cooled process with 7 Tesla magnetic field at 115 K. Almost -79% and -3% MR have been obtained at 5 K in field-cooled and zero-field-cooled-heating process with 7 Tesla magnetic field. This large difference in MR is not possible to obtain in Ni-Mn-Sn because at 5 K the MR is similar to that for austenitic phase [34]. This makes Ni-Mn-In system more flexible for potential application with magnetic field.

1.4.4 Zero-field-cooled exchange bias effect

Another interesting property Heusler alloys show is the exchange bias effect. When materials with ferromagnetic(FM)-antiferromagnetic(AFM), FM-spin glass (SG), AFM-ferrimagnetic (FI), and FM-FI interfaces are cooled with magnetic field through a ordering temperature (T_{NF}) [99] of nonferromagnetic phase (AFM, SG, or ferrimagnet) which is lower than the ferromagnetic Curie temperature (T_C), an exchange anisotropy is induced at the interfaces [100–104]. This exchange anisotropy created at the interface between FM and non-FM phase is called exchange bias effect. It is important to note that the ordering temperature in the case of FM-AFM interface is termed as

“Néel temperature” (T_N). Experimentally exchange bias effect is realized as shift of the magnetic hysteresis loop generally in the opposite (“negative”) direction to the cooling field [105]. The schematic representation of the spin configuration of an FM-AFM bilayer at different stages of an exchange biased hysteresis loop has been shown in fig. 1.8. When a magnetic field (H) is applied

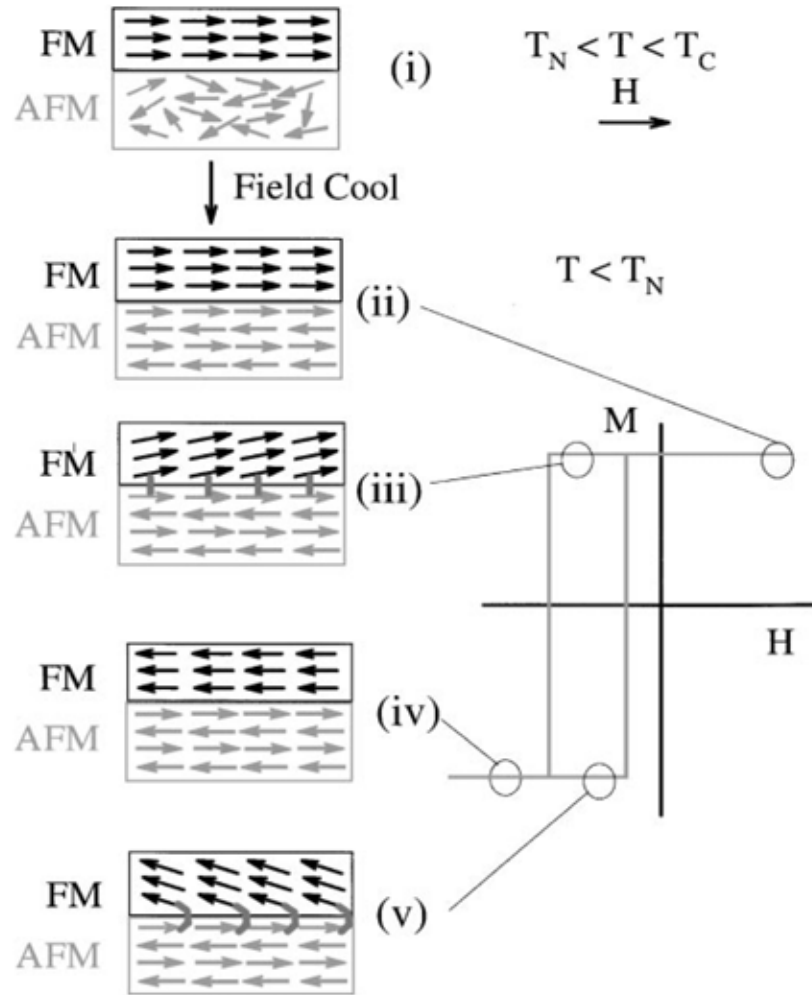


Figure 1.8 Schematic diagram of the spin configuration of an FM-AFM bilayer at different states of an exchange biased hysteresis loop [105].

in the temperature range $T_N < T < T_C$, the FM spins are aligned along the applied magnetic field. However, the AFM spins are randomly oriented. When cooling to $T < T_N$, the AFM spins are aligned ferromagnetically at the interface due to ferromagnetic interaction with the FM spins.

Other spins in the AFM bulk maintain their AFM order. When the magnetic field is reversed, the FM spins start to rotate in the negative magnetic field direction. But the AFM spins' orientations remain unchanged due to sufficiently large AFM anisotropy. Consequently, the AFM spins at the interface oppose the FM spins to be rotated along the negative magnetic field direction. Thus an extra magnetic field is needed to reverse completely the FM layer overcoming the microscopic torque. Therefore, the hysteresis loop is shifted in the field axis. This exchange bias effect is ascribed to FM unidirectional anisotropy formed at the interface between different magnetic phases in the process of field cooling (FC) and it is named as conventional exchange bias effect.

An unusual exchange bias effect under zero-field-cooling (ZFC) has also been obtained in many off-stoichiometric Ni-Mn-Z ($Z = \text{In}$ and Sn) [106, 107], $\text{Ni}_2\text{Mn}_{1.4}\text{Ga}_{0.6}$ [108], $\text{Ni}_{50}\text{Mn}_{36}\text{Co}_4\text{Sn}_{10}$ [109] Heusler alloys with martensitic transition. In off-stoichiometric Ni-Mn-Ga alloys, the ZFC-EB effect is believed to be due to irreversible growth of FM domains that change from non-percolating to percolating state and, consequently, forms the unidirectional anisotropy at the interface [108]. In $\text{Ni}_{50}\text{Mn}_{36}\text{Co}_4\text{Sn}_{10}$ Heusler alloy, the enhancement of AFM induces a strong interaction with superferromagnetic (SFM), super spin glass (SSG), and superparamagnetic (SPM) domains resulting in ZFC-EB effect [109]. In Ni-Mn-Z ($Z = \text{In}$, Sn) alloys the occurrence of ZFC-EB effect is attributed to the SFM unidirectional anisotropy below the blocking temperature (T_B). The exchange bias effect has been explored extensively due to its various applications in spintronics, magnetic recording and sensors devices.

1.5 Motivation to investigate Heusler alloy

The above discussions on structural and magnetic properties of Ni-Mn-Z alloys reveals that these compounds have tremendous research interest. However, despite a couple of decades of intense research on the martensitic structure, the structure is still debatable. We wish to revisit the martensitic structure of one of the Ni-Mn-Z alloys, such as, Ni-Mn-Sn in more details and want to find out the magnetic and structural relationship to explain some magnetic properties, e.g. , exchange bias effect. The probable origin is argued to be purely magnetic and does not originate from structural

modifications in martensitic phase [107]. However, it is important to mention that the magnetic behavior influences the crystal structure causing the martensitic transition in Ni-Mn based Heusler alloys. For example, in $\text{Ni}_2\text{Mn}_{1+x}\text{Sn}_{1-x}$ as x is increased, the magnetic exchange interactions between Mn2 and the neighboring Mn1 lead to substantial deviation from d^5 character on Mn1 in cubic austenitic structure. This then allows for energy gain from Mn1-Ni hybridization. So the Ni atom moves towards both Mn1 and Mn2 and this is achieved by moving along the resultant force which is along a lattice parameter in the cubic structure. Thus, the magnetic state of the Mn atom causes the martensitic structural transition [110]. This implies that the magnetic state and crystal structure are coupled to each other. Thus it requires a detailed insight into the crystal structure of Ni-Mn-Sn Heusler alloys and careful analysis to check whether the crystal structure influences the magnetic behavior even below martensitic finish temperature (M_f). Furthermore, fundamental questions regarding the energetics of twin boundary motion in relation to local atomic structure, chemical composition, magnetic state and magnetic anisotropy as well as the electronic structure have still to be worked out.

To get a flavour of the theoretical density functional calculation, some theoretical results of Heusler alloys have been discussed and have prepared a ground for the importance of the theoretical calculations. At first a detailed theoretical calculation of Heusler alloys had been performed by Ayuela *et al.* [111]. Ni_2MnZ ($Z : \text{Al, Ga, Sn}$) are studied by means of the full-potential linearized augmented-plane-wave (FLAPW) method, using a non-local approximation for the exchange and correlation potential. Carrying out an optimization of the lattice parameter of the austenitic phase of different alloys reveals that the equilibrium lattice constants are in good agreement with experimental data. Furthermore, the possibility of martensitic transformations was studied by making tetragonal and orthorhombic distortions to the cubic $L2_1$ structure with the volume fixed to the equilibrium value. The total energy difference relative to that of the $L2_1$ phase as a function of the axial ratio c/a in the martensitic phase has been discussed. The cubic structure is found to be stable only in Mn alloys, except for Ni_2MnGa . In addition, there is another metastable minimum for Ni_2MnAl at $c/a = 1.22$ with a higher energy, so the temperature-driven martensitic transformation is not possible. To understand in more detail the effects of the distortions in the band energy, the

electronic density of states has been studied as a function of c/a . For $c/a \neq 1$ the minority-spin electron states just below the Fermi level are split because of the lower crystal symmetry. When $c/a > 1$, the split peaks cross the Fermi level, lowering the band energy. For $c/a < 1$, the lower part of the split peak increases, so the density of states at the Fermi level diminishes, and the energy does not decrease as much as in the $c/a > 1$ case. In Ni_2MnGa the split peak is very near the Fermi level, while in Ni_2MnSn the peak does not cross the Fermi level for very small deformations because of the large number of electrons added by the Sn. Simultaneously many groups [112–122] also have done theoretical calculation of Ni-Mn-Z alloys using different formalisms of density functional theory (DFT) and detailed discussions of martensitic transition and how magnetic properties of those alloys changes with structural transition. Most interestingly, the reason behind the martensitic phase transformation has been tried to explain by all the groups. Different models for the origin of structural instability have been adopted.

Most of the theoretical explanations concerning the underlying mechanism of martensitic phase transition are phenomenological studies based on the free energy expansion [123–126]. Few first-principles calculations, especially on Ni-Mn-Ga systems have provided the interpretations on the origin of martensitic phase transition, such as a band Jahn-Teller distortion [113, 127] and Fermi surface nesting [114]. Fermi surface nesting gives rise to instability and results in a soft phonon in cubic unit cell. A lattice vibrational mode with a specific wave vector can be excited at a very low energy, which allows modulation along a particular direction.

In band Jahn-Teller mechanism model, the lattice distortion breaks the degeneracy of the d bands of Ni-Mn based alloys in the vicinity of the Fermi level, allowing a repopulation of electrons in the lower energy bands. A signature of the band Jahn-Teller effect is splitting of Ni 3d electron density of states feature exactly at the Fermi energy into two features below and above Fermi energy resulting in a lowering of total energy [113]. Although Ni has a $3d^84s^2$ ground state configuration, in bulk Ni, as well as Ni clusters, it possess $3d^94s^1$ configuration [128]. Ni 3d minority spin channel is partially filled. Thus, this electron configuration is energetically not favored and energy can be gained by a distortion of Ni octahedral environment by both an elongation in one direction and a compression along other directions. The band Jahn-Teller mechanism involves the

splitting of energy subbands which are degenerate in the ordered cubic phase, with the electrons redistributed among the energy levels so as to lower the free energy. This does not require a large density of states at the Fermi level, i.e., the system to be highly localized. Moreover, in this model there is a modification of the energy band-width depending on the overlap of the electron orbitals in different directions. The energy bands become narrow due to orbitals overlap in the direction of crystal elongation and broad for overlap of orbitals in the direction of contraction. For example, because of $c/a < 1$ in the martensitic phase of Ni₂MnGa, the energy bands associated with orbitals directed along c will be broader than those associated with orbitals in the $a - b$ plane. More specifically, the $3d_{3z^2-r^2}$ energy band will be broadened and the $3d_{x^2-y^2}$ will be narrowed. Brown *et al.* explained by neutron scattering experiments that the transition from the cubic to the tetragonal phase is accompanied by a transfer of magnetic moment from Mn to Ni [127]. However, Barman *et al.* [129] explains, although splitting occurs, the split features stay below Fermi energy. So, the stabilization of the martensitic phase cannot be described purely in terms of the band Jahn-Teller effect for Ni₂MnGa. The experimental ultraviolet photoelectron spectroscopy (UPS) of valence band spectra by Opeil *et al.* [114] shows the redistributions of the UPS intensity corresponding to the onset of the pre-martensitic transition and martensitic transition, respectively. The martensitic transition corresponds to Fermi surface nesting which involves redistribution between the two spin channels. However, till date the origin of martensitic transition for off-stoichiometric Ni-Mn-Z (Z : Sn and In) has been understood as Jahn-Teller distortion [112, 130, 131].

Moreover, in regard to the origin of formation modulated structure, there are some controversies. Two different models, adaptive phase model and soft phonon mode based displacive modulation model, have been adopted for the origin of modulation in Ni₂MnGa. In adaptive phase model, thermodynamically stable L1₀ type NM tetragonal unit cell structure is the basic building block. The 14M superlattice modulated structure is formed by periodic nanotwinning of tetragonal unit cell in two opposite directions to minimize the elastic strain energy at austenite and martensite phase boundary by decreasing the variant size to only few atomic layers. This microstructure is described as an adaptive martensite phase, adopted by Khachaturyan *et al.* [58]. The adaptive phase forms in such a way that the habit plane separating austenite and adaptive

martensite is an exact interface. This 14M modulated structure is metastable because this phase has excess energy than NM tetragonal phase due to microstructural defect. While, in the case of a transformation from 14M to NM, the twin boundary energy plays important role at very low temperature. However, during a transition from 14M to NM the crystal symmetry increases from orthorhombic or monoclinic to tetragonal, while in usual martensitic transition the symmetry is reduced in the low-temperature phase. This inconsistency in phase transition sequence can be explained considering that 14M-NM transition is not a usual phase transformation but only a change of the martensitic microstructure [57]. In the soft phonon model, the origin of modulation in the premartensite phase has been related to a TA_2 soft acoustic phonon mode of the austenite phase at $\mathbf{q} \sim (1/3 \ 1/3 \ 0)$ [132–138]. The incommensurate nature of modulation with nonuniform atomic displacements favors the soft phonon mode mechanism, in contrast to adaptive phase model which explains uniform atomic displacement with commensurate modulation. Singh *et al.* [51] suggested the incommensurate 14M modulated phase is the ground state of Ni_2MnGa , not the Bain distorted tetragonal L1_0 phase confirming the applicability of soft phonon model over adaptive phase model for the origin of modulation. Moreover, the formation of charge density wave [139] reveals the electronic origin of modulation [140].

Thus there are still controversies about the origin of martensitic transformation. In this work the electronic structure of Ni_2MnGa for both non-modulated and modulated structure have been discussed to understand the nature of Jahn-Teller mechanism. Moreover, it has been pointed out that the stoichiometric Ni_2MnZ ($Z : \text{Sn, In}$) does not undergo any structural transformation in contrast to Ni_2MnGa . This suggests that an important role is played by the Z element in inducing the martensitic transformation. However, the detailed mechanism is still not been discussed in the literature. The reason, why Ni_2MnGa is so different from Ni_2MnZ ($Z : \text{Sn, In}$), is needed to be found out. Interestingly, off-stoichiometric $\text{Ni}_2\text{Mn}_{1+x}\text{Z}_{1-x}$ ($Z : \text{Sn, In}$) undergo martensitic transformation. Although the reason of the martensitic transformation has been also related to Jahn Teller effect, the detailed change in orbital energies has not been elucidated. In this work, the trend of doped Mn occupancy in $\text{Ni}_2\text{Mn}_{1+x}\text{Sn}_{1-x}$ has been discussed which was not investigated till now. Another interesting aspect about martensitic structure is that experimentally investigated structure

is orthorhombic in nature. However, till now in literature tetragonal structure has been realized by density functional theory. Here we have tried to give a satisfactory explanation how one can obtain orthorhombic structure in theoretical calculation. The origin for structural transformation of $\text{Ni}_2\text{Mn}_{1+x}\text{Z}_{1-x}$ ($\text{Z} : \text{Sn}$ and In) has been discussed in more detail. Other interesting Heusler alloys are Co doped Ni-Mn-Z ($\text{Z} : \text{Sn}$, In). The substitution of Co in these alloys enhances the Curie temperature and magnetization compared to Ni-Mn-Z. Considering Ni-Mn-Sn, Ni-Co-Mn-In etc., the site preference and distribution tendency of doped atom have been discussed. This helps in understanding structural and magnetic properties of the system.

1.6 Outline of thesis

This thesis focuses on the origin of the martensitic transformation in Ni-Mn based Heusler alloys. The structural, magnetic, and electronic structure of Ni-Mn-Ga, Ni-Mn-Sn, Ni-Mn-In and Ni-Co-Mn-In Heusler alloy systems are examined by *ab-initio* density functional theory implemented in Vienna *ab-initio* simulation package (VASP). Moreover, the experimentally obtained crystal structure of $\text{Ni}_2\text{Mn}_{1+x}\text{Sn}_{1-x}$ ($x = 0.40, 0.44, 0.48$ and 0.52) has been discussed to understand the effect of crystal structure on magnetic properties.

Chapter 2 describes the fundamental developments of *ab-initio* density functional theory to the study electronic properties of material and importance of Wannier function to describe the band structure of any compound. This chapter also describes theoretical aspects of various instruments and methods used for study of structural and magnetic properties. Starting from the sample preparation by arc melting technique, differential scanning calorimetry (DSC) to obtain the transition temperatures and X-ray diffraction (XRD) method for the crystal structure determination, are discussed. The superconducting quantum interference device (SQUID) for susceptibility measurement is also discussed. The theory of photoelectron spectroscopy and schematic experimental setup of ultra violet photoelectron spectroscopy (UPS) measurement are briefly discussed.

Chapter 3 talks about the origin of band Jahn Teller effect which drives the martensitic transition martensitic transformation in Ni_2MnGa which is the only member in the Ni-Mn based alloys

in which the martensitic transformation takes place for the stoichiometric composition.

Chapter 4 describes the microscopic mechanism operative for driving the martensitic transformation in $\text{Ni}_2\text{Mn}_{1+x}\text{Sn}_{1-x}$. Moreover, the site occupation of the atoms is one of the important issues to understand the alloying effect on the properties. This chapter investigates the site configuration preference of substituted Mn at Sn sites in the austenitic phase and its role in martensitic phase transition.

Chapter 5 discusses the temperature dependent crystal structure analysis in martensitic phase of $\text{Ni}_2\text{Mn}_{1+x}\text{Sn}_{1-x}$ ($x = 0.40, 0.44, 0.48$ and 0.52) magnetic shape memory alloy obtained by synchrotron X-ray diffraction to understand the effect of crystal structures on magnetic behavior and electronic structure.

In **Chapter 6** the underlying mechanism of martensitic transformation of $\text{Ni}_2\text{Mn}_{1+x}\text{In}_{1-x}$ has been discussed in detail. Moreover, Co doped Ni-Mn-In system is studied because the substitution of Co in these alloys enhances both the Curie temperature and the magnetization in austenitic phase which lead to giant inverse magnetocaloric effect, giant magnetoresistance etc. due to structural transformation. When Co is doped in Ni-Mn-In, the fundamental question arises about its site preference and distribution tendency, which helps in understanding the enhanced Curie temperature and magnetization of the system.

Chapter 7 describes the summary of the thesis in a nut shell.

Appendix A deals with role of Coulomb interaction (U) of $3d$ electrons of Mn and Ni atom in the properties of $\text{Ni}_2\text{Mn}_{1+x}\text{Sn}_{1-x}$ ($x = 0$ and 0.50) using Generalized Gradient Approximation (GGA) exchange functional with and without U . The obtained lattice parameter, magnetic moment and electronic structure are compared with the experimental results for both stoichiometric ($x = 0$) and off-stoichiometric ($x = 0.50$) compositions.

Bibliography

- [1] F. Heusler, Verhandl. Deut. Physik. Ges. **5**, 219 (1903).
- [2] A. J. Bradley and J. W. Rodgers, Proc. R. Soc. A. **144**, 340 (1934).
- [3] O. Heusler, Ann. Phys. **155**, 411 (1934).
- [4] J. Dubowik, I. Gościańska, A. Szlaferek, and Y. V. Kudryavtsev, Mater. Sci. (Poland) **25**, 583 (2007).
- [5] T. Graf, S. Parkin, and C. Felser, IEEE Trans. Mag. **47**, 367 (2011).
- [6] V. Alijani, J. Winterlik, G. H. Fecher, S. S. Naghavi, and C. Felser, Phys. Rev. B **83**, 184428 (2011).
- [7] K. Özdoğan and I. Galanakis, J. Appl. Phys. **110**, 076101 (2011).
- [8] V. V. Sokolovskiy, V. D. Buchelnikov, M. A. Zagrebin, P. Entel, S. Sahool, and M. Ogura, Phys. Rev. B **86**, 134418 (2012).
- [9] P. J. Webster and K. R. A. Ziebeck, *Alloys and Compounds of d-Elements with Main Group Elements. Part 2.*, Landolt-Bornstein, New Series, Group III, vol 19c, ed. by H. R. J. Wijn, (Springer, Berlin 1988) pp **75-184**.
- [10] K. R. A. Ziebeck and K. U. Neumann in *Magnetic Properties of Metals*, ed. by H. R. J. Wijn, Landolt-Boërnstein, New Series, Group III, vol 32/c(Springer, Berlin 2001) pp **64-414**.

- [11] J. Pierre, R. V. Skolozdra, J. Tobola, S. Kaprzyk, C. Hordequin, M. A. Kouacou, I. Karla, R. Currat, and E. Lelièvre-Berna, *J. Alloys Comp.* **262**, 101 (1997).
- [12] J. Tobola and J. Pierre, *J. Alloys Comp.* **296**, 243 (2000).
- [13] J. Kübler, A. R. Williams, and C. B. Sommers, *Phys. Rev. B* **28**, 1745 (1983).
- [14] D. P. Oxley, R. S. Tebble, and K. C. Williams, *J. Appl. Phys.* **34**, 1362 (1963).
- [15] A. Hamzic, R. Asomoza, and I. A. Campbell, *J. Phys. F: Metal Phys.* **11**, 1441 (1981).
- [16] Y. Liu, D. Shindo, and D. J. Sellmyer, *Handbook of advanced magnetic materials: Volume 1*, Springer Science + Business Media, Inc. (2006).
- [17] A. Sozinov, A. A. Likhachev, N. Lanska, and K. Ullakko, *Appl. Phys. Lett.* **80**, 1746 (2002).
- [18] F. X. Hu, B. G. Shen, and J. R. Sun, *Appl. Phys. Lett.* **76**, 3460 (2000).
- [19] T. Krenke, E. Duman, M. Acet, E. F. Wassermann, X. Moya, L. Mañosa, and A. Planes, *Nat. Mater.* **4**, 450 (2005).
- [20] K. Oikawa, W. Ito, Y. Imano, Y. Sutou, R. Kainuma, K. Ishida, S. Okamoto, O. Kitakami, and T. Kanomata, *Appl. Phys. Lett.* **88**, 122507 (2006).
- [21] M. Khan, N. Ali, and S. Stadler, *J. Appl. Phys.* **101**, 053919 (2007).
- [22] T. Krenke, E. Duman, M. Acet, E. F. Wassermann, X. Moya, L. Mañosa, A. Planes, E. Suard, and B. Ouladdiaf, *Phys. Rev. B* **75**, 104414 (2007).
- [23] M. Khan, I. Dubenko, S. Stadler, and N. Ali, *Appl. Phys. Lett.* **91**, 072510 (2007).
- [24] H. E. Karaca, I. Karaman, B. Basaran, Y. Ren, Y. I. Chumlyakov, and H. J. Maier, *Adv. Funct. Mater.* **19**, 983 (2009).
- [25] D. C. Jiles and C. C. H. Lo, *Sens. Actuators, A* **106**, 3 (2003).

- [26] L. Mañosa, D. G. Alonso, A. Planes, E. Bonnot, M. Barrio, J. L. Tamarit, S. Aksoy, and M. Acet, *Nat. Mater.* **9**, 478 (2010).
- [27] N.B. Morgan, *Mat. Sci. Eng. A* **378**, 16 (2004).
- [28] T. W. Duerig, K. N. Melton, D. Stöckel, and C. M. Wayman, *Engineering Aspects of Shape Memory Alloys*, Butterworth-Heinemann Ltd. (1990).
- [29] D. J. Hartl and D C Lagoudas, *Proc. IMechE Part G: J. Aerospace Engineering.* **221**, 535 (2007).
- [30] K. Otsuka and C.M. Wayman, *Shape Memory Materials*, Cambridge University Press, Cambridge, 1998, p. 1.
- [31] R. W. Overholser, M. Wuttig, and D. A. Neumann, *Scripta Mater.* **40**, 1095 (1999).
- [32] V.V. Khovailo, T. Takagi, A.N. Vasilev, H. Miki, M. Matsumoto, and R. Kainuma, *Phys. Status Solidi (a)* **183**, R1 (2001)
- [33] R. McCormack and D. de Fontaine, *Phys. Rev. B* **54**, 9746 (1996).
- [34] S. Singh and C. Biswas, *Appl. Phys. Lett.* **98**, 212101 (2011).
- [35] V. A. Chernenko, C. Segui, E. Cesari, J. Pons, and V. V. Kokorin, *Phys. Rev. B* **57**, 2659 (1998).
- [36] J. Pons, V. A. Chernenko, R. Santamarta, and E. Cesari, *Acta. Mater.* **48**, 3027 (2000).
- [37] J. Pons, R. Santamarta, V. A. Chernenko, and E. Cesari, *J. Appl. Phys.* **97**, 083516 (2005).
- [38] E. C. Bain and N. Y. Dunkirk, *Trans. AIME* **70**, 25 (1924).
- [39] N. Xu, J. M. Raulot, Z. B. Li, J. Bai, Y. D. Zhang, X. Zhao, L. Zuo, and C. Esling, *Appl. Phys. Lett.* **100**, 084106 (2012).

- [40] R. Niemann, U. K. Rößbler, M. E. Gruner, L. Schultz, and S. Fähler, *Adv. Eng. Mater.* **14**, 562 (2012).
- [41] B. Dutta, A. Çakir, C. Giacobbe, A. Al-Zubi, T. Hickel, M. Acet, and J. Neugebauer, *Phys. Rev. Lett.* **116**, 025503 (2016).
- [42] P. J. Brown, J. Crangle, T. Kanomata, M. Matsumoto, K. U. Neumann, B. Ouladdiaf, and K. R. A. Ziebeck, *J. Phys.: Condens. Matter* **14**, 10159 (2002).
- [43] D. Seguí, V. A. Chernenko, J. Pons, E. Cesari, V. Khovailo, and T. Takagi, *Acta Mater.* **53**, 111 (2005).
- [44] L. Straka, O. Heczko, and N. Lanska, *IEEE Trans. Magn.* **38**, 2835 (2002).
- [45] S. Singh, S. R. Barman, and D. Pandey, *Z. Kristallogr.* **230**, 13 (2015).
- [46] A. Çakir, L. Righi, F. Albertini, M. Acet, M. Farle, and S. Aktürk, *J. Appl. Phys.* **114**, 183912 (2013).
- [47] L. Righi, F. Albertini, S. Fabricci, and A. Paoluzi, *Mater. Sci. Forum* **684**, 105 (2011).
- [48] L. Righi, F. Albertini, G. Calestani, L. Paretì, A. Paoluzi, C. Ritter, P. A. Algarabel, L. Morello, and M. R. Ibarra, *J. Solid State Chem.* **179**, 3525 (2006).
- [49] S. O. Mariager, T. Huber, and G. Ingold, *Acta Mater.* **66**, 192 (2014).
- [50] P. Bak, *Rep. Prog. Phys.* **45**, 587 (1982).
- [51] S. Singh, J. Bednarcik, S. R. Barman, C. Felser, and D. Pandey, *Phys. Rev. B* **92**, 054112 (2015).
- [52] V. V. Martynov, and V. V. Kokorin, *J. Phys. III France* **2**, 739 (1992).
- [53] V. V. Martynov, *J. de Physique IV* **5**, C8-91 (1995).

- [54] S. Kaufmann, U. K. Rößbler, O. Heczko, M. Wuttig, J. Buschbeck, L. Schultz, and S. Fähler, Phys. Rev. Lett. **104**, 145702 (2010).
- [55] R. Niemann and S. Fähler, *arXiv:1611.02535*.
- [56] M. Zelený, L. Straka, A. Sozinov, and O. Heczko, Phys. Rev. B **94**, 224108 (2016).
- [57] S. Kaufmann, R. Niemann, T. Thersleff, U. K. Rößbler, O. Heczko, J. Buschbeck, B. Holzapfel, L. Schultz, and S. Fähler, New J. Phys. **13**, 053029 (2011).
- [58] A. G. Khachaturyan, S. M. Shapiro, and S. Semenovskaya, Phys. Rev. B **43**, 10832 (1991).
- [59] T. Krenke, M. Acet, E. F. Wassermann, X. Moya, L. Mañosa, and A. Planes, Phys. Rev. B **72**, 014412 (2005).
- [60] H. Zheng, W. Wang, S. Xue, Q. Zhai, J. Frenzel, and Z. Luo, Acta Mater. **61**, 4648 (2013).
- [61] T. Krenke, M. Acet, E. F. Wassermann, X. Moya, L. Mañosa, and A. Planes, Phys. Rev. B **73**, 174413 (2006).
- [62] X. Moya, L. Mañosa, A. Planes, T. Krenke, M. Acet, and E. F. Wassermann, Mater. Sci. Eng., A **438**, 911 (2006).
- [63] H. Yan, Y. Zhang, N. Xu, A. Senyshyn, H. G. Brokmeier, C. Esling, X. Zhao, and L. Zuo, Acta Mater. **88**, 375 (2015).
- [64] Y. Sutou, Y. Imano, N. Koeda, T. Omori, R. Kainuma, K. Ishida, and K. Oikawa, Appl. Phys. Lett. **85**, 4358 (2004).
- [65] P. J. Brown, A. P. Gandy, K. Ishida, R. Kainuma, T. Kanomata, K. U. Neumann¹, K. Oikawa, B. Ouladdiaf, and K. R. A. Ziebeck, J. Phys.: Condens. Matter **18**, 2249 (2006).
- [66] K. Otsuka, T. Ohba, M. Tokonami, and C. M. Wayman, Scripta Metall. Mater. **29**, 1359 (1993).

- [67] J. D. Santos, T. Sánchez, P. Alvarez, M.L. Sanchez, J. L. Sánchez Llamazares, and B. Hernando, *J. Appl. Phys.* **103**, 07B326 (2008).
- [68] B. Hernando, J.L. Sánchez Llamazares, J. D. Santos, M. L. Sánchez, Ll. Escoda, J. J. Suñol, R. Varga, C. García, and J. González, *J. Magn. Magn. Mater.* **321**, 763 (2009).
- [69] S. E. Muthu, N. V. R. Rao, D. V. S. Rao, M. M. Raja, U. Devarajan, and S. Arumugam, *J. Appl. Phys.* **110**, 023904 (2011).
- [70] S. E. Muthu, N. V. R. Rao, M. M. Raja, D. M. R. Kumar, D. M. Radheep, and S. Arumugam, *J. Phys. D: Appl. Phys.* **43**, 425002 (2010).
- [71] H. E. Karaca, I. Karaman, B. Basaran, D. C. Lagoudas, Y. I. Chumlyakov, and H. J. Maier, *Acta Mater.* **55**, 4253 (2007).
- [72] V. D. Buchelnikov, P. Entel, S. V. Taskaev, V. V. Sokolovskiy, A. Hucht, M. Ogura, H. Akai, M. E. Gruner, and S. K. Nayak, *Phys. Rev. B* **78**, 184427 (2008).
- [73] B. M. Wang, Y. Liu, L. Wang, S. L. Huang, Y. Zhao, Y. Yang, and H. Zhang, *J. Appl. Phys.* **104**, 043916 (2008).
- [74] Z. Li, C. Jing, J. Chen, S. Yuan, S. Cao, and J. Zhang, *Appl. Phys. Lett.* **91**, 112505 (2007).
- [75] V. V. Khovaylo, T. Kanomata, T. Tanaka, M. Nakashima, Y. Amako, R. Kainuma, R. Y. Umetsu, H. Morito, and H. Miki, *Phys. Rev. B* **80**, 144409 (2009).
- [76] S. Chatterjee, S. Giri, S. K. De, and S. Majumdar, *Phys. Rev. B* **79**, 092410 (2009).
- [77] T. Kanomata, K. Fukushima, H. Nishihara, R. Kainuma, W. Ito, K. Oikawa, K. Ishida , K. -U. Neumann, and K. R. A. Ziebeck, *Mater. Sci. Forum* **583**, 119 (2008).
- [78] T. Kanomata, T. Yasuda, S. Sasaki, H. Nishihara, R. Kainuma, W. Ito, K. Oikawa, K. Ishida , K. U. Neumann, and K. R. A. Ziebeck, *J. Magn. Magn. Mater.* **321**, 773 (2009).
- [79] A. Planes, L. Mañosa, and M Acet, *J. Phys.: Condens. Matter* **21**, 233201 (2009).

- [80] X. Zhou, W. Li, H. P. Kunkel, and G. Williams, *J. Phys.: Condens. Matter* **16**, L39 (2004).
- [81] J. Marcos, L. Mañosa, A. Planes, F. Casanova, X. Batlle, and A. Labarta, *Phys. Rev. B* **68**, 094401 (2003).
- [82] A. M. Tishin, *Handbook of Magnetic Materials*, edited by K. H. J. Buschow (Elsevier, Amsterdam, 1999), Vol. **12**, pp. 395-524.
- [83] T. Krenke, S. Aksoy, E. Duman, M. Acet, X. Moya, L. Mañosa, and A. Planes, *J. Appl. Phys.* **108**, 043914 (2010).
- [84] M. Khan, I. Dubenko, S. Stadler, and N. Ali, *J. Phys.: Condens. Matter* **20**, 235204 (2008).
- [85] R. C. O'Handley, S. J. Murray, M. Marioni, H. Nembach, and S. M. Allen, *J. Appl. Phys.* **87**, 4712 (2000).
- [86] R. Tickle and R. D. James, *J. Magn. Magn. Mater.* **195**, 627 (1999).
- [87] B. Gao, F. X. Hu, J. Wang, J. R. Sun, and B. G. Shen, *J. Magn. Magn. Mater.* **321**, 2571 (2009).
- [88] P. J. Shamberger and F. S. Ohuchi, *Phys. Rev. B* **79**, 144407 (2009).
- [89] R. Kainuma, Y. Imano, W. Ito, Y. Sutou, H. Morito, S. Okamoto, O. Kitakami, K. Oikawa, A. Fujita, T. Kanomata, and K. Ishida, *Nature* **439**, 04493 (2006).
- [90] C. Biswas, R. Rawat, and S. R. Barman, *Appl. Phys. Lett.* **86**, 202508 (2005).
- [91] S. Banik, R. Rawat, P. K. Mukhopadhyay, B. L. Ahuja, A. Chakrabarti, P. L. Paulose, S. Singh, A. K. Singh, D. Pandey, and S. R. Barman, *Phys. Rev. B* **77**, 224417 (2008); S. Banik, R. Rawat, P. K. Mukhopadhyay, B. L. Ahuja, A. Chakrabarti and S. R. Barman, *Adv. Mater. Res.* **52**, 207 (2008).
- [92] S. Banik, S. Singh, R. Rawat, P. K. Mukhopadhyay, B. L. Ahuja, A. M. Awasthi, S. R. Barman, and E. V. Sampathkumaran, *J. Appl. Phys.* **106**, 103919 (2009).

- [93] M. Kataoka, Phys. Rev. B **63**, 134435 (2001).
- [94] T. Kasuya, Prog. Theor. Phys. **16**, 58 (1956).
- [95] K. Koyama, H. Okada, K. Watanabe, T. Kanomata, R. Kainuma, K. Oikawa, W. Ito, and K. Ishida, Appl. Phys. Lett. **89**, 182510 (2006).
- [96] S. Y. Yu, Z. H. Liu, G. D. Liu, J. L. Chen, Z. X. Cao, G.H. Wu, B. Zhang, and X. X. Zhang, Appl. Phys. Lett. **89**, 162503 (2006).
- [97] V. K. Sharma, M. K. Chatopadhyay, K. H. B. Shaeb, A. Chouhan, and S. B. Roy, Appl. Phys. Lett. **89**, 222509 (2006).
- [98] S. Singh, I. Glavatskyy, and C. Biswas, J. Alloys Compd. **615**, 994 (2014).
- [99] S. Chatterjee, S. Giri, S. K. De, and S. Majumdar, Phys. Rev. B **79**, 092410 (2009).
- [100] W. H. Meiklejohn and C. P. Bean, Phys. Rev. **102**, 1413 (1956).
- [101] M. Ali, P. Adie, C. H. Marrows, D. Greig, B. J. Hickey, and R. L. Stamps, Nature Mater. **6**, 70 (2007).
- [102] S. Giri, M. Patra, and S. Majumdar, J. Phys.: Condens. Matter **23**, 073201 (2011).
- [103] W. A. Razzaq and J. S. Kouvel, J. Appl. Phys. **55**, 1623 (1984).
- [104] W. C. Cain and M. H. Kryder, J. Appl. Phys. **67**, 5722 (1990).
- [105] J. Nogués and I. K. Schuller, J. Magn. Magn. Mater. **192**, 203 (1999).
- [106] B. M. Wang, Y. Liu, P. Ren, B. Xia, K. B. Ruan, J. B. Yi, J. Ding, X. G. Li, and L. Wang, Phys. Rev. Lett. **106**, 077203 (2011).
- [107] B. M. Wang, Y. Liu, B. Xia, P. Ren, and L. Wang, J. Appl. Phys. **111**, 043912 (2012).
- [108] Z. D. Han, B. Qian, D. H. Wang, P. Zhang, X. F. Jiang, C. L. Zhang, and Y. W. Du, Appl. Phys. Lett. **103**, 172403 (2013).

- [109] P. Liao, C. Jing, X. L. Wang, Y. J. Yang, D. Zheng, Z. Li, B. J. Kang, D. M. Deng, S. X. Cao, J. C. Zhang, and B. Lu, *Appl. Phys. Lett.* **104**, 092410 (2014).
- [110] S. Pal, S. Sarkar, S. K. Pandey, C. Maji, and P. Mahadevan, *Phy. Rev. B* **94**, 115143 (2016).
- [111] A. Ayuela, J. Enkovaara, K. Ullakko, and R. M. Nieminen, *J. Phys.: Condens. Matter* **11**, 2017 (1999).
- [112] M. Ye, A. Kimura, Y. Miura, M. Shirai, Y. T. Cui, K. Shimada, H. Namatame, M. Taniguchi, S. Ueda, K. Kobayashi, R. Kainuma, T. Shishido, K. Fukushima, and T. Kanomata, *Phys. Rev. Lett.* **104**, 176401 (2010).
- [113] S. Fujii, S. Ishida, and S. Asano, *J. Phys. Soc. Jpn.* **58**, 3657 (1989).
- [114] C. P. Opeil, B. Mihaila, R. K. Schulze, L. Mañosa, A. Planes, W. L. Hults, R. A. Fisher, P. S. Riseborough, P. B. Littlewood, J. L. Smith, and J. C. Lashley, *Phys. Rev. Lett.* **100**, 165703 (2008).
- [115] V. V. Godlevsky and K. M. Rabe, *arXiv:cond-mat/0009406v1 [cond-mat.mtrl-sci]* (2000).
- [116] B. R. K. Nanda and I. Dasgupta, *arXiv:cond-mat/0611476v1 [cond-mat.mtrl-sci]* (2006).
- [117] P. Entel, M. E. Gruner, A. Dannenberg, M. Siewert, S. K. Nayak, H. C. Herper, and V. D. Buchelnikov, *Mater. Sci. Forum* **635**, 3 (2010).
- [118] T. Büsgen, J. Feydt, R. Hassdorf, S. Thienhaus, A. Zayak, P. Entel, and M. Moske, *Phase Transitions* **78**, 267 (2005).
- [119] A. T. Zayak and P. Entel, *arXiv:cond-mat/0406139v1 [cond-mat.mtrl-sci]* (2004).
- [120] S. Plogmann, T. Schlathölter, J. Braun, M. Neumann, Y. M. Yarmoshenko, M. V. Yablon-skikh, E. I. Shreder, E. Z. Kurmaev, A. Wrona, and A. Ślebarski, *Phys. Rev. B* **60**, 6428 (1999).
- [121] A. Ayuela, J. Enkovaara, and R. M. Nieminen, *J. Phys.: Condens. Matter* **14**, 5325 (2002).

- [122] S. K. Bose, J. Kudrnovský, V. Drchal, and I. Turek, Phys. Rev. B **82**, 174402 (2010).
- [123] P. Entel, V. D. Buchelnikov, V. V. Khovailo, A. T. Zayak, W. A. Adeagbo, M. E. Gruner, H. C. Herper, and E. F. Wassermann, J. Phys. D: Appl. Phys. **39**, 865 (2006).
- [124] V. Berti, M. Fabrizio, and D. Grandi, Physica D **239**, 95 (2010).
- [125] D. Grandi, M. Maraldi, and L. Molari, Acta Mater. **60**, 179 (2012).
- [126] F. Falk, Journal de Physique, **43**, C4-3 (1982).
- [127] P. J. Brown, A. Y. Bargawi, J. Crangle, K. U. Neumann, and K. R. A. Ziebeck, J. Phys.: Condens. Matter **11**, 4715 (1999).
- [128] S. R. Liu, H. J. Zhai, and L. S. Wang, Phys. Rev. B **65**, 113401 (2002).
- [129] S. R. Barman, S. Banik, and A. Chakrabarti, Phys. Rev. B **72**, 184410 (2005).
- [130] C. L. Tan, Y. W. Huang, X. H. Tian, J. X. Jiang, and W. Cai, Appl. Phys. Lett. **100**, 132402 (2012).
- [131] H. B. Xiao, C. P. Yang, R. L. Wang, V. V. Marchenkov, and X. Luo, J. Appl. Phys. **115**, 203703 (2014).
- [132] G. Fritsch, V. V. Kokorin, and A. Kempf, J. Phys.: Condens. Matter **6**, L107 (1994).
- [133] A. Zheludev, S. M. Shapiro, P. Wochner, A. Schwartz, M. Wall, and L. E. Tanner, Phys. Rev. B **51**, 11310 (1995).
- [134] A. Zheludev, S. M. Shapiro, P. Wochner, and L. E. Tanner, Phys. Rev. B **54**, 15045 (1996).
- [135] V. V. Kokorin, V. A. Chernenko, J. Pons, C. Segu, and E. Cesari, Solid State Commun. **101**, 7 (1997).
- [136] U. Stuhr, P. Vorderwisch, V. V. Kokorin, and P. -A. Lindgard, Phys. Rev. B **56**, 14360 (1997).

- [137] L. Mañosa, A. Planes, J. Zarestky, T. Lograsso, D. L. Schlagel, and C. Stassis, Phys. Rev. B **64**, 024305 (2001).
- [138] S. M. Shapiro, P. Vorderwisch, K. Habicht, K. Hradil, and H. Schneider, Europhys. Lett. **77**, 56004 (2007).
- [139] S. W. D'Souza, A. Rai, J. Nayak, M. Maniraj, R. S. Dhaka, S. R. Barman, D. L. Schlagel, T. A. Lograsso, and A. Chakrabarti, Phys. Rev. B **85**, 085123 (2012).
- [140] S. O. Mariager, C. Dornes, J. A. Johnson, A. Ferrer, S. Grubel, T. Huber, A. Caviezel, S. L. Johnson, T. Eichhorn, G. Jakob, H. J. Elmers, P. Beaud, C. Quitmann, and G. Ingold, Phys. Rev. B **90**, 161103(R) (2014).

Chapter 2

Theoretical and Experimental methods

2.1 Theoretical methods

2.1.1 Introduction

Density-functional theory (DFT) becomes one of the most popular and successful *ab-initio* quantum mechanical approaches to the study of solid state physics since 1970s. Interfacing with high performance computer this theory provides a simple and powerful way for calculating the ground-state properties of interacting systems. It has tremendous applications for calculating the band structure and density of states of electrons in solids. In particular, it has been exceptionally successful in explaining the structural and magnetic properties of transition metals and their alloys.

Conventional methods in electronic structure calculations, like Hartree-Fock theory and variational approaches are based on the complicated many-electron Schrödinger wavefunctions. The main idea of DFT is to deal with the electronic density ($\rho(\mathbf{r})$) as the fundamental quantity instead of many-electron wavefunctions. The advantage of use of $\rho(\mathbf{r})$ is that it has only three variables which are the position co-ordinates while many-electron wavefunction has $3N$ (N , number of electrons). Considering other degrees of freedom, such as spin, the number of variables will be changed accordingly. Consequently, many-body wave-equations can be treated as single particle Hartree-type equations in terms of electron density, which experiences an effective potential.

2.1.2 Born-Oppenheimer Approximation

The simplification of the many body Hamiltonian can be carried out on the basis of Born-Oppenheimer approximation. Due to heavier masses of nuclei than electrons, it is reasonable to assume that the nuclei move very slowly with respect to the electrons. This implies that one can consider the electrons as moving in the field of fixed nuclei. As a result of this, the kinetic energy terms associated with the nuclei and their potential energy can be ignored from total many body Hamiltonian. Thus,

the electronic part of the Schrödinger equation can be written as

$$\begin{aligned}\widehat{H}_{\text{electron}} \Psi_{\text{electron}} (\mathbf{r}_1, \mathbf{r}_2, \mathbf{r}_3 \dots \mathbf{r}_N) &= \left[-\frac{\hbar^2}{2m} \sum_i^N \nabla_i^2 + \sum_i^N V(\mathbf{r}_i) + \sum_{i \neq j}^N U(\mathbf{r}_i, \mathbf{r}_j) \right] \Psi_{\text{electron}} (\mathbf{r}_1, \mathbf{r}_2, \mathbf{r}_3 \dots \mathbf{r}_N) \\ &= [\widehat{T} + \widehat{V}_{\text{ext}} + \widehat{U}_{\text{ee}}] \Psi_{\text{electron}} (\mathbf{r}_1, \mathbf{r}_2, \mathbf{r}_3 \dots \mathbf{r}_N)\end{aligned}\quad (2.1)$$

where $\Psi_{\text{electron}} (\mathbf{r}_1, \mathbf{r}_2, \mathbf{r}_3 \dots \mathbf{r}_N)$ is the wave function of stationary electronic state, N is the number of electrons and U_{ee} is the electron-electron interaction. V_{ext} varies from system to system. Traditional analysis of this many-electron equation is cumbersome and involves huge computational effort. DFT provides a way to systematically map the many-electron problem onto a single-electron problem considering the fundamental variable the electron density $\rho(\mathbf{r})$ which has the form

$$\begin{aligned}\rho(\mathbf{r}) &= \langle \Psi | \sum_i^N \delta(\mathbf{r} - \mathbf{r}_i) | \Psi \rangle \\ &= N \int d^3 r_2 \dots \int d^3 r_N |\Psi_{\text{electron}} (\mathbf{r}, \mathbf{r}_2, \mathbf{r}_3 \dots \mathbf{r}_N)|^2\end{aligned}\quad (2.2)$$

2.1.3 Thomas-Fermi model

The most simplified DFT is mainly based on the Thomas-Fermi model [1], which was formulated by L. H. Thomas and E. Fermi in 1927, just after Schrödinger proposed his quantum-mechanical wave equation. In this model electrons in an atom are approximated to move independently in an effective potential ($v_{\text{eff}}(\mathbf{r})$), to describe the electron density ($\rho(\mathbf{r})$) and ground state energy ($E(N)$), for a large number of electrons N [2].

$$v_{\text{eff}}(\mathbf{r}) = v_{\text{ext}}(\mathbf{r}) + \int \frac{\rho(r')}{|r - r'|} d^3 r \quad (2.3)$$

Although this was an important consideration, the Thomas-Fermi equation's validity is limited because it neglects exchange and correlation effects. Later Palskett modified Thomas-Fermi formula which is similar to Von Weizsäcker [3].

Later in 1964, Hohenberg and Kohn formulated a theory of density functional mainly motivated by Thomas-Fermi theory and established the relation between the electron density $\rho(\mathbf{r})$ and the many-electron Schrödinger wave equation [4].

2.1.4 Hohenberg-Kohn theorems

The first Hohenberg-Kohn theorem states that,

The ground state density $\rho_0(\mathbf{r})$ of the interacting electrons in some external potential $v_{\text{ext}}(\mathbf{r})$ determines this potential uniquely and hence the ground state energy.

$$E_0 = E[\rho_0] = \langle \Psi_0 | \hat{T} + \hat{V}_{\text{ext}} + \hat{U}_{\text{ee}} | \Psi_0 \rangle \quad (2.4)$$

where $\Psi_0 = \Psi[\rho_0]$. The external potential $\langle \Psi_0 | \hat{V}_{\text{ext}} | \Psi_0 \rangle = V_{\text{ext}}[\rho_0] = \int v_{\text{ext}}(r) \rho_0(r) d^3r$.

The functionals $T[\rho_0]$ and $U_{\text{ee}}[\rho_0]$ are called universal functionals while $V_{\text{ext}}[\rho_0]$ is not universal and depends on the system under consideration.

The second Hohenberg-Kohn theorem provides a variational principle,

For any given density $\rho(\mathbf{r})$ associated to an N electron system with external potential $v_{\text{ext}}(\mathbf{r})$ the minimum of the energy functional is obtained with the ground state density.

$$E_0 \leq E[\rho] = T[\rho] + V_{\text{ext}}[\rho] + U_{\text{ee}}[\rho] \quad (2.5)$$

The ground state can be obtained by minimizing the functional $E[\rho]$ with respect to $\rho(\mathbf{r})$. A successful minimization of the energy functional will provide the ground state density $\rho_0(\mathbf{r})$ and thus all other ground state properties of interest.

2.1.5 Kohn-Sham equations

Based on the second theorem of Hohenberg and Kohn, in 1965 Kohn and Sham showed that the variational problem of minimizing the energy functional can be solved by applying the Lagrangian method of undetermined multipliers subject to the condition of constant number of electrons $N = \int \rho(r) d^3r$ [5]. Kohn and Sham's intuition was to find out a one-particle equation with effective

potentials within the framework of the DFT. In order to proceed one has to write the total energy functional $E[\rho]$ as,

$$E[\rho] = T[\rho] + \int v_{\text{ext}}(r)\rho(r)d^3r + \frac{1}{2}e^2 \int \frac{\rho(r)\rho(r')}{|r-r'|} d^3rd^3r' + E_{\text{XC}}[\rho(r)] \quad (2.6)$$

In the above total energy functional, the first term is total kinetic energy functional. As suggested by Kohn and Sham, it is convenient to split up the kinetic energy term into two terms $T[\rho] = T_0[\rho] + T_1[\rho]$. T_0 is the the kinetic energy of non-interacting electrons, while $T_1[\rho]$ includes the electron-electron interaction. $T_0[\rho]$ represents a good approximation to the exact kinetic energy functional because contribution of $T_1[\rho]$ is negligibly small in $T[\rho]$. Other terms are the energy functional because of the the external potential, the energy functional of the static electron-electron Coulomb repulsion (Hartree term, $E_H[\rho(r)]$) and the exchange-correlation energy functional, respectively. The exact Coulomb functional $U_{\text{ee}}[\rho]$ is the sum of $E_H[\rho(r)]$ and $E_{\text{XC}}[\rho(r)]$.

The variational equation for the total energy functional is:

$$\frac{\delta E[\rho]}{\delta \rho(r)} = \frac{\delta T_0[\rho]}{\delta \rho(r)} + v_{\text{ext}}(r) + e^2 \int \frac{\rho(r')}{|r-r'|} d^3r' + \frac{\delta E_{\text{XC}}[\rho]}{\delta \rho(r)} = \mu \quad (2.7)$$

where μ is a Lagrange multiplier which guaranties the particle number conservation.

Kohn and Sham hypothesized that, for any system of N interacting electrons in a given external potential $v_{\text{ext}}(r)$, there is a virtual system of N non-interacting electrons with exactly the same density as the original system. In this assumption, the non-interacting electrons are considered to be subjected to an effective potential $v_{\text{eff}}(r)$. For this type of virtual system the variational equation can be written as,

$$\frac{\delta E[\rho]}{\delta \rho(r)} = \frac{\delta T_0[\rho]}{\delta \rho(r)} + v_{\text{eff}}(r) = \mu \quad (2.8)$$

From Equ. 2.7, one can write,

$$v_{\text{eff}}(r) = v_{\text{ext}}(r) + e^2 \int \frac{\rho(r')}{|r-r'|} d^3r' + v_{\text{XC}}(r) \quad (2.9)$$

where $v_{\text{XC}}(r) = \frac{\delta E_{\text{XC}}[\rho]}{\delta \rho(r)}$ is the functional derivative of the exchange-correlation energy, which is usually referred to as the “exchange-correlation potential”.

In addition, for such a fictitious system, in which the electrons do not interact at all, the wavefunction can be written as Slater determinant. As in Hartree-Fock theory, the N-electron system is reduced to a set of N non-interacting one-electron systems. Here the kinetic energy for this (T_{HF}) is known exactly. The Slater determinant consists of orbitals $\phi_i(\mathbf{r}) (i = 1, N)$, termed Kohn-Sham orbitals. Then one obtain a set of effective single-particle equations called the Kohn-Sham equations.

$$\left[-\frac{\hbar^2 \nabla^2}{2m} + v_{\text{eff}}(\mathbf{r}) \right] \phi_i(\mathbf{r}) = \epsilon_i \phi_i(\mathbf{r}) \quad (2.10)$$

The corresponding electron density can be written as,

$$\rho(\mathbf{r}) = \sum_i p_i |\phi_i(\mathbf{r})|^2 \quad (2.11)$$

where p_i is probability of occupation of $\phi_i(\mathbf{r})$ orbital. Above Kohn-Sham equation has no electron spin dependence. For spin-polarized systems, for each of the two spin components, a set of spin-polarized Kohn-Sham equations are formulated, which leads to two set of Kohn-Sham orbitals, depending on their spin.

The Kohn-Sham equation has to be solved self-consistently. Starting with initial guess for the electron density $\rho(\mathbf{r})$, the corresponding effective potential $v_{\text{eff}}(\mathbf{r})$ and the Kohn-Sham equations for the $\phi_i(\mathbf{r})$ are solved. From these a new electron density is computed and the previous steps are carried out. This procedure is then repeated until convergence is reached. Once this is done, the ground state energy can be expressed by,

$$E_0 = \sum_i p_i \epsilon_i - \frac{1}{2} e^2 \int \frac{\rho(r) \rho(r')}{|r - r'|} d^3 r d^3 r' + E_{\text{XC}}[\rho(r)] - \int v_{\text{XC}}(r) \rho(r) d^3 r \quad (2.12)$$

2.1.6 Electron exchange and correlation interactions

In many-electron systems, the motion of one electron is influenced by the motion of the other electrons. First effect arises on the basis of Pauli exclusion principle which states that two electrons with similar spin state cannot occupy the same energy state. Hence, the electron wavefunction must be antisymmetric when either the spin or spatial coordinates are interchanged which means $\Psi(\mathbf{r}_1, \mathbf{r}_2) = -\Psi(\mathbf{r}_2, \mathbf{r}_1)$.

Hartree-Fock approximation incorporates exact exchange energy, while the effect of electron correlation is ignored. Here, the difference in exact ground state energy and the Hartree-Fock approximated energy, which is the energy of uncorrelated state, is called “correlation energy”, E_C . Correlation plays important role for electrons with opposite spin tending to occupy the same orbital state.

The major drawback is that the exact functionals for exchange and correlation are not known except for the free electron gas. However, exchange and correlation effects can be properly treated within the many-body theory, which is largely based on Green functions and diagrammatic techniques, which are beyond our discussions. Although, there exist some approximations of the form of the exchange and correlation which describes certain physical quantities quite accurately by DFT.

Local Density Approximation (LDA)

The simplest and common way of approximating the exchange-correlation energy is called local-density approximation (LDA). In this approximation, the value of E_{XC} per electron at each point in the system is taken to be similar as that of an electron in a uniform gas of electrons having the same density. In this approximation, the electron density is considered to be locally smooth varying. In general, for a spin-unpolarized system, a local-density approximation for the exchange-correlation energy is written as

$$E_{XC}[\rho(r)] = \int \rho(r) \epsilon_{XC}[\rho(r)] d^3r \quad (2.13)$$

ϵ_{XC} is exchange and correlation energy per particle of the homogeneous electron gas of density $\rho(r)$. The exchange-correlation energy density can be further decomposed into exchange and correlation parts as

$$\epsilon_{XC}[\rho(r)] = \epsilon_X[\rho(r)] + \epsilon_C[\rho(r)] \quad (2.14)$$

The exchange energy is given by the Dirac functional [6].

$$E_X[\rho(r)] = -\frac{3}{4} \left(\frac{3}{\pi}\right)^{\frac{1}{3}} \int \rho(r)^{\frac{4}{3}} d^3r \quad (2.15)$$

The correlation energy is mainly calculated numerically with high accuracy by means of quantum Monte Carlo calculations. However, this energy can be evaluated analytically in the high and low electron density limits corresponding to infinitely-weak and infinitely-strong correlation. The high-density limit of the correlation energy density is of the form $\varepsilon_C = A \ln(r_s) + B + r_s(C \ln(r_s) + D)$ and that for low limit is $\varepsilon_C = \frac{1}{2} \left(\frac{g_0}{r_s} + \frac{g_1}{r_s^2} + \dots \right)$ [7]. r_s represents the Wigner-Seitz parameter and it is related to the density by $\frac{4}{3}\pi r_s^3 = \frac{1}{\rho}$.

The exchange-correlation potential corresponding to the exchange-correlation energy is given by

$$v_{XC}[\rho(r)] = \varepsilon_{XC}[\rho(r)] + \rho(r) \frac{\partial \varepsilon_{XC}[\rho(r)]}{\partial \rho(r)} \quad (2.16)$$

LDA works very much accurate for bulk metals, where slowly varying electron density can be compared with the homogeneous electron gas. However, in this approximation cell parameters are usually underestimated, the bulk modulus is overestimated. Binding energies are almost always overestimated; while it tends to underestimate atomic ground state energies and ionization energies. Moreover, sometimes the wrong ground state is predicted. For example, insulating systems (e.g., NiO) are predicted to be metallic. Spin polarised calculations considering the correct ground state for NiO do get an insulating state. However, the bandgap is grossly underestimated.

Generalized Gradient Approximation (GGA)

In a most of the real systems, the electron density can not be considered homogeneous because there are non-local correlation effects. The electron density varies non-homogeneously in space. So, in that circumstance the density variations is given by the expansion of the density in terms of its gradients, i.e., $\nabla\rho(\mathbf{r}), \nabla^2\rho(\mathbf{r})$ etc. Considering only the linear term of the electron density gradient, the generalized gradient approximation (GGA) can be written as

$$E_{XC}[\rho(r)] = \int \rho(r) \varepsilon_{XC}[\rho(r), \nabla\rho(r)] d^3r \quad (2.17)$$

GGA describes the magnetic and structural ground state quite accurately for transitional metals and alloys than LDA.

2.1.7 Plane-waves as basis functions

Most easily usable basis functions for describing crystal periodicity can be described as plane wave functions. The theorem of Bloch shows that the wavefunction in a periodic potential can be expressed as a form of a plane wave times a function with the periodicity of the Bravais lattice.

$$\Psi_{n,\mathbf{k}}(\mathbf{r}) = u_n(\mathbf{r}) \exp(i\mathbf{k} \cdot \mathbf{r}) \quad (2.18)$$

The periodic function $u_n(\mathbf{r})$ can be expanded as a linear combination of plane wave function with wave vectors that are reciprocal lattice vectors of the crystal, \mathbf{G} .

$$u_n(\mathbf{r}) = \sum_{\mathbf{G}} c_{n,\mathbf{G}} \exp(i\mathbf{G} \cdot \mathbf{r}) \quad (2.19)$$

This plane wave basis set can be used to expand the Kohn-Sham orbitals.

2.1.8 DFT implementation by Vienna *ab-initio* simulation package (VASP)

A computationally less expensive but reasonably accurate calculation these days use pseudopotentials or projector augmented wave (PAW) potentials where the corelevels are not a part of the basis states [8–11]. This has been applied in key areas of modern solid-state physics and chemistry. In this thesis we use a plane wave PAW implementation of DFT in VASP. It attempts to match the accuracy of the most advanced all-electron codes by using a projector-augmented-wave approach (PAW) [12] for describing the electron-ion interaction. A stable and accurate solution of the Kohn-Sham equations, as well as a favorable scaling of the computational effort with system size, are achieved by adopting iterative diagonalization techniques and optimized charge-mixing routines. Different levels of exchange-correlation functionals and different post-DFT approaches have been implemented.

There are other different procedures such as full-potential linearized augmented-plane-wave (FLAPW) method using a non-local approximation for the exchange and correlation potential, augmented-spherical-wave (ASW) formalism within the local spin-density (LSD) treatment of exchange and correlation, linear muffin-tin orbital (LMTO) method with the LSD approximation and a muffin tin for the potential, full-potential local-orbital (FPLO) *ab-initio* method etc.

2.1.9 Wannier functions

According to Bloch theorem, the eigenfunctions of the wave equation for a periodic potential in crystal are the product of a plane wave ($\exp(i \vec{k} \cdot \vec{r})$) times a function $u_n(\vec{r})$ with the periodicity of the crystal lattice. $\Psi_{n, \vec{k}}(\vec{r}) = u_n(\vec{r}) \exp(i \vec{k} \cdot \vec{r})$, where a crystal momentum \vec{k} lying inside the Brillouin zone and a band index n . This function is widely used in electronic-structure calculations. However, sometimes in tight binding method, it is useful to construct a localized wave functions from the Bloch wave functions. To explain electronic properties of any material, inclusion of all possible states of every atom is unfeasible and are not necessary to understand the relevant physical properties. For example in Ni-Mn-Ga system, Ni d , Mn d and Ga s & p orbitals are sufficient to explain the band structure. Wannier functions are very useful for analyzing the nature of the chemical bonding in materials.

Wannier function, first proposed by G. Wannier [13], is a candidate of localized orbital. Wannier functions can be constructed by linear combination of atomic orbital wavefunctions, which are Blöch functions. These maximally localized wavefunctions are constructed by superposing Blöch functions of different \vec{k} as,

$$W_{n, \vec{R}}(\vec{r}) = \frac{V}{(2\pi)^3} \int_{BZ} e^{-\vec{k} \cdot \vec{R}} \Psi_{n, \vec{k}}(\vec{r}) d\vec{k} \quad (2.20)$$

where \vec{R} is the real-space lattice vector [14]. A particular Wannier function is localized around a particular lattice point (\vec{R}) and rapidly goes to zero away from the lattice point where atom is situated. Under the translation by lattice vector \vec{R} , the real space Wannier function can be transformed to other Wannier functions. All the $W_{n, \vec{R}}$ form orthonormal basis set. The Fourier transform of Eq. 2.20 gives the Blöch function back and takes the form as,

$$\Psi_{n, \vec{k}}(\vec{r}) = \frac{V}{(2\pi)^3} \int_{BZ} e^{\vec{k} \cdot \vec{R}} W_{n, \vec{R}}(\vec{r}) d\vec{R} \quad (2.21)$$

Thus Bloch and Wannier functions can be transformed to each other under unitary transformation. Thus both Bloch and Wannier functions provide identical band description. It is important to mention that the Wannier functions are not unique due to gauge indeterminacy because different choices of gauge associated with Bloch states.

In this thesis we use a mapping of the *ab-initio* band structure onto a tight binding model to understand the changes in the electronic structure quantitatively due to the structural transformation. Here one can monitor the changes of the onsite energies to understand the effect.

2.2 Experimental methods

2.2.1 Sample preparation: Arc melting

The polycrystalline sample with the nominal composition $\text{Ni}_2\text{Mn}_{1+x}\text{Sn}_{1-x}$ was prepared by arc melting of 99.99 % pure elements in an argon gas atmosphere. Fig. 2.1 shows the schematic

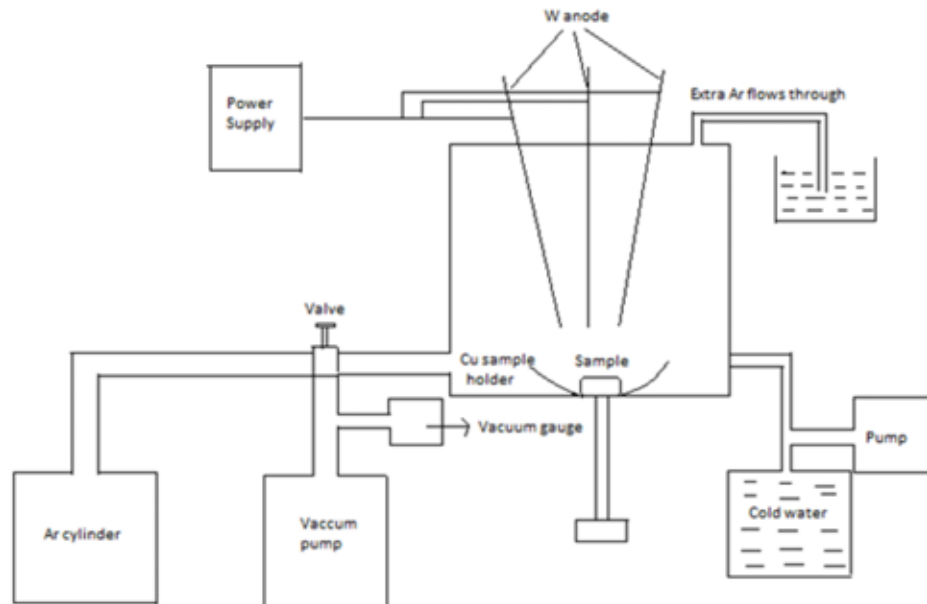


Figure 2.1 Schematic diagram of vacuum arc melting furnace.

diagram of vacuum arc melting furnace. The arc melting furnace consists of a cylindrical chamber inside which the sample is kept on a Cu crucible, a rotary vacuum pump to make vacuum inside the cylindrical chamber and a gauge to monitor, Ar gas to make the environment of the sample air free and inert, valve to connect vacuum pump and Ar cylinder alternately to the cylindrical chamber, a water bath to flush out extra Ar gas from the cylindrical chamber, three tungsten anodes connected

to power supply to produce arc, cold water supply to keep the furnace cool. Initially, the air inside the chamber is evacuated by the rotary vacuum pump. The vacuum achieved is of the order of 1×10^{-3} mbar. The Ar gas is introduced in the chamber to flush out the remaining light gases like O₂, N₂, C etc. Ar is used because this is an inert gas and has more weight than air. So, any small amount of air in the furnace is replaced by Ar. This process is repeated 3-4 times in order to ensure good inert atmosphere inside the chamber. The arc melting is done under argon atmosphere. The sample was flipped and remelted several times to ensure homogeneity. Then the sample was cut with a low speed diamond saw and parts of the sample were encapsulated in a quartz glass tube under vacuum for annealing. The sample were annealed at 900° C for 1 day and then quenched in ice water. As a result the desired structure is stabilized.

2.2.2 Differential Scanning Calorimetry (DSC)

The DSC is a thermo-analytical technique by which structural and magnetic phase transition temperatures of materials can be determined, measuring the differences in the amount of heat flow in endothermic or exothermic processes. The heat flow can be plotted as a function of temperature or time. There are two types of DSC systems available : Heat-flux DSC and Power Compensation DSC.

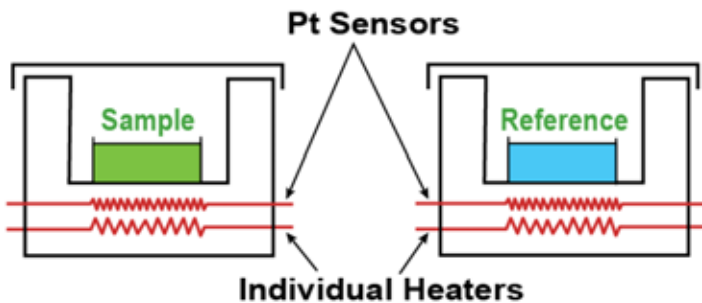


Figure 2.2 Schematic diagram of Power Compensation DSC [Ref:<http://nptel.ac.in/courses/115103030/module4/lec22/2.html>].

The differential scanning calorimeter Q 2000 of TA instrument is used for the measurement of structural and magnetic transition temperature. This is basically a Power-Compensation DSC

which is shown in fig. 2.2. In Power-Compensation DSC both sample and reference pans are heated by separate, identical furnaces. Here the sample and reference are maintained at the same temperature throughout the experiment. Due to temperature variation when an endothermic or exothermic transition occurs in the sample, Platinum sensor detects the thermal changes in the sample. Then input energy or power is required to maintain the temperature of the sample to that of the reference pan and it actually measures the amount of excess heat absorbed or released by sample during endothermic or exothermic process in cooling and heating cycle. Then plotting the heat flow as a function of temperature, one can obtain the temperatures of various phase transitions. Over Heat-Flux DSC, the Power-Compensation DSC technique is very much easy to handle because no complicated heat flux equations are necessary and the system directly measures rate of energy flow to and from the sample.

2.2.3 X-ray diffraction

The X-ray diffraction (XRD) is one of the basic tools to find out the unknown crystal structure of a material. X-rays are used because their wavelength is comparable with interatomic spacing of bulk material. When X-rays fall on a material, it scatters in all directions from the atomic sites. Subsequently, in some directions the constructive interference condition $2dsin\theta = n\lambda$ is satisfied. This is the Bragg law of diffraction established by W. L. Bragg, which relates crystal lattice parameters d (spacing between the atomic planes of the solid) and wavelength of incident radiation (λ) with the diffraction angles (θ) and n is the order of diffraction [15]. Fig. 2.3 shows the schematic of Bragg diffraction condition. The powder method is used for polycrystalline material. The bulk material to be examined is ground to very fine powder and placed in a beam of monochromatic X-rays to capture the information of reflections from all the lattice planes in a crystal structure. The diffractometer is used in either $\theta - \theta$ or $\theta - 2\theta$ geometry [16]. In $\theta - \theta$ geometry, sample is fixed and both X-ray source and detector move at the same angular rate ω toward each other. In $\theta - 2\theta$ geometry, the source does not move, the sample rotates around its axis at a speed ω , whereas the detector is moving at a speed 2ω along the circle, centered on the sample. For the

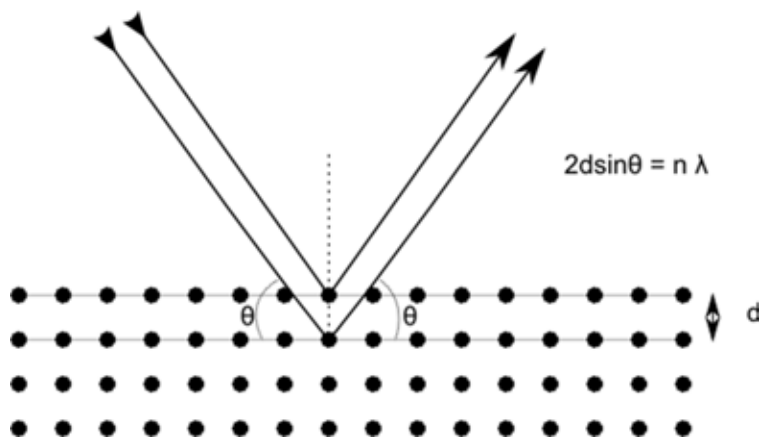


Figure 2.3 Schematic diagram of Bragg diffraction [Ref: <https://www2.warwick.ac.uk/fac/sci/physics/current/postgraduate/regis/mpags/ex5/techniques/structural/xrd/>].

present experiment, the powder diffraction is performed in $\theta - 2\theta$ geometry. The schematic representation of $\theta - 2\theta$ geometry is depicted in fig. 2.4. One can choose different X-ray sources to

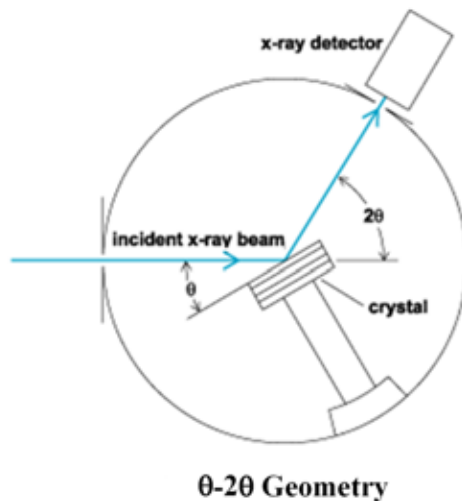


Figure 2.4 Schematic representation of $\theta - 2\theta$ geometry of diffractometer [Ref: <http://www.ehs.columbia.edu/NewsLetter/FA09Page4.html>].

find out the crystal structure. The PANalytical X-PERT PRO XRD diffractometer has been used for the room temperature XRD measurement using CuK_α radiation of wavelength $\lambda = 1.54 \text{ \AA}$. The low temperature XRD is performed by synchrotron radiation source in KEK-Photon Factory, Japan. It has highly collimated photon beam generated by a small divergence ($\sim 0.1^\circ$) and high

intensity photon beam (flux ~ 500000 count/area/sec) which help to capture the crystal structure more accurately ($\lambda = 0.68 \text{ \AA}$).

Here the Le Bail method is applied using Fullprof software to extract the crystal structure parameters corresponding to different crystal planes from powder diffraction data. First, the possible approximate unit cell lattice parameters (a, b, c, α, β & γ) and space group are speculated. This can be carried out by the following steps. The correct Miller indices (hkl) corresponding to a lattice plane are assigned to each intensity peak position. This step is called “indexing the pattern” [15]. Once this is done, the the lattice spacing, d_{hkl} , is calculated for a particular lattice plane and for a particular Bragg angle. Using the mathematical relation $d_{hkl} = \frac{1}{\sqrt{(h/a)^2 + (k/b)^2 + (l/c)^2}}$ the lattice parameters of the unit cell can be calculated. Afterwards, the unit cell lattice parameters, other profile parameters (Instrumental zero error; Peak-width parameters etc.) are refined and the calculated peak intensities are matched with the measured powder diffraction pattern by the least-square fitting technique of the diffraction profile. The technique is basically an iterative process. In each iteration a fresh set of observed intensities are obtained which are matched with experimentally obtained diffraction pattern. It continues until a convergence criterion is satisfied and a good agreement with measured X-ray pattern is achieved with physically valid parameter values.

The goodness of fit can be estimated from the difference pattern and also from the reliability (R) factor. The R factor is defined as the following.

$$\text{Weighted profile } R - \text{factor } (R_{wp}) = \left[\frac{\sum_i w_i (y_{io} - y_{ic})^2}{\sum_i w_i y_{io}^2} \right]^{\frac{1}{2}}$$

Here y_{io} and y_{ic} are the observed and calculated intensities.

$$\text{Expected } R - \text{factor } (R_{exp}) = \left[\frac{N-P+C}{\sum_i w_i y_{io}^2} \right]^{\frac{1}{2}}$$

$$\text{Goodness of fit parameter } (\chi^2) = \frac{\sum_i w_i (y_{io} - y_{ic})^2}{N-P+C} = \left(\frac{R_{wp}}{R_{exp}} \right)^2$$

Here, $w_i = \frac{1}{y_i}$ is the weighting factor. N is the total number of points used in the refinement, P is the number of refined parameters, C is the number of constraint. $N - P + C$ is the number of degrees of freedom. The signature of good fitting is to obtain low value of R_{wp} and χ^2 after the final iteration. The average value of goodness of fit from our fitting for all compositions and

temperatures is around 1.6. The goodness of fit value between 1 and 2 is considered to be good fitting. Thus Le Bail method provided reliable estimate of the intensities of allowed reflections for different crystal symmetries and structural parameters for our samples.

2.2.4 Magnetic susceptibility

Magnetic susceptibility is defined as the quantitative measure of the extent to which a material can be magnetized by applying an external magnetic field. It is equal to the ratio of the magnetization (M) within the material to the applied magnetic field strength (H).

$$\chi_m = \frac{M}{H}$$

The susceptibility has been measured by superconducting quantum interference device (SQUID).

The SQUID is highly sensitive to small changes in magnetization. A very small magnetic field can be detected by SQUID. A SQUID consists of a superconducting loop separated by two Josephson junctions which are basically thin insulating barrier. It operates basically on the principle of flux quantization within a superconducting loop. First, the sample is placed inside a superconducting detection coil in presence of a magnetic field produced by superconducting magnet. When the sample is moved periodically inside the coil, magnetic flux due to the magnetic moment of the sample changes inside coil. The change in magnetic flux is linked to a Direct Current (DC) SQUID. When the flux is integer multiple of ϕ_0 ($\phi_0 = \frac{h}{2e}$), same phase difference occurs between electron-pair waves propagating along two different paths around the loop. This leads to constructive interference causing the critical current which is usually obtained by measuring the voltage drop across the junction. This voltage is converted by Radio Frequency (RF) SQUID and is then amplified. This measured voltage oscillates which depends on the change in magnetic flux and gives an accurate measurement of magnetic properties. It is important to mention that the value of ϕ_0 (2×10^{-15} Tesla-m²) determines the sensitivity of the measurement. For the magnetization measurement as a function of temperature, the quantum design SQUID magnetometer is used in the temperature range 5 - 300 K.

2.2.5 Ultra-violet photo-electron spectroscopy (UPS)

In order to understand the electronic structure effect on martensitic phase the high resolution valence band spectra of $\text{Ni}_2\text{Mn}_{1+x}\text{Sn}_{1-x}$ are recorded with ultra-violet (UV) He I radiation of energy $h\nu = 21.2 \text{ eV}$, h = Planck's constant, ν = frequency of the radiation. Such radiation is only able to ionize the electrons from the valence band. The kinetic energy distribution of the emitted photoelectrons can be measured using an electron-energy selective analyser and detector. These photoelectrons emitted from the solid surface due to irradiation of photon follow certain distribution curve which represents the occupied density of electronic states. Schematic representation of ultra-violet photo-electron spectroscopy measurement has been shown in fig. 2.5. The process of

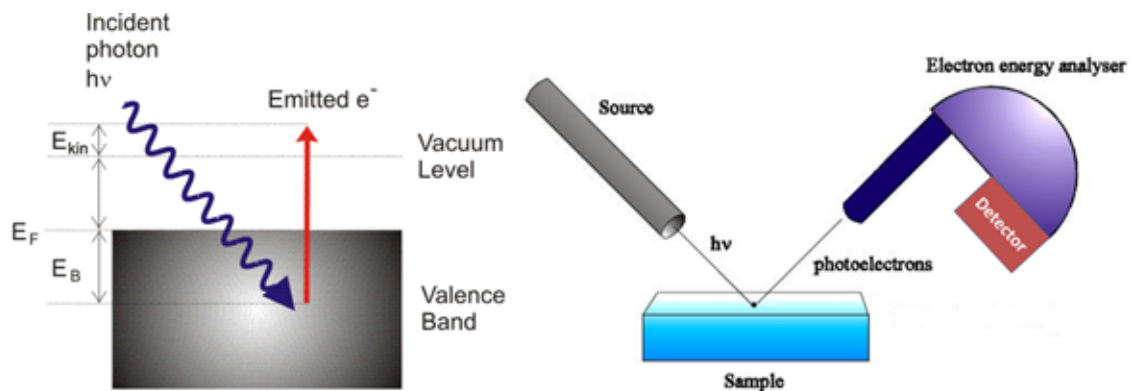
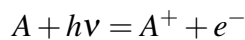


Figure 2.5 Schematic representation of ultra-violet photo-electron spectroscopy measurement [Ref: <http://www-users.york.ac.uk/~phys24/Pages/Techniques/UPS/>] .

photoelectron can be explained as follows: If A be the sample, the excitation of the material by UV radiation is written as



According to conservation of charge

$$E(A) + h\nu = E(A^+) + E(e^-)$$

Since energy of the electron is associated with kinetic energy (KE), then

$$E(e^-) = E_K(e^-) = h\nu - [E(A^+) - E(A)]$$

$E(A^+) - E(A)$ is the binding energy (E_B) of the material. This is the difference between the ionized and neutral atom. This is conventionally measured with respect to the Fermi-level of the

solid rather than the vacuum level. However, in this case the work function (φ) of the solid has to be considered. Thus the expression of the binding energy can be written as:

$$E_B = h\nu - E_K(e^-) - \varphi$$

The high intensity He photon source based on He plasma, generated with the electron cyclotron resonance technique, is used as ultra-violet source to study the valence band spectra. The He gas maintained at a pressure of about 1.5×10^{-6} mbar in the ultra-high-vacuum chamber. Due to the surface sensitivity of photo-electron spectroscopy technique the experiments are performed under ultra-high vacuum. A hemispherical high-resolution electron energy analyzer (Scienta R4000) of 200 mm radius is used for recording the photoelectron spectra. The overall energy resolution of He I photon source with Scienta R4000 analyzer is 1.5 meV at 10 K.

Bibliography

- [1] L.H. Thomas, Proc. Camb. Phil. Soc. **23**, 542(1927).
- [2] Dr. von Herrn Ersoy Şaşloğlu, PhD thesis, *First-principles study of the exchange interactions and Curie temperature in Heusler alloys*, 2006.
- [3] J. S. Plaskett, Proc. Phys. Soc. A **66**, 178 (1953).
- [4] P. Hohenberg and W. Kohn, Phys. Rev. **136**, 3864 (1964).
- [5] W. Kohn and L. J. Sham, Phys. Rev. **140**, A1133 (1965).
- [6] P. A. M. Dirac, Proc. Cambridge Phil. Roy. Soc. **26**, 376 (1930).
- [7] R. G. Parr and W. Yang, *Density-Functional Theory of Atoms and Molecules*, Oxford: Oxford University Press (1994).
- [8] G. Kresse and J. Hafner, Phys. Rev. B **47**, 558 1993.
- [9] G. Kresse and J. Furthmüller, Comput. Mater. Sci. **6**, 15 (1996).
- [10] G. Kresse and J. Furthmüller, Phys. Rev. B **54**, 11169 (1996).
- [11] G. Kresse and D. Joubert, Phys. Rev. B **59**, 1758 (1999).
- [12] P. E. Blöchl, Phys. Rev. B **50**, 17953 (1994).
- [13] G. H. Wannier, Phys. Rev. **52**, 191 (1937).

- [14] N. Marzari, A. A. Mostofi, J. R. Yates, I. Souza, and D. Vanderbilt, Rev. Mod. Phys. **84**, 1419 (2012).
- [15] B. D. Cullity, *Elements of X-ray Diffraction*, Addison-Wesley Publishing Company, Inc. (1978).
- [16] R. Guinebretière, *X-ray Diffraction by Polycrystalline Materials*, ISTE Ltd. (2007).

Chapter 3

The band Jahn-Teller effect in Ni₂MnGa: What drives it?

3.1 Introduction

The discovery of a change in the shape of a material, which, in addition to being tuned by external parameters such as temperature [1], pressure [2], magnetic field [3] etc., is also entirely reversible, has driven the research in these materials called shape memory alloys. However, despite a couple of decades of intense research, the microscopic mechanism driving the transition still remains hotly debated. Here, we consider the example of Ni₂MnGa which is the only member in the Ni-Mn based family of materials in which the transition from a high temperature cubic (austenitic) phase to a low temperature lower symmetry (martensitic) phase takes place for the stoichiometric case also [4]. The transition away from the cubic phase starts much before the martensitic phase sets in. In this temperature range, referred to as the pre-martensitic regime, one usually finds the presence of other crystallographic phases, with even two phases existing at times [5].

Unravelling the origin of the electronic structure changes should provide us with a handle on the martensitic transition. A direct probe of the electronic structure are photoemission experiments. These experiments carried out as a function of temperature reveal spectral weight transfers away from the near Fermi energy region and a pseudogap formation in a temperature range associated with the pre-martensitic transition. This continues as the temperature is decreased down to the martensitic transition temperature. These electronic structure changes have been associated with a reorganization of the Ni e_g states, which has led to the origin being described as a band Jahn-Teller mechanism [6]. An alternate picture of a charge density wave driving the transition has also been proposed [7].

The Jahn-Teller effect is operative in localized systems in which one has degenerate states at the Fermi level. The system distorts and lowers its energy and in the process is rendered insulating also. A prerequisite for such a mechanism to operate is a high density of states at the Fermi level in the undistorted structure and a strong electron-phonon coupling. Examining the density of states for Ni₂MnGa, one finds a low contribution at the Fermi level. This has led to the nomenclature of a band Jahn-Teller mechanism, suggestive of an alternate mechanism at work. Unlike the usual Jahn-Teller mechanism, it is not clear what the driving factors are over here. This is the reason

why we chose the example of Ni₂MnGa to understand how the mechanism works. Further, a common feature that one finds between the various structures present in the martensitic phase is the tetragonality. While the additional modulations present in the martensitic phase can be understood as a route to minimize the strain, the tetragonal distortions which could be associated with a Jahn-Teller mechanism are not well understood.

Mn in Ni₂MnGa has almost completely filled Mn *d* levels in the majority spin channel. The absence of any degeneracy with the Mn *d* states makes them improbable candidates to associate Jahn-Teller physics with. The minority spin Ni *e_g* states are found to contribute at the Fermi energy [8] and so one associates the structural changes that one finds with Ni. The only other atom in the unit cell, Ga, contributes very wide bands in the near Fermi energy region and so cannot be associated with any Jahn-Teller activity. The structure however throws some clues on the microscopic considerations driving the transition. In going from the cubic to the tetragonal phase, one finds an increase in all the nearest neighbour Ni-Mn and Ni-Ga bond-lengths. This could lead to a decrease in the Coulomb interactions felt by the electrons on Ni due to the electrons on its neighbours, leading to a modification of the electrostatic potential felt by the electrons on Ni. However as these distortions are uniform in all directions, all orbitals on Ni will experience the same electrostatic potential. Consequently this elongation cannot lead to any lifting of the degeneracy of the Ni *d* orbitals. The second neighbours of the Ni atoms are also Ni atoms which form a cube and in the presence of a tetragonal distortion one has a degeneracy lifting of the Ni *d* orbitals. This effect on the onsite energies of the Ni *d* orbitals is found to be very small. Ga atoms also have Mn atoms as their second neighbours forming a cube. Hence a distortion into the tetragonal phase leads to a degeneracy lifting of the Ga *p* orbital energies. The three-fold degenerate partially occupied *p* orbitals on Ga found in the cubic phase split into lower energy *p_z* orbital and doubly degenerate *p_x* and *p_y* orbitals at higher energies. This immediately shows that Coulomb interactions between the electrons on Ga and those on its second neighbour atoms are significant. This leads to a modified electrostatic potential felt by the electrons in the different Ga *p* orbitals which leads to large splittings of the otherwise degenerate Ga *p* levels. While the role of Coulomb interactions due to electrons at neighbouring sites modifying the electrostatic potential

felt by the electrons in different orbitals at the central site and thereby lifting the degeneracy of the orbitals is well-known and forms the basis of crystal-field theory, the present work goes on to show that the nomenclature of a band Jahn-Teller effect is a consequence of these principles at work. Indeed the martensitic transition is not driven in all systems. There is a balance of energetics to be considered. We have carried out a similar analysis for Mn_2NiGa and Ni_2MnSn . The former is found to show a martensitic transition while the latter does not. The crystal field splittings found for Ga and Sn in the tetragonal phase support the view that the electrostatic potential generated by the electrons on the second neighbour atoms of Ga are substantial in Mn_2NiGa while they are much weaker in Ni_2MnSn . These results support the picture of the martensitic transition discussed in the context of Ni_2MnGa .

Although the above analysis was for the tetragonal phase, the conclusions are similar for the modulated martensitic phases. Hence the band Jahn-Teller effect results in a degeneracy lifting of the Ga levels and is driven by strong electrostatic potentials generated by electrons on neighbouring atoms.

3.2 Methodology

Ab-initio electronic structure calculations are carried out using density functional theory (DFT) as implemented in the Vienna *ab-initio* simulation package (VASP) [9]. We use the projected augmented wave implementation and work with the generalized gradient approximation (GGA) Perdew-Wang [10] for the exchange correlation functional. This has been seen to give a better description of the magnetism in Heusler compounds [11] compared to the calculations using the local density approximation for the exchange correlation functional. Monkhorst-Pack k-points mesh of $10 \times 10 \times 10$ was used to perform the k space integrations and a cut-off energy of 270 eV was used to determine the plane-waves used in the basis. The lattice parameters of the unit cell as well as the ionic positions have been optimised in each of the cases considered and the optimized value is mentioned in the text. An analysis of the electronic structure has been carried out in terms of the band dispersions as well as the partial density of states (PDOS) calculated using spheres of radii

$\sim 1.3 \text{ \AA}$ around each atom. Additionally an analysis of the electronic structure has been carried out using an interface of VASP to WANNIER90 [12–14] using a basis consisting of Ni *d*, Mn *d* as well as Ga *s* and *p* states. A mapping of the Bloch states is made onto Wannier functions, localized on the respective atoms with their angular parts given by the relevant spherical harmonics, via a unitary transformation. A unique transformation is obtained with the requirement of minimizing the quadratic spread of the Wannier functions. The criterion of convergence was that the spread changed by less than 10^{-10} between successive iterations and. The spreads (Ω) of Wannier functions corresponding to Ni *d*, Mn *d* both are $< 1 \text{ \AA}^2$ and Ga *s* & *p* are $\sim 2 \text{ \AA}^2$ and 4 \AA^2 , respectively. Once the transformation matrices are determined, one has a tight binding representation of the Hamiltonian in the basis of the maximally localized Wannier functions. This enables us to quantify some of the electronic structure changes. Besides Ni₂MnGa, we have considered few other systems which are Mn₂NiGa and Ni₂MnSn. For each case a Monkhorst-Pack k-points mesh of $10 \times 10 \times 10$ was used and a cut-off energy of 270 eV was considered. In each case, we have started the calculations with the experimental cubic structure [4, 15, 16]. Subsequently the lattice parameters of the 16 atom unit cell as well as the ionic positions have been optimised. A similar analysis of mapping onto a tight binding model was carried out for Mn₂NiGa and Ni₂MnSn. In these calculations Ni *d*, Mn *d*, Ga *s* and *p* states and Ni *d*, Mn *d*, Sn *s* and *p* states were included as basis states.

3.3 Results and Discussions

The experimentally reported unit cell of Ni₂MnGa is cubic with a lattice parameter of 5.82 \AA [4]. Carrying out an optimization of the lattice parameter of the austenitic phase within our calculations, the theoretical lattice parameter is found to be 5.80 \AA . With this optimized structure we examine the atom and orbital projected partial density of states. This is shown in fig. 3.1. Ni *d* states are found to contribute in the energy window from -4 to 2 eV with the majority spin channel fully filled. However, the minority spin states are partially filled with the Fermi level in the Ni *e_g* states. Presence of some states near the Fermi energy (E_F) suggests that Ni *d* states might be Jahn-Teller

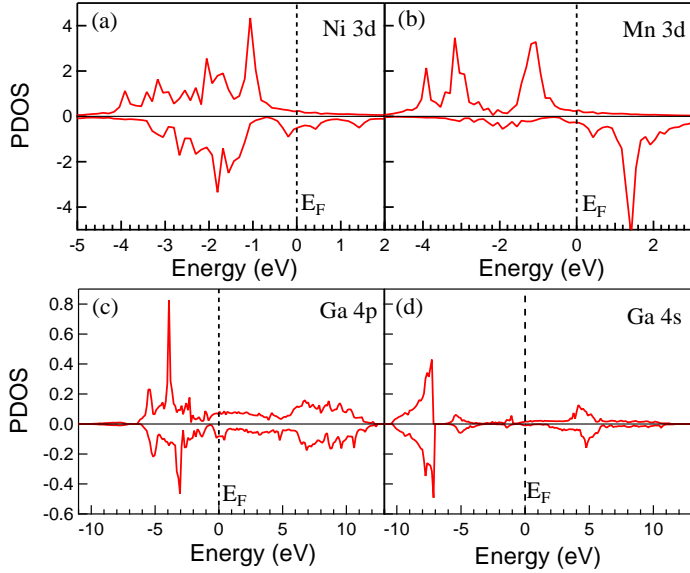


Figure 3.1 Atom and angular momentum projected partial density of states for (a) Ni 3d, (b) Mn 3d, (c) Ga 4p and (d) Ga 4s in the cubic phase of parent compound Ni_2MnGa . The Fermi energy E_F is at zero eV. The upper/lower panel is for the majority/minority spin channel.

active though the weight of the states at E_F is low. Examining the Mn d PDOS, one finds that the majority spin states are completely filled while the minority spin states are empty, indicating a d^5 configuration at the Mn site. Therefore Mn is Jahn-Teller inactive. Moreover, Ga 4p states are found to have a low weight in the same energy window and are more extended. One also finds the Ga 4s states contributing in an energy window between -8 to -10 eV below the Fermi level. These states have been referred to as lone pair states as they are not involved in any bonding with the neighbouring atoms similar to Ni-Mn-Sn system [17].

In the context of martensitic transformations it is interesting that, Ni_2MnGa is found to undergo a structural transformation and favors a tetragonal phase at low temperature, in contrast to Ni_2MnSn [4, 16, 18]. This suggests that an important role is played by the p element in inducing the martensitic transformation. One can achieve a stable tetragonal structure with lattice parameters $a = b = 5.36 \text{ \AA}$, $c = 6.76 \text{ \AA}$ having $c/a \approx 1.26$, which agrees very well with the previously reported theoretical results [19–21]. The variation of the ground state energy (per unit cell) as a function

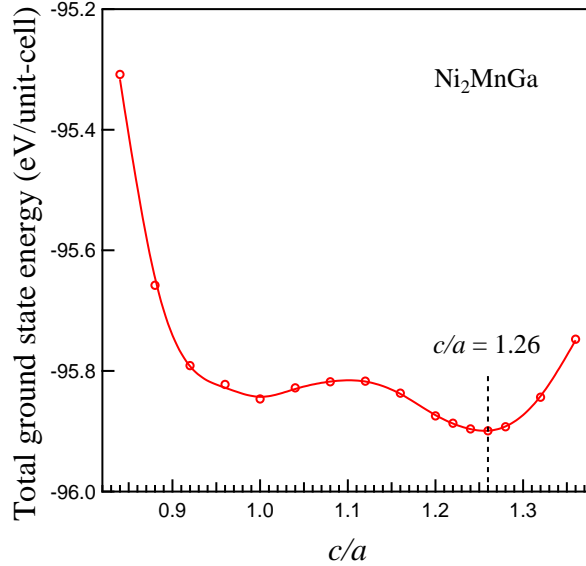


Figure 3.2 The ground state energy (per unit cell) as a function of the axial ratio, c/a of Ni₂MnGa.

of the axial ratio, c/a of Ni₂MnSn has been shown in fig. 3.2 which reveals that the ground state energy of the system has the lowest energy at $c/a = 1.26$.

In order to understand the driving force for the distortions, we examined the local environment around each atom. Ni has the Mn and Ga atoms as its nearest neighbours and this is shown in fig. 3.3. The nearest neighbour bondlengths are found to increase from 2.51 Å to 2.54 Å. As the increase in bond-lengths are uniform in all directions, one does not expect any degeneracy lifting of the energies of the Ni d orbitals emerging from these structural changes. Ni atoms are the second neighbours, forming a cubic lattice about the central Ni atom in the austenitic structure. This reduces to a tetragonal arrangement in the martensitic phase. The lowering in symmetry is expected to bring about a lifting of the degeneracy of the Ni e_g orbitals with the $d_{3z^2-r^2}$ orbital at lower energies compared to the $d_{x^2-y^2}$ orbital [22]. To explore the origin of the phase transition from cubic to tetragonal, we examine the occupancy of the Ni e_g orbitals in the two phases. If a Jahn-Teller distortion of the Ni d orbitals was responsible, one expects an increase in the d electron count in one of the e_g orbitals over the other in the tetragonal structure. However from Table 3.1 it

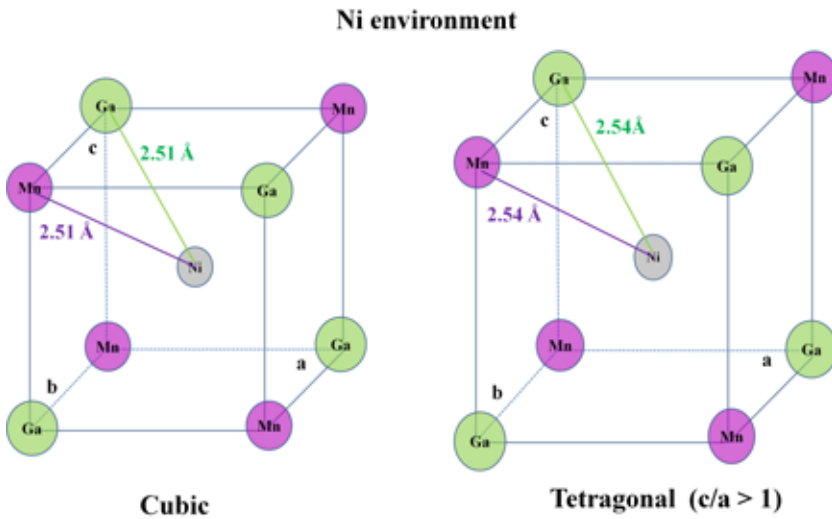


Figure 3.3 Ni environment in the cubic and tetragonal structures of Ni_2MnGa with bondlengths indicated.

Table 3.1 No. of electrons on Ni d orbitals in cubic and tetragonal phase.

Structure	Ni ₂ MnGa		No. of electrons
	$\text{Ni } d_{x^2-y^2}$	$\text{Ni } d_{3z^2-r^2}$	
Cubic	1.57	1.73	
Tetragonal	1.57	1.70	

is clearly evident that there is hardly any change in the occupancies of the Ni e_g states. In order to quantify this symmetry lowering, we have mapped the band dispersions calculated along various symmetry directions for both cubic as well as tetragonal Ni_2MnGa to a tight binding model which uses maximally localized wannier functions as the radial parts of the wave functions. The Ni d , Mn d as well as Ga s and p states were included in the basis.

The tight-binding bands are superposed on the *ab-initio* bands for the cubic and tetragonal structure and are shown in figs. 3.4(a) and 3.4(b), respectively. In both cases, one finds an excellent mapping of the *ab-initio* band structure within the tight-binding model. The relative on-site energies of Ni d , Mn d and Ga s, p states have been referenced with respect to the Ni d_{xz} spin-up state and are listed in Table 3.2. The changes one finds in the Ni d energies are small. Mn d orbitals

Table 3.2 Relative on-site energies (eV) of Ni d, Mn d, Ga s & p with respect to the spin-up d_{xz} state of Ni in cubic and tetragonal structure of Ni_2MnGa .

Atom	Orbital	Cubic Unit cell		Tetragonal unit cell	
		Spin up	Spin down	Spin up	Spin down
Ni	$d_{3z^2-r^2}$	0.01	0.41	0.01	0.40
	d_{xz}	0.0	0.36	-0.01	0.38
	d_{yz}	0.0	0.36	-0.01	0.38
	$d_{x^2-y^2}$	0.01	0.41	-0.12	0.41
	d_{xy}	0.0	0.36	-0.01	0.40
Mn	$d_{3z^2-r^2}$	0.13	3.48	0.14	3.27
	d_{xz}	-0.28	2.34	-0.18	2.32
	d_{yz}	-0.28	2.34	-0.18	2.32
	$d_{x^2-y^2}$	0.13	3.48	0.29	3.48
	d_{xy}	-0.28	2.34	-0.12	2.53
Ga	s	-5.54	-5.48	-5.49	-5.44
	p_z	0.51	0.77	-0.03	0.36
	p_x	0.51	0.77	0.83	1.05
	p_y	0.51	0.77	0.83	1.05

with e_g character show a small lifting of the degeneracy of the d orbitals of ~ 0.2 eV. This emerges from the crystal field environment in the tetragonal phase. However, one finds significant changes in the energies of the Ga p orbitals in the tetragonal phase. The three-fold degenerate p orbitals on Ga in cubic phase split into lower energy p_z orbital and doubly degenerate p_x and p_y orbitals at higher energies.

Examining the structure, one finds that the Mn and Ga atoms are placed alternatively on a cubic lattice. As is evident from fig. 3.5, the neighbours of the Ga atoms in this lattice are the Mn atoms. Reducing the symmetry from cubic to tetragonal, changes the nearest neighbour bondlengths from 2.90 Å to four at 2.68 Å in the ab plane and two others at 3.38 Å along the c-direction. As a result, the electrons in the p_z orbitals on Ga face smaller Coulomb repulsion from the electrons on Mn than those which are in the p_x and p_y orbitals. This leads to a lifting of the degeneracy of the Ga p orbitals, with the p_z orbitals found to be 0.86 eV (up spin channel) and 0.69 eV (down spin channel) lower in energy than the Ga p_x and p_y orbitals. The Ga p orbitals are partially occupied

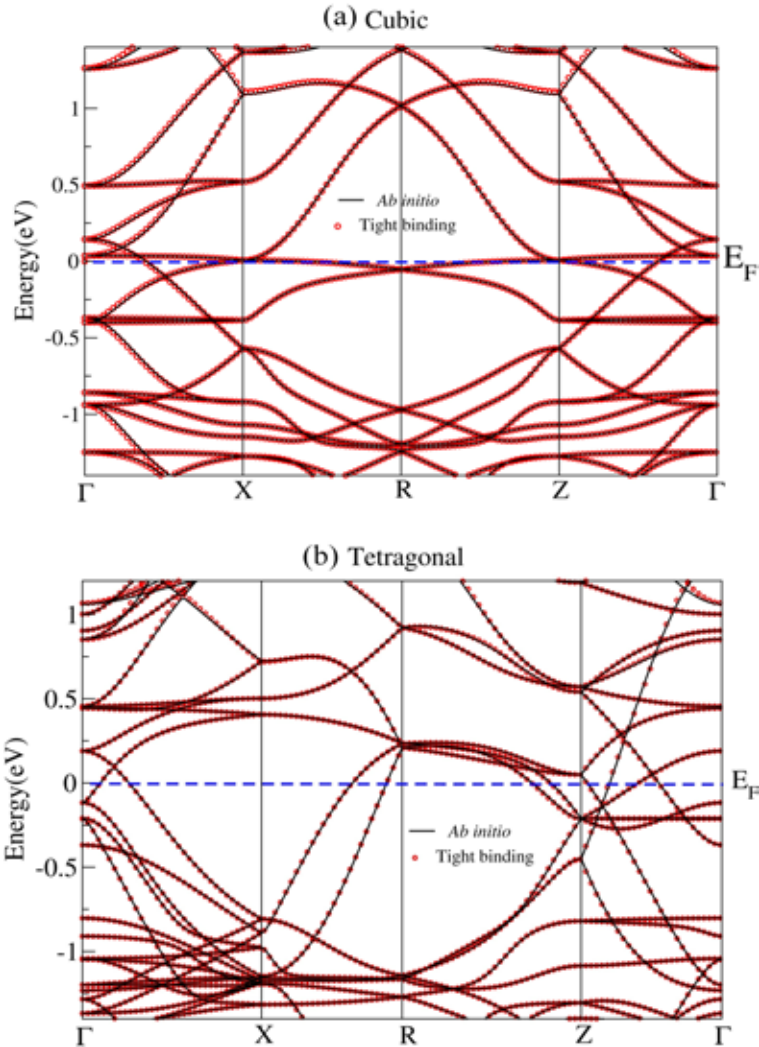


Figure 3.4 The tight-binding fit (circles) of the *ab-initio* band structure (solid line) of Ni_2MnGa in the (a) cubic and (b) tetragonal ($c/a = 1.26$) phase. The zero of energy is the Fermi energy (E_F).

and as a result one gains energy by lowering the symmetry to tetragonal.

There have been experimental as well as theoretical studies on the temperature dependent phase diagram of Ni_2MnGa . The tetragonal crystal structure has never been found to be the low temperature phase in experiments. In contrast, several modulated crystal structures have been proposed/found to be the ground state structure at low temperatures, though there is a transition between various modulated structures as a function of temperature [4]. It is therefore necessary

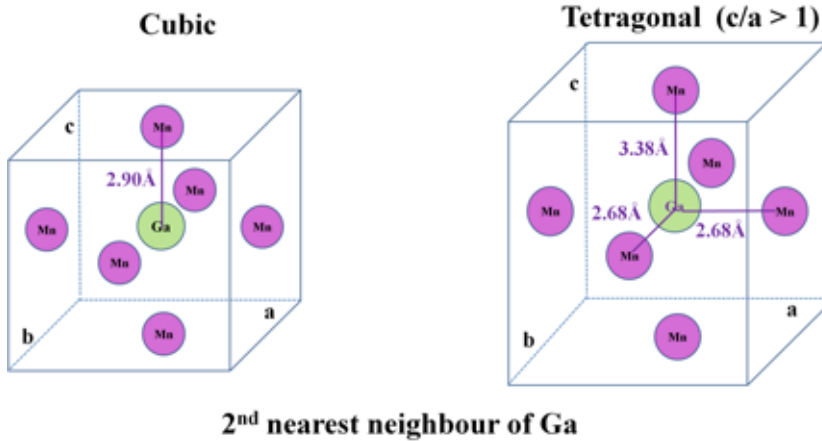


Figure 3.5 The second nearest neighbour Ga environment in cubic and tetragonal structures of Ni_2MnGa with bondlengths indicated.

to demonstrate the generality of the results that are found for the transition into the tetragonal phase [23–25].

A transformation from the cubic to the tetragonal phase has a large strain component to it. The alternating shifts of atomic positions in the Mn-Ga sublattice result in a significant reduction of the stabilization of structures which contain a nanotwin double layer. Zelený *et al.* [26] examined the relative energetics between various modulated/twinned martensitic structures and found the 4O structure to have the lowest energy. We have therefore carried out a similar analysis for the 4O optimised structure which is found to have the lattice parameters $a = 4.28 \text{ \AA}$, $b = 8.41 \text{ \AA}$ and $c = 5.41 \text{ \AA}$. The optimized 4O structure with modulation along [110] direction is shown in fig. 3.6(a). The *ab-initio* band structure was calculated and then mapped onto a tight-binding model for 4O modulated orthorhombic structure. This is shown in fig. 3.7. As earlier, here also a good description is obtained.

The changes in the Ni and Mn *d* on-site energies are small as found earlier. However, significant changes in the energies of the Ga *p* orbitals in the 4O phase are found. As the environment around each Ga atom is highly distorted, the local coordinate system and global coordinate system don't coincide. So the p_x , p_y and p_z orbitals on each Ga are strongly mixed in the global coordinate system. Hence we do not provide the onsite energies as was done earlier for the tetragonal structure,

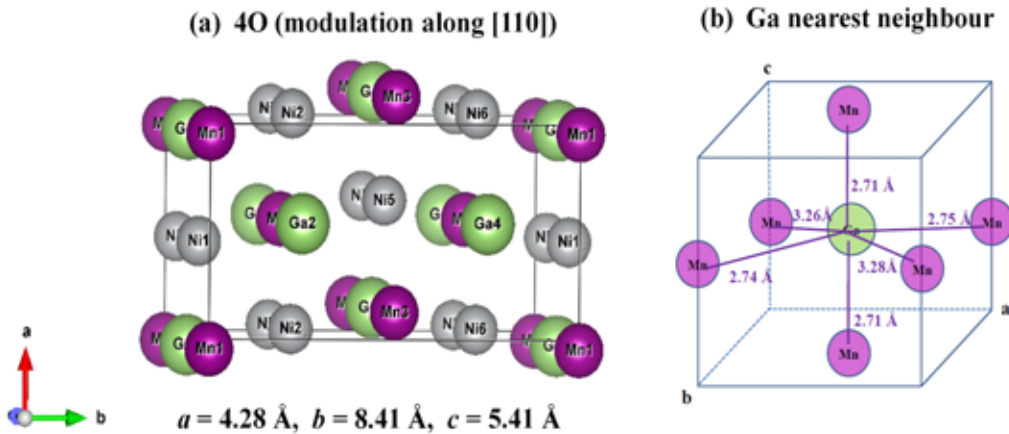


Figure 3.6 (a) 4O modulated orthorhombic structure with relaxed lattice parameters, (b) Ga environment with bondlengths indicated.

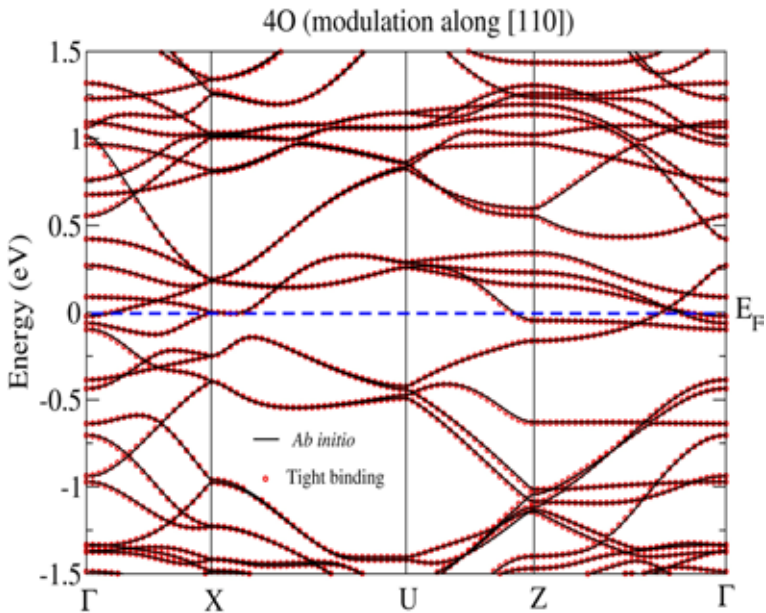


Figure 3.7 The tight-binding fit (circles) of the *ab-initio* band structure (solid line) of Ni_2MnGa in the 4O modulated phase.

but instead discuss the degeneracy lifting in terms of the dominant character of the orbital. The three-fold degenerate p orbitals on Ga in the cubic phase are found to split into higher energy p_z and p_y orbital with the p_x orbital at lower energy. This is evident in the local coordinate system for one Ga-Mn₆ octahedron shown in fig. 3.6 (b) with the x -axis lying along the long Mn-Ga bond

in the 4O structure. Similar distortions exist for various octahedral units, leading to the energy lowering. These distortions are along different directions so the strain energy component is small in these modulated structures compared to the tetragonal structure. These structural distortions induce electronic structure changes also. Examining the region near the Fermi energy, we do see a reduction in the minority spin total density of states (TDOS) in going from the cubic to the tetragonal or the 4O phase. This is shown in fig. 3.8, where the region near the Fermi energy is

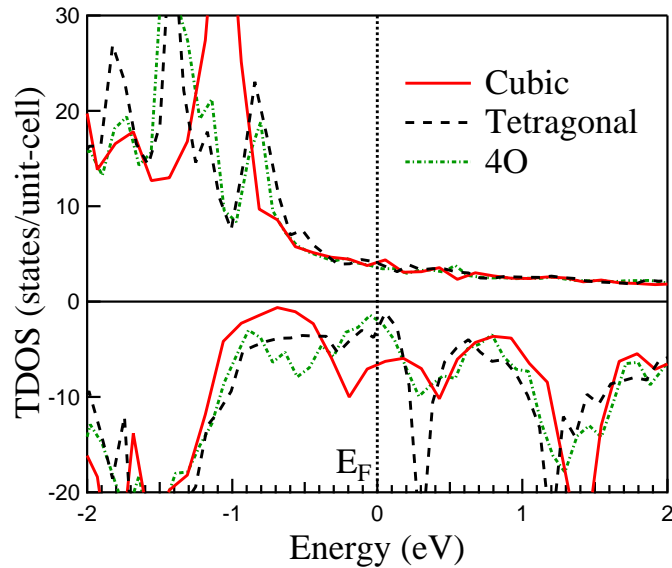


Figure 3.8 Total density of states for Ni_2MnGa in the cubic (solid line), tetragonal (dashed line) and 4O (dot dashed) structures. The zero of energy is the Fermi energy (E_F). The upper/lower panel is for the majority/minority spin channel.

zoomed out. The results indicate a lowering of the density of states at the Fermi level in going from the cubic structure to the lower symmetry tetragonal and 4O structures. While in the tetragonal structure there is an increase in the density of states above the Fermi energy, and a decrease in the region below the Fermi energy, the changes in the density of states associated with the 4O structure are not so systematic. These changes in the vicinity of the Fermi level have been observed in temperature dependent photoemission experiments across the transition into the martensitic phase. Our calculations have captured the effect, and making a quantitative analysis, we find that the decrease in Ni d contribution is just $\sim 8\%$. This supports the analysis of the band structure within

a tight binding model which finds large changes in the onsite energies of the Ga p orbitals. A movement of the Ga p levels and consequently of the states which hybridize with the d states is responsible for the density of states changes in the vicinity of Fermi energy.

The tight binding analysis of the *ab-initio* band structure of Ni_2MnGa in the tetragonal phase reveals a large degeneracy lifting of the energies of the Ga p orbitals, $\simeq 0.86$ eV in the majority spin channel. This implies that the electrostatic potential felt by electrons on Ga due to the electrons on its second neighbour Mn atoms are sizeable, giving rise to such large splittings. As the states with dominantly Ga p character are partially occupied, the system lowers its energy through the distortion. Considering the case of Mn_2NiGa , another example of a system which shows a martensitic transition with $c/a = 1.21$ [15], we find that a similar analysis (see Table 3.3 for onsite energies) carried out at the same c/a as Ni_2MnGa leads to a splitting $\simeq 0.82$ eV of the energies

Table 3.3 Relative on-site energies (eV) of Ni d, Mn d, Ga s & p with respect to the spin-up d_{xz} state of Ni in cubic and tetragonal structure of Mn_2NiGa .

Atom	Orbital	Cubic Unit cell		Tetragonal unit cell	
		Spin up	Spin down	Spin up	Spin down
Ni	$d_{3z^2-r^2}$	0.02	0.74	0.16	0.66
	d_{xz}	0.0	0.60	0.14	0.68
	d_{yz}	0.0	0.60	0.14	0.68
	$d_{x^2-y^2}$	0.01	0.73	0.19	0.67
	d_{xy}	0.01	0.63	0.24	0.76
Mn	$d_{3z^2-r^2}$	0.53	2.8	0.50	3.0
	d_{xz}	0.49	2.66	0.49	2.66
	d_{yz}	0.49	2.66	0.49	2.66
	$d_{x^2-y^2}$	0.51	2.78	0.32	2.69
	d_{xy}	0.54	2.70	0.44	3.08
Ga	s	-5.13	-5.01	-5.08	-4.99
	p_z	0.89	1.46	0.42	0.86
	p_x	0.88	1.44	1.24	1.65
	p_y	0.88	1.44	1.24	1.65

associated with the Ga p orbitals in the tetragonal phase in the majority spin channel. This again supports the role of the electrostatic potential due to electrons on the neighbouring atoms in lifting

the degeneracy of the orbitals at the central site, and thereby stabilising the martensitic phase.

We then went on to examine the crystal-field splitting of the Sn p orbitals in Ni₂MnSn considering the hypothetical case of a c/a equal to that found in Ni₂MnGa. This is found to be just $\simeq 0.66$ eV, indicating that the electrostatic potential felt by the electrons on the Sn atoms due to the second neighbour Mn atoms is not as large as it is in the other two examples Ni₂MnGa and Mn₂NiGa presented here. This suggests that the larger electrostatic potentials encountered are responsible for driving the martensitic transition. After the distortion, not only do we have a lifting of degeneracy which could push the energy balance towards the distorted structure, the shorter bondlengths also increase the hopping interaction strengths of electrons between the atoms involved. An important ingredient for the energy stabilization to come from these processes is the partial occupancy of these levels.

In conventional Jahn-Teller systems, the electrons in the vicinity of the Fermi energy are localized. This results in a high density of states at the Fermi energy, which leads to a diverging susceptibility and hence drives an electronic instability. This leads to a structural distortion resulting in a redistribution of states which usually renders the system insulating. A strong electron phonon coupling is behind the observed electronic and structural changes. In contrast, what one has here are delocalized systems which have a low weight at the Fermi level. Hence, there is no diverging susceptibility here, which demands sizeable electron-phonon coupling strengths. Electronic considerations involving significant electrostatic potential generated by electrons on neighbouring atoms at the central site drive the energy lowering in this candidate system identified with the band Jahn-Teller mechanism. The effect of the potential is significant in Ni₂MnGa and Mn₂NiGa which is the reason that it tries to distort to a lower symmetry structure.

There have been several explanations for the martensitic transitions that are found to take place. One explanation involves the presence of a soft phonon mode found in calculations for the high symmetry cubic phase which leads to a shearing of the lattice planes [27]. This alone cannot explain the observed structures where additionally a strain component is present. For instance as the strain involved in forming a phase boundary between the cubic austentic phase and the tetragonal martensitic one is large, various structural adaptions which minimize the strain have been pro-

posed. These include twinning as well as other modulations. Recent work [28] have invoked both the explanations to explain the hierarchy of structures that emerges. The present work complements these earlier studies in that it tries to understand the energetics which go into the observed structural distortions. In the context of Ni₂MnGa, the distortions also lead to spectral weight transfer away from the Fermi energy region in the martensitic phase. This has led to the nomenclature of a band Jahn-Teller effect. This however is not a generic feature of all martensitic transitions. Ye *et al.* [22] have experimentally observed spectral weight transfers for some compositions of Ni₂Mn_{1+x}Sn_{1-x} ($x = 0.36$ and 0.42). Further, the microscopic mechanism is different from here as it is operative only at off-stoichiometric compositions [17]. It is the Ni-Mn hybridization and Sn lone pair effect on Ni which are operative in these off-stoichiometric compounds, which drive the martensitic transition. However, the Sn lone pair effect alone is unable to drive the structural transition at the stoichiometric limit. Additionally there are examples beyond the martensites in which the band Jahn-Teller effect is operative [7]. The study of these systems will be the purview of future work.

3.4 Conclusion

The origin of the band Jahn-Teller effect has been examined considering the example of Ni₂MnGa. In contrast to the conventional Jahn-Teller effect operative in localized systems, here, one finds that one has delocalized states at the Fermi level. The electrostatic potential generated by the electrons on Mn at the Ga site are believed to drive the distortions which result in the lifting of degeneracy of the three-fold degenerate *p* orbitals on Ga. Thus, large crystal field effects are responsible for the degeneracy lifting/band Jahn Teller effect which drive the martensitic transition. The systems in which it doesn't happen could be those in which the crystal field effects are smaller. In those instances, the energy cost of the distortion is large and does not equal the lowering due to the degeneracy lifting of the levels. In the systems in which one has a transition, it is accompanied by a redistribution of the density of states associated with the Ga *p* states as well as the Ni *d* and Mn *d* states admixed with these states.

Bibliography

- [1] O. Heczko and L. Straka, *J. Appl. Phys.* **94**, 7139 (2003).
- [2] T. Kakeshita, Y. Yoshimura, K. Shimizu, S. Endo, Y. Akahama, and F. E. Fujita, *T. Jpn. I. Met.* **29**, 781 (1988).
- [3] R. Kainuma, Y. Imano, W. Ito, Y. Sutou, H. Morito, S. Okamoto, O. Kitakami, K. Oikawa, A. Fujita, T. Kanomata, and K. Ishida, *Nature* **439**, 957 (2006).
- [4] P J Brown, J. Crangle, T. Kanomata, M. Matsumoto, K. -U. Neumann, B. Ouladdiaf, and K. R. A. Ziebeck, *J. Phys.: Condens. Matter* **14**, 10159 (2002).
- [5] S. Singh, J. Bednarcik, S. R. Barman, C. Felser, and D. Pandey, *Phys. Rev. B* **92**, 054112 (2015).
- [6] P. J. Brown, A. Y. Bargawi, J. Crangle, K.-U. Neumann, and K. R. A. Ziebeck, *J. Phys.: Condens. Matter* **11**, 4715 (1999).
- [7] C. P. Opeil, B. Mihaila, R. K. Schulze, L. Mañosa, A. Planes, W. L. Hults, R. A. Fisher, P. S. Riseborough, P. B. Littlewood, J. L. Smith, and J. C. Lashley, *Phys. Rev. Lett.* **100**, 165703 (2008).
- [8] S. R. Barman, S. Banik, and A. Chakrabarti, *Phys. Rev. B* **72**, 184410 (2005).
- [9] G. Kresse and J. Furthmüller, *Phys. Rev. B* **54**, 11169 (1996).
- [10] J.P. Perdew, K. Burke, and Y. Wang, *Phys. Rev. B* **54**, 16533 (1996).

- [11] H. C. Kandpal, G. H. Fecher, and C. Felser, *J Phys. D* **40**, 1507 (2007).
- [12] A. A. Mostofi, J. R. Yates, Y. -S. Lee, I. Souza, D. Vanderbilt, and N. Marzari, *Comput. Phys. Commun.* **178**, 685 (2008).
- [13] N. Marzari and D. Vanderbilt, *Phys. Rev. B* **56**, 12847 (1997).
- [14] I. Souza, N. Marzari, and D. Vanderbilt, *Phys. Rev. B* **65**, 035109 (2001).
- [15] G. D. Liu, X. F. Dai, S. Y. Yu, Z. Y. Zhu, J. L. Chen, G. H. Wu, H. Zhu, and J. Q. Xiao, *Phys. Rev. B* **74**, 054435 (2006).
- [16] T. Krenke, M. Acet, E. F. Wassermann, X. Moya, L. Mañosa, and A. Planes, *Phys. Rev. B* **72**, 014412 (2005).
- [17] S. Pal, S. Sarkar, S. K. Pandey, C. Maji, and P. Mahadevan, *Phys. Rev. B* **94**, 115143 (2016).
- [18] A. Ayuela, J. Enkovaara, K. Ullakko, and R. M. Nieminen, *J. Phys.: Condens. Matter* **11**, 2017 (1999).
- [19] A. Ayuela, J. Enkovaara, and R. M. Nieminen, *J. Phys.: Condens. Matter* **14**, 5325 (2002).
- [20] A. T. Zayak, P. Entel, J. Enkovaara, and R. M. Nieminen, *J. Phys.: Condens. Matter* **15**, 159 (2003).
- [21] A. T. Zayak and P. Entel, *Mater. Sci. Eng. A* **348**, 419 (2004).
- [22] M. Ye, A. Kimura, Y. Miura, M. Shirai, Y. T. Cui, K. Shimada, H. Namatame, M. Taniguchi, S. Ueda, K. Kobayashi, R. Kainuma, T. Shishido, K. Fukushima, and T. Kanomata, *Phys. Rev. Lett.* **104**, 176401 (2010).
- [23] N. Xu, J. M. Raulot, Z. B. Li, J. Bai, Y. D. Zhang, X. Zhao, L. Zuo, and C. Esling, *Appl. Phys. Lett.* **100**, 084106 (2012).
- [24] R. Niemann, U. K. Rößbler, M. E. Gruner, L. Schultz, and S. Fähler, *Adv. Eng. Mater.* **14**, 562 (2012).

- [25] B. Dutta, A. Çakir, C. Giacobbe, A. Al-Zubi, T. Hickel, M. Acet, and J. Neugebauer, Phys. Rev. Lett. **116**, 025503 (2016).
- [26] M. Zelený, L. Straka, A. Sozinov, and O. Heczko, Phys. Rev. B **94**, 224108 (2016).
- [27] G. Fritsch, V. V. Kokorin, and A. Kempf, J. Phys. Condens. Matter **6**, L107 (1994).
- [28] M. E. Gruner, R. Niemann, P. Entel, R. Pentcheva, U. K. Rössler, K. Nielsch, and S. Fähler, *arXiv:1701.01562* (2017).

Chapter 4

Origin of martensitic transformation of

Ni₂Mn_{1+x}Sn_{1-x}

4.1 Introduction

The microscopic mechanism that drives the martensitic transition in Heusler alloys is of great interest for last few years which would help us to identify which materials would undergo this martensitic structural transition. Fermi surface nesting [1] and soft phonon modes [2] have often been invoked to explain the martensitic transformation, with the microscopic origin usually being associated with a band Jahn Teller effect [3]. These reasons however do not seem to be valid across all systems. Examples among Heusler alloys are seen, where inspite of a soft phonon mode being found in the calculations, no martensitic transformation has been observed [4]. We consider the example of compounds given by $Ni_2Mn_{1+x}Sn_{1-x}$. The unusual feature of this class of compounds is that the martensitic transition is seen only for off-stoichiometric compositions where x ranges from 0.36 to 0.80 in contrast to other martensites such as Ni_2MnGa where the transition is seen for stoichiometric members. The martensitic transition in Ni_2MnGa has been explained by Jahn-Teller effects [3]. On the other hand the usual explanation offered in the case of $Ni_2Mn_{1+x}Sn_{1-x}$ is the increased hybridization between the Ni and Mn d states being responsible for the observed martensitic transition [5]. This effect should be present in the stoichiometric composition also, and these ideas do not explain why one doesn't have a martensitic transition there.

In this chapter the origin of the martensitic phase transformation has been elucidated considering several compositions of $Ni_2Mn_{1+x}Sn_{1-x}$. Moreover, the site occupation of the alloying atoms in the lattice is one of the basic issues for understanding the alloying effect on the properties. Our motivation is to investigate the preference of Mn substitution at Sn sites in the cubic L2₁ austenitic phase. How does the magnetic moment and structure of Ni-Mn-Sn systems change with Mn substitution in the ternary alloys? Recently, Sokolovskiy *et al.* [6] has investigated the magnetic interactions in austenitic and martensitic phases in different “structural disorder” concentrations. They have mentioned two types of disorders, “structural” and “chemical” disorder. The “chemical disorder” in this case is defined as substitution of Sn atoms on Sn sublattice by excess Mn atoms. In this chapter the character of “chemical disorder” has been investigated.

4.2 Theoretical Method

The *ab-initio* calculation is carried out using density functional theory (DFT) [7], with the help of the projector augmented wave (PAW) [8, 9] method implemented in the Vienna *ab-initio* simulation package (VASP) [10, 11] within generalized gradient approximation (GGA) [12, 13] for the exchange-correlation functional. To find out the trend of excess Mn substitution at Sn sites, the input crystal structure is considered 100 atom superlattice L₂1 structure for calculation. The conventional vectors are taken as face centered cubic (FCC) basis. The lattice parameters of cubic L₂1 structure for various compositions (x) of off-stoichiometric Ni₂Mn_{1+x}Sn_{1-x} were taken from the linear variation of experimental lattice parameters reported by different research groups [14–17]. The mesh of k- points is taken $4 \times 4 \times 4$ depending on the convergence test of ground state energy (E0). The Mn at parent site is labelled Mn1 while the Mn doped at Sn site has been labelled Mn2. The magnetic interaction between Mn1 and Mn2 is antiferromagnetic, while that between Ni and Mn1 is ferromagnetic. Then with the superlattice structure the self consistent electronic as well as ionic iterations have been performed starting from initial positions of the atoms. When the total forces between atoms reach $\sim 10^{-2} - 10^{-3}$ eV/Å, the calculation is stopped and the system reaches the Kohn Sham (KS) ground-state.

Furthermore, to explain the driving force for martensitic transformation and nature of martensitic structure, different compositions like $x = 0.25, 0.375, 0.50, 0.625, 0.75, 0.875$ of off-stoichiometric Ni₂Mn_{1+x}Sn_{1-x} have been adopted. Monkhorst-Pack k-points mesh of $10 \times 10 \times 10$ for 16 atom unit cell and $10 \times 5 \times 10$ for 32 atom supercell were used to perform the k space integrations and a cut-off energy of 340 eV was used to determine the plane-waves used in the basis. The lattice parameters of the unit cell as well as the ionic positions have been optimized in each of the cases considered. An analysis of the electronic structure has been carried out in terms of the band dispersions as well as the partial density of states (PDOS) calculated using spheres of radii ~ 1.3 Å around each atom. The magnetic moments have been reported within the same spheres. Additionally an analysis of the electronic structure has been carried out using an interface of VASP to WANNIER90 [18–20]. A basis consists of Ni *s* and *d*, Mn *s* and *d* as well as Sn *p* states. A

mapping of the Bloch states is made onto Wannier functions, localized on the respective atoms with their angular parts given by the relevant spherical harmonics, via a unitary transformation. A unique transformation is obtained with the requirement of minimizing the quadratic spread of the Wannier functions. The criterion of convergence was that the spread changed by less than 10^{-6} between successive iterations. Once the transformation matrices are determined, one has a tight binding representation of the Hamiltonian in the basis of the maximally localized Wannier functions.

4.3 Site Occupancy and Magnetic Ground State

When excess Mn atoms are substituted at Sn sites (referred to as Mn2), the Mn2 atoms can occupy the Sn sublattices in random manner or form clusters of Mn atoms. Adopting ferromagnetic or antiferromagnetic magnetic configurations of Mn2, various doping configurations have been considered. If Mn1 are ferromagnetically coupled to Mn2 and the Mn atoms are doped at Sn sites in such a way that some Mn atoms form clusters in the supercell, then the configuration is called ferro-cluster. Similarly, this nomenclature is applicable for other configurations also. When Mn1 are antiferromagnetically coupled to Mn2 and a cluster of Mn atoms is formed, then the configuration is called antiferro-cluster. If the magnetic coupling between Mn1 and Mn2 is ferromagnetic and the doping of Mn is random at Sn sites, then the configuration is called ferro-random. When the magnetic coupling between Mn1 and Mn2 is antiferromagnetic and the Mn atoms are doped at random Sn sites, then the configuration is called as antiferro-random. In figs. 4.1 (a) and (b), a particular cluster and random configuration of $Ni_2Mn_{1.4}Sn_{0.6}$ supercell structure with the conventional vector as FCC basis have been shown. The Mn cluster region is indicated by the yellow oval shape and random doping of Mn atoms is indicated by arrows. Now to know which configuration is energetically favorable, the formation energy of $Ni_2Mn_{1+x}Sn_{1-x}$ for different x compositions has been calculated for the four different configurations of supercell structures of $x \leq 0.40$. For each x composition, a representative Mn doping configuration of each cluster and random arrangement has been considered. The formation energy per unit cell of $Ni_2Mn_{1+x}Sn_{1-x}$ as a function of doped

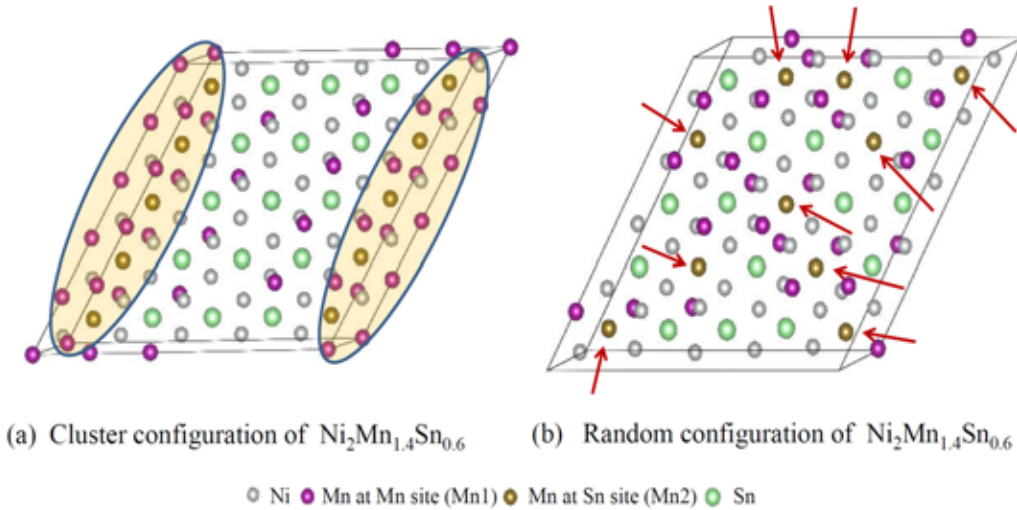


Figure 4.1 (a) Cluster and (b) Random configuration of $\text{Ni}_2\text{Mn}_{1.4}\text{Sn}_{0.6}$ supercell.

Mn concentration is plotted in fig. 4.2 for different magnetic and structural configurations. From the fig. 4.2 it is observed that, the antiferro-random configuration has the lowest formation energy. This is the most stable configuration of $\text{Ni}_2\text{Mn}_{1+x}\text{Sn}_{1-x}$. It should be noted that antiferromagnetic interactions are observed in the whole composition range upto $x = 0.40$ of L₂1 cubic structure, which is exactly same as Sokolovskiy *et al.* result [6]. The average inter-atomic bond-lengths are found to be higher in the cluster regions than the other regions in the antiferro-cluster configuration. But, the average inter-atomic bond-distances in the different regions of antiferro-random configuration are almost same. So, the average strain in the antiferro-cluster configuration is higher than that of antiferro-random configuration. This large strain in antiferro-cluster configuration costs higher formation energy than antiferro-random configuration. Hence antiferro-random configuration is the lowest energy configuration. It is observed from fig. 4.2, the formation energy increases with doped Mn concentration. So, the off stoichiometric alloys of Ni-Mn-Sn system cost more energy in the austenitic phase with L₂1 structure than stoichiometric alloy. It is also observed that, the formation energy of different configurations are very much near to each other upto $x = 0.20$ and the separation of formation energy of different configurations increases suddenly from $x = 0.32$. This rapid difference of formation energy between antiferro-random and ferro-random configura-

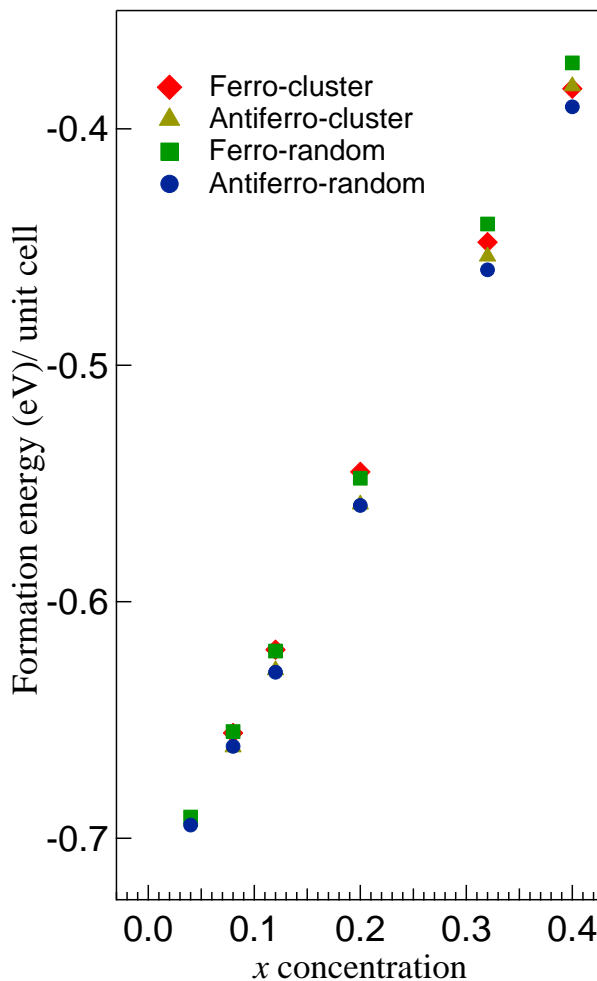


Figure 4.2 Formation energy per unit cell plot of $\text{Ni}_2\text{Mn}_{1+x}\text{Sn}_{1-x}$ with x concentration of different configurations.

tion around $x \approx 0.32$ indicates the destabilization of the ferromagnetic order in cubic austenitic phase of Ni-Mn-Sn and favors the appearance of antiferromagnetic exchange interactions. The exchange interaction is short range which is confirmed by the random configuration of Mn atoms substitution. Interestingly, it has been found experimentally that alloys with composition $x \geq 0.36$ undergo martensitic transformation [5]. Thus, the increase in antiferromagnetic exchange between Mn1 and Mn2 beyond a particular composition can be associated to one of the triggering factors of structural instability. We obtain the most favourable magnetic configuration of $\text{Ni}_2\text{Mn}_{1+x}\text{Sn}_{1-x}$

as antiferromagnetic coupling between Mn at Mn sites and Mn at Sn sites, which sustains from very low Mn doping concentration to higher Mn doping concentration. This result matches with findings from other groups [5, 6, 21–30]. Mn-Mn distances in off-stoichiometric Ni-Mn-Sn systems are smaller than the stoichiometric compound which introduces antiferromagnetic exchange interaction between Mn-Mn nearest neighbours [22].

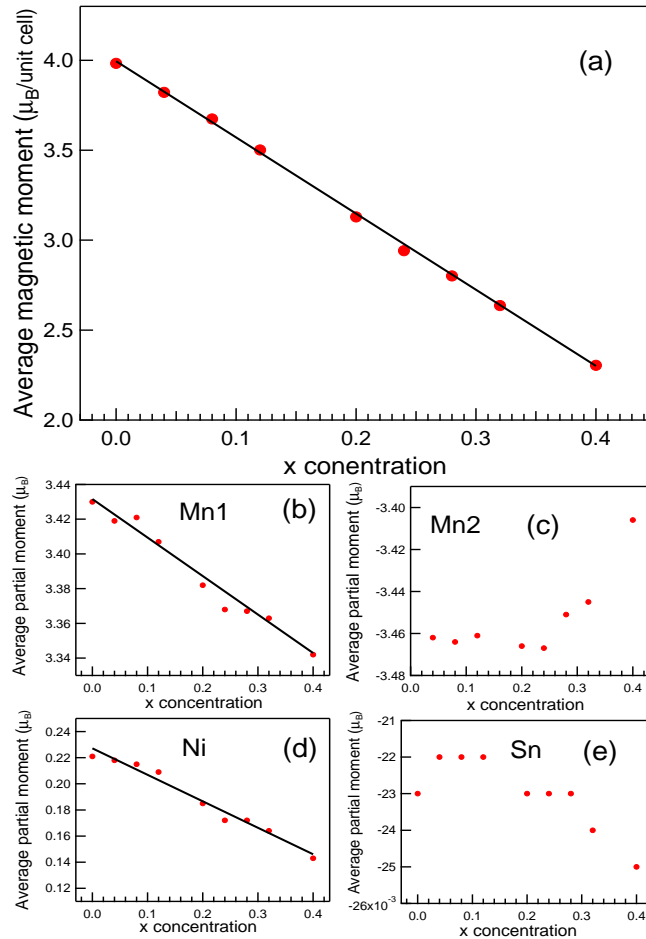


Figure 4.3 (a) Average total magnetic moment ($\mu_B/\text{unit cell}$) and average partial moments of Ni (b), Mn1 (c), Mn2 (d) and Sn (e) variation of $\text{Ni}_2\text{Mn}_{1+x}\text{Sn}_{1-x}$ with x concentration.

Due to antiferromagnetic exchange interaction the magnetic moment of the system decreases with doped Mn concentration. Figs. 4.3 (a), (b), (c), (d) and (e) show the variation of average total magnetic moment per unit cell and average partial moments of Ni, Mn1, Mn2 and Sn with

x concentration, respectively. Kanomata *et al.* [23, 25] has also reported that the magnetic moments per formula unit in the austenitic phase of $\text{Ni}_2\text{Mn}_{1+x}\text{Sn}_{1-x}$ decreases with increasing x . It should be noted that the magnetic moment in the stoichiometric Ni_2MnSn ($x = 0$) alloy total magnetic moment (μ_m) $\approx 4\mu_B/\text{formula unit}$. The magnetic moment of Mn1 contributes more in total magnetic moment of the system. Due to above shown (in fig. 4.3) change in average magnetic moment of Mn1, Mn2 and Ni with increasing concentration of doped Mn2, average total moment of the system decreases accordingly. Contribution of Sn moment in average total moment of the system is negligible. So, the total magnetic moment of the system can be written as $\mu(x) = 2 \times \mu_{\text{Ni}} + (1 - x) \times \mu_{\text{Mn}}$ [31] where the Ni moment μ_{Ni} is varied around the stoichiometric value $0.2 \mu_B$ and Mn moment μ_{Mn} is varied around the stoichiometric value $3.4 \mu_B$. Planes *et al.* [32] have reported a similar relation for the total magnetic moment for Ni-Mn-Z ($Z = \text{Ga}, \text{In}, \text{Sn}$ and Sb) and pointed out that the total magnetic moment of these systems, which are plotted as function the electron concentration, follow the Slater-Pauling curve with the same slope. From fig. 4.3 (c) it is observed that the average magnetic moment of Mn2 is constant upto $x \lesssim 0.28$ and after that magnetic moment suddenly increases. As, the concentration of doped Mn2 increases, the antiferromagnetic domain increases. So, average magnitude of magnetic moment of Mn2 increases. Consequently, the growth of antiferromagnetic domains at $x \geq 0.28$ destabilizes the ferromagnetic order in austenitic phase. Moreover, from the phase diagram of $\text{Ni}_2\text{Mn}_{1+x}\text{Sn}_{1-x}$ [23, 25] one can infer that the martensitic transition starts around $x \gtrsim 0.3$ and before this concentration there is no martensitic transition. Sokolovskiy *et al.* [6] has also predicted the same trend by theoretical calculation. So, the effect of Mn2 plays important role in martensitic transformation from $x \gtrsim 0.30$ composition.

4.4 Driving force for martensitic transformation

To understand the driving force for martensitic transformation more microscopically, we continue our discussion starting from stoichiometric composition and then considering other off-stoichiometric compositions. The experimentally reported unit cell of Ni_2MnSn is cubic with a

lattice parameter of 6.05 Å [33]. Carrying out an optimization of the lattice parameter within our calculations, the theoretical lattice parameter is found to be 6.06 Å and the structure remains cubic. The variation of the ground state energy (per unit cell) as a function of the axial ratio, c/a of Ni₂MnSn has been shown in fig. 4.4 which reveals that the ground state energy of the system has the lowest energy at $c/a = 1$. The distances between Ni and Mn as well as between Ni and

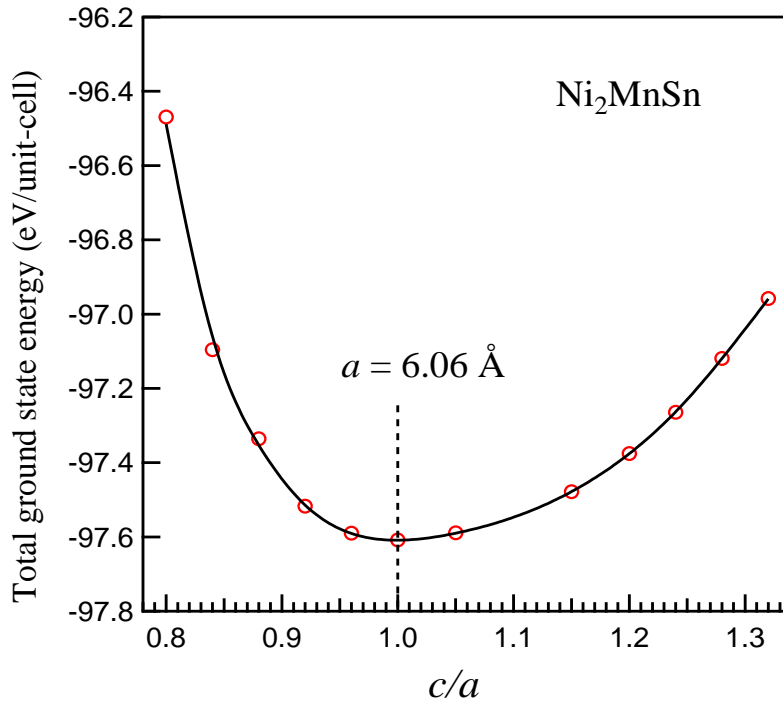


Figure 4.4 The ground state energy (per unit cell) as a function of the axial ratio, c/a of Ni₂MnSn.

Sn are found to be 2.62 Å. In contrast to what we find in Ni₂MnSn, Ni₂MnGa is found to undergo a structural transformation and favors a tetragonal phase at low temperature. This suggests that an important role is played by the *p* block-element in inducing the martensitic transformation. In order to understand this further we examine the atom and orbital projected partial density of states. This is shown in fig. 4.5. This implies that the cubic structure is the most favorable structure of Ni₂MnSn which shows no martensitic transformation. Ni *d* states are found to contribute in the energy window -4 to 2 eV, which is also the energy window in which Mn 3*d* states contribute. Sn

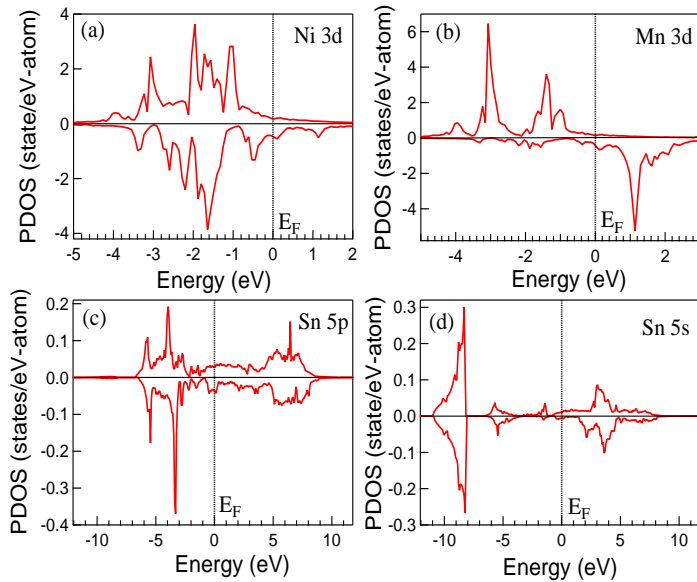


Figure 4.5 Atom and angular momentum projected partial density of states (PDOS) for (a) Ni 3d, (b) Mn 3d, (c) Sn 5p and (d) Sn 5s in the parent compound Ni₂MnSn. The Fermi energy E_F is at 0 eV. The upper/lower panel is for the majority/minority spin channel.

5p states are found to have a low weight in the same energy window. Sn 5s states are localized and are found to contribute -8 to -10 eV below the Fermi level, with low weight in the unoccupied part. These states have been referred to as lone pair states as they are not involved in any bonding with the neighbouring atoms. This indicates that the electronic structure of Ni₂MnSn emerges from the bonding of the Ni 3d and Mn 3d states. Examining the Mn *d* PDOS, one finds that the majority spin states are completely filled while the minority spin states are empty, indicating a *d*⁵ configuration at the Mn site. The exchange splitting of the Mn *d* states and the Ni *d* states are found to be in the same direction.

Now when one of the Sn atoms is replaced by Mn, corresponding to the composition Ni₂Mn_{1.25}Sn_{0.75}, we find that despite allowing for changes in the cell shape upon optimization, the structure remains cubic. The optimized lattice constant is found to 5.99 Å as against 6.06 Å that was found for the parent compound. The variation of the ground state energy (per unit cell) as a function of the axial ratio, *c/a* of Ni₂Mn_{1.25}Sn_{0.75} has been shown in fig. 4.6. It is evident that the ground state energy of the system has the lowest energy at *c/a* = 1. The absence of a tetragonal transition at

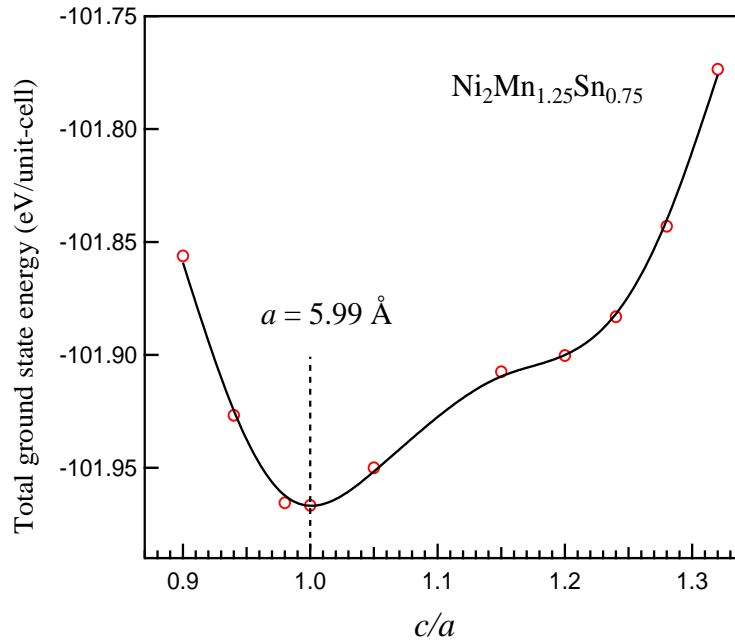


Figure 4.6 The ground state energy (per unit cell) as a function of the axial ratio, c/a of $\text{Ni}_2\text{Mn}_{1.25}\text{Sn}_{0.75}$.

this composition, which is usually associated with the existence of a martensitic transition, is consistent with experiment. There is also a volume contraction found when we replace Sn with Mn. This is expected as the ionic radius of Mn is smaller than that of Sn. The bond lengths between Ni-Mn1, Ni-Mn2 and Ni-Sn are found to be 2.57 Å, 2.52 Å and 2.62 Å (shown in fig. 4.7) as against the bondlengths of 2.59 Å found before the atomic relaxations. There is a reduction in the Ni-Mn bondlengths, with a larger reduction in the Ni-Mn2 bondlengths. The decrease of Ni-Mn2 bond-lengths are uniform in all diagonal directions. The direction of movement of Ni atoms towards Mn2 atom has been shown in fig. 4.8. Thus the structure remains in cubic having smaller lattice parameter.

We then consider the composition $x = 0.375$ in the formula $\text{Ni}_2\text{Mn}_{1+x}\text{Sn}_{1-x}$. This is close to the composition $x = 0.36$ at which point one finds the onset of the martensitic transitions in experiment. This can be realized in a 32 atom supercell. Starting with a cubic unit cell one finds that a tetragonal unit cell is favored at the end of the unit cell optimization with lattice parameters

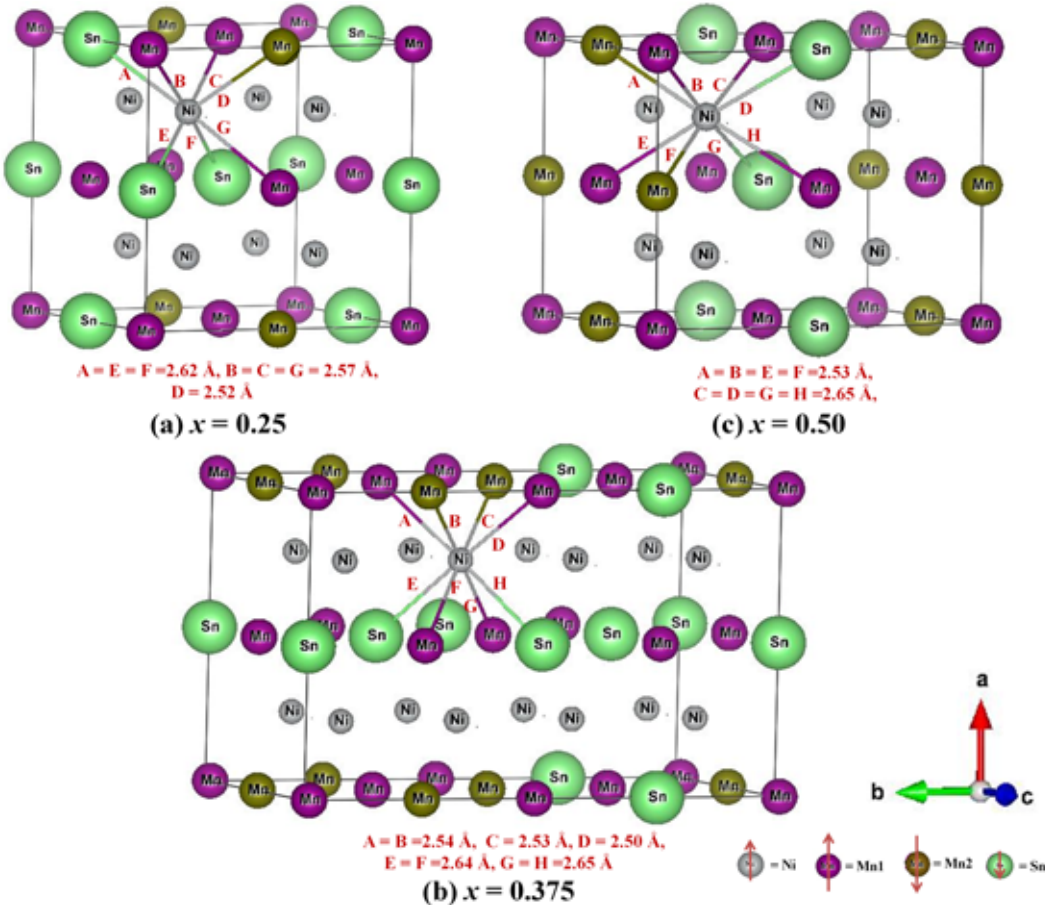


Figure 4.7 Ni-Mn1 and Ni-Mn2 bond distances in \AA unit, after full relaxation of cubic structure of composition $x = 0.25, 0.375$ and 0.50 of $Ni_2Mn_{1+x}Sn_{1-x}$. The direction of magnetic moment on each atom has been indicated by arrow.

$a = 6.83 \text{ \AA}$, $b \approx c = 5.55 \text{ \AA}$, resulting in a tetragonality $a/c \approx 1.23$. However, the tetragonality reported in experiment [33–35] is ~ 1.10 . This might be due to structural disorder which are not accounted for in the theoretical calculation. The difference in the lattice parameters by GGA based DFT and the experiment has been also reported for Ni-Mn-Ga system [36]. Moreover, one finds a reduction in some of the Ni-Mn bond lengths. These are found to be in the range 2.50-2.64 \AA for Ni-Mn1, 2.53-2.54 \AA for Ni-Mn2. Additionally there is a substantial increase of the Ni-Sn bond lengths from the stoichiometric compound. The question that follows is whether this aids the tetragonality and how. Understanding this would help us to explain the observed martensitic phase transition.

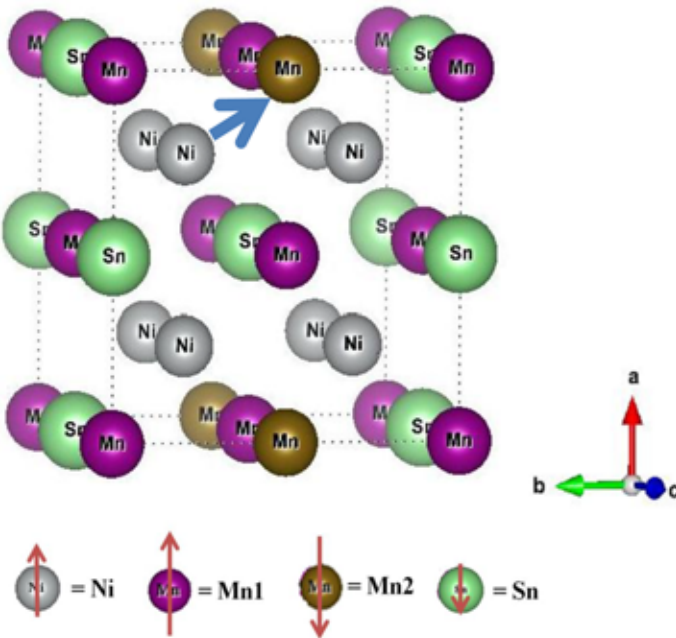


Figure 4.8 The direction of movement of Ni atoms towards Mn2 atom of composition $x = 0.25$.

We then continue the discussion by considering the composition $x = 0.50$. Here again one finds that there is a reduction in Ni-Mn1 and Ni-Mn2 bond lengths. Additionally there is a tetragonal unit cell which is found to be favored for different combinations of $x = 0.50$ which is the indicator of the martensitic transition.

In fig. 4.7, fully relaxed crystal structures of initial cubic structure of composition $x = 0.25$, 0.375 and 0.50 of $\text{Ni}_2\text{Mn}_{1+x}\text{Sn}_{1-x}$ have been shown. In each case the optimized Ni-Mn1 and Ni-Mn2 bond lengths have been indicated. Examining the structures closely, we can identify a pattern that emerges in the relaxations. Ni atoms are found to move towards Mn2 atoms, with their bondlengths with Sn increasing. Their movement towards Mn1 atoms is less though at larger concentrations they move towards those Mn1 atoms which are nearest neighbors of Mn2. This is consistent with extended X-ray absorption fine structure (EXAFS) measurements of $\text{Ni}_2\text{Mn}_{1.4}\text{Sn}_{0.6}$ [37] where one finds that Ni-Mn bond lengths decrease upon martensitic transformation. In the low temperature martensitic phase in the case of Ni K-edge, Ni-Mn and Ni-Sn bond lengths are 2.569

\AA and 2.607 \AA changing from 2.595 \AA . This seems surprising at first and the question we ask next is what are the underlying energetics that dictate the Ni movement. At $x = 0.25$ we find that both Mn1 and Mn2 have an almost d^5 configuration though their exchange splittings are opposite in direction. This results in stronger hybridization between Ni and Mn2 atoms, compared to that with Mn1. This is the reason the Ni atom moves towards Mn2. As x is increased, one has Mn1 and Mn2 atoms occupying nearest neighbor sites. They interact with each other and as a result one finds a deviation of Mn1 from a d^5 configuration, found at $x = 0.25$. This results in a smaller moment on those Mn1 atoms which are closer to Mn2 and is found to be $3.383 \mu_B$ as against $3.486 \mu_B$ for the stoichiometric Ni_2MnSn . Now one finds that Ni atoms can gain energy from hopping of electrons from both Mn1 (only the low moment atoms) and Mn2. The schematic representation of this has been shown in fig. 4.9. This is what we find for $x = 0.375$ and beyond. The Ni atoms move

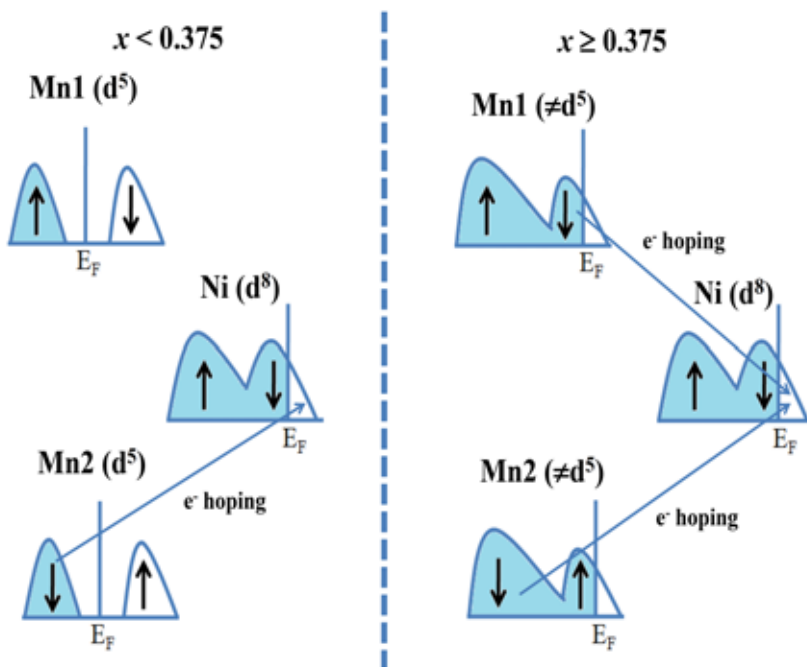


Figure 4.9 Schematic representation of Ni-Mn1 and Ni-Mn2 interactions for $x < 0.375$ and $x \geq 0.375$.

towards both Mn1 and Mn2. Consequently, the resultant movement is along a lattice parameter. Hence in each case one finds that the lattice parameter increases along the direction of movement

and there is further lowering of energy. The natural question that follows is why does the Ni atom move away from a centro-symmetric position towards the Mn atoms.

In each of the structures shown in fig. 4.7, one finds that the movement of the Ni atoms is away from the Sn atoms. The reason for this is apparent when we plot the line profile of the Sn 5s charge density along the Sn-Mn and Sn-Ni bonds of Ni_2MnSn in fig 4.10. The chosen Mn atom

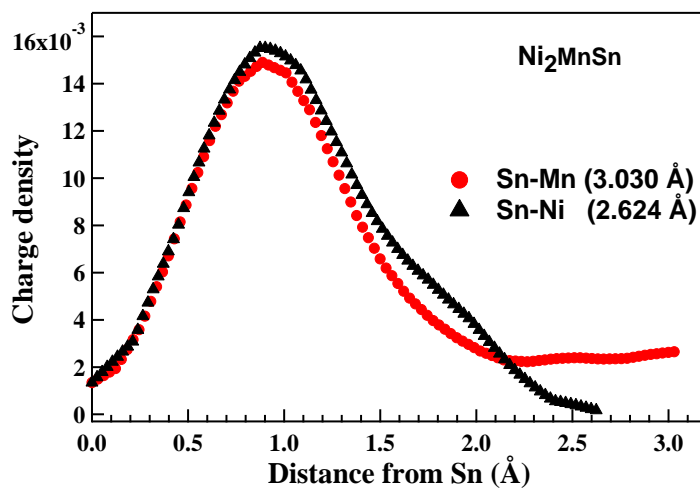


Figure 4.10 Line charge density of the Sn 5s states along the Sn-Mn and Sn-Ni bond. The respective bondlengths are indicated in parentheses.

is further away and is at 3.03 Å from the Sn atom. However, the Ni atom is at 2.62 Å from the Sn atom. If there were strong covalent interactions between the Ni and Sn atoms, one would expect the charge density to be more delocalized along the bond. Instead we find that the charge density is more localized along the Sn-Ni bond than along the Sn-Mn bond, the spread reflecting the increased separation of the pair of atoms. This verifies that the driving force of the distortions is additionally the repulsion the electrons on Ni face from those on Sn. The schematic diagram of movement of Ni atom due to Ni-Mn hybridization in cubic structure and further elongation of the structure along one direction due to Sn lone pair repulsion on Ni electrons has been shown in fig. 4.11.

An alternate explanation for the martensitic transition that has been offered has been the band Jahn Teller effect. The idea is that Jahn Teller distortions lift the degeneracy of the d orbitals. This

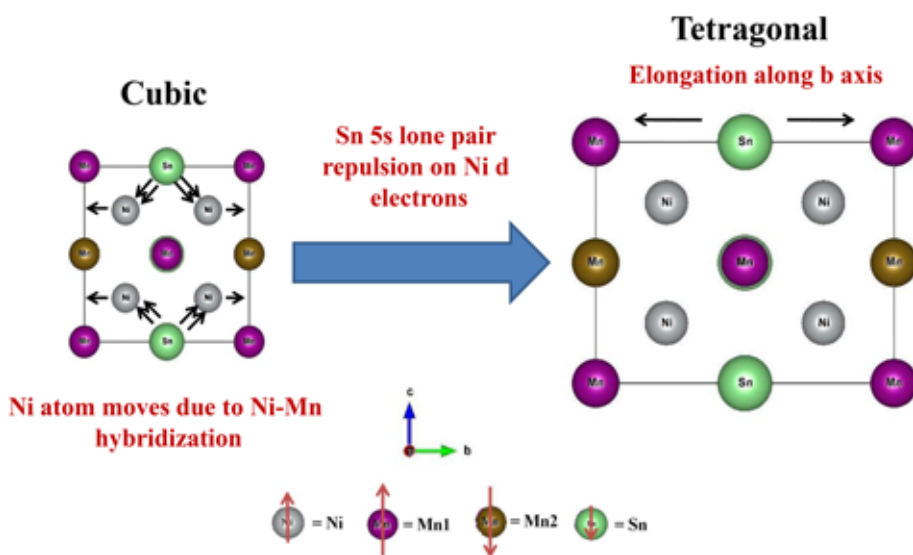


Figure 4.11 Schematic diagram of movement of Ni atom due to Ni-Mn hybridization in cubic structure and further elongation of the structure along one direction due to Sn lone pair repulsion on Ni electrons.

is aided by tetragonality and hence the conclusion that Jahn-Teller distortions drive the martensitic transition. In order to quantify this we map the *ab-initio* band dispersions for $x = 0.50$ to a tight binding model which included *s* and *d* orbital states of Ni and Mn and *p* orbital states of Sn in the basis. Maximally localized wannier functions were considered for the radial parts of the wavefunction. The tight-binding bands are superposed on the *ab-initio* bands of unstable cubic and fully relaxed tetragonal structure in figs. 4.12 (a) and (b), respectively.

In both cases, one finds an excellent mapping of the *ab-initio* band structure within the tight-binding model. The relative on-site energy of Ni *d* states with respect to d_{xz} spin up state are listed in Table 4.1. The changes one finds in the energies are small. This suggests that Jahn-Teller distortions associated with Ni *d* states cannot be the driving force for the martensitic transitions seen in this system. Our fitting of *ab-initio* band structure did not give us good enough description of the Sn *p* states and so we could not talk of the effect of the distortion on the on-site energies of the Sn *p* states. Thus our analysis reveals that the lone pair effect of Sn 5s electrons is the main triggering factor for additional tetragonality.

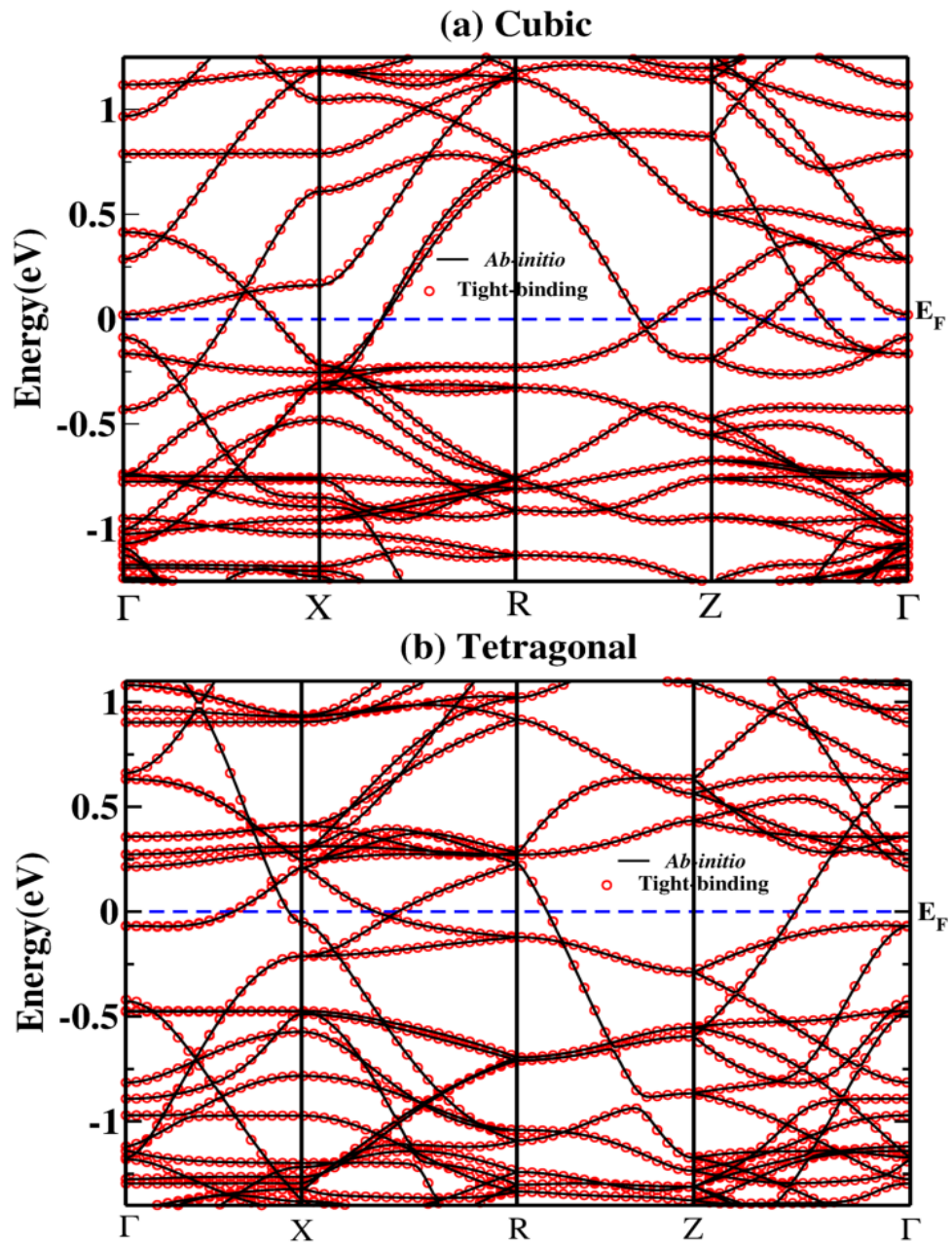


Figure 4.12 The tight-binding (circles) as well as the *ab-initio* band structure (solid line) of $\text{Ni}_2\text{Mn}_{1.5}\text{Sn}_{0.5}$ in the (a) cubic and the (b) fully relaxed tetragonal phase.

Table 4.1 Relative on-site energies with respect to spin up d_{xz} state of Ni in cubic and fully relaxed tetragonal structure of $Ni_2Mn_{1.5}Sn_{0.5}$.

Atom	Orbital	Cubic Unit cell		Tetragonal unit cell	
		Spin up	Spin down	Spin up	Spin down
Ni	d_{z^2}	0.11	0.27	-0.01	0.24
	d_{xz}	0.0	0.12	0.0	0.05
	d_{yz}	0.07	0.23	0.06	0.03
	$d_{x^2-y^2}$	0.10	0.30	0.02	0.10
	d_{xy}	0.03	0.15	0.03	0.19

4.5 Theoretical realization of Orthorhombic structure

Though theoretical *ab-initio* calculation predicts the tetragonality of the martensitic phase of the Ni-Mn-Sn system, experimental results [17, 33, 38] show that the martensite phase of Ni-Mn-Z (Z = In, Sn, Sb), transformed from cubic austenite phase, has orthorhombic structure. Now to check if there is any orthorhombicity in the theoretical structure, the symmetry in *ab*, *bc* or *ac* plane has to be broken. That is why, the crystal structure is doubled in *b* direction and the structure is fully relaxed for all possible combinations. All these combinations are formed due to various distribution of doped Mn atoms. In fig. 4.13, the energetically stable combination of 32 atom supercell of $Ni_2Mn_{1.5}Sn_{0.5}$ has been shown after doubling the stable tetragonal 16 atom unit cell structure. After full relaxation, the supercell structure achieves the lattice parameters $a = 7.18 \text{ \AA}$, $b = 5.32 \text{ \AA}$ and $c = 5.38 \text{ \AA}$ for this combination. Thus the energetically stable orthorhombic unit cell structure having lattice parameters $a = 7.18 \text{ \AA}$, $b = 5.32 \text{ \AA}$ and $c = 5.38 \text{ \AA}$ of $Ni_2Mn_{1.5}Sn_{0.5}$ is obtained. It is important to note that, this idea of doubling the *b*-axis is similar to the experimentally obtained 4O structure [35]. Interestingly, in the above said energetically stable combination the Mn atoms are doped at random Sn sites. Due to random distribution of Mn atoms at Sn sites, the symmetry in all directions breaks, which favors the orthorhombic character of the structure. The total density of states (TDOS) and partial density of states (PDOS) of Ni $3d_{x^2-y^2}$ and $d_{3z^2-r^2}$ of the orthorhombic structure doubled along *b*-axis are shown in fig. 4.14. The TDOS near the Fermi energy (E_F) indicated by an arrow decreases due to the orthorhombic structural transformation from cubic phase. It confirms the experimental observation by Ye *et al.* [5] that the spectral weight

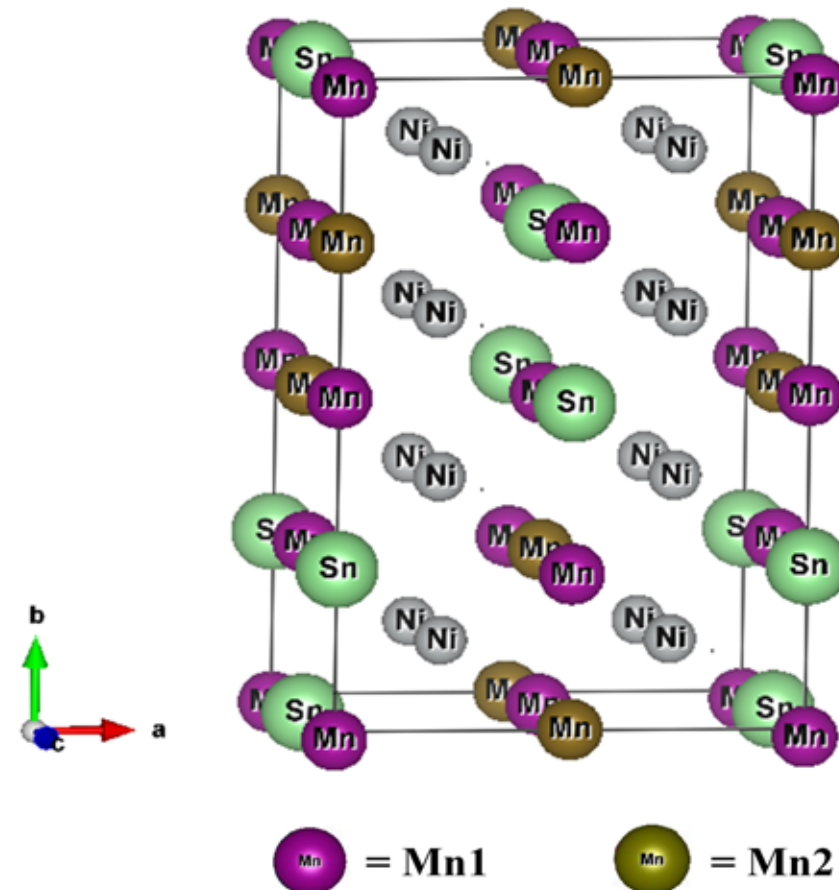


Figure 4.13 The energetically stable combination after doubling the stable tetragonal structure of $\text{Ni}_2\text{Mn}_{1.5}\text{Sn}_{0.5}$.

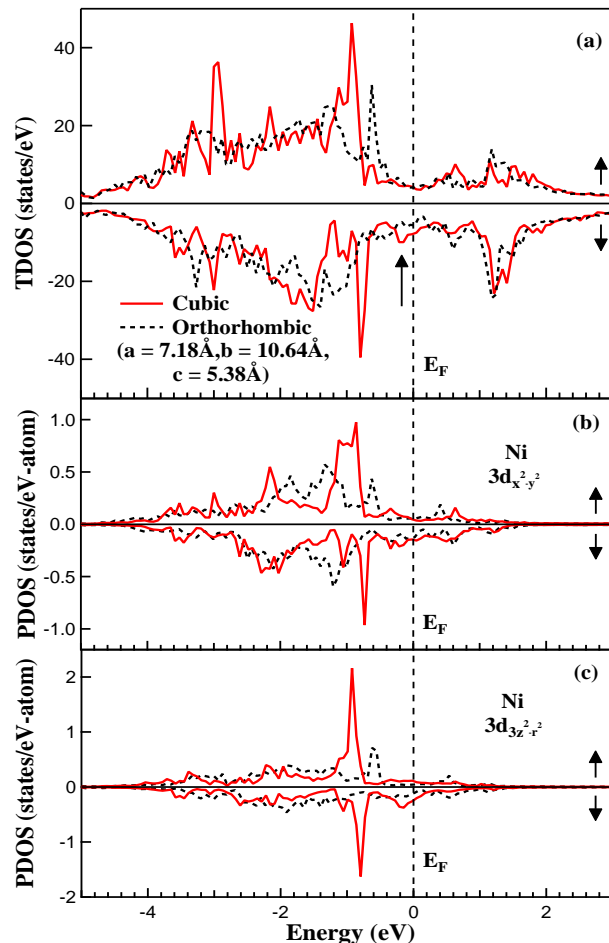


Figure 4.14 Spin polarized TDOS and PDOS of Ni $3d_{x^2-y^2}$ and $d_{z^2-r^2}$ of energetically stable orthorhombic structure doubled along b -axis of $Ni_2Mn_{1.5}Sn_{0.5}$. The Fermi energy E_F is at 0 eV. The upper/lower panel is for the majority/minority spin channel.

near Fermi energy of $x = 0.36$ & 0.42 reduces due to martensitic transformation.

4.6 Conclusions

In summary, when the Mn atoms are doped at the Sn sites of $\text{Ni}_2\text{Mn}_{1+x}\text{Sn}_{1-x}$, the random kind of distribution of Mn is energetically favorable. Mn at Mn sites are antiferromagnetically coupled to Mn at Sn sites. So, magnetic moment of the Ni-Mn-Sn system decreases with doped Mn concentration with the growth of random antiferromagnetic domains at $x \gtrsim 0.3$. Furthermore, we have investigated the structural properties of $\text{Ni}_2\text{Mn}_{1+x}\text{Sn}_{1-x}$ by means of *ab-initio* density functional theory. We have obtained martensitic transformation for $x \geq 0.375$ which is in good agreement with the experimental value of $x \geq 0.36$. The relative on-site energies of Ni *d* states in cubic and fully relaxed tetragonal structure of $\text{Ni}_2\text{Mn}_{1.5}\text{Sn}_{0.5}$ reveals that the changes in the energies are very small and the Jahn-Teller effect associated with Ni *d* states cannot be the driving force for the martensitic transitions seen in this system. It is the Ni-Mn hybridization and Sn lone pair effect on Ni which makes the cubic structure unstable and triggers the structural transformation for Ni-Mn-Sn systems.

Additionally, it should be noted that the formation of plane of Mn atoms gives rise to development of theoretical tetragonal structure in $\text{Ni}_2\text{Mn}_{1.5}\text{Sn}_{0.5}$. However, the system has the tendency to go to more energetically favorable orthorhombic structure when the symmetry in all directions is broken by random distribution of Mn atoms in the supercell.

Bibliography

- [1] C. P. Opeil, B. Mihaila, R. K. Schulze, L. Mañosa, A. Planes, W. L. Hults, R. A. Fisher, P. S. Riseborough, P. B. Littlewood, J. L. Smith, and J. C. Lashley, Phys. Rev. Lett. **100**, 165703 (2008).
- [2] M. S. Wechsler, D. S. Lieberman, and T. A. Read, J. Met. **5**, 1503 (1953).
- [3] P. J. Brown, A. Y. Bargawi, J. Crangle, K. -U. Neumann, and K. R. A. Ziebeck, J. Phys.: Condens. Matter **11**, 4715 (1999).
- [4] S. Ağduk and G. Gökoğlu, J. Alloys Compd. **511**, 9 (2012).
- [5] M. Ye, A. Kimura, Y. Miura, M. Shirai, Y. T. Cui, K. Shimada, H. Namatame, M. Taniguchi, S. Ueda, K. Kobayashi, R. Kainuma, T. Shishido, K. Fukushima, and T. Kanomata, Phys. Rev. Lett. **104**, 176401 (2010).
- [6] V. V. Sokolovskiy, V. D. Buchelnikov, M.A. Zagrebin, P. Entel, S. Sahool, and M. Ogura, Phy. Rev. B **86**, 134418 (2012).
- [7] R. Hafner, J. Comp. Chem. **29**, 2044 (2008).
- [8] P. E. Blöchl, Phys. Rev. B **50**, 17953 (1994).
- [9] G. Kresse, and D. Joubert, Phys. Rev. B **59**, 1758 (1999).
- [10] G. Kresse, and J. Hafner, Phys. Rev. B **47**, 558 (1993).

- [11] G. Kresse, and J. Furthmüller, *Comput. Mater. Sci.* **6**, 15 (1996); *Phys. Rev. B* **54**, 11169 (1996).
- [12] J. P. Perdew, J. A. Chevary, S. H. Vosko, K. A. Jackson, M. R. Pederson, D. J. Singh, and C. Fiolhais, *Phys. Rev. B* **46**, 6671 (1992).
- [13] J. P. Perdew, K. Burke, and M. Ernzerhof, *Phys. Rev. Lett.* **77**, 3865 (1996).
- [14] S. Singh and C. Biswas, *Appl. Phys. Lett.* **98**, 212101 (2011).
- [15] Y. Kurtulus, R. Dronskowski, G. D. Samolyuk, and V. P. Antropov, *Phys. Rev. B* **71**, 014425 (2005).
- [16] S. Chatterjee, S. Giri, S. Majumdar, and S. K. De, *Phys. Rev. B* **77**, 224440 (2008).
- [17] Y. Sutou, Y. Imano, N. Koeda, T. Omori, R. Kainuma, K. Ishida, and K. Oikawa, *Appl. Phys. Lett.* **85**, 4358 (2004).
- [18] A. A. Mostofi, J. R. Yates, Y. -S. Lee, I. Souza, D. Vanderbilt, and N. Marzari, *Comput. Phys. Commun.* **178**, 685 (2008).
- [19] N. Marzari and D. Vanderbilt, *Phys. Rev. B* **56**, 12847 (1997).
- [20] I. Souza, N. Marzari and D. Vanderbilt, *Phys. Rev. B* **65**, 035109 (2001).
- [21] C. V. Stager, and C. C. M. Campbell, *Can. J. Phys.* **56**, 674 (1978).
- [22] T. Krenke, E. Duman, M. Acet, E. F. Wassermann, X. Moya, L. Mañosa, and A. Planes, *Nature Materials* **4**, 450 (2005).
- [23] T. Kanomata, K. Fukushima, H. Nishihara, R. Kainuma, W. Ito, K. Oikawa, K. Ishida , K. U. Neumann, and K. R. A. Ziebeck, *Mater. Sci. Forum* **583**, 119 (2008).
- [24] S. Chatterjee, S. Giri, S. K. De, and S. Majumdar, *Phys. Rev. B* **79**, 092410 (2009).

- [25] R. Kainuma, K. Ito, W. Ito, R. Y. Umetsu, T. Kanomata, and K. Ishida, Mater. Sci. Forum **635**, 23 (2010).
- [26] S. Chatterjee, and S. Majumdar, Mater. Sci. Forum **635**, 97 (2010).
- [27] W. Ito, X. Xu, R. Y. Umetsu, T. Kanomata K. Ishida, and R. Kainuma Appl. Phys. Lett. **97**, 242512 (2010).
- [28] S. Chatterjee, S. Giri, S. K. De, and S. Majumdar, Journal of Physics: Conference Series **200**, 032011 (2010).
- [29] V. V. Khovaylo, K. P. Skokov, O. Gutfleisch, H. Miki, T. Takagi, T. Kanomata, V. V. Koledov, V. G. Shavrov, G. Wang, E. Palacios, J. Bartolomé, and R. Burriel, Phys. Rev. B **81**, 214406 (2010).
- [30] S. E. Muthu, N. V. Rama Rao, D. V. Sridhara Rao, M. M. Raja, U. Devarajan, and S. Arumugam, J. Appl. Phys. **110**, 023904 (2011).
- [31] J. Enkovaara, O. Heczko, A. Ayuela, and R. M. Nieminen, Phy. Rev. B **67**, 212405 (2003).
- [32] A. Planes, L. Mañosa, and M. Acet, J. Phys.: Cond. Matt. **21**, 233201 (2005).
- [33] T. Krenke, M. Acet, E. F. Wassermann, X. Moya, L. Mañosa, and A. Planes, Phys. Rev. B **72**, 014412 (2005).
- [34] Y. Sutou, Y. Imano, N. Koeda, T. Omori, R. Kainuma, K. Ishida, and K. Oikawa, Appl. Phys. Lett. **85**, 4358 (2004).
- [35] P. J. Brown, A. P. Gandy, K. Ishida, R. Kainuma, T. Kanomata, K-U Neumann, K. Oikawa, B. Ouladdiaf, and K .R. A. Ziebeck, J. Phys.: Condens. Matter **18**, 2249 (2006).
- [36] S. Banik, R. Ranjan, A. Chakrabarti, S. Bhardwaj, N. P. Lalla, A. M. Awasthi, V. Sathe, D. M. Phase, P. K. Mukhopadhyay, D. Pandey, and S. R. Barman, Phys. Rev. B **75**, 104107 (2007).
- [37] P A Bhobe, K R Priolkar, and P R Sarode, J. Phys.: Condens. Matter **20**, 015219 (2008).

- [38] P. J. Brown, A. P. Gandy, K. Ishida, R. Kainuma, T. Kanomata, K.-U. Neumann, K. Oikawa, B. Ouladdiaf, and K. R. A. Ziebeck, *J. Phys.: Condens. Matter* **18**, 2249 (2006).

Chapter 5

Crystal structure effect on properties of Ni-Mn-Sn

5.1 Introduction

The new class of off-stoichiometric magnetic shape memory alloys that exhibit shift of martensitic transition to lower temperature with applied magnetic field have gained adequate scientific attention due to shift induced attractive properties like giant magnetocaloric effects [1], giant magneto-resistance [2], magnetic shape memory effects [3] and exchange bias effects [4]. These fascinating properties make the alloys a potential candidate for applications in solid-state magnetic refrigeration [1], magnetic actuators [5, 6] and magnetic sensors [6], spintronics [7], magnetic recording [8, 9] etc. This class of material is very important for replacing present way of cooling with hazardous gases. The above properties arise due to martensitic structural phase transition accompanied by magnetic phase change. Thus martensitic magneto-structural transformation plays an important role in various applications of Heusler alloys.

Since the pioneering work on exchange bias (EB)effect by Meikleohn and Bean in 1956 [10], this phenomenon has been explored extensively due to its various applications in spintronics, magnetic recording and sensors devices [6–9, 11–14]. It was usually observed in materials with interface between different magnetic phases such as ferromagnetic (FM)-antiferromagnetic (AFM), FM-spin glass (SG), AFM-ferrimagnetic (FI), and FM-FI phases [10, 15–18] during cooling with magnetic field. The conventional exchange bias effect is ascribed to ferromagnetic unidirectional anisotropy formed at the interface between different magnetic phases in the process of field cooling (FC).

An unusual EB effect under zero-field-cooled-heating (ZFC) has also been obtained in different systems, such as Mn_2PtGa alloy [19], $\text{BiFeO}_3\text{Bi}_2\text{Fe}_4\text{O}_9$ nanocomposite [20], YMnO_3 nanoparticles [21], $\text{La}_{1.5}\text{Sr}_{0.5}\text{CoMnO}_6$ polycrystalline ceramics [22], $\text{Pr}_{1-x}\text{Ca}_x\text{MnO}_3$ nanosheet [23], antiperovskite compound PdNCr_3 [24], $\text{Co}_{0.8}\text{Cu}_{0.2}\text{Cr}_2\text{O}_4$ [25], $\text{Y}_{0.9}\text{Pr}_{0.1}\text{CrO}_3$ ceramics [26] and $\text{La}_{0.5}\text{Sr}_{0.5}\text{Mn}_{0.8}\text{-Co}_{0.2}\text{O}_3$ ceramics [27]. The appearance of such ZFC-EB effect is related to newly formed interface with AFM unidirectional anisotropy, and the formation or growth of FM (or superferromagnet) domains at the expense of pinning subsystem (AFM matrix or spin glass).

Interestingly, the unusual ZFC-EB effect is also found in many off-stoichiometric Ni-Mn-Z (Z

= In and Sn) [4, 28], $\text{Ni}_2\text{Mn}_{1.4}\text{Ga}_{0.6}$ [29], $\text{Ni}_{50}\text{Mn}_{36}\text{Co}_4\text{Sn}_{10}$ [30] Heusler alloys with martensitic transition. In off-stoichiometric Ni-Mn-Ga alloys, the ZFC-EB effect is believed to be due to irreversible growth of ferromagnetic domains that change from non-percolating to percolating state and, consequently, forms the unidirectional anisotropy at the interface [29]. In $\text{Ni}_{50}\text{Mn}_{36}\text{Co}_4\text{Sn}_{10}$ Heusler alloy, the enhancement of antiferromagnetism induces a strong interaction with super-ferromagnetic (SFM), super spin glass (SSG), and superparamagnetic (SPM) domains resulting in ZFC-EB effect [30]. In Ni-Mn-Z ($Z = \text{In}, \text{Sn}$) alloys the occurrence of ZFC-EB effect is attributed to the SFM unidirectional anisotropy below the blocking temperature (T_B). The probable origin is argued to be purely magnetic and does not originate from structural modifications due to martensitic transition [28]. However, it is important to mention that in Heusler alloys magnetic and structural transitions driven multifunctionality are caused by magneto-structural coupling [31–40].

The magnetic behavior influences the crystal structure causing the martensitic transition in Ni-Mn based Heusler alloys [41]. In $\text{Ni}_2\text{Mn}_{1+x}\text{Sn}_{1-x}$ as x is increased, the magnetic exchange interactions between doped Mn at Sn site (Mn2) and the neighboring Mn at parent Mn site (Mn1) lead to substantial deviation from a perfectly d^5 character on Mn1 in cubic austenitic structure. This then allows for energy gain from both Mn1-Ni and Mn2-Ni hybridization. So the Ni atom moves towards both Mn1 and Mn2. This results in a resultant force along a lattice parameter in the cubic structure giving rise to structural instability. Thus, the magnetic state of the Mn atom triggers the instability in the cubic phase and further presence of Sn lone pair repulsion to electrons on neighbouring atoms gives rise to the martensitic structural transition [41]. This implies that the magnetic state and crystal structure are coupled to each other. Thus it requires a detailed insight into the crystal structure of Ni-Mn-Sn Heusler alloys and careful analysis to check whether the crystal structure influences the magnetic behavior even below martensitic finish temperature under ZFC.

In Ni-Mn-Sn martensitic phase ferromagnetic and antiferromagnetic magnetic phases co-exist. The antiferromagnetic coupling occurs between Mn1 and Mn2 [42, 44–46]. This occurs due to the decrease in Mn-Mn bond length. This happens by decrease in lattice parameter along one direction and increase along other directions [41]. At low temperatures the antiferromagnetic

exchange interaction changes due to change in crystal structure and contributing phases [47]. This might play important role in producing unusual exchange bias effect under ZFC. Despite intense research on the martensitic structure of Ni-Mn-Sn, the structure is still debatable. The X-ray diffraction reveals that the martensitic structure is mainly modulated structure. Depending on the sample preparation conditions and the doping concentration of Mn, the modulations could be 4O orthorhombic, 10M (or 10O) orthorhombic, 14M monoclinic and L1₀ (unmodulated double tetragonal) [31, 32, 42]. Recently, mixed modulated martensitic phase has also been confirmed for different compositions of Ni-Mn-Sn [43]. The crystal structures of martensitic phase are confirmed to be 14M modulated structure for Ni₂Mn_{1.64}Sn_{0.36}, mixed modulated structure 4O + 10M + L1₀ for Ni₂Mn_{1.56}Sn_{0.44} and 4O structure for Ni₂Mn_{1.48}Sn_{0.52}, respectively. Moreover, substitution of Sn with Mn increases valence electron concentration (*e/a*) and the phase transition temperatures. With increasing *e/a* the crystal structure of the martensitic phase transforms in a sequence of 4O → 10M → 14M → L1₀ during the phase transformation of bulk Ni-Mn-Sn alloys. The literature has many different reports on the crystal structure of Ni-Mn-Sn. Thus, the martensitic structure of Ni-Mn-Sn needs to be revisited in more details. The magnetic and structural relationship needs to be established to explain low temperature magnetic phenomena, e.g., ZFC exchange bias effect. Moreover, the theoretical electronic structure could be supported by calculated electronic structure using experimental crystal structure parameters. The crystal structure changes with temperature gives rise to significant reconstructions in density of states.

In this chapter, the crystal structure as a function of temperature for Ni₂Mn_{1+x}Sn_{1-x} (*x* = 0.40 and 0.44) alloys are investigated till 10 K under cooling and heating (without magnetic field) condition. In the martensitic phase the co-existence of 4-layered (4L) and 14-layered (14L) orthorhombic crystal structure is revealed. Interestingly, the phase fraction of 4L and 14L crystal structures change with temperature. The changes occur at temperatures where magnetic transitions also occur. This implies that there is a possible coupling between crystal structure and magnetic behavior. In order to establish the relation, the magnetic exchange parameter (*J*) between first nearest neighbour Mn1-Mn2 is calculated for 4L and 14L structures finding out the magnetic ground state of these two structures. The calculation reveals the antiferromagnetic exchange inter-

action with different strength of antiferromagnetic coupling for 4L and 14L orthorhombic crystal structure. Important to note that not only ferromagnetic-antiferromagnetic domains co-exists, also different strength of antiferromagnetic coupling exists. Thus, frustrated state of martensitic phase arises that causes spin-glass-like behavior of $\text{Ni}_2\text{Mn}_{1+x}\text{Sn}_{1-x}$ ($x = 0.40$ and 0.44). This possibly leads to exchange bias phenomena even under ZFC. Thus, crystal structure of martensitic phase affects the magnetic behavior of Ni-Mn-Sn in martensitic phase.

5.2 Experimental and Theoretical Method

The polycrystalline ingots of $\text{Ni}_2\text{Mn}_{1+x}\text{Sn}_{1-x}$ ($x = 0.40, 0.44, 0.48 \& 0.52$) alloys are prepared by arc melting appropriate amount of high purity ($\geq 99.99\%$) constituent elements under argon atmosphere and were annealed at 1173 K (24 hours) with subsequent quenching to ice water. The polycrystalline ingots are crushed to very fine powder and annealed again at 1173 K (12 hours) followed by quenching to ice water. The alloys are characterized as mentioned in Ref. [2]. The structural and magnetic transition temperatures are determined by differential scanning calorimetry (DSC) measurements (fig. 5.1) and magnetization behavior. The transition temperatures, i.e., martensitic start (M_s), martensitic finish (M_f), austenitic start (A_s) and austenitic finish (A_f) are tabulated in Table 5.1. Below room temperature, $x = 0.40$ and 0.44 transform from ferromagnetic

Table 5.1 The structural and magnetic transition temperatures of $x = 0.40, 0.44, 0.48 \& 0.52$, obtained from DSC and magnetization. The maximum error is ± 10 K [2].

Composition (x)	M_s (K)	M_f (K)	A_s (K)	A_f (K)	T_C^M (K)	T_C^A (K)	T_B (K)
0.40	189	159	173	208	-	326	70
0.44	260	229	245	275	-	323	80
0.48	396	353	368	407	231	320	130
0.52	416	378	388	425	175	-	106

austenitic phase to mixed magnetic martensitic phase where co-existence of ferromagnetic and antiferromagnetic coupling is reported [42, 44–46]. In these systems the Mn2 is antiferromagnet-

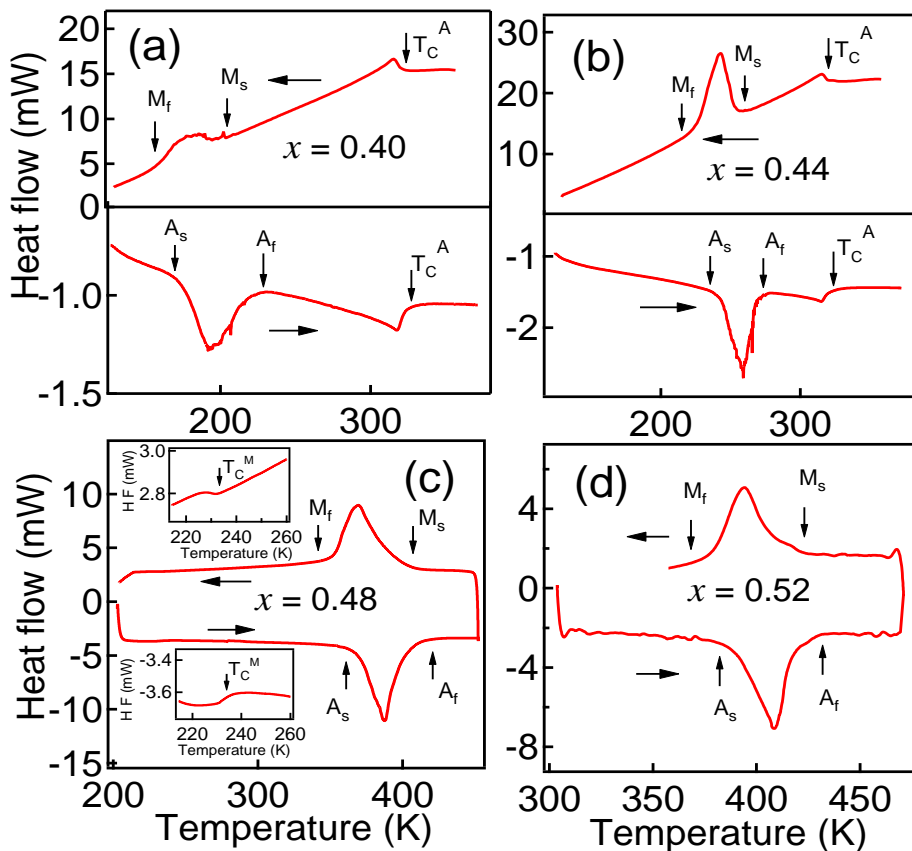


Figure 5.1 Exothermic and endothermic behavior of $\text{Ni}_2\text{Mn}_{1+x}\text{Sn}_{1-x}$ (0.40 , 0.44 , 0.48 and 0.52) using differential scanning calorimetry during cooling and heating, respectively [2].

ically coupled to Ni and Mn1 [42, 44–46], whereas Mn1 is ferromagnetically coupled to Ni. The temperature dependent X-ray powder diffraction (XRD) measurements are performed using synchrotron radiation of energy 18 KeV from room temperature to 10 K and reverse at Indian Beam line, Photon factory, KEK, Japan. The thermo-susceptibility behaviour is recorded during heating after cooling to 10 K under zero field.

Since, during cooling, the martensitic transition temperatures are well below 300K, the clarity of phases during cooling is better. While heating even at 300 K the system does not fully transform to austenitic phase. It has some martensite fraction in austenitic phase in both $x = 0.40$ and 0.44 . Hence, XRD during cooling is compared with magnetic results.

The magnetic exchange parameter between first nearest neighbour Mn1-Mn2 of 16 atom unit cell of $x = 0.50$ is calculated using experimentally obtained lattice parameters at different temperatures of $x = 0.44$ on the basis of the idea of ising model where the energy of any spin system can be described by $E = - \sum_{i \neq j} J_{ij} S_i S_j$. The theoretically adopted composition $x = 0.50$, close to $x = 0.44$, shows martensitic transformation in 16 atom unit cell structure. The nature of transformation in $x = 0.50$ is similar to $x = 0.44$. So, the behaviour of exchange parameter of $x = 0.50$ can be attributed to the nature of magnetic exchange in $x = 0.44$. The *ab-initio* calculations are performed using the projector augmented wave (PAW) method as implemented in the Vienna *ab-initio* simulation package (VASP) [48] code within generalized gradient approximation (GGA) for the exchange correlation functional. Monkhorst-Pack k-points mesh of $10 \times 10 \times 10$ is used for calculation.

5.3 Results and Discussion

5.3.1 Temperature variations of crystal structure

The X-ray diffraction patterns of $x = 0.40$ composition in austenitic phase at room temperature in both cooling and heating cycle are shown in fig. 5.2. The crystal structure is cubic L₂ having lattice parameter $a \approx 5.98 \text{ \AA}$ with crystal symmetry $Fm\bar{3}m$. The temperature dependent diffraction patterns with proper peak indexing for $x = 0.40, 0.44, 0.48$ and 0.52 are shown in fig. 5.3, fig. 5.4, fig. 5.5 and fig. 5.6, respectively. The LeBail fitting is employed (as discussed in Chapter 2) to extract out the contributing phase information and corresponding lattice parameters. Initially, the LeBail fitting is done for the diffraction patterns of all the samples by 4L modulated orthorhombic structure with space group *Pmma* in martensitic phase which is similar to the previous reported results [42, 49]. The diffraction patterns at 200 K of $x = 0.40$ and at 255 K & 265 K of $x = 0.44$ are indexed properly by 4L martensitic structure and cubic L₂ structure. For $x = 0.48$ and 0.52 , the XRD patterns at all temperatures below 300 K, could not be indexed appropriately by 4L structural phase only. These two compositions are in martensitic phase below 300K. Afterward, the patterns were fitted only by 14L modulated structure. Again fittings are not satisfactory. Then

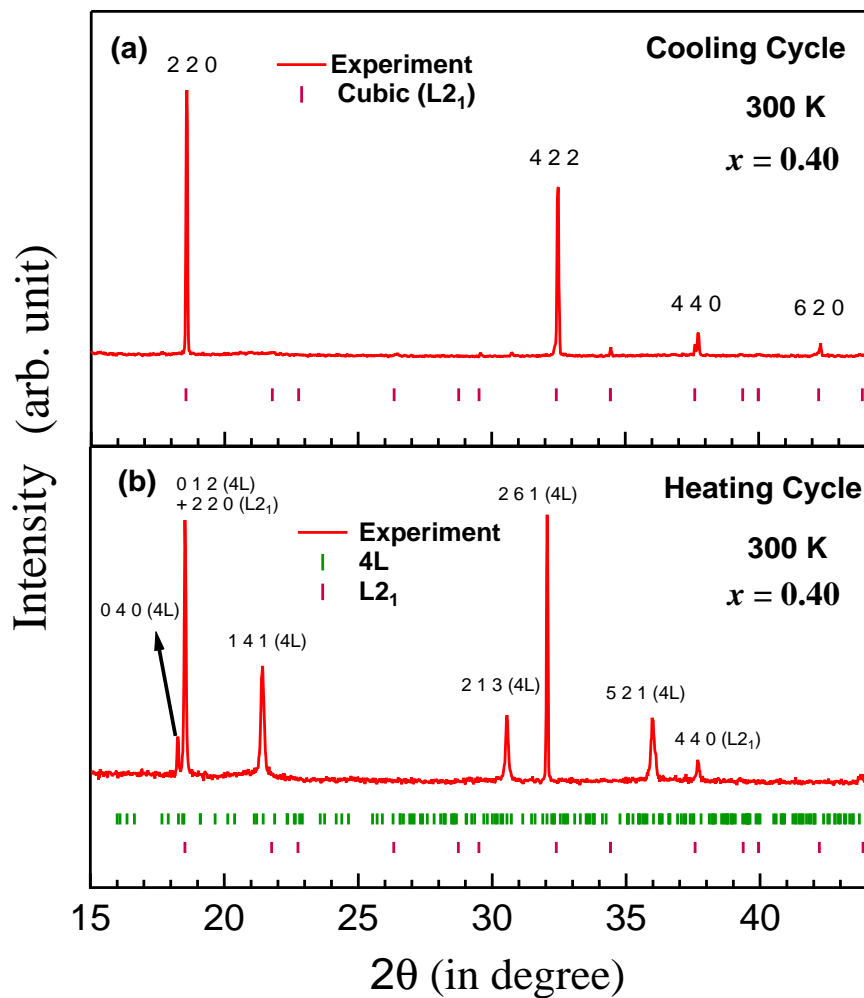


Figure 5.2 Room temperature synchrotron X-ray diffraction pattern indexed by $L2_1$ and 4-layered orthorhombic crystal structure of $x = 0.40$ in (a) cooling and (b) heating cycle.

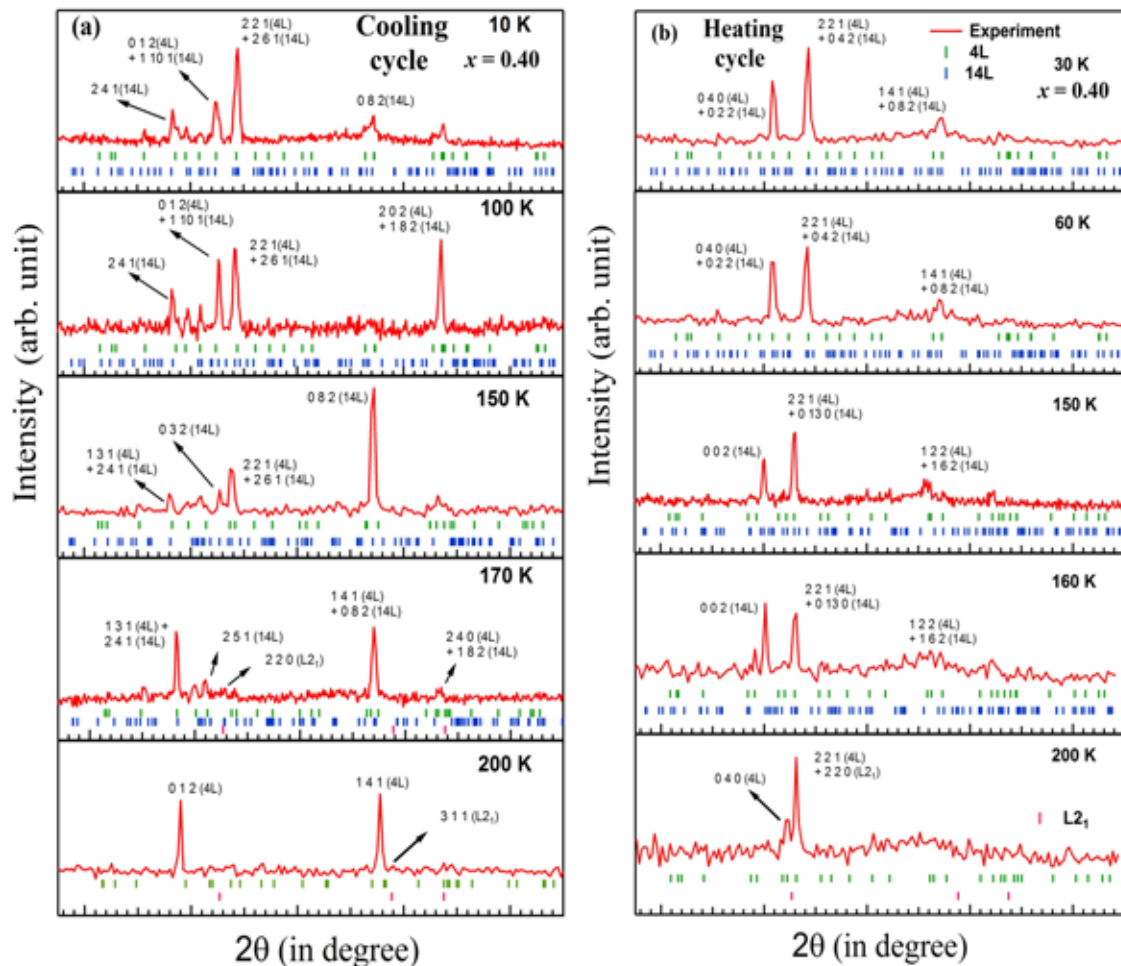


Figure 5.3 Temperature variation of synchrotron X-ray diffraction pattern indexed by co-existing 4-layered and 14-layered orthorhombic crystal structure of $x = 0.40$ in (a) cooling and (b) heating cycle.

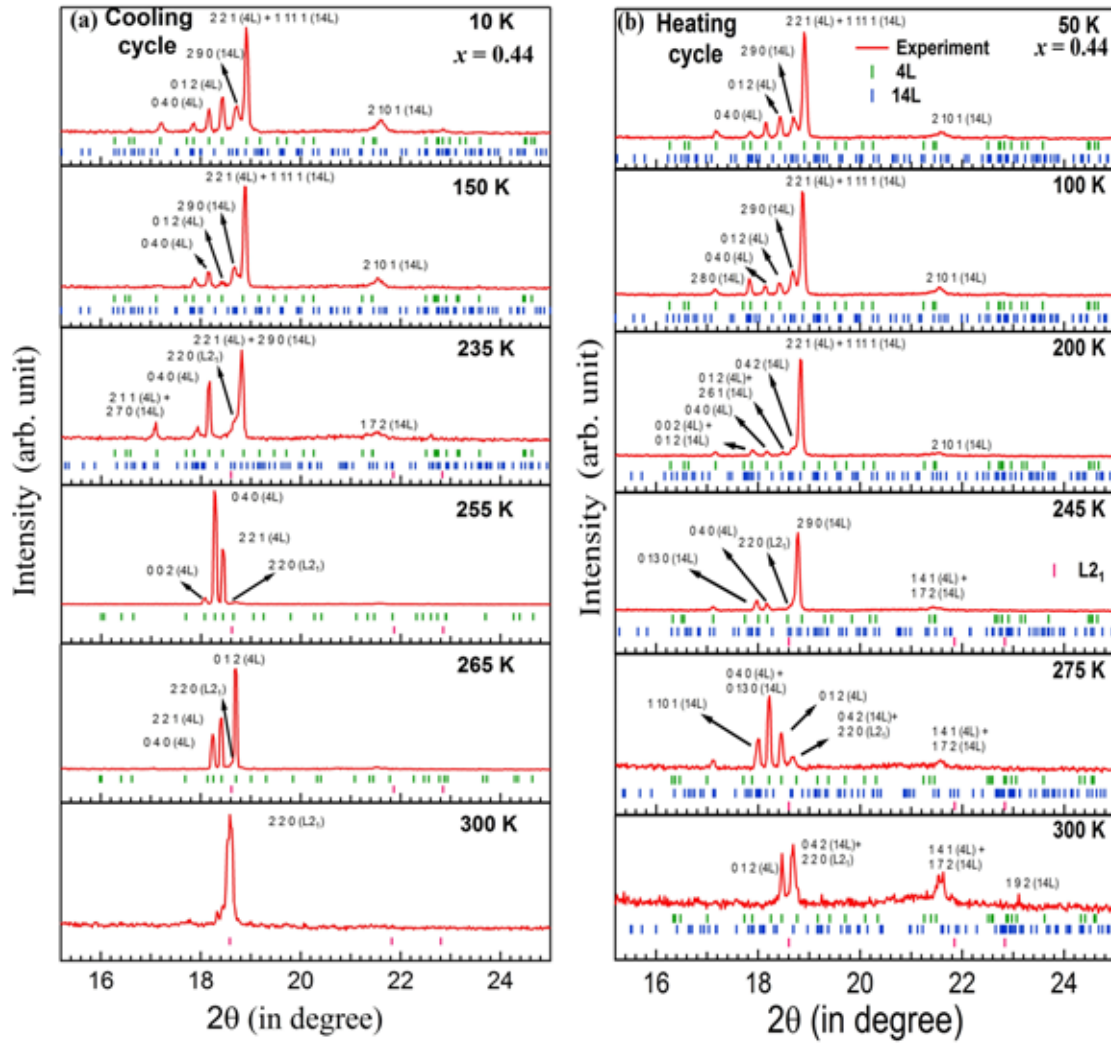


Figure 5.4 Temperature variation of synchrotron X-ray diffraction pattern indexed by co-existing 4-layered and 14-layered orthorhombic crystal structure of $x = 0.44$ in (a) cooling and (b) heating cycle.

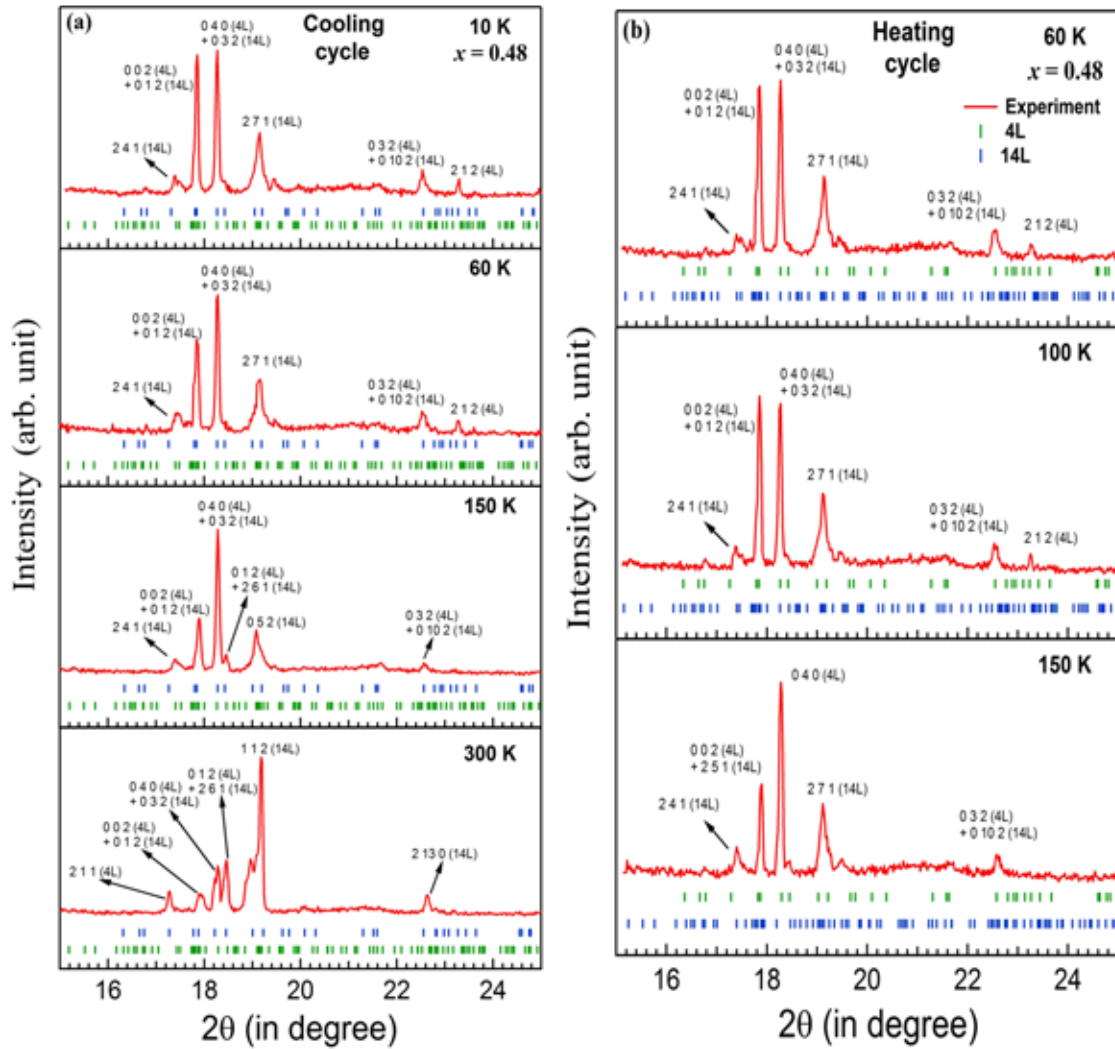


Figure 5.5 Temperature variation of synchrotron X-ray diffraction pattern indexed by co-existing 4-layered and 14-layered orthorhombic crystal structure of $x = 0.48$ in (a) cooling and (b) heating cycle.

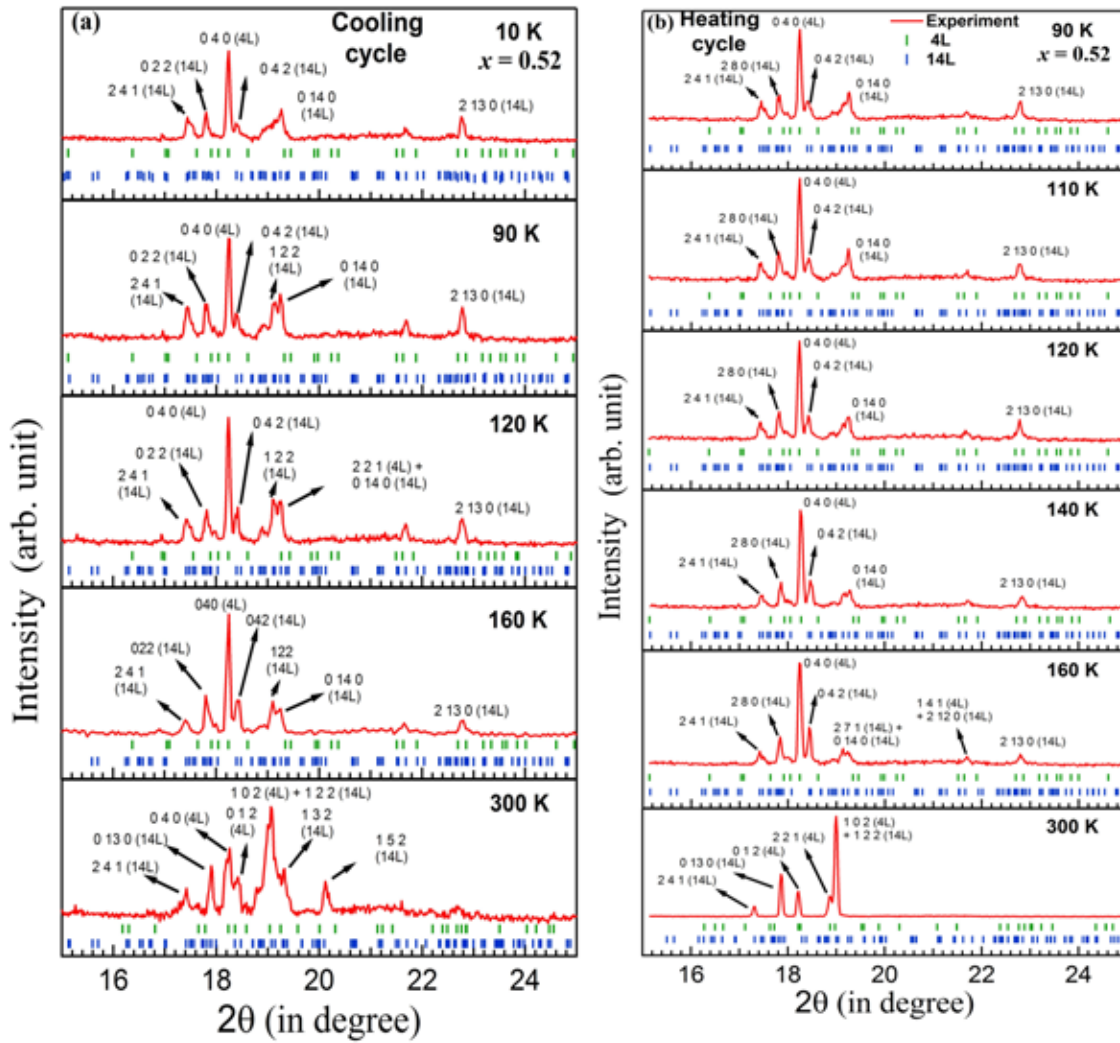


Figure 5.6 Temperature variation of synchrotron X-ray diffraction indexed by co-existing 4-layered and 14-layered orthorhombic crystal structure of $x = 0.52$ in (a) cooling and (b) heating cycle.

the diffraction peaks of both the compositions are indexed by both 4L and 14L orthorhombic structures. All the diffraction peaks could be indexed accurately. Thus, martensitic phase has two co-existing orthorhombic structures, namely, 4L with space group *Pmma* and 14L with space group *P2/m* having slight monoclinicity. The 14M orthorhombic structure was also proposed by Santos *et al.* [50, 51] for $\text{Ni}_2\text{Mn}_{1.48}\text{Sn}_{0.52}$ ribbons, Brown *et al.* [52] for Ni_2MnGa and Ranjan *et al.* [53] for $\text{Ni}_2\text{Mn}_{1.05}\text{Ga}_{0.95}$. Similarly, the low temperature (below 200 K for $x = 0.40$ and below 255 K for $x = 0.44$) diffraction behavior of $x = 0.40$ and $x = 0.44$ compositions are fitted well with 4L and 14L orthorhombic crystal structure.

The mixture of two structures in martensitic phase is, also, found in other Heusler alloys [54–56]. The transformation from L2₁ cubic to 4L and 14L takes place by contraction along *c*-axis and elongation along *b*-axis according to Bain transformation. relation: $a_{\text{ortho}} \approx a_{\text{cubic}}, b_{\text{ortho}} \approx \frac{2}{\sqrt{2}}b_{\text{cubic}}, c_{\text{ortho}} \approx \frac{1}{\sqrt{2}}c_{\text{cubic}}$ and $a_{\text{ortho}} \approx a_{\text{cubic}}, b_{\text{ortho}} \approx \frac{7}{\sqrt{2}}b_{\text{cubic}}, c_{\text{ortho}} \approx \frac{1}{\sqrt{2}}c_{\text{cubic}}$, respectively. The lattice parameters for all the compositions at different temperatures during cooling and heating cycle are summarized in Table 5.2 and Table 5.3, respectively.

In fig. 5.7, schematic representation of 4L and 14L modulated supercell structure of $x = 0.5$ are depicted. Where Mn2 is randomly distributed. Here the modulation is along *b* axis of orthorhombic structure. The high temperature phase is cubic L2₁ austenitic phase. With the decrease in temperature cubic structure transforms to 4L structure through two times elongation of unit cell along [011]_{cubic} direction and contraction of *a*-axis along [100]_{cubic} direction. With further lowering of temperature more elongation gives rise to 14L modulated orthorhombic structure and further contraction along *a*-axis. The *a*-axis contraction of 4L structure is observed, mainly, when 4L and 14L structure co-exist.

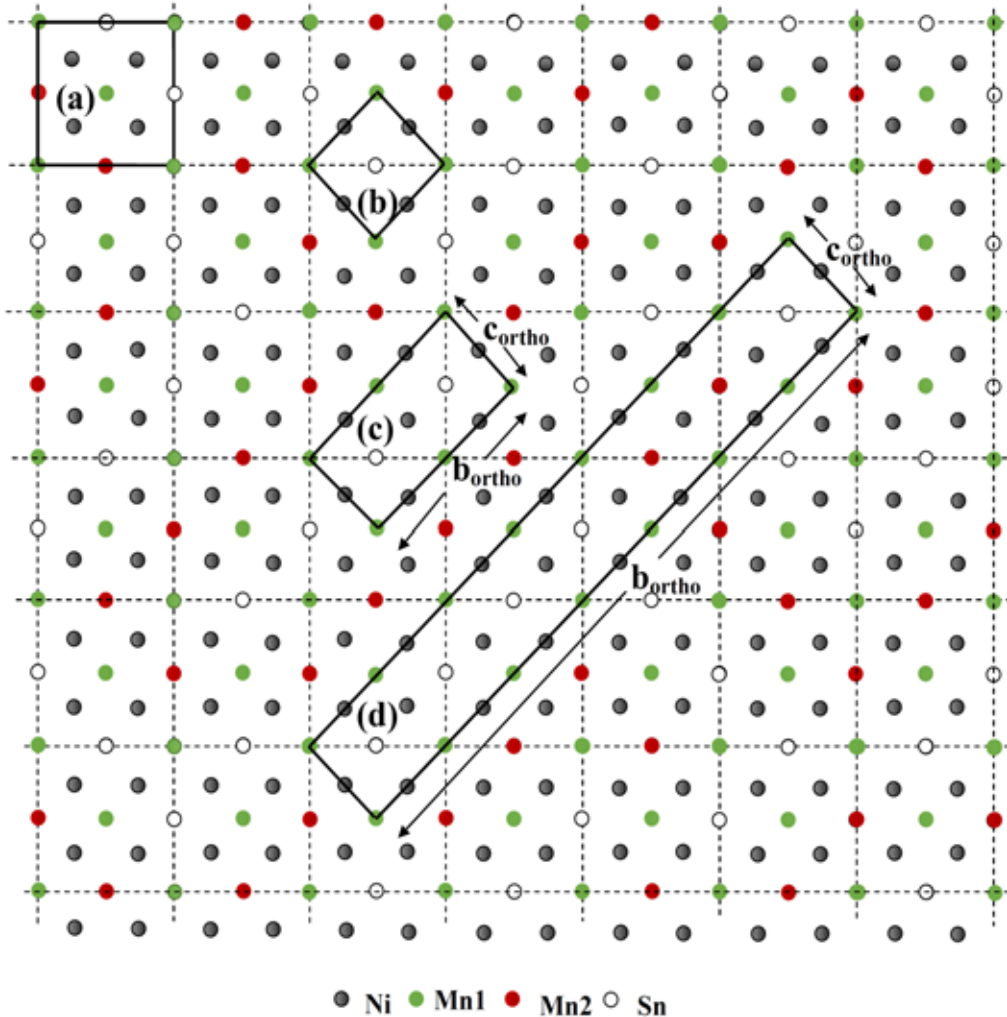


Figure 5.7 Schematic representation of (a) projection on (100) of the L₂₁ cell, (b) fundamental unit of the L₂₁ cell which will be Bain transformed; $a_{\text{Bain}} = [100]_{\text{cubic}}$, the transformed (c) 4L and (d) 14L supercell. Here the Mn2 is randomly distributed at Sn sites of Ni₂Mn_{1.5}Sn_{0.5}.

Table 5.2 Lattice parameters and nearest neighbor Mn1-Mn2 bond-lengths of different structural phases after fitting at various temperatures in cooling cycle for $x = 0.40, 0.44, 0.48$ and 0.52 compositions.

Compo-	Tempe-	Struc-	Lattice	Mn1-Mn2
sition	rature	tural	parameter (\AA)	bond length (\AA)
(x)	(K)	phase		($a_{\text{ortho}}/2$)
0.40	300	L2 ₁	$a \approx 5.98$	2.99
	200	4L	$a \approx 5.83, b \approx 8.57, c \approx 4.30$	2.92
		L2 ₁	$a \approx 5.98$	2.99
	170	4L	$a \approx 5.77, b \approx 8.71, c \approx 4.30$	2.88
		14L	$a \approx 5.57, b \approx 27.48, c \approx 4.34$	2.79
		L2 ₁	$a \approx 5.98$	2.99
	150	4L	$a \approx 5.74, b \approx 8.74, c \approx 4.29$	2.82
		14L	$a \approx 5.60, b \approx 27.26, c \approx 4.35$	2.80
	100	4L	$a \approx 5.64, b \approx 8.63, c \approx 4.38$	2.82
		14L	$a \approx 5.60, b \approx 26.95, c \approx 4.32$	2.80
0.44	10	4L	$a \approx 5.65, b \approx 8.64, c \approx 4.38$	2.82
		14L	$a \approx 5.59, b \approx 26.99, c \approx 4.37$	2.80
	300	L2 ₁	$a \approx 5.97$	2.985
	265	4L	$a \sim 5.95, b \sim 8.60, c \sim 4.32$	2.98
		L2 ₁	$a \approx 5.97$	2.985
	255	4L	$a \sim 5.93, b \sim 8.58, c \sim 4.34$	2.96
		L2 ₁	$a \approx 5.97$	2.985
	235	4L	$a \approx 5.65, b \approx 8.64, c \approx 4.39$	2.82
		14L	$a \approx 5.59, b \approx 28.21, c \approx 4.40$	2.80
		L2 ₁	$a \approx 5.97$	2.985
0.48	150	4L	$a \approx 5.65, b \approx 8.64, c \approx 4.39$	2.82
		14L	$a \approx 5.59, b \approx 28.63, c \approx 4.40$	2.80
	10	4L	$a \approx 5.61, b \approx 8.64, c \approx 4.39$	2.81
		14L	$a \approx 5.58, b \approx 28.56, c \approx 4.41$	2.79
	300	4L	$a \approx 5.57, b \approx 8.61, c \approx 4.39$	2.78
		14L	$a \approx 5.62, b \approx 28.64, c \approx 4.40$	2.81
	150	4L	$a \approx 5.58, b \approx 8.58, c \approx 4.39$	2.79
		14L	$a \approx 5.63, b \approx 28.57, c \approx 4.41$	2.82
	60	4L	$a \approx 5.58, b \approx 8.59, c \approx 4.40$	2.79
		14L	$a \approx 5.63, b \approx 28.66, c \approx 4.41$	2.82
0.52	10	4L	$a \approx 5.55, b \approx 8.59, c \approx 4.40$	2.78
		14L	$a \approx 5.62, b \approx 28.66, c \approx 4.41$	2.81
	300	4L	$a \approx 5.80, b \approx 8.60, c \approx 4.41$	2.90
		14L	$a \approx 5.60, b \approx 28.48, c \approx 4.48$	2.80
	160	4L	$a \approx 5.42, b \approx 8.60, c \approx 4.35$	2.71
		14L	$a \approx 5.60, b \approx 28.53, c \approx 4.47$	2.80
	120	4L	$a \approx 5.46, b \approx 8.60, c \approx 4.35$	2.73
		14L	$a \approx 5.60, b \approx 28.53, c \approx 4.47$	2.80
	90	4L	$a \approx 5.43, b \approx 8.60, c \approx 4.35$	2.72
		14L	$a \approx 5.59, b \approx 28.55, c \approx 4.47$	2.80
0.52	10	4L	$a \approx 5.43, b \approx 8.60, c \approx 4.35$	2.72
		14L	$a \approx 5.59, b \approx 28.54, c \approx 4.47$	2.80

Table 5.3 Lattice parameters and nearest neighbor Mn1-Mn2 bond-lengths of different structural phases after fitting at various temperatures in heating cycle for $x = 0.40, 0.44, 0.48$ and 0.52 compositions.

Compo-	Tempe-	Struc-	Lattice	Mn1-Mn2
sition	rature	tural	parameter (\AA)	bond length (\AA)
(x)	(K)	phase		($a_{\text{ortho}}/2$)
0.40	300	4L	$a \approx 5.91, b \approx 8.58, c \approx 4.38$	2.955
		L2 ₁	$a \approx 5.98$	2.99
		200	$a \approx 5.80, b \approx 8.55, c \approx 4.39$	2.9
		L2 ₁	$a \approx 5.98$	2.99
		160	$a \approx 5.80, b \approx 8.58, c \approx 4.40$	2.9
		14L	$a \approx 5.82, b \approx 27.42, c \approx 4.35$	2.91
	150	4L	$a \approx 5.81, b \approx 8.58, c \approx 4.39$	2.905
		14L	$a \approx 5.79, b \approx 27.43, c \approx 4.37$	2.895
		60	$a \approx 5.65, b \approx 8.63, c \approx 4.38$	2.825
		14L	$a \approx 5.59, b \approx 26.90, c \approx 4.37$	2.795
		30	$a \approx 5.65, b \approx 8.63, c \approx 4.38$	2.825
		14L	$a \approx 5.58, b \approx 26.90, c \approx 4.38$	2.79
0.44	300	4L	$a \approx 5.71, b \approx 8.60, c \approx 4.38$	2.855
		14L	$a \approx 5.58, b \approx 27.76, c \approx 4.40$	2.79
		L2 ₁	$a \approx 5.97$	2.985
		275	$a \approx 5.71, b \approx 8.62, c \approx 4.39$	2.855
		14L	$a \approx 5.58, b \approx 28.08, c \approx 4.40$	2.79
		L2 ₁	$a \approx 5.97$	2.985
	255	4L	$a \approx 5.71, b \approx 8.63, c \approx 4.38$	2.855
		14L	$a \approx 5.58, b \approx 28.36, c \approx 4.41$	2.79
		L2 ₁	$a \approx 5.97$	2.985
		245	$a \approx 5.67, b \approx 8.63, c \approx 4.36$	2.835
		14L	$a \approx 5.58, b \approx 28.37, c \approx 4.41$	2.79
		L2 ₁	$a \approx 5.97$	2.985
0.48	200	4L	$a \approx 5.63, b \approx 8.63, c \approx 4.39$	2.815
		14L	$a \approx 5.63, b \approx 28.67, c \approx 4.41$	2.815
		100	$a \approx 5.62, b \approx 8.64, c \approx 4.39$	2.81
		14L	$a \approx 5.61, b \approx 28.59, c \approx 4.40$	2.805
		50	$a \approx 5.62, b \approx 8.64, c \approx 4.39$	2.81
		14L	$a \approx 5.60, b \approx 28.51, c \approx 4.40$	2.8
	150	4L	$a \approx 5.58, b \approx 8.63, c \approx 4.39$	2.79
		14L	$a \approx 5.63, b \approx 28.52, c \approx 4.41$	2.815
		100	$a \approx 5.58, b \approx 8.58, c \approx 4.39$	2.79
		14L	$a \approx 5.63, b \approx 28.41, c \approx 4.43$	2.815
		60	$a \approx 5.58, b \approx 8.59, c \approx 4.40$	2.79
		14L	$a \approx 5.63, b \approx 28.66, c \approx 4.41$	2.815
0.52	300	4L	$a \approx 5.62, b \approx 8.59, c \approx 4.45$	2.81
		14L	$a \approx 5.64, b \approx 28.54, c \approx 4.49$	2.82
		160	$a \approx 5.43, b \approx 8.60, c \approx 4.35$	2.715
		14L	$a \approx 5.60, b \approx 28.56, c \approx 4.46$	2.8
		140	$a \approx 5.42, b \approx 8.59, c \approx 4.34$	2.71
		120	$a \approx 5.60, b \approx 28.53, c \approx 4.46$	2.8
	90	4L	$a \approx 5.43, b \approx 8.60, c \approx 4.35$	2.715
		14L	$a \approx 5.60, b \approx 28.52, c \approx 4.47$	2.8

5.3.2 Change in phase fraction of 4L and 14L with temperature

The percentage of phase fractions as a function of temperature are obtained from the ratio of integrated peak areas of individual 4L and 14L calculated intensity pattern and total calculated pattern. Interestingly, the phase fraction of co-existing 4L and 14L structure varies as a function of tem-

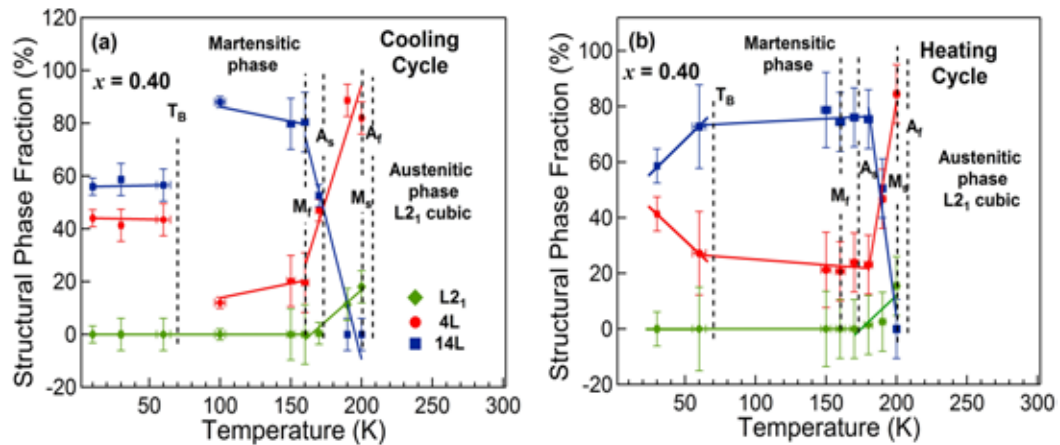


Figure 5.8 4-layered and 14-layered structural phase fraction variation as a function of temperature in martensitic transition region, martensitic phase, and below T_B region of $x = 0.40$ in both (a) cooling and (b) heating.

perature. The fig. 5.8 shows the phase fraction percentage of L_2_1 , 4L and 14L as a function of temperature for $x = 0.40$ during cooling and heating cycle. Initially, cubic L_2_1 structure transforms to 4L structure upon start of martensitic transition. During cooling in between M_s and M_f temperature range, the 14L structure evolves at the cost of 4L structure. Between M_f and spin freezing temperature T_B (referred as T_f in Ref. [57]) the phase fraction is almost constant (80 % 14L). Note-worthy that with further lowering of the temperature, the 4L phase fraction increases and 14L phase fraction decreases. The phase fraction of 4L and 14L is around 50 % at 10 K. The intermartensitic transition is reported earlier for Ni-Mn-Ga, Ni-Mn-Fe-Ga, Ni-Mn-In and Ni-Fe-Ga [58–63]. The stability of the martensitic phase is achieved by transition to either 14M or non-modulated structure mainly through 10M structure. For Ni-Mn-Sn alloys the martensitic transition to 14L structure is happening through 4L structure. For $Ni_2Mn_{1.44}Sn_{0.56}$ the transition from L_2_1 to 4L is reported earlier [42]. The broad, asymmetric line-shape with humps in exothermic and endothermic behaviour

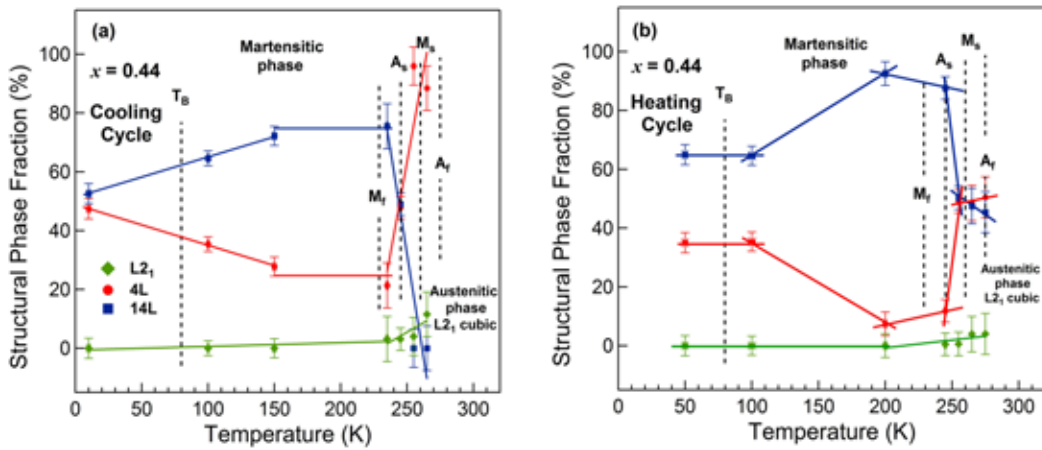


Figure 5.9 4-layered and 14-layered structural phase fraction variation as a function of temperature in martensitic transition region, martensitic phase, and below T_B region of $x = 0.44$ in both (a) cooling and (b) heating.

of heat flow (fig. 5.1) also imply existence of intermartensitic transition [33, 43].

The formation energy per unit cell of 4L and 14L structures ($x = 0.4$) is calculated using experimental lattice constants of 4L and 14L structures at 190 K and 150 K, respectively, by *ab initio* density functional theory. The formation energy per unit cell of 4L (-1.040315 eV) and 14L (-1.023121 eV) are very close to each other. Nevertheless, 4L requires less formation energy than 14L. Thus, initially, the martensitic transformation from parent phase to 4L structure occurs. To accommodate the stress accumulation by 4L structure, the transition to stacking sequence 14L occurs. This internal stress-related selectivity of intermartensitic transformation is also found in other systems like Ni-Mn-Ga, Ni-Mn-Fe-Ga, Ni-Mn-In, Ni-Fe-Ga etc. [58–63]. Since 4L is more favorable structure, the 80% phase fraction of 14L below M_f induces instability in the martensitic phase. Hence, to minimize the free energy of the system, the phase fraction of 4L structure increases once more. The changes of structural phase fractions of 4L and 14L at different temperatures for $x = 0.44$ in both cooling and heating, shown in fig. 5.9. The behaviour is very much similar to $x = 0.40$.

In contrast to $x = 0.40$ and 0.44, for $x = 0.48$ and 0.52 the structural phase fraction (4L $\approx 40\%$ for $x = 0.48$ & 30 % for $x = 0.52$ and 14L $\approx 60\%$ for $x = 0.48$ & 70 % for $x = 0.52$) remains almost

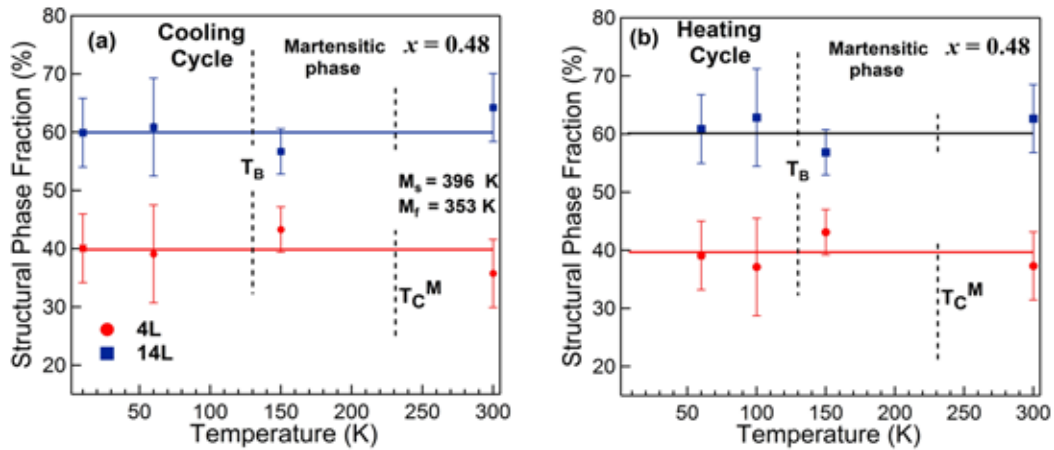


Figure 5.10 4-layered and 14-layered structural phase fraction variation as a function of temperature in martensitic transition region, martensitic phase, and below T_B region of $x = 0.48$ in both (a) cooling and (b) heating.

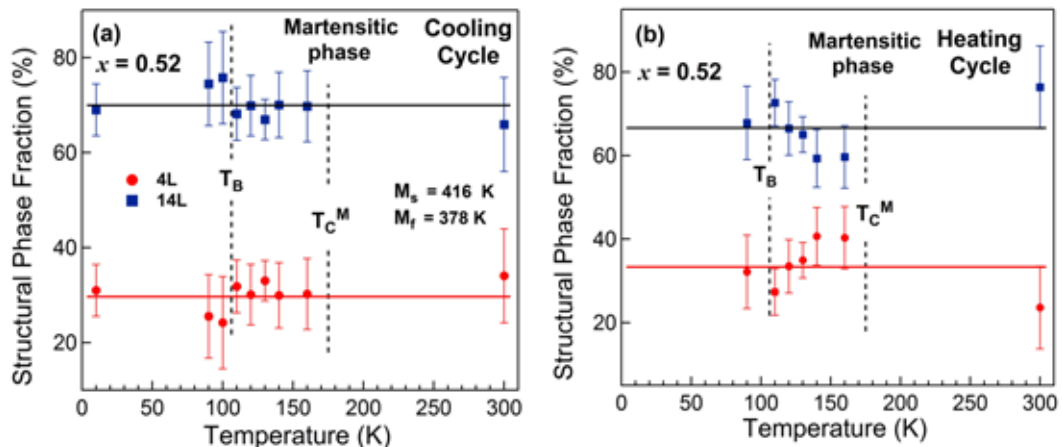


Figure 5.11 4-layered and 14-layered structural phase fraction variation as a function of temperature in martensitic transition region, martensitic phase, and below T_B region of $x = 0.52$ in both (a) cooling and (b) heating.

unchanged over the whole temperature range as evident from fig. 5.10 and fig. 5.11. The $x = 0.48$ and 0.52 alloys are in martensitic phase below 300 K. It remains constant till lowest temperature unlike $x = 0.40$ and 0.44.

5.3.3 Thermo-susceptibility behavior

It is very important to note that the change in phase fraction of 4L and 14L occurs at the temperatures where magnetic phase change also occurs. The thermo-susceptibility behavior in zero field cooled heating (ZFC) for $x = 0.40$ and 0.44 are shown in figs. 5.12 (a) and (b). Between M_s and M_f , the susceptibility decreases. The lowering of susceptibility between $M_s - M_f$ indicates that if there is magneto-structural coupling then the 14L structure possibly strengthens the anti-ferromagnetic exchange interaction that lowers the susceptibility. Below M_f the susceptibility is almost constant. Interestingly, the structural phase fraction is almost constant below M_f . Around T_B susceptibility drops again. This phase is reported to be spin-glass phase [2, 57], that decreases the susceptibility. In this phase, the 4L phase fraction increases and 14L phase fraction decreases. The phase fractions become almost equal \approx around 50 % each. So, the decrease in magnetization at T_B may have structural correspondence.

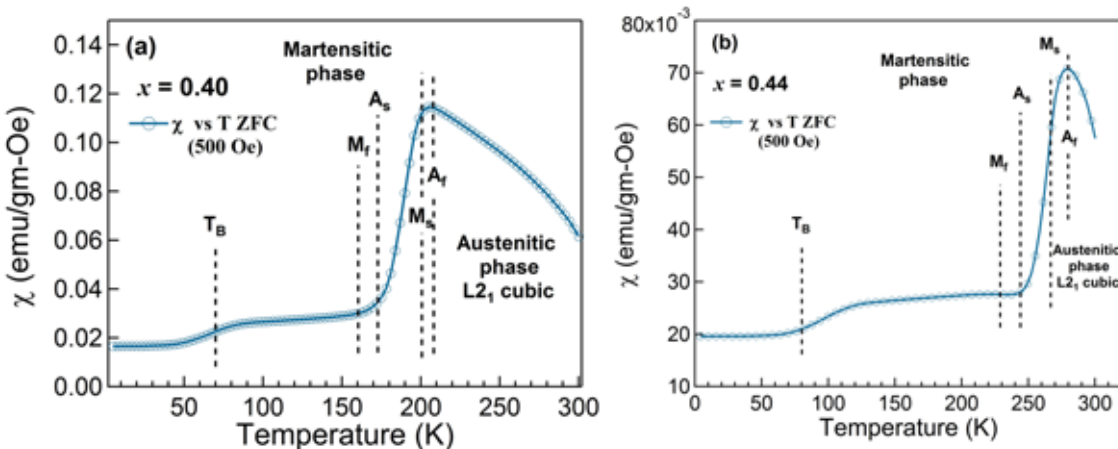


Figure 5.12 Zero-field-cooled-heating thermo-susceptibility variation in martensitic transition region, martensitic phase, and below T_B region of (a) $x = 0.40$ and (b) 0.44 .

The thermo-susceptibility (fig. 5.13) change of $x = 0.48$ and 0.52 do not follow structural changes. For both the alloys, the M_s is around 396 K for $x = 0.48$ and 416 K for $x = 0.52$. The austenite magnetic transition temperature T_C^A is around 320 K. Thus, the structural transition occurs from paramagnetic austenite to paramagnetic martensite. This indicates that there might not be magneto-structural coupling. Although the structure changes, the magnetic state does not change.

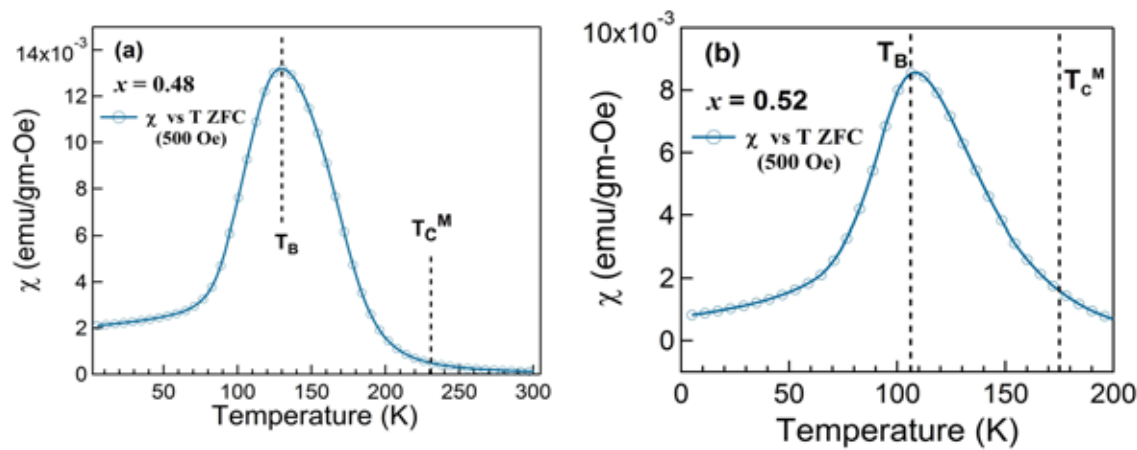


Figure 5.13 Zero-field-cooled-heating thermo-susceptibility variation in martensitic transition region, martensitic phase, and below T_B region of (a) $x = 0.48$ and (b) 0.52.

Below T_C^M , the increase in susceptibility is due to ferromagnetic ordering from paramagnetic phase. Although, below T_B the phase fraction as well as Mn1-Mn2 bond distance remains same, the magnetization decreases. The structural martensitic transition for $x = 0.48$ and 0.52 occurs at 396 K and 416 K, respectively. The structure changes from L2₁ to mixed modulated 4L and 14L. Whereas upon structural transition the magnetic phase change does not occur. The paramagnetic austenitic phase changes to paramagnetic martensitic phase. So, there is no magneto-structural coupling in $x = 0.48$ and 0.52. The coupling does not occur even below T_C^M . Thus, below T_B the decrease in magnetization of $x = 0.48$ and 0.52 has purely magnetic origin.

5.3.4 Magnetic ground state of Mn1-Mn2

In Ni-Mn-Sn off-stoichiometric alloys the bond distance between Mn1 and Mn2 gives rise to the antiferromagnetism [1, 44]. Thus, the bond distance between Mn1-Mn2 is deduced from the structural analysis as mentioned in Table 5.2. Further, the exchange integral between Mn1-Mn2 ($J_{\text{Mn1-Mn2}}$) is calculated as a function of temperature (fig. 5.14) in the cooling cycle. The behavior of exchange interaction is similar even in heating cycle.

The calculation shows that antiferromagnetic exchange interaction exists between Mn1-Mn2 in both 4L and 14L structures. However, the anti-ferromagnetic exchange interaction is stronger in

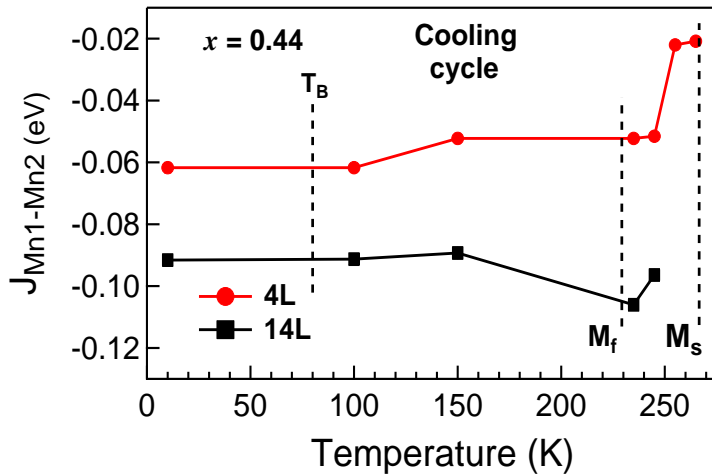


Figure 5.14 Calculated magnetic exchange coupling constant (J) between first nearest neighbour Mn1-Mn2 of $x = 0.50$ using experimentally obtained lattice parameters of $x = 0.44$.

14L than 4L. This is also visible from the Mn1-Mn2 bond distances in Table 5.2 as well as Table 5.3. The 4L and 14L have bond distances less than 3 Å implying anti-ferromagnetic interaction. Also, the Mn1-Mn2 bond distance of 14L is less than that of 4L. Thus, the anti-ferromagnetic interaction in 14L is expected to be stronger than that in 4L. Thus, presence of two structural phases with different strength of antiferromagnetic exchange interaction along with ferromagnetic interaction gives rise to magnetically inhomogeneous phase. Moreover, it is known that the low temperature phase consists of various martensitic variants oriented in different directions derived from high symmetry cubic phase [43]. The variants of orthorhombic 4L and 14L evolve randomly oriented. Thus, the average spin of the variants are also randomly oriented. A diffuse anti-ferromagnetic phase starts to develop below M_s and becomes strong enough below T_B (or T_f) to cause the spin freezing [57]. The temperature variation of Mn1-Mn2 bond distance and corresponding exchange integral of 4L and 14L of $x = 0.40$ is similar to $x = 0.44$. Thus, the re-entrant spin-glass like magnetic phase of Ni-Mn-Sn is obtained as reported in Ref. [57]. However, for $x = 0.48$ and 0.52, the Mn1-Mn2 bond-distances remains constant throughout the temperature range upto 10K in the martensitic phase. Consequently, anti-ferromagnetic exchange interactions in 4L

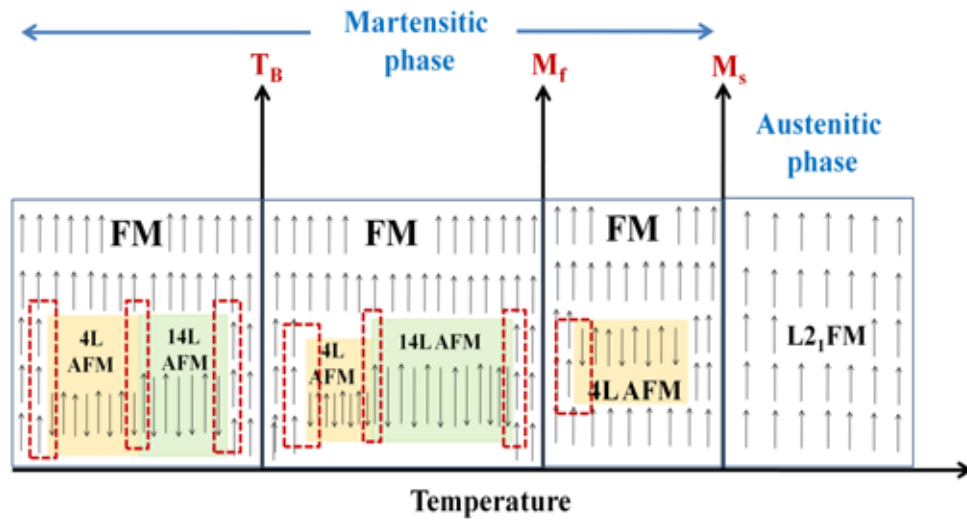


Figure 5.15 Schematic representation of evolution of 4L and 14L phase with coexisting ferromagnetic and antiferromagnetic magnetic phases from L₂₁ phase of $x = 0.40$ and 0.44 .

and 14L phase have no temperature variations below T_C^M . A schematic representation of evolution of 4L and 14L phase with coexisting ferromagnetic and anti-ferromagnetic magnetic phases has been shown in fig. 5.15. The length of the spins in antiferromagnetic domains represent the strength of the antiferromagnetic magnetic exchange interaction. In the martensitic phase, different interfaces between ferromagnetic and antiferromagnetic domains are identified by the dotted regions. In between M_s and M_f , an interface of ferromagnetic and 4L antiferromagnetic is formed. Furthermore, ferromagnetic-4L antiferromagnetic interface, ferromagnetic-14L antiferromagnetic interface and 4L antiferromagnetic-14L antiferromagnetic interface are formed in between M_f and T_B . Here the bigger size of the 14L antiferromagnetic domain represents that 14L phase fraction is more than the 4L phase fraction. Below T_B , the 4L and 14L phase fraction becomes almost 50 %. Moreover, the exchange interaction strength is different at different interfaces. These competing exchange interactions result in spin-glass state which gives rise to exchange bias effect below a certain low temperature, called the blocking temperature T_B .

5.3.5 Crystal structure effect on electronic structure

Understanding electronic structure can help to understand the origin of martensitic structural transition and magnetic properties. Now whether the experimental electronic structure at different temperatures capture the theoretically calculated electronic structure or not, needs to be verified. This will establish the cause of martensitic transition strongly. Electronic structure can be examined by photoelectron spectroscopy experiment and *ab-initio* first principle density functional calculation. However, the detailed density of states of individual atomic orbitals in valence band can not be obtained by photoelectron spectroscopy experiment. Thus, to verify the electronic structure experimentally the experimental crystal lattice parameters of $x = 0.40$ at different temperatures are considered for theoretical calculation. The bond-lengths, thus obtained, is compared with bond-lengths obtained at 0 K as discussed in Chapter 4. Also, the spin integrated total density states obtained using experimental lattice parameters at different temperatures is compared with experimentally obtained high resolution valence band spectra.

In Chapter 4 the martensitic transformation in $\text{Ni}_2\text{Mn}_{1+x}\text{Sn}_{1-x}$ alloys has been investigated within *ab-initio* density functional theory. Martensitic transition happening beyond $x = 0.36$ is captured within these calculations. The reason behind the martensitic transition is increased Ni-Mn hybridization, which results from the Ni atom experiencing a resultant force along a lattice vector and moves towards the Mn atoms above a critical concentration. Additionally the presence of the lone pair electrons on Sn forces the movement of Ni atoms away from Sn. The change in density of states due to martensitic transformation is also observed.

In the experimentally obtained crystal structures at different temperatures, the ionic positions have been relaxed keeping the experimental crystal volume fixed. The ionic relaxed structures indicating the Ni-Mn1, Ni-Mn2 and Ni-Sn bond-distances at different temperatures have been shown in fig. 5.16, fig. 5.17 and listed in Table 5.4. It is observed that at different temperatures, the average Ni-Mn2 bond-lengths are less than Ni-Mn1. The average Ni-Mn bond-distances decrease compared to average Ni-Sn bond-distances. Similar trend of decrease of Ni-Mn bond-distances of Mn1-Mn2 plane region has been found by theoretical calculations in both austenitic phase and

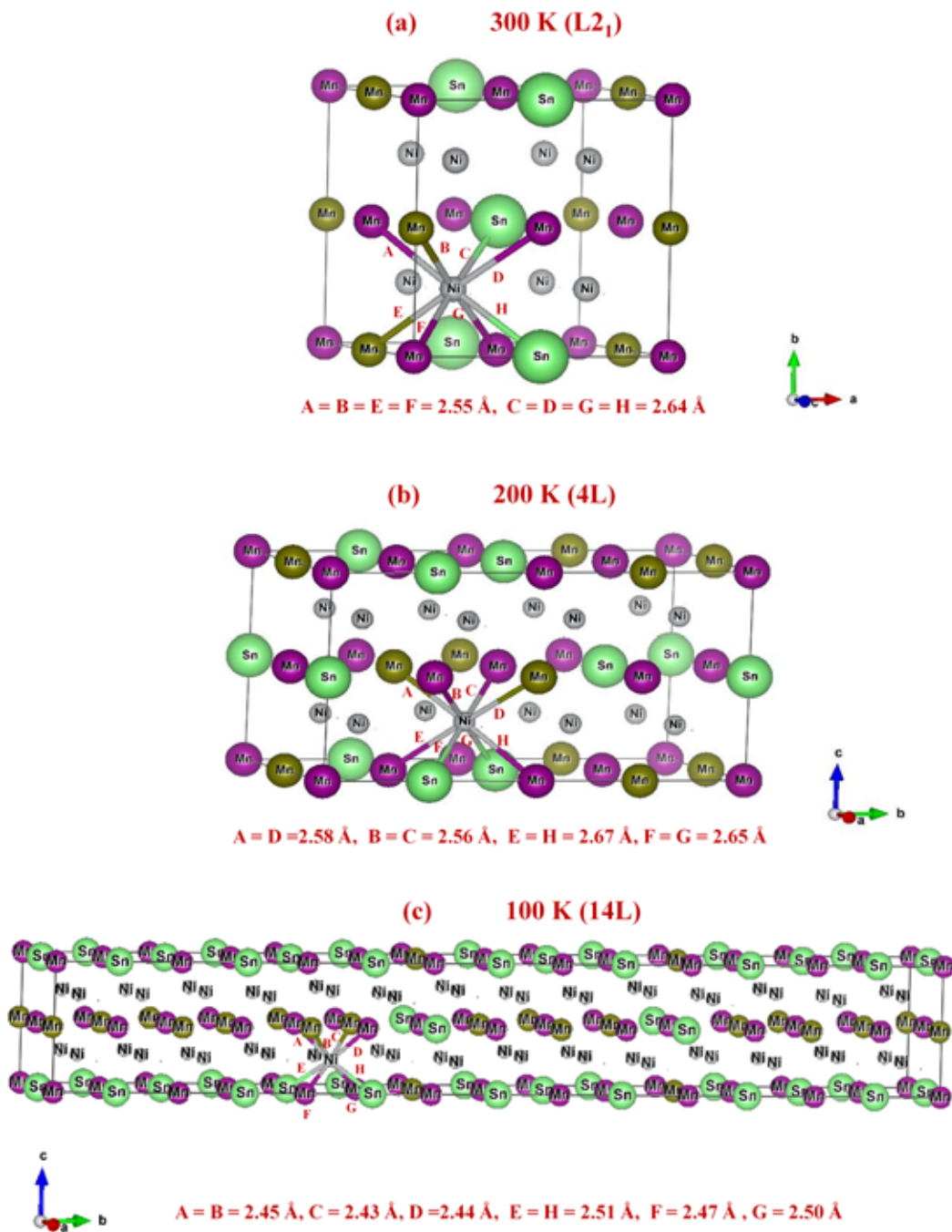


Figure 5.16 Crystal structure of $x = 0.50$ composition having experimentally obtained lattice parameters of $x = 0.40$ at (a) 300 K, (b) 200 K and (c) 100 K indicating Ni-Mn1, Ni-Mn2 and Ni-Sn bond-lengths.

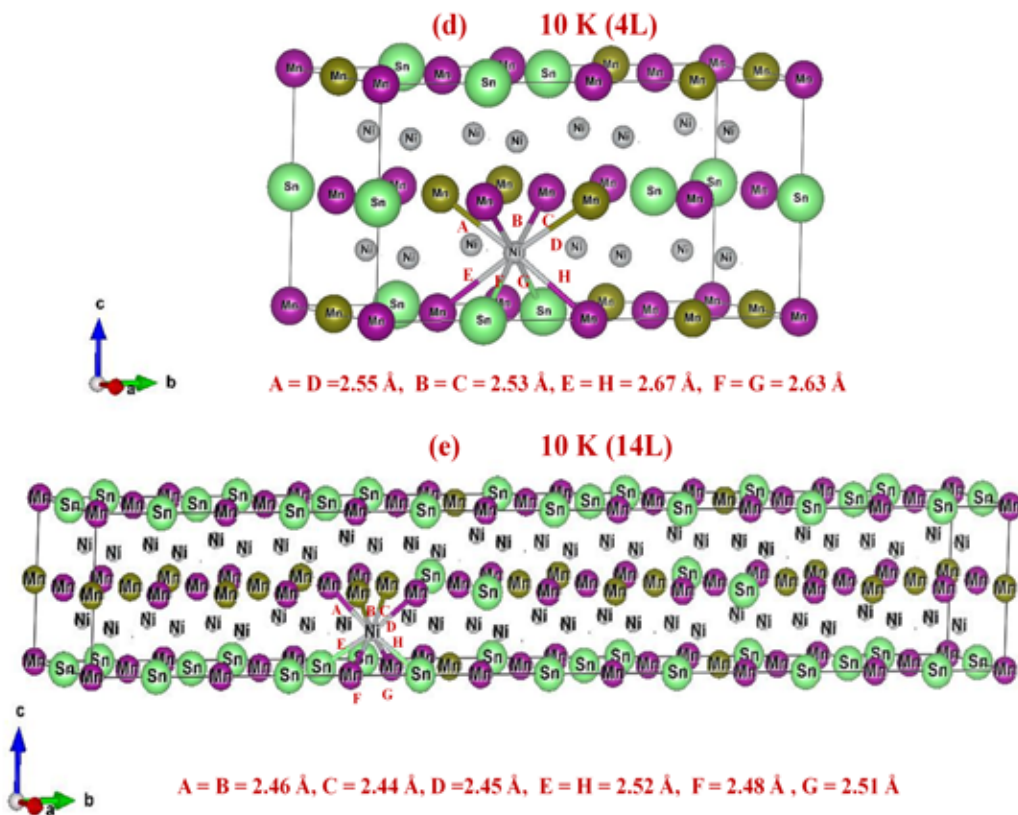


Figure 5.17 Crystal structure of $x = 0.50$ composition having experimentally obtained lattice parameters of (d) 4L and (e) 14L of $x = 0.40$ at 10 K indicating Ni-Mn1, Ni-Mn2 and Ni-Sn bond-lengths.

Table 5.4 Nearest neighbor Ni-Mn1, Ni-Mn2 and Ni-Sn bond-lengths of $x = 0.50$ composition considering different structural phases at various temperatures in cooling cycle of $x = 0.40$.

Temperature (K)	Structural phase	Ni-Mn1 bond length (\AA)	Ni-Mn2 bond length (\AA)	Ni-Sn bond length (\AA)
300	L2 ₁	2.55-2.64	2.55	2.64
200	4L	2.56-2.67	2.58	2.65
100	14L	2.44-2.50	2.43-2.45	2.51
10	4L	2.53-2.67	2.55	2.63
	14L	2.45-2.51	2.44-2.46	2.52

martensitic phase, starting from optimized cubic structure, which is discussed in Chapter 4. This is due to increased Ni-Mn hybridization at the Mn1-Mn2 plane. This makes the structure unstable in cubic phase. The increase of Ni-Sn bond-distance explains the existence of repulsive interaction between Sn 5s electrons and electrons of neighboring atoms which gives rise to structural transformation from cubic phase to 4L phase. The 4L structure further transforms to 14L structure to reduce the average strain in the system.

It is important to mention that the change in atomic bond-distances accounts for the change in orbital hybridization which initiates the change in electronic structure of atomic orbital. In fig. 5.18, the experimentally obtained high resolution valence band spectra by ultraviolet photoelectron spectroscopy (UPS) ($h\nu = 21.2$ eV) at different temperatures are shown for $x = 0.40$ composition [64]. Interestingly, a notable change is observed in shape of valence band with temperature. The change in valence band shape is also observed within the martensitic phase at different temperatures. In austenitic phase, the spectral weight is mainly around 1 eV and 1.6 eV. Below M_s , the average spectral weight is around 1.3 eV. Below T_B , the spectral weight is again averaged around 1 eV and 1.6 eV. The change in shape of valence band might be related to redistribution of density of states with phase fraction of 4L and 14L. Similar change in shape of valence band has also been observed for other compositions [64].

To understand the redistribution of density of states in experimental electronic structure, total density of states of $x = 0.50$ composition considering different structural phases at various temperatures in cooling cycle of $x = 0.40$ are calculated by *ab-initio* density functional theory and convoluted with experimental broadening factors. Then it is multiplied with Fermi function at the measurement temperature and convoluted with a Voigt function to compare with experimental valence band [65]. The half width at half maximum accounts for Gaussian component of the Voigt function. The energy-dependent Lorentzian full width half maximum that represents the lifetime broadening is $0.1(E-E_F)$. Therefore spin integrated total density of states for different experimentally obtained structures at different temperatures of $x = 0.40$ has been compared with experimentally obtained UPS-valence band spectra in fig. 5.18.

The partial DOS of Ni *d*, Mn1 *d*, Mn2 *d* and Sn *p* have been depicted in fig. 5.19. The feature

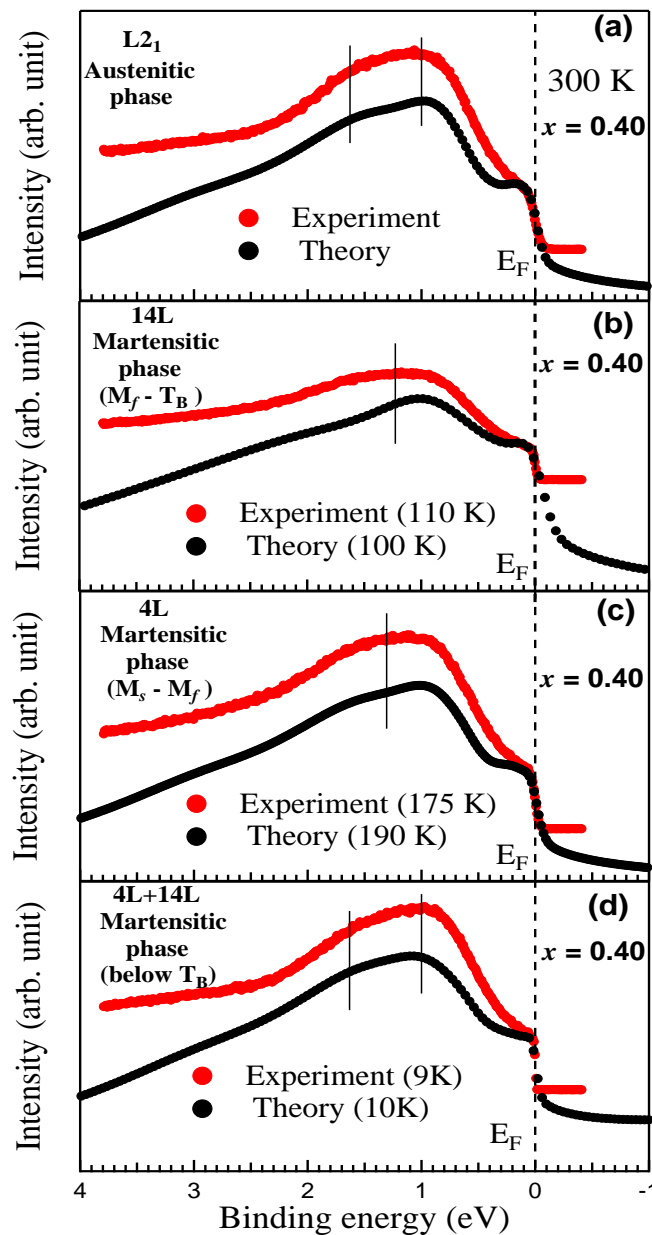


Figure 5.18 Valence band spectra comparison of $x = 0.40$ with convoluted theoretically obtained density of states of $x = 0.50$ at different temperatures. The experimental data is taken from Ref [64]. The Fermi energy E_F is at 0 eV.

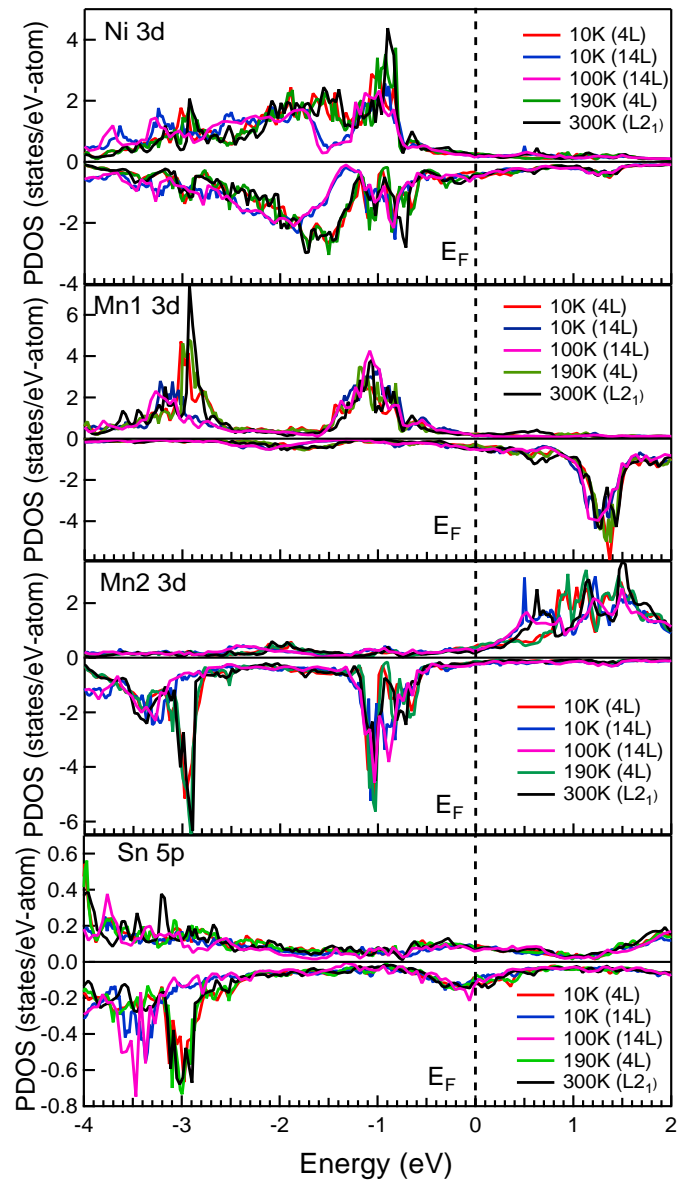


Figure 5.19 Partial density of states variation of Ni 3d, Mn1 3d, Mn2 3d and Sn 5p of $x = 0.40$ at different temperatures. The Fermi energy E_F is at 0 eV. The upper/lower panel is for the majority/minority spin channel.

at 1.0 eV has dominant Ni *d* and Mn *d* character. These are hybridized Ni 3*d* - Mn1 3*d* and Ni 3*d* - Mn2 3*d* states. The feature at 1.6 eV has mainly Ni 3*d* character. After martensitic transition, the Ni *d* density of states at 1 eV decreases and redistributes over an energy range 1 eV to 2 eV. While 14L lacks Ni 3*d* density of states over energy range 1.2 eV to 1.5 eV, the 4L density of states is dominant over this energy range. The Mn1 3*d* majority spin channel density of states spans over energy range 0.5 eV to 1.6 eV. The Mn2 3*d* minority spin channel density of states is distributed over the energy range 0.4 eV to 1.3 eV. Thus, as a function of temperature and depending on the phase fraction of 4L and 14L, the shape of valence band also changes.

5.4 Conclusion

In the martensitic phase the co-existence of two crystal structures (4L and 14L orthorhombic structures), change in crystal structure phase fraction with magnetic transition, co-existence of ferromagnetic and anti-ferromagnetic magnetic domains, and different strength of antiferromagnetic coupling gives rise to structurally and magnetically frustrated martensitic phase that causes spin-glass-like behavior of $\text{Ni}_2\text{Mn}_{1+x}\text{Sn}_{1-x}$ ($x = 0.40$ and 0.44) and lead to exchange bias phenomena under ZFC. Thus, the ZFC exchange bias in Ni-Mn-Sn alloys is related to the crystal structure of martensite. The Sn lone pair effect on the martensitic transition is established using experimental crystal structure parameters also.

Moreover, the change in valence band shape due to temperature variation in experimental electronic structure has been captured by *ab-initio* density functional theory. The redistribution of density of states due to 4L and 14L phase fraction change gives rise to valence band shape change.

Bibliography

- [1] T. Krenke, E. Duman, M. Acet, E. F. Wassermann, X. Moya, L. Mañosa, and A. Planes, *Nat. Mater.* **4**, 450 (2005).
- [2] S. Singh and C. Biswas, *Appl. Phys. Lett.* **98**, 212101 (2011).
- [3] R. Kainuma, Y. Imano, W. Ito, Y. Sutou, H. Morito, S. Okamoto, O. Kitakami, K. Oikawa, A. Fujita, T. Kanomata, and K. Ishida, *Nature (London)* **439**, 957 (2006).
- [4] B. M. Wang, Y. Liu, P. Ren, B. Xia, K. B. Ruan, J. B. Yi, J. Ding, X. G. Li, and L. Wang, *Phys. Rev. Lett.* **106**, 077203 (2011).
- [5] H. E. Karaca, I. Karaman, B. Basaran, Y. Ren, Y. I. Chumlyakov, and H. J. Maier, *Adv. Funct. Mater.* **19**, 983 (2009).
- [6] D.C. Jiles, and C.C.H. Lo, *Sens. Actuators, A* **106**, 3 (2003).
- [7] C. Felser, G. H. Fecher (Eds.), *Spintronics*, Springer Netherlands, Dordrecht, 2013.
- [8] M. Ohkoshi, K. Tamari, M. Harada, S. Honda, and T. Kusuda, *IEEE Transl. J. Magn. Japan* **1**, 37 (1985).
- [9] A. A. Glazer, A. P. Potapov, and R. I. Tagirov, *Sov. Phys. JETP. Lett.* **15**, 259 (1972).
- [10] W. H. Meiklejohn and C. P. Bean, *Phys. Rev.* **102**, 1413 (1956).
- [11] K. A. Kilian and R. H. Victora, *J. Appl. Phys.* **87**, 7064 (2000).

- [12] H. Mori, Y. Odahara, D. Shigyo, T. Yoshitake, and E. Miyoshi, *Thin Solid Films* **520**, 4979 (2012).
- [13] L. Bainsla and K. G. Suresh, *Appl. Phys. Rev.* **3**, 031101 (2016).
- [14] K. Nikolaev, P. Anderson, P. Kolbo, D. Dimitrov, S. Xue, X. Peng, T. Pokhil, H. Cho, and Y. Chen, *J. Appl. Phys* **103**, 07F533 (2008).
- [15] M. Ali, P. Adie, C. H. Marrows, D. Greig, B. J. Hickey, and R. L. Stamps, *Nature Mater.* **6**, 70 (2007).
- [16] S. Giri, M. Patra, and S. Majumdar, *J. Phys.: Condens. Matter* **23**, 073201 (2011).
- [17] W. A. Razzaq and J. S. Kouvel, *J. Appl. Phys.* **55**, 1623 (1984).
- [18] W. C. Cain and M. H. Kryder, *J. Appl. Phys.* **67**, 5722 (1990).
- [19] A. K. Nayak, M. Nicklas, S. Chadov, C. Shekhar, Y. Skourski, J. Winterlik, and C. Felser, *Phys. Rev. Lett.* **110**, 127204 (2013).
- [20] T. Maity, S. Goswami, D. Bhattacharya, and S. Roy, *Phys. Rev. Lett.* **110**, 107201 (2013).
- [21] S. Chauhan, S. K. Srivastava, and R. Chandra, *Appl. Phys. Lett.* **103**, 042416 (2013).
- [22] J. K. Murthy and A. Venimadhav, *Appl. Phys. Lett.* **103**, 252410 (2013).
- [23] A. Sadhu and S. Bhattacharyya, *J. Phys. Chem. C* **117**, 26351 (2013).
- [24] S. Lin, D. F. Shao, J. C. Lin, L. Zu, X. C. Kan, B. S. Wang, Y. N. Huang, W. H. Song, W. J. Lu, P. Tong, and Y. P. Sun, *J. Mater. Chem. C* **3**, 5683 (2015).
- [25] L. G. Wang, C. M. Zhu, Z. M. Tian, H. Luo, D. L. G. C. Bao, and S. L. Yuan, *Appl. Phys. Lett.* **107**, 152406 (2015).
- [26] D. Deng, J. Zheng, D. Yu, B. Wang, D. Sun, M. Avdeev, Z. Feng, C. Jing, B. Lu, W. Ren, S. Cao, and J. Zhang, *Appl. Phys. Lett.* **107**, 102404 (2015).

- [27] C. Shang, S. Guo, R. Wang, Z. Sun, H. Xiao, L. Xu, C. Yang, and Z. Xia, *Sci. Rep.* **6**, 25703 (2016).
- [28] B. M. Wang, Y. Liu, B. Xia, P. Ren, and L. Wang, *J. Appl. Phys.* **111**, 043912 (2012).
- [29] Z. D. Han, B. Qian, D. H. Wang, P. Zhang, X. F. Jiang, C. L. Zhang, and Y. W. Du, *Appl. Phys. Lett.* **103**, 172403 (2013).
- [30] P. Liao, C. Jing, X. L. Wang, Y. J. Yang, D. Zheng, Z. Li, B. J. Kang, D. M. Deng, S. X. Cao, J. C. Zhang, and B. Lu, *Appl. Phys. Lett.* **104**, 092410 (2014).
- [31] Y. Sutou, Y. Imano, N. Koeda, T. Omori, R. Kainuma, K. Ishida, and K. Oikawa, *Appl. Phys. Lett.* **85**, 4358 (2004).
- [32] T. Krenke, M. Acet, E. F. Wassermann, X. Moya, L. Mañosa, and A. Planes, *Phys. Rev. B* **72**, 014412 (2005).
- [33] T. Krenke, M. Acet, E. F. Wassermann, X. Moya, L. Mañosa, and A. Planes, *Phys. Rev. B* **73**, 174413 (2006).
- [34] B. Hernando, J. L. S. Llamazares, J. D. Santos, Ll. Escoda, J. J. Suñol, R. Varga, D. Baldomir, and D. Serantes, *Appl. Phys. Lett.* **92**, 042504 (2008).
- [35] K. R. Priolkar, D. N. Lobo, P. A. Bhobe, S. Emura, and A. K. Niga, *Europhys. Lett.* **94**, 38006 (2011).
- [36] M. Khan, J. Jung, S. S. Stoyko, A. Mar, A. Quetz, T. Samanta, I. Dubenko, N. Ali, S. Stadler, and K. H. Chow, *Appl. Phys. Lett.* **100**, 172403 (2012).
- [37] H. C. Xuan, Q. Q. Cao, C. L. Zhang, S. C. Ma, S. Y. Chen, D. H. Wang, and Y. W. Du, *Appl. Phys. Lett.* **96**, 202502 (2010).
- [38] M. Khan, I. Dubenko, S. Stadler, J. Jung, S. S. Stoyko, A. Mar, A. Quetz, T. Samanta, N. Ali, and K. H. Chow, *Appl. Phys. Lett.* **102**, 112402 (2013).

- [39] H. Luo, G. Liu, Z. Feng, Y. Li, L. Ma, G. Wu, X. Zhu, C. Jiang, and H. Xu, *J. Magn. Magn. Mater.* **321**, 4063 (2009).
- [40] G. D. Liu, X. F. Dai, H. Y. Liu, J. L. Chen, Y. X. Li, G. Xiao, and G. H. Wu, *Phys. Rev. B* **77**, 014424 (2008).
- [41] S. Pal, S. Sarkar, S. K. Pandey, C. Maji, and P. Mahadevan, *Phy. Rev. B* **94**, 115143 (2016).
- [42] P. J. Brown, A. P. Gandy, K. Ishida, R. Kainuma, T. Kanomata, K. U. Neumann1, K. Oikawa, B. Ouladdiaf, and K. R. A. Ziebeck, *J. Phys.: Condens. Matter* **18**, 2249 (2006).
- [43] H. Zheng, W. Wang, S. Xue, Q. Zhai, J. Frenzel, and Z. Luo, *Acta Mater.* **61**, 4648 (2013).
- [44] S. Pal, P. Mahadevan, and C. Biswas, *AIP Conf. Proc.* **1591**, 58 (2014).
- [45] M. Ye, A. Kimura, Y. Miura, M. Shirai, Y. T. Cui, K. Shimada, H. Namatame, M. Taniguchi, S. Ueda, K. Kobayashi, R. Kainuma, T. Shishido, K. Fukushima, and T. Kanomata, *Phys. Rev. Lett.* **104**, 176401 (2010).
- [46] T. Kanomata, K. Fukushima, H. Nishihara, R. Kainuma, W. Itoh, K. Oikawa, K. Ishida, K. -U. Neumann, and K. R. A. Ziebeck, *Mater. Sci. Forum* **583**, 119 (2008).
- [47] V. V. Sokolovskiy, V. D. Buchelnikov, M. A. Zagrebin, P. Entel, S. Sahool, and M. Ogura, *Phys. Rev. B* **86**, 134418 (2012).
- [48] G. Kresse and J. Furthmüller, *Phys. Rev. B* **54**, 11169 (1996).
- [49] P. A. Bhobe, K. R. Priolkar, and P. R. Sarode, *J. Phys.: Condens. Matter* **20**, 015219 (2008).
- [50] J. D. Santos, T. Sanchez, P. Alvarez, M. L. Sánchez, J. L. Sánchez Llamazares, B. Hernando, Ll. Escoda, J. J. Suñol, and R. Varga, *J. Appl. Phys.* **103**, 07B326 (2008).
- [51] B. Hernando, J. L. Sánchez Llamazares, J. D. Santos, M. L. Sánchez, Ll. Escoda, J. J. Suñol, R. Varga, C. García, J. González, *J. Magn. Magn. Mater.* **321**, 763 (2009).

- [52] P. J. Brown, J. Crangle, T. Kanomata, M. Matsumoto, K. U. Neumann, B. Ouladdiaf, and K. R. A. Ziebeck, *J. Phys.: Condens. Matter* **14**, 10159 (2002).
- [53] R. Ranjan, S. Banik, S. R. Barman, U. Kumar, P. K. Mukhopadhyay, and D. Pandey, *Phys. Rev. B* **74**, 224443 (2006).
- [54] K. Oikawa, W. Ito, Y. Imano, Y. Sutou, R. Kainuma, K. Ishida, S. Okamoto, O. Kitakami, and T. Kanomata, *Appl. Phys. Lett.* **88**, 122507 (2006).
- [55] V. V. Khovaylo, T. Kanomata, T. Tanaka, M. Nakashima, Y. Amako, R. Kainuma, R. Y. Umetsu, H. Morito, and H. Miki, *Phys. Rev. B* **80**, 144409 (2009).
- [56] W. Ito, Y. Imano, R. Kainuma, Y. Sutou, K. Oikawa, and K. Ishida, *Metall. Mater. Trans. A* **38**, 759 (2007).
- [57] S. Chatterjee, S. Giri, S. K. De, and S. Majumdar, *Phys. Rev. B* **79**, 092410 (2009).
- [58] C. Seguí, E. Cesari, and J. Pons, *Adv. Mater. Res.* **52**, 47 (2008).
- [59] K. Koho, O. Söderberg, N. Lanska, Y. Ge, X. Liu, L. Straka, J. Vimpari, O. Heczko, and V.K. Lindroos, *Mat. Sci. Eng. A* **378**, 384 (2004).
- [60] Y. J. Huang, Q. D. Hu, J. Liu, L. Zeng, D. F. Zhang, and J. G. Li, *Acta Mater.* **61**, 5702 (2013).
- [61] W. H. Wang, Z. H. Liu, J. Zhang, J. L. Chen, G. H. Wu, W. S. Zhan, T. S. Chin, G. H. Wen, and X. X. Zhang, *Phys. Rev. B* **66**, 052411 (2002).
- [62] C. Seguí, J. Pons, and E. Cesari, *Acta Mater.* **55**, 1649 (2007).
- [63] R. F. Hamilton, H. Sehitoglu, C. Efstatheou, and H. J. Maier, *Acta Mater.* **55**, 4867 (2007).
- [64] Dr. Sandeep Singh, PhD thesis, “*Properties of Ni-Mn based Heusler alloys with Martensitic Transition*”, 2014.

- [65] A. Chakrabarti, C. Biswas, S. Banik, R. S. Dhaka, A. K. Shukla, and S. R. Barman, Phys. Rev. B **72**, 073103 (2005).

Chapter 6

Electronic structure of $\text{Ni}_2\text{Mn}_{1+x}\text{In}_{1-x}$ and Co doped $\text{Ni}_2\text{Mn}_{1+x}\text{In}_{1-x}$

6.1 Introduction

Till now it has been observed that unlike Ni-Mn-Ga, Ni-Mn-Sn Heusler alloys undergo martensitic transformation only for offstoichiometric compositions. The underlying mechanism of martensitic transformation of Ni-Mn-Ga and Ni-Mn-Sn has been discussed in detail in previous chapters. Another member of this Ni-Mn series is Ni-Mn-In system. It shows significant differences in the magnetic properties from other Ni-Mn-based Heusler alloys. In off-stoichiometric $Ni_2Mn_{1+x}In_{1-x}$ the magnetic exchange between Mn at parent Mn site (Mn1) and doped Mn at In site (Mn2) is ferromagnetic in nature in the austenitic phase [1, 2]. However, the Mn1 and Mn2 magnetic interaction is antiferromagnetic in $Ni_2Mn_{1+x}Ga_{1-x}$ [3, 4] and $Ni_2Mn_{1+x}Sn_{1-x}$ [5, 6]. Interestingly, in the martensitic phase the magnetic exchange between Mn1 and Mn2 becomes antiferromagnetic in $Ni_2Mn_{1+x}In_{1-x}$ [1, 2, 7] while it remains antiferromagnetic for $Ni_2Mn_{1+x}Ga_{1-x}$ and $Ni_2Mn_{1+x}Sn_{1-x}$. This unusual behaviour in the magnetic properties of $Ni_2Mn_{1+x}In_{1-x}$ compared to $Ni_2Mn_{1+x}Ga_{1-x}$ and $Ni_2Mn_{1+x}Sn_{1-x}$ originates from the change of Mn-Mn interatomic distances upon martensitic transformation.

Moreover, till date the origin of martensitic transformation has been discussed as arising from the enhanced Ni-Mn hybridization in off-stoichiometric alloys [8]. This leads to the energy shift of the Ni 3d states toward the Fermi level and one finds a reduction in density of states in the vicinity of the Fermi energy (E_F) in the martensitic phase arising from a degeneracy lifting of the Ni 3 d_{eg} states. The $d_{3z^2-r^2}$ states moves to lower energies compared to $d_{x^2-y^2}$ states in the martensitic phase [9]. This degeneracy lifting lowers the total energy, thereby stabilizing the martensitic phase. This phenomenon is associated with band Jahn-Teller effect. This happens beyond a particular Mn doping concentration ($x \geq 0.36$) [1]. Thus, usual explanation for martensitic transformation in off-stoichiometric Ni-Mn based Heusler alloys has been discussed as the increased hybridization between the Ni 3d and Mn 3d states. However this should be present in the stoichiometric composition also, and this idea does not explain why martensitic transition is not obtained there. This then calls for a detailed investigation of the underlying mechanism to understand the driving force for the martensitic transformation. In this chapter the origin of the martensitic transformation has

been explained considering several compositions of $\text{Ni}_2\text{Mn}_{1+x}\text{In}_{1-x}$.

Moreover, Co doped Ni-Mn-X (X = Sn, In) Heusler alloys have attracted recent interest due to their multifunctional properties [10–13]. The substitution of Co in these alloys enhances both the Curie temperature and the magnetization in austenitic phase, while the magnetic moment of the martensitic phase decreases [10]. Hence, the large difference in magnetization between austenitic phase and martensitic phase leads to giant inverse magnetocaloric effect [14, 15], giant magnetoresistance [16, 17]. In Co_2MnSn exchange interaction between Co-Mn is several times larger than the Ni-Mn exchange interaction in Ni_2MnSn [18]. Thus, when Co is doped at Ni-Mn based ternary Heusler alloy the fundamental question arises about its site preference and distribution tendency, which helps in understanding the enhanced Curie temperature and magnetization of the system. This chapter investigates the site preference, distribution tendency, structural and magnetic ground states of doped Co in stoichiometric Ni_2MnIn as well as $\text{Ni}_{1.625}\text{Co}_{0.375}\text{Mn}_{1.5}\text{In}_{0.5}$.

6.2 Computational Details

Ab-initio electronic structure calculations are carried out using density functional theory (DFT) as implemented in the Vienna *ab-initio* simulation package (VASP) [19]. We use the projector augmented wave implementation and work with the generalized gradient approximation (GGA) Perdew-Wang [20] for the exchange correlation functional. This has been seen to give a better description of the magnetism and crystal structure in Heusler compounds [21] in our GGA calculations compared to the LDA calculations. In off-stoichiometric $\text{Ni}_2\text{Mn}_{1+x}\text{In}_{1-x}$ ($x = 0.25, 0.375, 0.50$) the Mn at parent site is labelled Mn1 while the Mn doped at In site has been labelled Mn2. The magnetic interaction between Ni, Mn1 & Mn2 are ferromagnetic in austenitic phase. However, in martensitic phase the interaction between Mn1 and Mn2 is antiferromagnetic, while that between Ni and Mn1 is ferromagnetic. Monkhorst-Pack k-points mesh of $12 \times 12 \times 12$ for 16 atom $\text{L}2_1$ unit cell and $12 \times 6 \times 10$ for 4O, $12 \times 2 \times 10$ for 10M & for 14M modulated structure are used to perform the k space integrations and a cut-off energy of 270 eV was used to determine the plane-waves used in the basis. The lattice parameters of the unit cell as well as the ionic positions have

been optimised in each of the cases considered and the optimised value is mentioned in the text. An analysis of the electronic structure has been carried out in terms of the band dispersions as well as the partial density of states (PDOS) calculated using spheres of radii $\sim 1.4 \text{ \AA}$ around each atom. Additionally an analysis of the electronic structure has been carried out using an interface of VASP to WANNIER90 [22–24]. A basis consisting of Ni *s* and *d*, Mn *s* and *d* as well as In *p* states. A mapping of the Blöch states is made onto Wannier functions, localized on the respective atoms with their angular parts given by the relevant spherical harmonics, via a unitary transformation. A unique transformation is obtained with the requirement of minimizing the quadratic spread of the Wannier functions. The criterion of convergence was that the spread changed by less than 10^{-6} between successive iterations. Once the transformation matrices are determined, one has a tight binding representation of the Hamiltonian in the basis of the maximally localized Wannier functions.

For Ni-Co-Mn-In k-points mesh of $12 \times 12 \times 12$ and a plane wave cutoff energy 450 eV were used in the calculations and total energy was found to be converged within 5 meV using these parameters. For different Co concentrations structural optimization has been carried out to find out the equilibrium magnetic and crystal structure.

6.3 Results and Discussions

6.3.1 Electronic structure of $\text{Ni}_2\text{Mn}_{1+x}\text{In}_{1-x}$

Origin of martensitic transformation of $\text{Ni}_2\text{Mn}_{1+x}\text{In}_{1-x}$

The experimentally reported unit cell of Ni_2MnIn is cubic with a lattice parameter of 6.07 \AA [1]. Carrying out an optimization of the lattice parameter within our calculations, the theoretical lattice parameter is also found to be 6.07 \AA and the structure remains cubic which is shown in fig. 6.1 (a). Thus theoretical calculations give a good description of the lattice parameter. The variation of the ground state energy (per unit cell) as a function of the axial ratio, c/a of Ni_2MnIn has been shown in fig. 6.1 (b) which reveals that the ground state energy of the system has the lowest energy at c/a

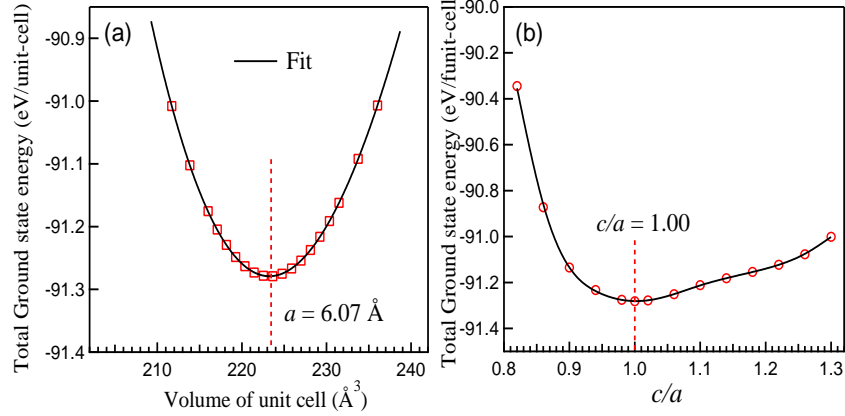


Figure 6.1 (a) Volume optimization in Cubic L₂1 phase and (b) the ground state energy (per unit cell) as a function of the axial ratio, c/a of Ni₂MnIn.

= 1. This implies that the cubic structure is the most favorable structure of Ni₂MnIn which shows no martensitic transformation.

The distances between Ni and Mn as well as between Ni and In are found to be 2.63 Å. These distances are similar to what is found in Ni₂MnSn. However, it should be noted that the Ni-Mn and Ni-In bond-distances are significantly shorter and equal to 2.51 Å in Ni₂MnGa and this system is found to undergo a structural transformation in contrast to Ni₂MnSn and Ni₂MnIn. Thus the *p* element plays an important role in the structural transformations.

In order to understand this further we examine the atom and orbital projected partial density of states which is shown in fig. 6.2. Ni *d* states are found to contribute in the energy window -4 to 2 eV, which is also the energy window in which Mn 3*d* states contribute. In 5*p* states are found to have a low weight in the same energy window. Examining the Mn *d* partial density of states, one finds that the majority spin states are completely filled while the minority spin states are empty, indicating a *d*⁵ configuration at the Mn site. The exchange splitting of the Mn *d* states and the Ni *d* states are found to be in the same direction. In 5*s* states are localized and are found to contribute in the energy interval -6 to -10 eV below the Fermi level, with low weight in the unoccupied part. These states have been referred to as lone pair states as they are not involved in any bonding with the neighboring atoms. Due to this lone pair effect of In 5*s* electrons the electron

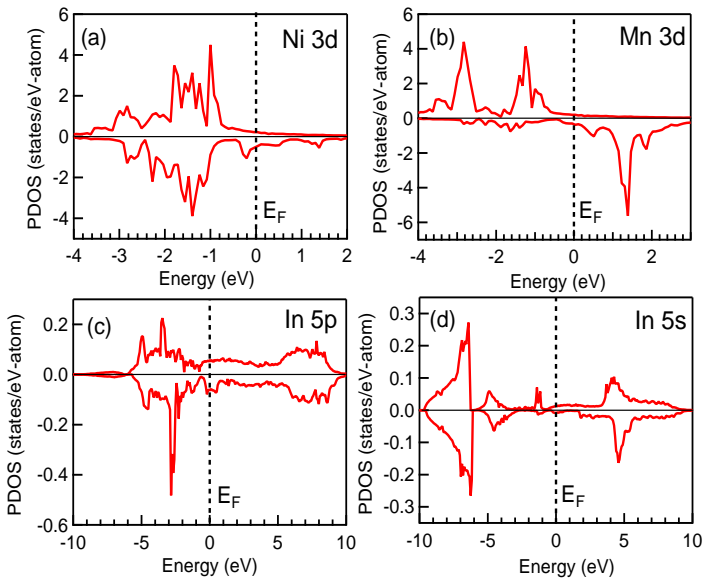


Figure 6.2 Atom and angular momentum projected partial density of states for (a) Ni 3d, (b) Mn 3d, (c) In 5p, and (d) In 5s in the parent compound Ni_2MnIn in cubic phase. The Fermi energy (E_F) is at 0 eV. The upper/lower panel is for the majority/minority spin channel.

clouds of neighboring Ni and Mn atoms feel a repulsion in all directions in a uniform manner. The comparison of charge density plot of Ga 4s and In 5s along Ni has been shown in fig. 6.3. The charge density of Ga 4s electrons is higher than that of In 5s electrons at Ni site. Thus the electron lone pair repulsion is also higher for Ga than In.

Now to understand the martensitic transformation in off-stoichiometric $\text{Ni}_2\text{Mn}_{1+x}\text{In}_{1-x}$, one should start with the system where one of the In atoms is replaced by Mn, giving rise to the composition $\text{Ni}_2\text{Mn}_{1.25}\text{In}_{0.75}$. Here allowing for changes in the cell shape upon optimization, the structure remains cubic. The two Mn atoms Mn1 and Mn2 favour a ferromagnetic alignment of their spins over an antiferromagnetic one by 0.11 eV/unit-cell. The optimized lattice constant is found to be 6.01 Å. Thus, cell volume contraction is found when In is replaced by Mn. This is because the ionic radius of Mn is smaller than that of In. Moreover, it is found that Ni atoms shift towards the Mn2 atoms. Consequently, Ni-Mn2 bond-distance decreases compared to Ni-Mn1 and Ni-In bond-lengths. The bond lengths between Ni-Mn1, Ni-Mn2, and Ni-In are found

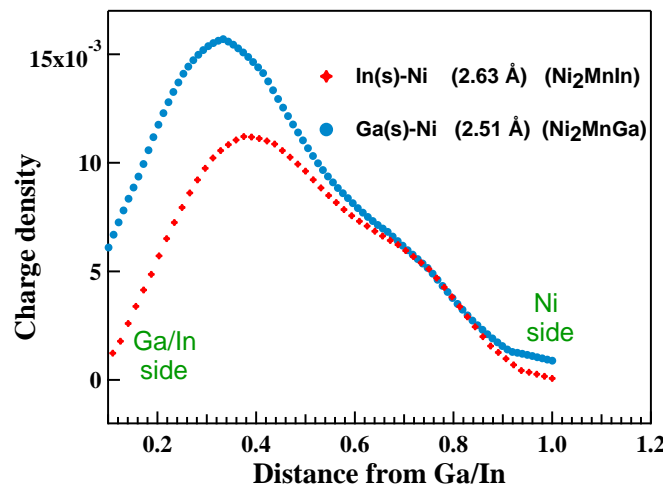


Figure 6.3 Line charge density of Ga/In *s* states along the Ga/In-Ni bond in austenitic phase of Ni₂MnIn.

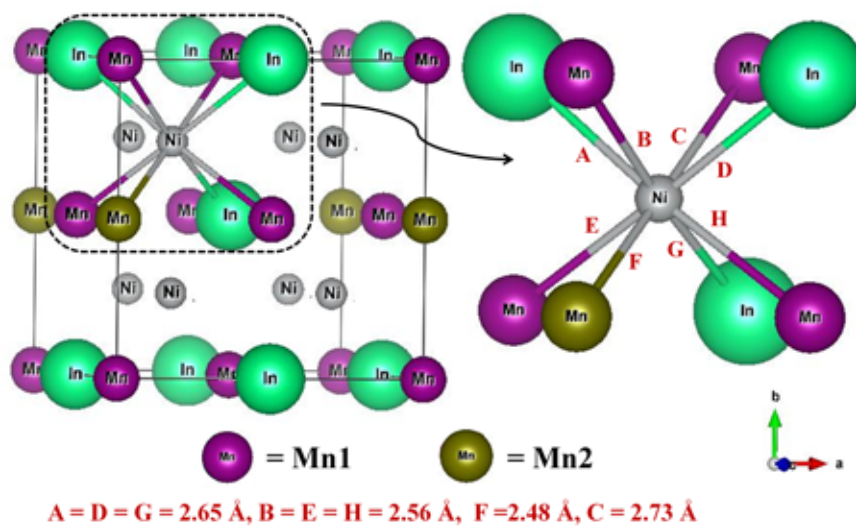


Figure 6.4 Ni-Mn1, Ni-Mn2 and Ni-In bond distances in Å units, after full relaxation of the cubic structure of composition $x = 0.25$.

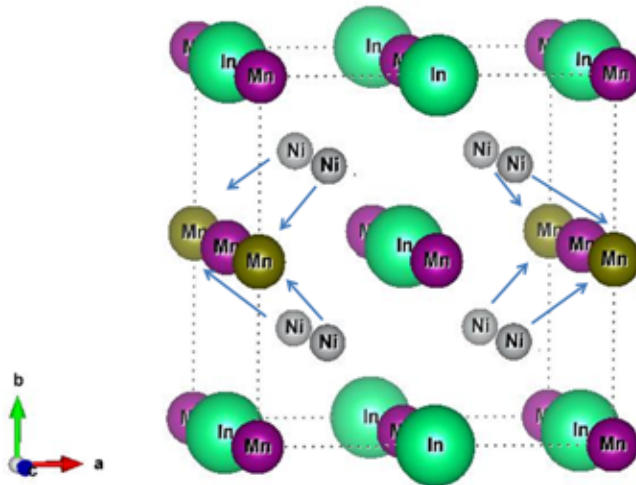


Figure 6.5 The direction of movement of Ni atoms towards Mn2 atom of composition $x = 0.25$.

to be 2.56 Å, 2.48 Å, and 2.65 Å as against the bond lengths of 2.60 Å found before the atomic relaxations. The decrease of Ni-Mn2 bond-lengths are uniform in all diagonal directions. The direction of movement of Ni atoms towards Mn2 atom has been shown in fig. 6.5. Thus the structure remains in cubic having smaller lattice parameter. Experimental thermo-magnetization measurement [1] and hard x-ray photoelectron spectroscopy measurement of valence band [9] reveal that the compositions $0 \leq x < 0.36$ do not exhibit a martensitic transformation.

In order to understand the martensitic transformation the composition $x = 0.375$ of $Ni_2Mn_{1+x}In_{1-x}$ is considered within our theoretical calculations as this point is close to the experimental composition ($x = 0.36$) from which martensitic phase begins to transformation. A 32 atom unit cell is constructed to examine if there is a martensitic transformation or not. Starting with a cubic unit cell a tetragonal (small orthorhombicity) unit cell is favored after the unit cell optimization. The optimized lattice parameters are $a = 6.87$ Å, $b = 5.52$ Å and $c = 5.53$ Å, resulting in $a/c = 1.24$. For this composition different combinations were examined and the atomic arrangement with the lowest energy is shown in fig. 6.6. It is important to note that in the cubic structure the energetically favorable magnetic exchange interaction between nearest neighbour Mn1 and Mn2 is ferromagnetic which changes to antiferromagnetic in the martensitic structure. This happens because in the

cubic phase Mn1-Mn2 bond-length is 3 Å which decreases to 2.66 Å. Here, the doping concen-

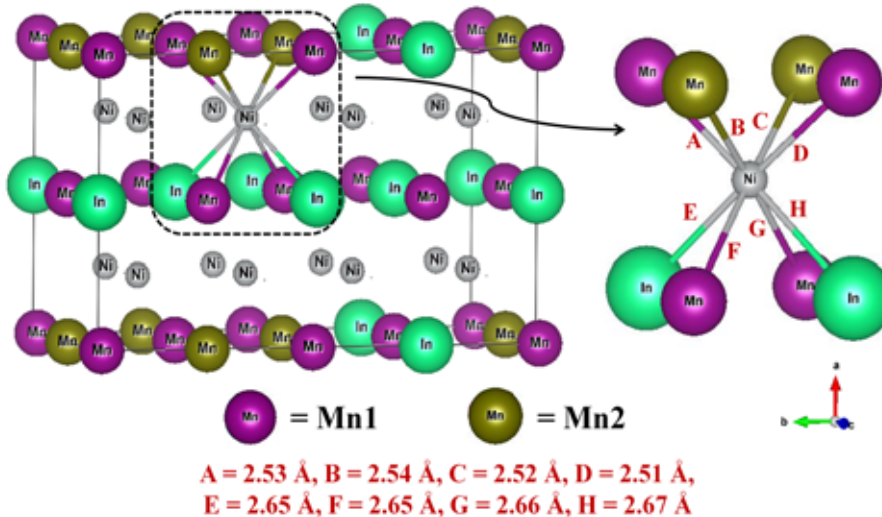


Figure 6.6 Ni-Mn1, Ni-Mn2 and Ni-In bond distances in Å units, after volume as well as ionic relaxation of the cubic structure of composition $x = 0.375$.

tration is such that in this 32-atom supercell the Mn atoms form a region of Mn-rich planes. Here, one finds a reduction in some of the Ni-Mn bond-distances. These are found to be in the range 2.51-2.66 Å for Ni-Mn1, 2.52-2.54 Å for Ni-Mn2. Additionally there is a substantial increase of the Ni-In bond lengths from the stoichiometric compound. The question that follows is whether this aids the tetragonality and how.

To understand the martensitic transformation further, we consider the composition $x = 0.50$ which is realized in the 16 atom unit cell in the fig. 6.7. In austenitic phase the structure is cubic having lattice parameter 5.96 Å. After ionic relaxation, the Ni-Mn1 and Ni-Mn2 bond-distances decrease uniformly because Ni atoms shift towards the Mn-cluster plane compared to parent stoichiometric compound. Ni-Mn hybridization allows for energy gain by this movement of Ni from centrosymmetric position. Additionally, Ni atoms further move away from the In atoms. The resultant movement is along a lattice parameter. This gives rise to tetragonal structure. The optimized lattice parameters are $a = 6.98 \text{ Å}$, $b = c = 5.43 \text{ Å}$, resulting in $a/c = 1.28$. This is confirmed by increased Ni-In bond-distances (shown in fig. 6.7) from cubic to tetragonal structure. This is consistent with EXAFS measurements of $\text{Ni}_2\text{Mn}_{1.4}\text{In}_{0.6}$ [25]. In the low temperature martensitic phase

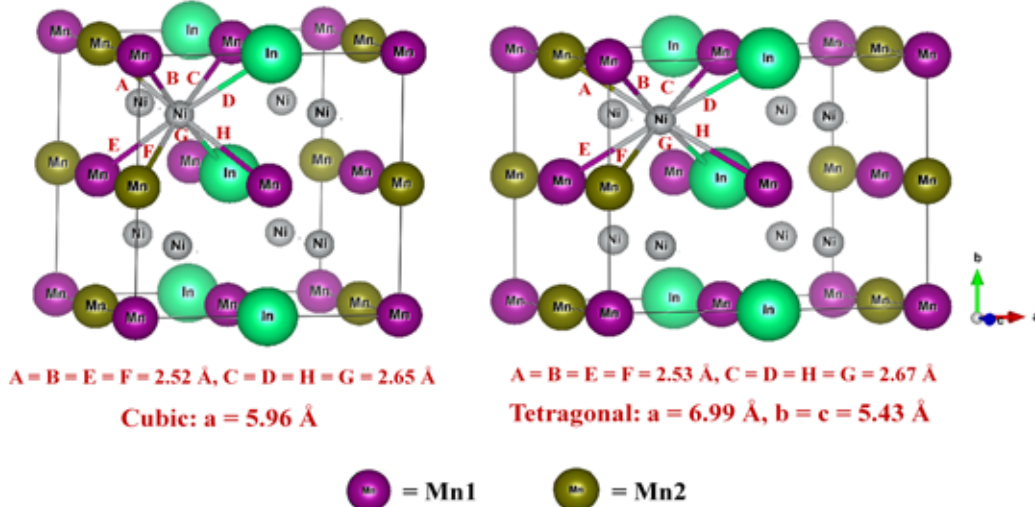


Figure 6.7 Ni-Mn1, Ni-Mn2 and Ni-In bond distances in \AA units, after volume as well as ionic relaxation of the cubic structure of composition $x = 0.5$.

in the case of the Ni K-edge EXAFS experiments, Ni-Mn and Ni-In bond lengths are 2.56 \AA and 2.70 \AA changing from 2.58 \AA and 2.63 \AA in austenitic phase, respectively. This happens due to movement of Ni atoms towards Mn atoms because of strong Ni-Mn hybridization. The strength of hybridization depends on the exchange splitting on Mn1, Mn2 and Ni. In Ni-Mn-In exchange splitting on all the atoms are in the same direction in austenitic phase which is different from Ni-Mn-Sn. Furthermore, the elongation along one direction happens to reduce electrostatic potential felt by the electrons on the In atoms due to the first neighbor Ni atoms in the cubic structure. This is what we find for $x = 0.375$ and beyond.

Moreover, for further understanding of the change in electronic structure triggered by martensitic transformation, the spin resolved total density of states and Ni partial density of states are shown in fig. 6.8 in both cubic and tetragonal structure of $x = 0.50$. A prominent density of states feature at the Fermi energy (E_F) in cubic austenitic phase reduces in martensitic phase. These electronic structure changes near E_F can be predominantly associated with a reorganization of the Ni e_g states.

It is important to note that, in cubic structure the presence of significant density of states due to degenerate states at the Fermi level is prerequisite for Jahn-Teller distortion. In this scenario

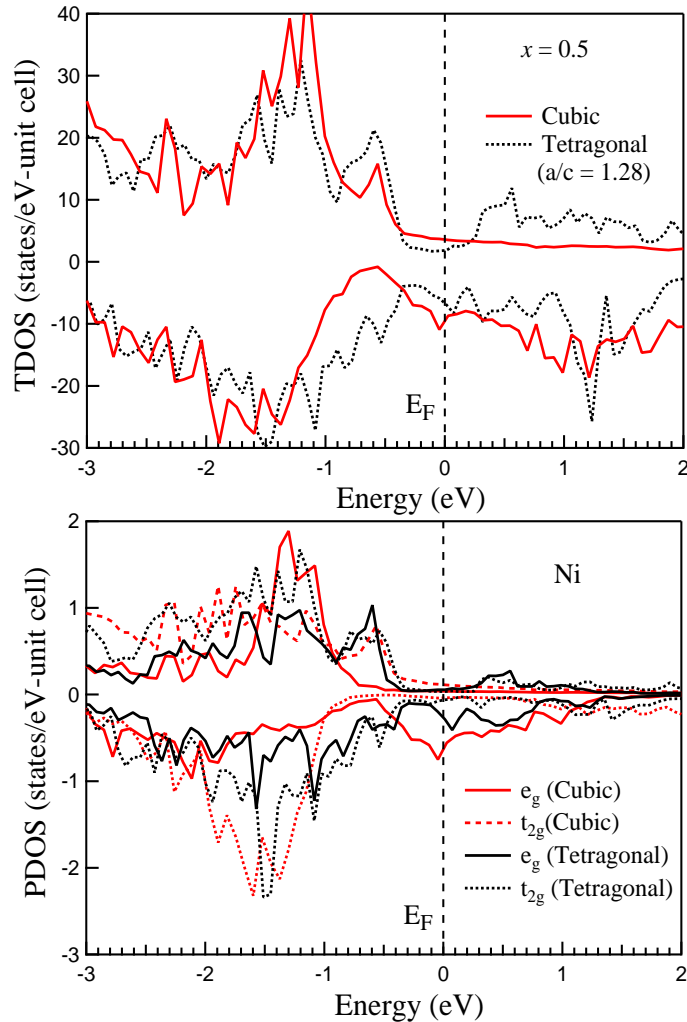


Figure 6.8 Spin resolved total density of states (TDOS) and Ni partial density of states (PDOS) of $x = 0.5$ in Cubic and Tetragonal structure. The Fermi energy (E_F) is at 0 eV. The upper/lower panel is for the majority/minority spin channel.

the system can lower its energy by lifting the degeneracy giving rise to pseudo gap near Fermi energy due to tetragonal structural transformation. To quantify this symmetry lowering we map the *ab-initio* band dispersions for $x = 0.50$ to a tight binding model which includes *s* and *d* orbital states of Ni and Mn and *p* orbital states of In in the basis. Maximally localized Wannier functions were considered for the radial parts of the wave function. The tight-binding bands are superposed on the *ab-initio* bands of unstable cubic and fully relaxed tetragonal structure in fig. 6.9.

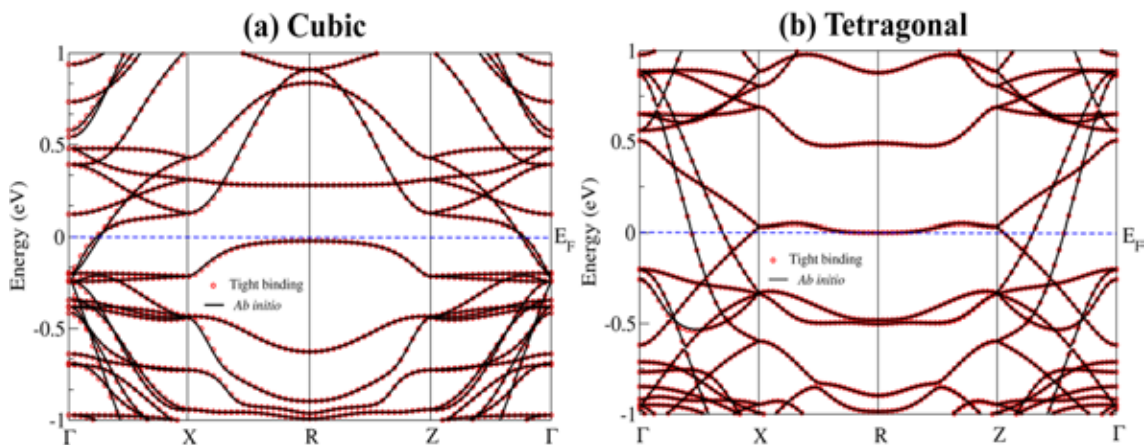


Figure 6.9 The tight-binding (circles) as well as the *ab initio* band structure (solid line) of $\text{Ni}_2\text{Mn}_{1.5}\text{In}_{0.5}$ in the (a) cubic and (b) fully relaxed tetragonal ($a/c = 1.28$) phase, respectively.

In both cases, one finds an excellent mapping of the *ab-initio* band structure within the tight-binding model. The relative on-site energy of Ni *d* states with respect to the d_{xz} spin-up state are listed in Table 6.1. The maximum energy level splitting of Ni *d* orbitals one finds in the cubic

Table 6.1 Relative on-site energies (eV) of Ni *d* states with respect to the spin-up d_{xz} state of Ni in cubic and tetragonal structure of $\text{Ni}_2\text{Mn}_{1.5}\text{In}_{0.5}$.

Atom	Orbital	Cubic Unit cell		Tetragonal unit cell	
		Spin up	Spin down	Spin up	Spin down
Ni	$d_{3z^2-r^2}$	-0.12	0.62	0.33	0.43
	d_{xz}	0.0	0.42	0.23	0.45
	d_{yz}	-0.17	0.47	0.22	0.43
	$d_{x^2-y^2}$	-0.05	0.53	0.24	0.46
	d_{xy}	-0.12	0.38	0.29	0.42

structure are ~ 0.17 eV (spin up channel) and 0.24 eV (spin down channel). It is interesting to note that even in cubic structure there exists energy level splitting due to distortion in Ni environment. This arises due to movement of Ni atoms towards Mn2 atoms. Moreover, in the tetragonal structure the maximum energy splitting of Ni *d* orbitals are obtained ~ 0.10 eV (spin up channel) and 0.04 eV (spin down channel). This suggests that Jahn-Teller distortions associated with the Ni atom

cannot be the driving force for the martensitic transitions seen in this system. However, for the off-stoichiometric compositions ($x \geq 0.375$) one have a non-uniform environment around the In atom. This could lead to a modification in the lone pair density favouring some distortions more. Our fitting of *ab-initio* band structure did not give us good enough description of the In *p* states & so we could not talk about the effect of the distortion on the onsite energies of the In *p* states.

Realization of modulated martensitic structure

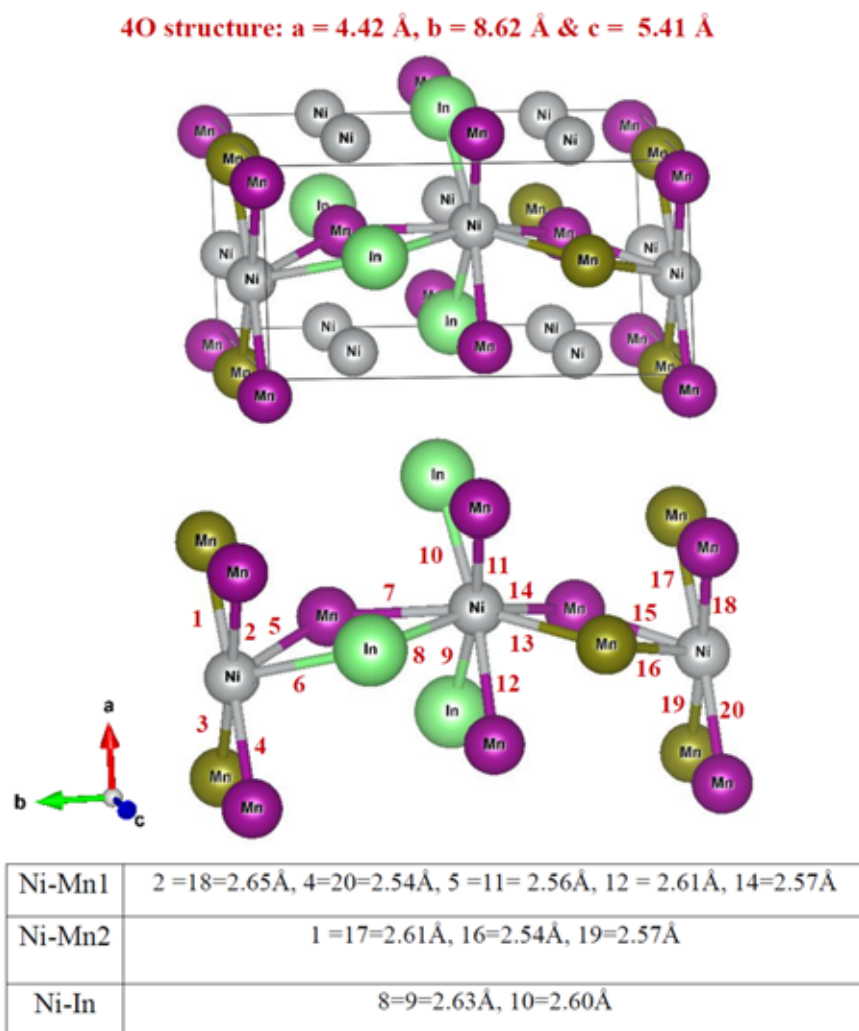


Figure 6.10 Optimized full relaxed 4O structure of $\text{Ni}_2\text{Mn}_{1.5}\text{In}_{0.5}$ with Ni-Mn1, Ni-Mn2 and Ni-In distances.

Although, *ab-initio* calculation predicts most stable tetragonal martensitic structure, the martensitic structure has been reported to be 4O, 10M or 14M modulated orthorhombic/monoclinic structure in experiment [26–30]. To accommodate the stress accumulated in 4O structure, the transition to stacking sequence 10M or 14M may occur.

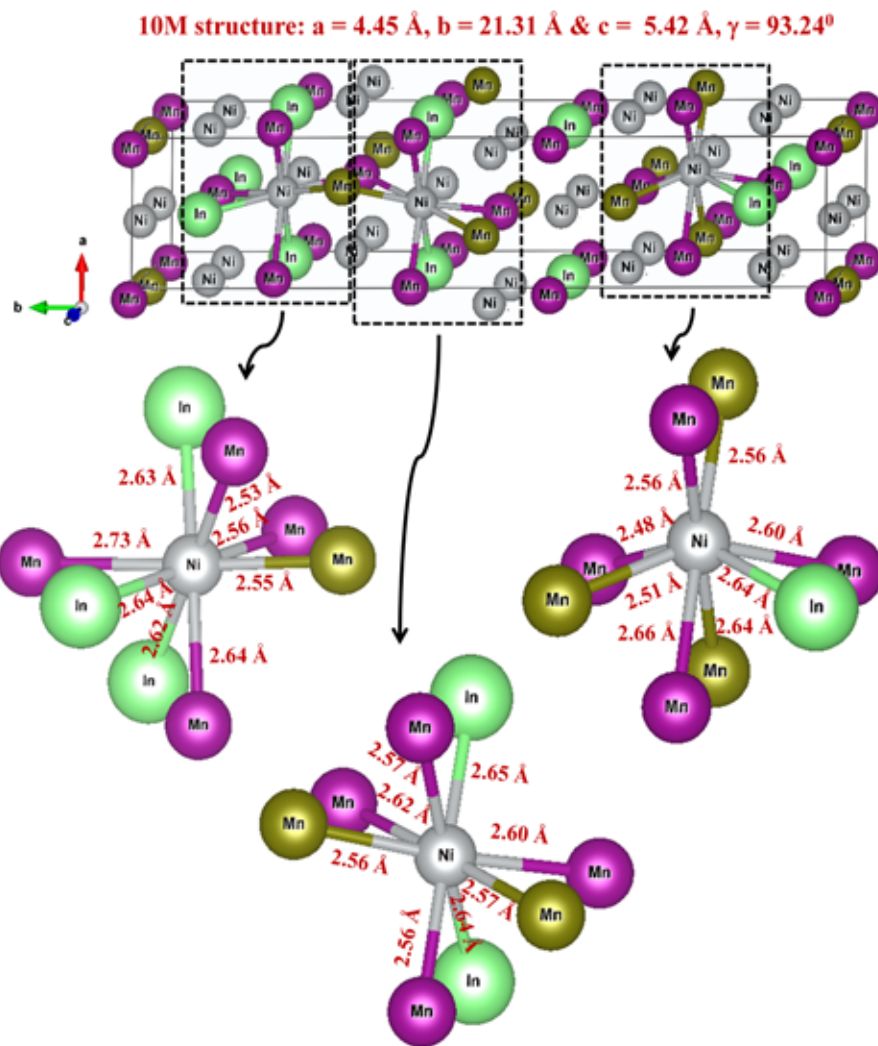


Figure 6.11 Optimized full relaxed 10M structure of $Ni_2Mn_{1.5}In_{0.5}$ with Ni-Mn1, Ni-Mn2 and Ni-In distances.

In fig. 6.10, fig. 6.11 and fig. 6.12, the theoretically obtained optimized 4O, 10M and 14M modulated structure with Ni-Mn1, Ni-Mn2 and Ni-In bond-lengths are shown. The larger Ni-In bond-distance indicates presence of electrostatic potential felt by the electrons on the In atoms due

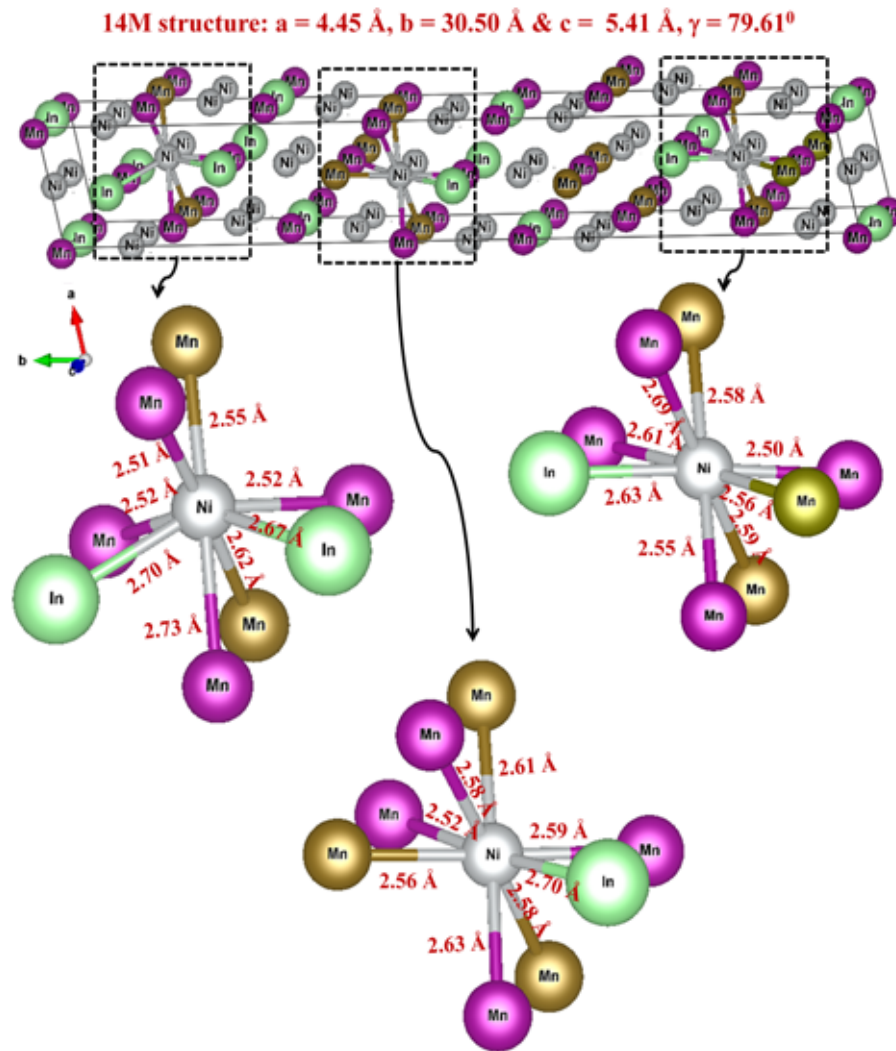


Figure 6.12 Optimized full relaxed 14M structure of $\text{Ni}_2\text{Mn}_{1.5}\text{In}_{0.5}$ with Ni-Mn1, Ni-Mn2 and Ni-In distances.

to the neighbor atoms which was discussed as the possible reason for martensitic transformation.

Moreover, the formation energy/formula unit of 4O, 10M and 14M modulated structure is calculated to understand most favourable modulated martensitic structure. The formation energy of 4O, 10M and 14M modulated structure are -0.6507 eV/formula unit, -0.52747 eV/formula unit and -0.64207 eV/formula unit, respectively. Thus, one finds that 4O and 14M have comparable formation energy which leads to favourable 4O and 14M mixed modulated martensitic phase.

6.3.2 Electronic structure of Co doped Ni-Mn-In

Site occupancy trend of Co in Ni-Mn-In

The ground state energy/unit-cell of Co doping at Mn site ($Ni_2Mn_{0.75}(Co_{0.25})In$) and Co doping at Ni site ($Ni_{1.75}(Co_{0.25})MnIn$) is compared. The formation energy for $Ni_2Mn_{0.75}(Co_{0.25})In$ and $Ni_{1.75}(Co_{0.25})MnIn$ are -0.79204 eV/formula-unit and -0.90171 eV/formula-unit, respectively. The later composition has 0.1097 eV/formula-unit lower formation energy than the former. Thus, Co atom prefers the Ni site rather than Mn site. The Co is found to be ferromagnetically coupled with Ni and Mn. The L₂₁ crystal structure with Co doped at different Ni sites for $Ni_{1.75}Co_{0.25}MnIn$ (NCMI1), $Ni_{1.5}Co_{0.5}MnIn$ (NCMI2) and $Ni_{1.25}Co_{0.75}MnIn$ (NCMI3) are shown in fig. 6.13(a), fig. 6.13[(b)-(d)] and fig. 6.13(e)-(f)], respectively. In NCMI1 (fig. 6.13(a)) Co is substituted at (1/4, 1/4, 3/4) site. For NCMI2 two Co atoms are doped at (1/4, 1/4, 1/4), (1/4, 1/4, 3/4) [1st configuration]; (1/4, 1/4, 3/4), (3/4, 3/4, 1/4) [2nd configuration] and (1/4, 1/4, 3/4), (1/4, 3/4, 1/4) [3rd configuration] Ni sites. In NCMI3 three Co atoms replace Ni sites at (1/4, 1/4, 3/4), (1/4, 3/4, 3/4), (3/4, 3/4, 1/4) [1st configuration] and (1/4, 1/4, 1/4), (1/4, 1/4, 3/4), (1/4, 3/4, 3/4) [2nd configuration]. After full relaxation of the cubic L₂₁ structure the lattice constants and total ground state energy/unit-cell are summarized in Table 6.2. The equilibrium structure of NCMI1 is cubic. The 1st and 3rd configuration of NCMI2 relaxes to tetragonal structure whereas 2nd configuration remains cubic. The tetragonal ground state structure is favorable for both 1st and 2nd configuration of NCMI3. The tetragonal structure has lower ground state energy (1st and 3rd configuration of NCMI2) than cubic structure (2nd configuration of NCMI2). Further, 1st configuration has lower

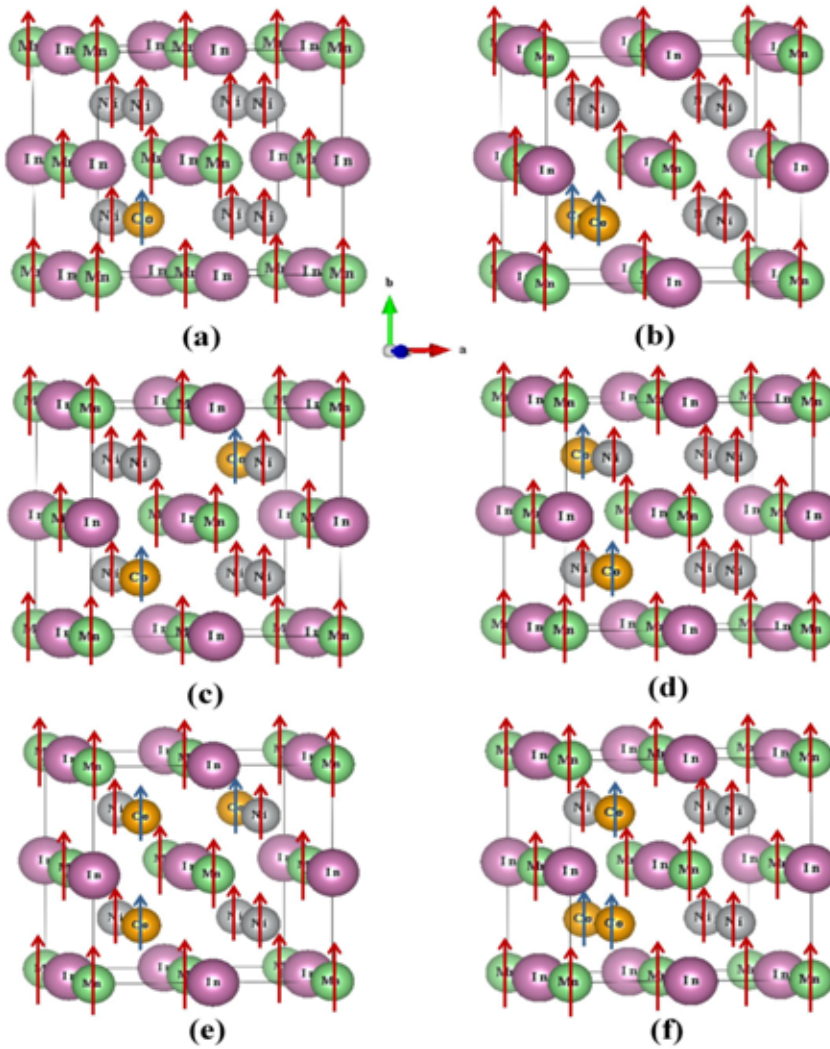


Figure 6.13 Cubic L₂₁ structure of (a) NCMI1, (b)-(d) 1st, 2nd and 3rd configurations of Co substitution at different Ni sites of NCMI2, respectively, (e)-(f) 1st and 2nd configurations of Co substitution at different Ni sites of NCMI3, respectively.

energy than 3rd configuration. For NCMI3, the 2nd configuration has lower ground state energy. In Table 6.3, the Co-Co bond distances are listed for different configurations. The average Co-Co bond lengths in 1st configuration of NCMI2 and 2nd configuration of NCMI3 are less than other configurations. This implies that Co atoms prefer to form cluster when doped at Ni site.

The clustering energy (Δ) is calculated with the formula proposed in Ref. [31]. $\Delta_{\text{NCMI2}} = [\text{E}_{\text{NCMI2}} - \text{E}_{\text{NMI}}] - 2 [\text{E}_{\text{NCMI1}} - \text{E}_{\text{NMI}}] = -35.43 \text{ meV/unit-cell}$ and $\Delta_{\text{NCMI3}} = [\text{E}_{\text{NCMI3}} - \text{E}_{\text{NMI}}] - 3$

Table 6.2 Lattice constant and total ground state energy/unit-cell (E0) of various configurations of NCMI1, NCMI2 and NCMI3 after full relaxation.

System	Configuration	Lattice Constant (Å)	Total ground state energy (eV)/unit-cell
NCMI1	-	$a = 6.060$	-92.5814
NCMI2	1 st	$a=b=6.015,$ $c=6.115$	-93.9191
	2 nd	$a=6.051$	-93.8441
	3 rd	$a=6.058,$ $b=c=6.051$	-93.8492
NCMI3	1 st	$a=c=6.005,$ $b=6.124$	-95.14098
	2 nd	$a=6.001,$ $b=c=6.061$	-95.2007

Table 6.3 Co positions and Co-Co bond length in different configurations of NCMI2 and NCMI3 after full relaxation.

System	Configu- ration	Co atom position	Co-Co bond length (Å)
NCMI2	1 st	(1/4,1/4,1/4), (1/4,1/4,3/4)	3.058
	2 nd	(1/4,1/4,3/4), (3/4,3/4,1/4)	5.240
	3 rd	(1/4,1/4,3/4), (1/4,3/4,1/4)	4.278
NCMI3	1 st	(1/4,1/4,3/4), (1/4,3/4,3/4) (1/4,3/4,3/4), (3/4,3/4,1/4) (1/4,1/4,3/4), (3/4,3/4,1/4)	3.062 4.246 5.235
	2 nd	(1/4,1/4,1/4), (1/4,1/4,3/4) (1/4,1/4,3/4), (1/4,3/4,3/4) (1/4,1/4,1/4), (1/4,3/4,3/4)	3.031 3.031 4.286

$[E_{\text{NCMI1}} - E_{\text{NMI}}] = -14.69 \text{ meV/unit-cell}$. The negative clustering energy of Co substituted systems reveal the favorable tendency of atomic association of Co rather than random distribution.

Thus, the substituted Co atoms prefer to be at Ni site with tetragonal ground state structure. Furthermore, Co substitution exhibits thermodynamic tendency for atomic association forming

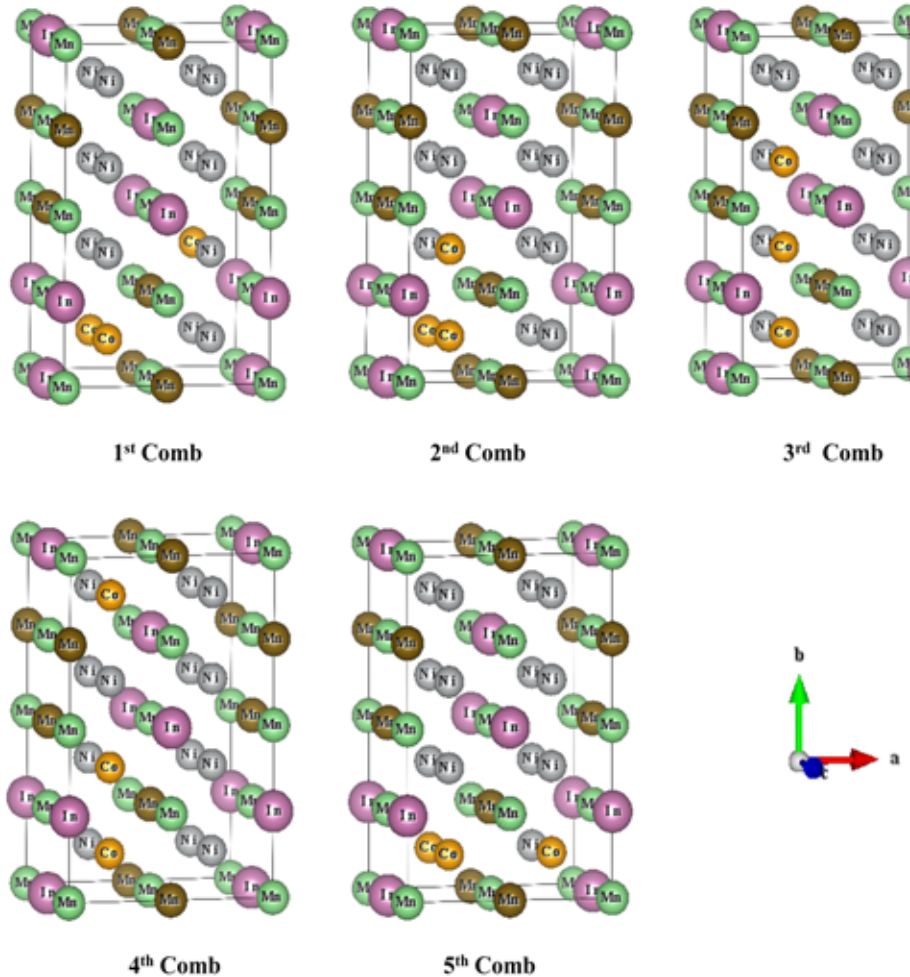


Figure 6.14 Different configurations of Co doping at Ni sites of $\text{Ni}_{1.625}\text{Co}_{0.375}\text{Mn}_{1.5}\text{In}_{0.5}$.

cluster, and makes the random distribution of Co difficult.

To understand the site occupancy trend of Co in off-stoichiometric Ni-Mn-In, we then continue the discussion considering the composition $\text{Ni}_{1.75}\text{Co}_{0.25}\text{Mn}_{1.5}\text{In}_{0.5}$ and $\text{Ni}_{1.625}\text{Co}_{0.375}\text{Mn}_{1.5}\text{In}_{0.5}$. $\text{Ni}_{1.75}\text{Co}_{0.25}\text{Mn}_{1.5}\text{In}_{0.5}$ can be realized in 16 atom unit cell structure where only one Co atom is substituted in $\text{Ni}_2\text{Mn}_{1.5}\text{In}_{0.5}$. This composition has stable tetragonal structure having lattice parameters $a = 6.95 \text{ \AA}$, $b = c = 5.44 \text{ \AA}$ which matches very well with experimentally obtained lattice parameters $a = 6.8 \text{ \AA}$, $b = c = 5.6 \text{ \AA}$ of $\text{Ni}_{1.81}\text{Co}_{0.22}\text{Mn}_{1.45}\text{In}_{0.52}$ [32]. Subsequently, $\text{Ni}_{1.625}\text{Co}_{0.375}\text{Mn}_{1.5}\text{In}_{0.5}$ is considered which is shown in fig. 6.14 and possible different configurations of Co doping at Ni sites have been depicted. Among these the 3rd combination has lowest

ground state energy. Here the Co atoms form a linear chain kind of structure, whereas the Mn2 are substituted at random In sites.

Effect of Co doping on elastic, magnetic and electronic properties of Ni_2MnIn

To understand the effect of Co doping in Ni-Mn-In on elastic properties, volume optimization of the cubic structure of Ni_2MnIn , $Ni_{1.75}Co_{0.25}MnIn$ and $Ni_{1.5}Co_{0.5}MnIn$ are performed. In fig. 6.15 the cubic volume optimization of total ground state energy of different compositions have been depicted.

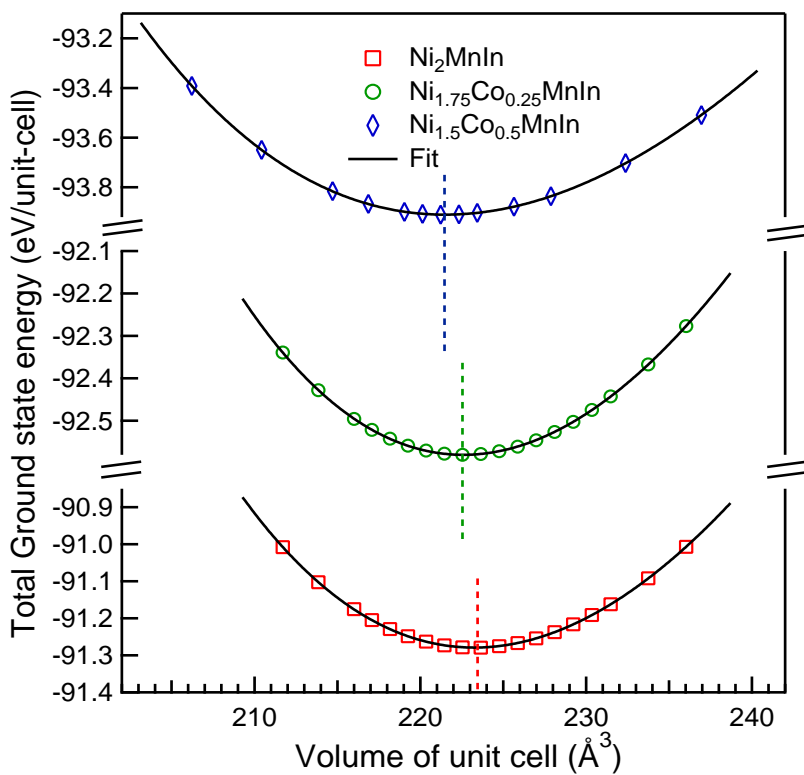


Figure 6.15 Total ground state energy/unit-cell and fitted curve vs. volume plot of Ni_2MnIn , $Ni_{1.75}Co_{0.25}MnIn$ and $Ni_{1.5}Co_{0.5}MnIn$.

The equilibrium lattice parameter of cubic unit cell and bulk modulus are found out by fitting the ground state energy with Murnaghan equation of state [33]. The lattice parameters, bulk mod-

ulus and total magnetic moment/f.u. in cubic structure of different compositions are listed in Table 6.4.

Table 6.4 Lattice constant, bulk modulus and magnetic moment/formula-unit(f.u.) in cubic structure of Ni_2MnIn , $\text{Ni}_{1.75}\text{Co}_{0.25}\text{MnIn}$ and $\text{Ni}_{1.5}\text{Co}_{0.5}\text{MnIn}$.

Composition	Lattice Constant (Å)	Bulk Modulus (GPa)	Magnetic Moment (μ_{B})/f.u.
Ni_2MnIn	6.069	131.854	4.2715
$\text{Ni}_{1.75}\text{Co}_{0.25}\text{MnIn}$	6.060	132.593	4.5022
$\text{Ni}_{1.5}\text{Co}_{0.5}\text{MnIn}$	6.050	136.142	4.5532

It is obtained from Table 6.4 that bulk modulus and total magnetic moment/f.u. increase with Co doping. In Ni_2MnIn , Ni and Mn individual magnetic moment are $0.346 \mu_{\text{B}}$ and $3.653 \mu_{\text{B}}$ respectively which mainly contribute in total magnetic moment. For $\text{Ni}_{1.75}\text{Co}_{0.25}\text{MnIn}$ and $\text{Ni}_{1.5}\text{Co}_{0.5}\text{MnIn}$ Ni, Co, Mn individual magnetic moment varies as $0.324\text{-}0.488 \mu_{\text{B}}$, $1.310 \mu_{\text{B}}$, $3.601\text{-}3.613 \mu_{\text{B}}$ and $0.266\text{-}0.418 \mu_{\text{B}}$, $1.240 \mu_{\text{B}}$, $3.516\text{-}3.523 \mu_{\text{B}}$. Thus, the Co has ferromagnetic exchange with Ni and Mn. Higher individual magnetic moment of Co atom than Ni makes the total magnetic moment higher in Co doped systems than Ni_2MnIn . Due to more ferromagnetic exchange between Ni-Co and Mn-Co in Co doped system [34, 35] the Curie temperature T_C will be higher than Ni_2MnIn because within the mean-field approximation Curie temperature is proportional to the strength of exchange interaction [36].

Moreover, introduction of Co affects the electronic structure which is evident from fig. 6.16 where the comparison between spin polarized total and partial density of states of Ni_2MnIn and $\text{Ni}_{1.75}\text{Co}_{0.25}\text{MnIn}$ have been shown. Significant contribution of Co d states near E_F around -0.3 eV increases the weight of the density of states near the Fermi energy.

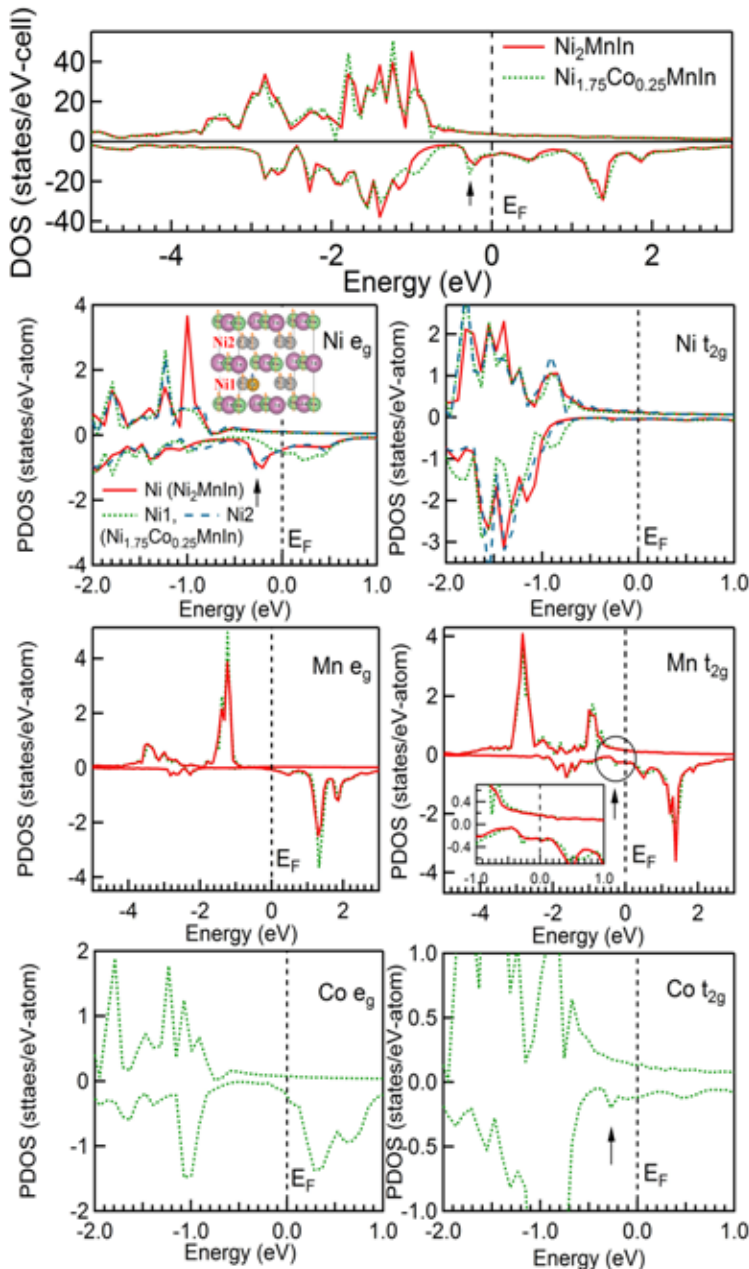


Figure 6.16 Spin polarized total and partial density of states of Ni_2MnIn and $\text{Ni}_{1.75}\text{Co}_{0.25}\text{MnIn}$. The Fermi energy (E_F) is at 0 eV. The upper/lower panel is for the majority/minority spin channel.

6.4 Conclusions

In summary, the structural properties of $\text{Ni}_2\text{Mn}_{1+x}\text{In}_{1-x}$ has been investigated. Martensitic transformation have been obtained for $x \geq 0.375$ which is in good agreement with the experimental value $x \geq 0.36$. Jahn-Teller effect associated with Ni is not the driving force for the martensitic transitions of this system. Similar to Ni-Mn-Sn system, it is the Ni-Mn hybridization and In lone pair electron density on the electrons of neighbouring atoms which make the cubic structure unstable and trigger the structural transition.

Moreover, the substituted Co atoms prefer to be at Ni site with stable tetragonal ground state structure. Furthermore, Co substitution exhibits thermodynamic tendency for atomic association forming cluster, and makes the random distribution of Co difficult. Introduction of Co enhances the ferromagnetic exchange interaction between Ni-Co and Mn-Co. Consequently, the Curie temperature of Co-doped system is more than stoichiometric Ni_2MnIn .

Bibliography

- [1] T. Krenke, M. Acet, E. F. Wassermann, X. Moya, L. Mañosa, and A. Planes, Phys. Rev. B **73**, 174413 (2006).
- [2] C. M. Li, H. B. Luo, Q. M. Hu, R. Yang, B. Johansson, and L. Vitos, Phys. Rev. B **86**, 214205 (2012).
- [3] J. Enkovaara, O. Heczko, A. Ayuela, and R. M. Nieminen, Phys. Rev. B **67**, 212405 (2003).
- [4] Q. M. Hu, C. M. Li, S. E. Kulkova, R. Yang, B. Johansson, and L. Vitos, Phys. Rev. B **81**, 064108 (2010).
- [5] T. Krenke, M. Acet, E. F. Wassermann, X. Moya, L. Mañosa, and A. Planes, Phys. Rev. B **72**, 014412 (2005).
- [6] M. Ye, A. Kimura, Y. Miura, M. Shirai, Y. T. Cui, K. Shimada, H. Namatame, M. Taniguchi, S. Ueda, K. Kobayashi, R. Kainuma, T. Shishido, K. Fukushima, and T. Kanomata, Phys. Rev. Lett. **104**, 176401 (2010).
- [7] K. R. Priolkar, P. A. Bhobe, D. N. Lobo, S. W. D’Souza, S. R. Barman, A. Chakrabarti, and S. Emura, Phys. Rev. B **87**, 144412 (2013).
- [8] C. L. Tan, Y. W. Huang, X. H. Tian, J. X. Jiang, and W. Cai, Appl. Phys. Lett. **100**, 132402 (2012).
- [9] S. Zhu, M. Ye, K. Shirai, M. Taniguchi, S. Ueda, Y. Miura, M. Shirai, R. Y. Umetsu, R. Kainuma, T. Kanomata and A. Kimura, J. Phys.: Condens. Matter **27**, 362201 (2015).

- [10] W. Ito, Y. Imano, R. Kainuma, Y. Sutou, K. Oikawa, and K. Ishida, *Metall. Mater. Trans. A* **38**, 759 (2007).
- [11] Y. Feng, J. H. Sui, Z. Y. Gao, G. F. Dong, and W. Cai, *J. Alloy. Compd.* **476**, 935 (2008).
- [12] W. Ito, X. Xu, R. Y. Umetsu, T. Kanomata, K. Ishida, and R. Kainuma, *Appl. Phys. Lett.* **97**, 242512 (2010).
- [13] D. Y. Cong, S. Roth, and L. Schultz, *Acta Mater.* **60**, 5335 (2012).
- [14] A. N. Vasiliev, O. Heczko, O. S. Volkova, T. N. Vasilchikova, T. N. Voloshok, K. V. Klimov, W. Ito, R. Kainuma, K. Ishida, K. Oikawa, and S. Fähler, *J. Phys. D: Appl. Phys.* **43**, 055004 (2010).
- [15] S. Singh, I. Glavatskyy, and C. Biswas, *J. Alloy. Compd.* **601**, 108 (2014).
- [16] Z. Han, D. Wang, B. Qian, J. Feng, X. Jiang, and Y. Du, *JPN. J. Appl. Phys.* **49**, 010211 (2010).
- [17] A. K. Pathak, I. Dubenko, and C. Pueblo, P. Basnyat, S. Stadler, and N. Ali, *IEEE. T. Magn.* **46**, 1444 (2010).
- [18] Y. Kurtulus, R. Dronkowski, G. D. Samolyuk, and V. P. Antropov, *Phys. Rev. B* **71**, 014425 (2005).
- [19] G. Kresse and J. Furthmüller, *Phys. Rev. B* **54**, 11169 (1996).
- [20] J.P. Perdew, K. Burke, and Y. Wang, *Phys. Rev. B* **54**, 16533 (1996).
- [21] H. C. Kandpal, G.H. Fecher, and C. Felser, *J Phys. D* **40**, 1507 (2007).
- [22] A. A. Mostofi, J. R. Yates, Y.-S. Lee, I. Souza, D. Vanderbilt, and N. Marzari, *Comput. Phys. Commun.* **178**, 685 (2008).
- [23] N. Marzari and D. Vanderbilt, *Phys. Rev. B* **56**, 12847 (1997).

- [24] I. Souza, N. Marzari and D. Vanderbilt, Phys. Rev. B **65**, 035109 (2001).
- [25] P. A. Bhobe, K. R. Priolkar, and P. R. Sarode, J. Phys. D: Appl. Phys. **41**, 045004 (2008).
- [26] Y. Sutou, Y. Imano, N. Koeda, T. Omori, R. Kainuma, K. Ishida, and K. Oikawa, Appl. Phys. Lett. **85**, 4358 (2004).
- [27] Y. J. Huang, Q. D. Hua, J. Liu, L. Zeng, D.F. Zhang, and J. G. Li, Acta Mater. **61**, 5702 (2013).
- [28] L. Zhou, A. Mehta, A. Giri, K. Cho, and Y. Sohn, Mater. Sci. Eng., A **646**, 57 (2015).
- [29] X. Moya, L. Mañosa, A. Planes, T. Krenke, M. Acet, and E. F. Wassermann, Mater. Sci. Eng., A **438**, 911 (2006).
- [30] T. Krenke, E. Duman, M. Acet, E. F. Wassermann, X. Moya, L. Mañosa, A. Planes, E. Suard, and B. Ouladdiaf, Phys. Rev. B **75**, 104414 (2007).
- [31] P. Mahadevan, J. M. O.- Guillén, and A. Zunger, Appl. Phys. Lett. **86**, 172504 (2005).
- [32] S. Singh, I. Glavatskyy, and C. Biswas, J. Alloy. Compd. **601**, 108 (2014).
- [33] F. Murnaghan, Proc. Nat. Acad. Sci. USA **30**, 244 (1944).
- [34] B. Gao, F. X. Hu, J. Shen, J. Wang, J. R. Sun, and B. G. Shen, J. Magn. Magn. Mater. **321**, 2571 (2009).
- [35] V. V. Sokolovskiy, P. Entel, V. D. Buchelnikov, and M. E. Gruner, Phys. Rev. B **91**, 220409(R) (2015).
- [36] E. Şaşloğlu, L. M. Sandratskii, and P. Bruno, Phys. Rev. B **77**, 064417 (2008).

Chapter 7

Conclusions

In summary, this thesis mainly focuses on the origin of the martensitic transformation and other properties of Ni-Mn based Heusler alloys. The structural, magnetic, and electronic structure of Ni_2MnGa , $\text{Ni}_2\text{Mn}_{1+x}\text{Sn}_{1-x}$, $\text{Ni}_2\text{Mn}_{1+x}\text{In}_{1-x}$ and $\text{Ni}_{2-y}\text{Co}_y\text{Mn}_{1+x}\text{In}_{1-x}$ Heusler alloy systems are examined theoretically using an ab-initio implementation of density functional theory.

Interestingly, Ni_2MnGa is the only member in the Ni-Mn based alloys in which the martensitic transformation takes place for the stoichiometric compound. Transfer of spectral weight in the near Fermi energy region has been observed at the martensitic transformation [1]. This has been attributed to a band Jahn-Teller associated with Ni $3d$ orbitals [2]. In contrast to the conventional Jahn-Teller effect operative in localized systems, here, one finds delocalized states at the Fermi level. We find that this effect on the onsite energies of the Ni d orbitals is found to be very small. However, here the mechanism is associated with the delocalized electrons on Ga which have a low weight at the Fermi energy. The Coulomb interactions between electrons on Mn and those on Ga lead to a large electrostatic potential being felt by the latter. This we believe drives the distortions which results in the lifting of degeneracy of the three-fold degenerate p orbitals on Ga. This drives the martensitic transition. We quantify this interaction and show for the first time that the systems in which the martensitic transition does not take place are those in which the effects are smaller. Ni_2MnSn and Ni_2MnIn are the examples of such systems where the weaker Coulomb interactions between electrons Sn/In and neighbouring atoms do not drive a martensitic transition.

However, the off-stoichiometric Ni-Mn-Sn compositions with $x \geq 0.375$ are found to have a transition which captures the experimental trend of martensitic transition beyond $x \geq 0.36$ [3]. It is found that when the Mn atoms are doped at the Sn sites of $\text{Ni}_2\text{Mn}_{1+x}\text{Sn}_{1-x}$, the random occupation of Sn by Mn is energetically favorable. Mn at Mn sites (Mn1) are antiferromagnetically coupled to Mn at Sn sites (Mn2) in the parent austenitic phase which persists in martensitic phase with enhanced exchange interaction. Thus, the exchange splitting on Mn1 and Ni are in the same direction, while that on Mn2 is opposite. This results in a larger energy gain when Ni and Mn2 interact. At larger doping concentrations one gains energy from Mn1 and Ni interactions also. Ni atom moves towards both Mn1 and Mn2 and this results in a resultant force along a lattice parameter. This leads to instability in the austenitic phase. Further energy lowering is possible by

an elongation of the lattice vector which gives rise to the martensitic transition due to presence of Sn electron lone pair repulsion to electrons on neighbouring atoms. Quantification of the electronic structure change of Ni *d* states by mapping of the *ab-initio* band structure within the tight-binding model in both austenitic phase and martensitic phase reveals that the changes in onsite energies at the transition are small. This suggests that Jahn-Teller distortions associated with Ni cannot be the driving force for the martensitic transitions of this system. Thus the microscopic origin at off-stoichiometric compositions of $\text{Ni}_2\text{Mn}_{1+x}\text{Sn}_{1-x}$ is the Ni-Mn hybridization and Sn lone pair effect which make the cubic structure unstable and triggers the structural transformation.

The above explanation for the driving force of martensitic transformation of $\text{Ni}_2\text{Mn}_{1+x}\text{Sn}_{1-x}$ also holds for $\text{Ni}_2\text{Mn}_{1+x}\text{In}_{1-x}$. Interestingly, here the magnetic exchange between Mn at parent Mn site (Mn1) and doped Mn at In site (Mn2) is ferromagnetic in nature in the austenitic phase in contrast to $\text{Ni}_2\text{Mn}_{1+x}\text{Ga}_{1-x}$ and $\text{Ni}_2\text{Mn}_{1+x}\text{Sn}_{1-x}$. In the martensitic phase the magnetic exchange between Mn1 and Mn2 becomes antiferromagnetic in $\text{Ni}_2\text{Mn}_{1+x}\text{In}_{1-x}$, while it remains antiferromagnetic for $\text{Ni}_2\text{Mn}_{1+x}\text{Ga}_{1-x}$ and $\text{Ni}_2\text{Mn}_{1+x}\text{Sn}_{1-x}$.

The X-ray diffraction and magnetic susceptibility measurements reveal that in the martensitic phase the co-existence of two crystal structures (4L and 14L orthorhombic structures), change in crystal structure phase fraction with magnetic transition, co-existence of ferromagnetic and antiferromagnetic domains, and different strength of antiferromagnetic coupling gives rise to structurally and magnetically frustrated martensitic phases that causes spin-glass-like behavior of $\text{Ni}_2\text{Mn}_{1+x}\text{Sn}_{1-x}$ ($x = 0.40$ and 0.44) and lead to exchange bias phenomena under zero field cooled heating (ZFC). Moreover, the change in valence band shape due to temperature variation in experimental electronic structure has been captured by *ab-initio* density functional theory. The redistribution of density of states due to 4L and 14L phase fraction change gives rise to valence band shape change.

Furthermore, it has been found that the substituted Co atoms prefer to be at Ni sites with stable tetragonal ground state structure. Co substitution exhibits a tendency to form clusters. Introduction of Co enhances the ferromagnetic exchange interaction between Ni-Co and Mn-Co. Consequently, the Curie temperature of Co-doped system is more than stoichiometric Ni_2MnIn .

Bibliography

- [1] C. P. Opeil, B. Mihaila, R. K. Schulze, L. Mañosa, A. Planes, W. L. Hults, R. A. Fisher, P. S. Riseborough, P. B. Littlewood, J. L. Smith, and J. C. Lashley, Phys. Rev. Lett. **100**, 165703 (2008).
- [2] P. J. Brown, A. Y. Bargawi, J. Crangle, K.-U. Neumann, and K. R. A. Ziebeck, J. Phys.: Condens. Matter **11**, 4715 (1999).
- [3] M. Ye, A. Kimura, Y. Miura, M. Shirai, Y. T. Cui, K. Shimada, H. Namatame, M. Taniguchi, S. Ueda, K. Kobayashi, R. Kainuma, T. Shishido, K. Fukushima, and T. Kanomata, Phys. Rev. Lett. **104**, 176401 (2010).

Appendix A

Role of Coulomb correlations in the properties of Heusler alloys

A.1 Introduction

Till date a lot of theoretical calculations on total ground state energy variation with different c/a ratios have been performed with GGA functional [1–4] for Ni_2MnGa which describe the local energy minima at $c/a \approx 0.94/0.955$ [2, 5] and a global minima around 1.25 [5]. Barman *et al.* [6] predicted global energy minima at $c/a \approx 0.97$ using GGA functional. Recently, it is suggested that GGA+U functional is more suitable for Ni_2MnGa [7]. The U is considered only on Mn and value is around 5.97 eV, which is large for metallic systems. The U on Ni *d* and Ga *p* states are neglected. Here U plays the role of additional Coulomb interaction between the electrons of atoms when interactions of localized electrons are strong. However, GGA functional takes account the Coulomb interactions to some extent.

Thus, the validity of the influence of U on the properties of Ni-Mn based Heusler alloys is necessary to investigate. The present chapter investigates the role of Coulomb correlation in understanding properties of both stoichiometric Ni_2MnSn and off-stoichiometric $\text{Ni}_2\text{Mn}_{1.5}\text{Sn}_{0.5}$. The U on both Ni and Mn states are considered.

A.2 Theoretical and Experimental Methods

Ab-initio electronic structure calculations are carried out using the projector augmented wave (PAW) method as implemented in the VASP [8] code within generalized gradient approximation (GGA) for the exchange correlation functional. Moreover, considering coulomb interaction due to Ni and Mn explicitly within GGA functional, we have adopted GGA + U_{Mn} , GGA + U_{Ni} and GGA + $U_{\text{Mn}} + U_{\text{Ni}}$. The U_{Ni} value is considered 5 eV and U_{Mn} is taken to be 3 eV and 4 eV [9–11]. Moreover, the density of states of Heusler alloy systems is characterized by the exchange-splitting of the Mn *d* states which is around 3 eV. The experimental L₂1 structure [12, 13] with the space group $Fm\bar{3}m$ was considered for Ni_2MnSn . A 16 atom L₂1 cubic unit cell is considered. A k-points mesh of $10 \times 10 \times 10$ and a plane wave cutoff energy 425 eV was used in the calculations. The total energy was found to converge within 5 meV. The volume as well as ionic positions of unit cell are

relaxed to obtain the stable ground state. Using the equilibrium structure, spin polarized total density of states (DOS) per unit cell and partial density of states (PDOS) per atom are calculated. The magnetic coupling between Mn at parent Mn sites and doped Mn at Sn sites is antiferromagnetic in off-stoichiometric $\text{Ni}_2\text{Mn}_{1+x}\text{Sn}_{1-x}$. The ionic positions are relaxed for different c/a ratios of the off-stoichiometric alloy.

The Ultra-violet Photoemission Spectroscopy (UPS) measurement was performed using monochromatic He I ($h\nu = 21.2$ eV) photon source to record the valence band spectra. The electron detection was done by Gammadata Scienta analyzer R4000. The total energy resolution of UPS is 1.5 meV.

A.3 Results and Discussions

The lattice parameter of Ni_2MnSn obtained using different exchange correlation functionals are listed in Table A.1. The cubic lattice parameter obtained using GGA and GGA + U_{Mn} (3 eV) + U_{Ni} (5 eV) functional.

Table A.1 Cubic L2₁ lattice parameter of Ni_2MnSn with GGA, GGA + U_{Mn} , GGA + U_{Ni} and GGA + $U_{\text{Mn}} + U_{\text{Ni}}$ functional.

	Functional	Lattice parameter (Å)
1.	GGA	6.059
2.	GGA + U_{Mn}	3 eV : 6.124
		4 eV : 6.144
3.	GGA + U_{Ni}	5.993
4.	GGA + $U_{\text{Mn}} + U_{\text{Ni}}$	3 eV : 6.063
		4 eV : 6.080

U_{Ni} (5 eV) are in good agreement with the experiment [12, 13] (6.06 Å). The lattice parameter differs by only 0.28 % with increase in U by 1 eV. Therefore, U_{Mn} could be considered either 3 eV or 4 eV. The use of U only on Mn or Ni does not agree with experimental lattice parameter. The U_{Ni} alone underestimates the lattice constant by 0.94 % while the U on Mn overestimates the lattice constant by 1.22 - 1.55 %.

Table A.2 Magnetic moments of Ni, Mn and Sn/atom and total moment/formula unit(f.u.) (in μ_B) of Ni_2MnSn with GGA, GGA + U_{Mn} , GGA + U_{Ni} and GGA + $U_{\text{Mn}} + U_{\text{Ni}}$ functional.

Atom type	GGA		GGA + U_{Mn}		GGA + U_{Ni}		GGA+ $U_{\text{Mn}} + U_{\text{Ni}}$	
	3eV	4eV	3eV	4eV	3eV	4eV	3eV	4eV
Ni	0.246	0.174	0.154	0.205	0.184	0.158		
Mn	3.486	4.045	4.167	3.480	4.076	4.188		
Sn	-0.021	-0.020	-0.019	-0.034	-0.025	-0.026		
Total	4.104	4.532	4.628	3.961	4.572	4.636		

The Table A.2 gives the magnetic moment of each atom and total magnetic moment using all the functionals. It is important to note that the total magnetic moment, obtained with GGA matches well with experiment [13–15] ($\sim 4 \mu_B/\text{f.u.}$). The total magnetic moment arises due to localized magnetic moment of Mn atoms. The Mn magnetic moment with GGA and GGA + U_{Ni} functional is in good agreement (< 10 %) with experiment ($\sim 3.2 \pm 0.1 \mu_B/\text{f.u.}$) [16]. The incorporation of U on Mn increases the magnetic moment on Mn by 26.4 - 30.2 %. As a result, total magnetic moment also increases by 13.3 - 15.7 % as compared to experimental value. Although Mn moment obtained using GGA + U_{Ni} agrees well with experiment, the total magnetic moment decreases by 0.98 %. Furthermore, U on both Mn and Ni increases the magnetic moment of Mn by 27.4 - 30.9 %. Consequently, total magnetic moment increases by 14.3 - 15.9 %. The increase of U on Mn by 1 eV does not change the total magnetic moment appreciably. Thus, consideration of U on Mn could be either 3 eV or 4 eV for further calculation. Although structural analysis reveals that GGA and GGA+ $U_{\text{Mn}}+U_{\text{Ni}}$ gives good agreement with experiment, the later one does not produce matching experimental magnetic moment value.

The fig. A.1 shows the effect of U on spin integrated total density of states (TDOS). The total DOS is multiplied with Fermi function at the measurement temperature and convoluted with a Voigt function to compare with experimental valence band [17]. The half width at half maximum (HWHM) accounts for Gaussian component of the Voigt function. The energy-dependent Lorentzian full width at half maximum (FWHM) that represents the lifetime broadening is 0.1(E-

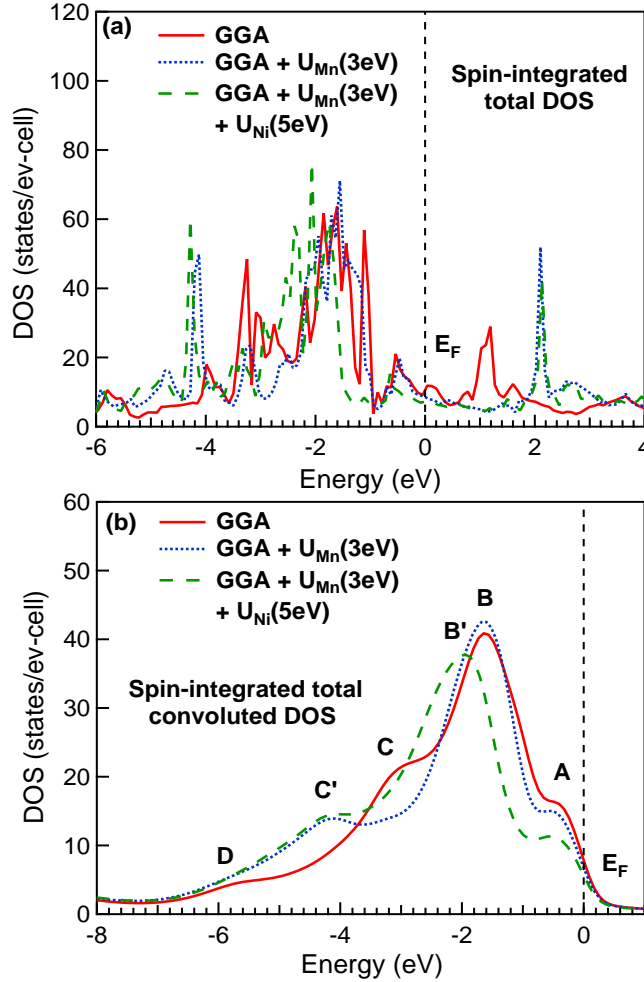


Figure A.1 (a) Spin integrated total DOS of Ni₂MnSn with GGA, GGA+U_{Mn}(3 eV) and GGA+U_{Mn}(3 eV)+U_{Ni} (5 eV), (b) Convolved total DOS by experimental broadening parameters.

E_F), where E_F represents the Fermi energy. The convoluted DOS has a peak around -1.6 eV (feature B in fig. A.1 (b)) with GGA and GGA+U_{Mn}(3 eV) and around -1.92 eV (feature B') with GGA+U_{Mn}(3 eV)+U_{Ni}(5 eV) functional. In experimental valence band spectra of Ni₂MnSn a peak is observed around -1.5 eV [14, 18]. Thus, GGA and GGA+U_{Mn}(3 eV) functional have good agreement with experiment. The valence band spectra does not match by considering U both on Mn and Ni with GGA functional. The VB is largely dominated by Ni 3d states as evident from partial DOS shown in fig. A.2. Due to Ni 3d-Mn 3d orbital hybridization, a feature arises

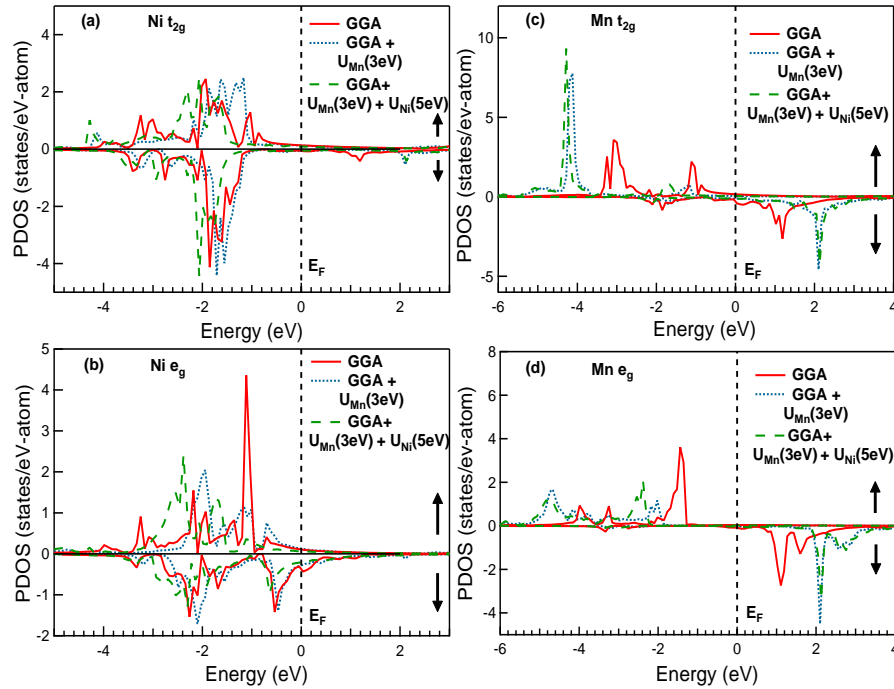


Figure A.2 Spin polarized partial DOS of Ni and Mn t_{2g} and e_g states of Ni_2MnSn with GGA, GGA+ U_{Mn} (3 eV) and GGA+ U_{Mn} (3 eV)+ U_{Ni} . The Fermi energy (E_F) is at 0 eV. The upper/lower panel is for the majority/minority spin channel.

around - 3.1 eV (feature C) for GGA functional. This state shifts to - 4.2 eV (feature C') binding energy for both GGA+ U_{Mn} (3 eV) and GGA+ U_{Mn} (3 eV)+ U_{Ni} (5 eV) functional. The feature around -5.8 eV (feature D) of the spectra corresponds to Mn e_g state. The features C and D match very well with valence band spectra of Ni_2MnGa [17]. The Ni $3d e_g$ state is around - 0.5 eV binding energy (A), which is responsible for martensitic phase transformation in off-stoichiometric composition [14]. Thus, the obtained lattice parameter, magnetic moment and DOS agree with experimental results [12–14] using GGA functional for stoichiometric composition Ni_2MnSn .

The structural transition is reported for off-stoichiometric compositions $\text{Ni}_2\text{Mn}_{1+x}\text{Sn}_{1-x}$ ($x \geq 0.36$) [19]. Thus, the validity of GGA functional for $\text{Ni}_2\text{Mn}_{1.5}\text{Sn}_{0.5}$ is also ascertained by comparing it with GGA+ U_{Mn} (3 eV)+ U_{Ni} (5 eV). In fig. A.3 the relative total ground state energy variation of $\text{Ni}_2\text{Mn}_{1.5}\text{Sn}_{0.5}$ is shown as a function of c/a for GGA and GGA+ U_{Mn} (3 eV)+ U_{Ni} (5 eV) functional. The ground state energy is measured with respect to the energy corresponding to $c/a =$

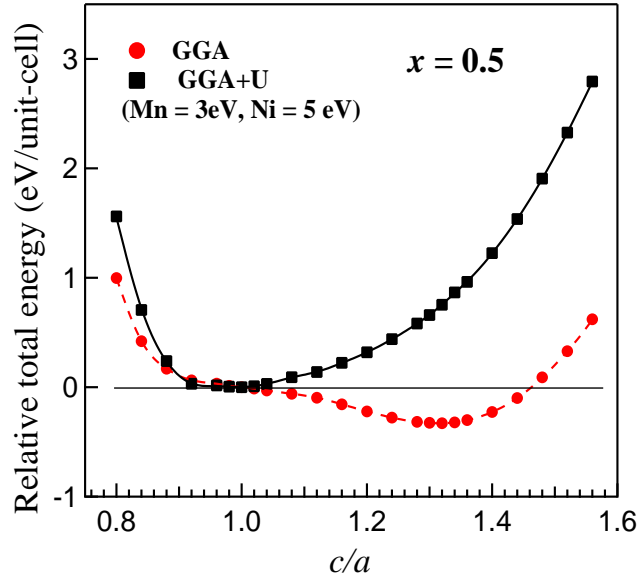


Figure A.3 Ground state energy vs c/a plot of $\text{Ni}_2\text{Mn}_{1.5}\text{Sn}_{0.5}$ calculated with GGA and GGA+U_{Mn}(3 eV)+U_{Ni}(5 eV).

1. A minima in the ground state energy is observed with GGA at $c/a \simeq 1.3$, whereas the minima vanishes for GGA+U functional. This minima corresponds to martensitic tetragonal structural distortion of cubic L2₁ crystal structure [14]. The GGA+U functional suppresses the martensitic phase transition. Thus, GGA functional gives a good agreement of experimental result supporting $c/a > 1$ for off-stoichiometric Ni-Mn-Sn systems [19, 20].

Fig. A.4 (a) - (d) shows the spin integrated total DOS and convoluted total DOS corresponding to $c/a = 1$ and $c/a = 1.32$ of $\text{Ni}_2\text{Mn}_{1.5}\text{Sn}_{0.5}$ using GGA and GGA+U (both Ni and Mn)functional. The convoluted DOS with GGA functional has peaks around -1.0 eV (feature P), -1.7 eV (feature Q) and -3.0 eV (feature R) in austenitic phase. Similar broad features are obtained in experimental UPS VB spectra (fig. A.4) around -1.0 eV, -1.5 eV and -3.1 eV, respectively. In MP, the convoluted DOS with GGA functional shows a peak around -1.4 eV (feature S). Corresponding feature is broad in experimental VB spectra with average spectral weight around -1.2 eV. The convoluted DOS with GGA+U functional has peaks around -2.0 eV (feature E) and -4.4 (feature F) eV in both austenitic phase and martensitic phase. Thus, features of experimental UPS valence band spectra

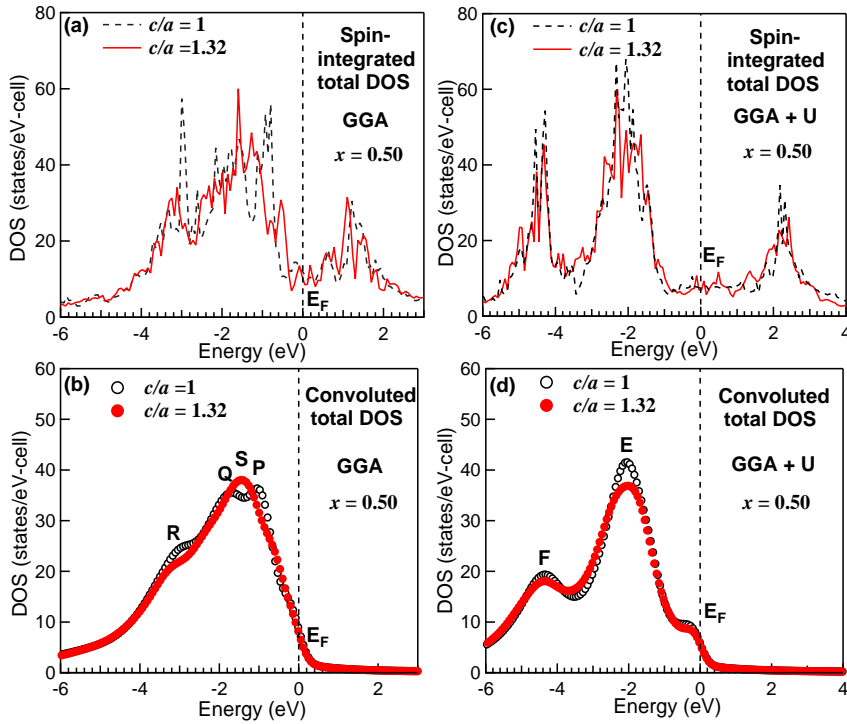


Figure A.4 Spin integrated total DOS, convoluted DOS of $\text{Ni}_2\text{Mn}_{1.5}\text{Sn}_{0.5}$ with GGA [(a) and (b)] and GGA+U (both Ni and Mn) functional [(c) and (d)] for both $c/a = 1$ and $c/a = 1.32$.

could be well explained by GGA functional.

Table A.3 Total magnetic moment/formula unit (in μ_B) of $\text{Ni}_2\text{Mn}_{1.5}\text{Sn}_{0.5}$ with GGA and GGA + U_{Mn} (3 eV)+ U_{Ni} (5 eV) functional in both austenitic and martensitic phase.

Functional	Magnetic moment ($\mu_B/\text{f.u.}$)	
	Austenite phase	Martensite phase
GGA	1.876	1.568
GGA+ U_{Mn} (4 eV)+ U_{Ni}	2.184	2.073

In Table A.3, the total magnetic moment of $\text{Ni}_2\text{Mn}_{1.5}\text{Sn}_{0.5}$ with GGA and GGA + U_{Mn} (3 eV)+ U_{Ni} (5 eV) functional in both austenitic phase and martensitic phase are listed. The experimentally obtained total magnetic moment of $x = 0.5$ in austenitic phase and martensitic phase are $\sim 1.92 \mu_B/\text{f.u.}$ and $\sim 1.355 \mu_B/\text{f.u.}$, respectively [13, 14]. The total magnetic moment obtained using GGA

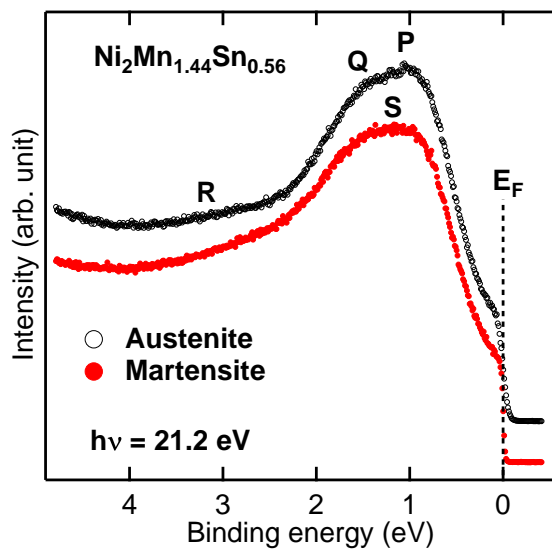


Figure A.5 UPS valence band spectra of $\text{Ni}_2\text{Mn}_{1+x}\text{Sn}_{1-x}$ ($x = 0.44$) in the austenitic and martensitic phases recorded with $h\nu = 21.2 \text{ eV}$.

functional agrees well with experiment than that with GGA+U.

A.4 Conclusions

The GGA functional gives a good support to the experimental observations of lattice parameter, magnetic moment and electronic structure. Thus, the extent of Coulomb correlation already existing within the GGA functional is adequate for description and understanding of both stoichiometric and non-stoichiometric $\text{Ni}_2\text{Mn}_{1+x}\text{Sn}_{1-x}$ properties. Further inclusion of Coulomb correlation term is not necessary.

Bibliography

- [1] A. Ayuela, J. Enkovaara, K. Ullakko, and R. M. Nieminen, *J. Phys.: Condens. Matter* **11**, 2017 (1999).
- [2] A. Ayuela, J. Enkovaara, and R. M. Nieminen, *J. Phys.: Condens. Matter* **14**, 5325 (2002).
- [3] M. E. Gruner, P. Entel, I. Opahle, and M. Richter, *J. Mater. Sci.* **43**, 3825 (2008).
- [4] S. Ö. Kart, M. Uludoğan, I. Karaman, and T. Çağın, *Phys. Stat. Sol. (a)* **205**, 1026 (2008).
- [5] A. T. Zayak, P. Entel, J. Enkovaara, and R. M. Nieminen, *J. Phys.: Condens. Matter* **15**, 159 (2003); A. T. Zayak and P. Entel, *Mater. Sci. Eng., A* **348**, 419 (2004).
- [6] S. R. Barman, S. Banik, and A. Chakrabarti, *Phys. Rev. B* **72**, 184410 (2005).
- [7] B. Himmetoglu, V. M Katukuri, and M. Cococcioni, *J. Phys.: Condens. Matter* **24**, 185501 (2012).
- [8] G. Kresse and J. Furthmüller, *Phys. Rev. B* **54**, 11169 (1996).
- [9] G. van der Laan, S. S. Dhesi, and E. Dudzik, *Phys. Rev. B* **61**, 12277 (2000).
- [10] I. V. Solovyev and M. Imada, *Phys. Rev. B* **71**, 045103 (2005).
- [11] L. Wang, T. Maxisch, and G. Ceder, *Phys. Rev. B* **73**, 195107 (2006).
- [12] T. Krenke, M. Acet, E. F. Wassermann, X. Moya, L. Mañosa, and A. Planes, *Phys. Rev. B* **72**, 014412 (2005).

- [13] T. Kanomata, K. Fukushima, H. Nishihara, R. Kainuma, W. Itoh, K. Oikawa, K. Ishida, K. U. Neumann, and K.R.A. Ziebeck, Mater. Sci. Forum **583**, 119 (2008).
- [14] M. Ye, A. Kimura, Y. Miura, M. Shirai, Y. T. Cui, K. Shimada, H. Namatame, M. Taniguchi, S. Ueda, K. Kobayashi, R. Kainuma, T. Shishido, K. Fukushima, and T. Kanomata, Phys. Rev. Lett. **104**, 176401 (2010).
- [15] R. Kainuma, K. Ito, W. Ito, R.Y. Umetsu, T. Kanomata, and K. Ishida, Mater. Sci. Forum **635**, 23 (2010).
- [16] A. Szytuła, A. Kołodziejczyk, H. Rżany, J. Todorović, and A. Wanic, Phys. Stat. Sol. (a) **10**, 57 (1972).
- [17] A. Chakrabarti, C. Biswas, S. Banik, R. S. Dhaka, A. K. Shukla, and S. R. Barman, Phys. Rev. B **72**, 073103 (2005).
- [18] S. Imada, A. Yamasaki, K. Kusuda, A. Higashiya, A. Irizawa, A. Sekiyama, T. Kanomata, and S. Suga, J. Electron. Spectrosc. Relat. Phenom. **156-158**, 433 (2007).
- [19] Y. Sutou, Y. Imano, N. Koeda, T. Omori, R. Kainuma, K. Ishida, and K. Oikawa, Appl. Phys. Lett. **85**, 4358 (2004).
- [20] Ref. [31] of M. Ye *et al.* Phys. Rev. Lett. **104**, 176401 (2010).